# INFORMATION TO USERS

This manuscript has been reproduced from the microfilm master. UMI films the text directly from the original or copy submitted. Thus, some thesis and dissertation copies are in typewriter face, while others may be from any type of computer printer.

**The quality of this reproduction is dependent upon the quality of the copy submitted.** Broken or indistinct print, colored or poor quality illustrations and photographs, print bleedthrough, substandard margins, and improper alignment can adversely affect reproduction.

In the unlikely event that the author did not send UMI a complete manuscript and there are missing pages, these will be noted. Also, if unauthorized copyright material had to be removed, a note will indicate the deletion.

Oversize materials (e.g., maps, drawings, charts) are reproduced by sectioning the original, beginning at the upper left-hand corner and continuing from left to right in equal sections with small overlaps. Each original is also photographed in one exposure and is included in reduced form at the back of the book.

Photographs included in the original manuscript have been reproduced xerographically in this copy. Higher quality 6" x 9" black and white photographic prints are available for any photographs or illustrations appearing in this copy for an additional charge. Contact UMI directly to order.

**UMI**

A Bell & Howell Information Company
300 North Zeeb Road, Ann Arbor MI 48106-1346 USA
313/761-4700 800/521-0600

# A Model Study of Natural Variability in the Arctic Climate

by

Cecilia M. Bitz

A dissertation submitted in partial fulfillment of
the requirements for the degree of

Doctor of Philosophy

University of Washington

1997

Approved by David S. Battisti
(Chairperson of Supervisory Committee)

Program Authorized
to Offer Degree Atmospheric Science

Date August 11, 1997

In presenting this dissertation in partial fulfillment of the requirements for the Doctoral degree at the University of Washington, I agree that the Library shall make its copies freely available for inspection. I further agree that extensive copying of this dissertation is allowable only for scholarly purposes, consistent with "fair use" as prescribed in the U. S. Copyright Law. Requests for copying or reproduction of this dissertation may be referred to University Microfilms, 1490 Eisenhower Place, P.O. Box 975, Ann Arbor, MI 48106, to whom the author has granted "the right to reproduce and sell (a) copies of the manuscript in microform and/or (b) printed copies of the manuscript made from microform."

Signature Cecilia M Bitz

Date August 11, 1997

University of Washington

Abstract

# A Model Study of Natural Variability in the Arctic Climate

by Cecilia M. Bitz

Chairperson of Supervisory Committee: *Professor David S. Battisti*
*Department of Atmospheric Sciences*

The arctic climate response to natural perturbations in the atmosphere is simulated with two numerical models. The first is a single-column, energy balance model of the atmosphere, sea ice, and upper-ocean system which I use to investigate how the variability in atmospheric energy transport is partitioned in the climate system between storage in the sea ice and net radiation to space. The processes of sea ice ablation/accretion and heat conduction through the sea ice, integrate stochastic variability forcing from the atmosphere. I find that significant, natural, low frequency variability in the arctic sea ice results solely from thermodynamic processes associated with the arctic climate system and the nature of the atmospheric energy transport into the Arctic.

The second model is a sea ice and upper ocean model that is designed to explore variability in the sea ice due to thermodynamics and dynamic processes in a laterally inhomogeneous system. Ice dynamics in this model (including ridging and advection) forced by winds with the proper synoptic scale variability increase the sensitivity of the ice to air temperature anomalies. The air temperature anomalies primarily influence interannual variability in the central region: without realistic air temperature

anomalies, the low-frequency variance of the ice volume is seriously underestimated.

The results provide an estimate for the magnitude and time scales of the natural variability in the arctic climate system. The implications of the low-frequency, natural variability in sea ice volume for detecting a climate change are discussed. Finally, calculations suggest that the variability in the thermodynamic forcing of the polar cap could lead to a freshening in the North Atlantic that is comparable to the freshening associated with the Great Salinity Anomaly.

# TABLE OF CONTENTS

# LIST OF FIGURES

# LIST OF TABLES

# ACKNOWLEDGMENTS

David Battisti, my principal advisor and chairperson of my committee, provided endless encouragement, creative ideas, and technical support. I thank David for his friendship and for making my working environment pleasant and stimulating. I am grateful to my second advisor Richard Moritz for suggesting the initial idea for my work and for lending his precision and attention to detail to my project. Norbert Untersteiner provided the inspiration for the early part of my work and his critical review of my ideas challenged me at all stages. I am also grateful to David Battisti, Richard Moritz, and Norbert Untersteinter for reading and patiently correcting a draft of this dissertation. I thank Christopher Bretherton for help with aspects of the numerical model in Chapter 4 and J. Michael Wallace for advise on the method for synthesizing the forcing fields in Chapter 6. All of the people mentioned thus far deserve credit for serving on my dissertation committee, as well as my out of department member William Zoller.

I am grateful to my husband Eric Sorenson, who listened understandingly to my thoughts about this project. Eric also shared his expertise in material science, helping me understand the material properties of sea ice. I thank my colleagues J. Anthony Beesley and William Lipscomb for helpful discussions.

# Chapter 1

# INTRODUCTION

Sea ice has a profound influence on the disposition of energy transfer between the atmosphere and ocean. Sea ice also stores energy in the climate system, integrating heat fluxes from the atmosphere and ocean. Due to its storage capacity, the mass of sea ice tends to change slowly compared to atmospheric conditions. Because sea ice regulates the exchange of heat fluxes between atmosphere and ocean and stores freshwater, low frequency variability in sea ice has an important influence on climate. Growing evidence exists for substantial interannual, decadal, and interdecadal variability in sea ice extent, sea level pressure, and surface temperature in the Arctic. However, the processes responsible for low-frequency variability in the arctic climate system have only recently been examined. The goal of this dissertation is to explore mechanisms that cause low-frequency variability in the arctic climate system.

The Arctic has received much interest in the past few decades due to concern over the effect of increasing levels of greenhouse gases in the atmosphere. The stability of the present arctic climate is thought to be vulnerable to an expected reduction of the sea ice volume (thickness and areal extent). Understanding processes that control natural variability of the climate system reduces our uncertainty in the evaluation and detection of climatic change.

Variations in sea ice and freshwater advected out of the Arctic Basin affect the near-surface density in the Greenland and Iceland Seas (Aagaard and Carmack, 1989), as evidenced from a coupled sea ice and ocean model simulation for 1955-1975 by

Häkkinen (1993). It is possible that there is a link between arctic outflow and the Atlantic thermohaline circulation which regulates the meridional transport of heat by the ocean.

The potential for relevant interactions between thermodynamic mechanisms and the ice mass in the Arctic and how such variations might affect the global climate system is the subject of this dissertation. I will focus on the central Arctic because the ice is thickest there, thus accounting for a large fraction of the total sea ice mass. Also the central Arctic is the source region of ice that passes into the North Atlantic. As noted by Untersteiner (1990), the variability in the ice extent is small compared to that of the atmospheric heat transport into the Arctic. I hypothesize that some portion of the variability in the heat transport is transferred into substantial low-frequency variability in the arctic sea ice which potentially may lead to significant climatic changes in the North Atlantic.

Measurements of sea ice thickness in the Arctic are too sparse to estimate variability reliably. The most complete record exists at the North Pole (Shy and Walsh, 1996; McLaren et al., 1994) which consists of measurements from 12 submarine voyages. While the variability of sea ice thickness at a single point might be a result of variability that is unrelated to changes in the large scale sea ice thickness, these data do show large interannual variability in the thickness ranging from 2.8 to 4.4 m. Using drifting buoy data, Shy and Walsh (1996) examined *dynamical* forcing mechanisms only and determined that the persistent direction deviation of ice motion from geostrophic wind-forcing and divergence of ice at the North Pole preceding the submarine cruises by 1-2 weeks explained a significant portion of the ice thickness variability. Thermodynamic mechanisms that might explain part of this thickness variability remain unexplored.

Chapman and Walsh (1993) present analysis of Arctic sea ice concentrations (1953-1990) and surface temperature (1960-1990). They found sea ice area anomalies range from interseasonal to interannual timescales. In particular, they found that the Green-

land and Iceland Sea region experienced a large, persistent positive ice area anomaly in the late 1960s and early 1970s. The timing of this anomaly is coincident with the "Great Salinity Anomaly" of the North Atlantic (Dickson et al., 1988). In assessing evidence of climate change in the Arctic over the past several decades, the authors find the largest temperature increase over land area in the Alaskan and western Canadian sector during winter and spring. There is an associated small decrease in the summertime sea ice concentration in the same region. The changes in sea ice extent are mainly confined to the summer months because the ice is land locked in the winter. Seasonally the warming occurs before the ice concentration is measurably decreased. If the warming is connected to the sea ice, this suggest that a decrease in the sea ice thickness and/or an earlier onset of melt are important causes of the warming. However, data are lacking to verify this speculation.

Recently Deser and Blackmon (1993) described a mode of decadal variability in the wintertime surface climate of the North Atlantic that is characterized by a dipole pattern surface temperature (both air and sea) with centers of opposite polarity east of Newfoundland and off the southeast coast of the United States. They find wind anomalies locally over the regions of large surface temperature anomalies and winters of heavy sea ice in the Labrador Sea preceded surface temperature anomalies east of Newfoundland. From these relationships they argue the decadal scale variability of the surface temperatures is the result of (1) a positive feedback between atmosphere and ocean and/or (2) low-frequency variability in arctic sea ice extent.

Two self-sustaining feedback loops have been proposed to explain interdecadal climate variability in the North Atlantic. Mysak et al. (1990) suggest that sea ice anomalies in the Greenland Sea are a result of variation in the sea ice extent in the western Arctic which is controlled by runoff into the western Arctic Ocean. The sea ice anomalies in the Greenland Sea influence convective overturning in the the Greenland sea which ultimately influence the river runoff. There is little evidence that sea ice growth in the western Arctic is controlled by surface salinity anomalies

and this remains a weakness in the feedback presented by Mysak et al. (1990). Later Wohlleben and Weaver (1995) reanalyzed the air-sea-ice relationships and argued that sea surface temperature anomalies in the Labrador Sea influence sea level pressure anomalies over Greenland. These pressure anomalies affect the export of sea ice and fresh water from the Arctic which ultimately affects convection in the Labrador Sea. Finally the loop is completed by variations in the sea surface temperature on the Labrador Sea as a result of the changes in convection.

The influence of low-frequency sea ice thickness anomalies created by atmospheric variability via *thermodynamic* processes in the Arctic was not considered in the feedback loops by either Mysak et al. (1990) or Wohlleben and Weaver (1995). The effect of such low-frequency variability in the sea ice thickness is likely to broaden the spectral range of climate variability in the North Atlantic and perhaps even excite new modes.

Coupled atmosphere-sea ice-ocean climate models with varying levels of sophistication have been used to examine the link between sea ice and variability in the Atlantic thermohaline circulation. Jayne and Marotzke (1997) explore the direct relationship between sea ice and transports of heat and moisture by the atmosphere and heat and salinity by the ocean. Using a simple, three-box model, they find sea ice destabilizes the thermohaline circulation through a positive feedback loop associated with increasing sea ice thickness weakening the thermohaline circulation by enhancing moisture transport to high latitudes in the atmosphere. Ultimately a weaker thermohaline circulation reduces the heat transport by the ocean which causes the sea ice thickness to increase further in their model. Although this model is relatively simple (e.g., the model lacks an annual cycle), the climatic importance of sea ice thickness shown in this study is intriguing.

The Geophysical Fluid Dynamics Laboratory's coupled atmosphere, sea ice, and ocean general circulation model also exhibits variability in the thermohaline circulation (Delworth et al., 1993). Although this model is far more complex than the

three-box model described above, both models simulate thermohaline circulation variability on timescales of approximately 50 years. From a 2000 year integrations with the same model, Delworth et al. (1997) present evidence for multidecadal variations of sea surface temperature and salinity in the Greenland and Iceland Seas that are coherent with the variations of the thermohaline circulation.

There are about a half-dozen (three-dimensional) thermodynamic/dynamic sea ice modeling studies concerning various aspects of sea ice variability in the literature (e.g., Walsh et al., 1985; Häkkinen, 1993; Chapman et al., 1994; Flato, 1995). All these models exhibit rather modest ice mass variability. For example, the annual minimum sea ice area in the Northern Hemisphere from 1960-1989 simulated by Chapman et al. (1994) (typical among the studies) has peak-to-peak variability that is about 16% of the mean (estimated from their Fig. 7). In this hindcast, the annual minimum ice area has considerably smaller variations than those based on observation where the peak-to-peak variability is about 28% (estimated from Fig. 6 Chapman and Walsh, 1993). An objective of this dissertation is to determine what aspects of sea ice models are important for simulating realistic natural variability.

Most modeling studies of arctic climate variability focus on sea ice extent because it can be verified against observations and because the relationship between extent of polar sea ice and surface albedo leads to a positive feedback mechanism. When applied to climate change, the ice-albedo feedback mechanism is thought to be driven by changes in temperature. However, most of the modeling studies of ice variability emphasize how the ice is driven by variability in the wind stress (e.g., Walsh et al., 1985). Sea ice variability associated with thermodynamic processes is often overlooked - in part because of sparse surface observation over the Arctic Ocean and the lack of comprehensive ice thickness measurements for comparison. In fact, sea ice models used in hindcasts are typically forced with monthly mean temperature anomalies which are spatially interpolated from land station data (e.g., Walsh et al., 1985; Chapman and Walsh, 1993; Flato, 1995) or without temperature anomalies altogether

(Häkkinen, 1993).

This dissertation is a compilation of three separate but related parts. The first part is a study of low-frequency natural variability in a one-dimensional coupled atmosphere, sea ice, and mixed layer climate model. These results are summarized in chapter 2. In chapter 3, I present an analysis of the sensitivity of the simulated low-frequency natural variability of the sea ice thickness as a function of the treatment of the thermodynamic processes that are included in a typical global climate model. In chapter 4, I describe a new thermodynamic/dynamic model based on what I have learned from the earlier parts of this study. This model is the first model that is appropriate for climate studies involving arctic sea ice. Finally I employ the new model, in chapters 5 and 6, to explore the patterns, timescales, and processes associated with the variability in sea ice. I summarize the dissertation and draw general conclusions based on all three parts in chapter 7.

# Chapter 2

# LOW-FREQUENCY VARIABILITY IN THE ARCTIC ATMOSPHERE, SEA ICE, UPPER-OCEAN CLIMATE SYSTEM

## *2.1 Introduction*

In this chapter I will use a coupled, thermodynamic atmosphere/sea ice/upper ocean model of the maritime arctic polar cap to investigate how the variability in atmospheric energy transport is partitioned in the climate system between storage in the sea ice and net radiation to space. The processes of sea ice ablation/accretion and heat conduction through the sea ice, integrate stochastic variability in the meridional energy transport.[1] The atmospheric variability is expected to reflect the variability in the forcing (the meridional atmospheric energy transport) on the sub-seasonal to monthly radiative timescale. At longer periods (e.g., decadal) the atmospheric variability will be affected mainly by the variations in the sea ice, the latter due to the integrated and nonlinear effects of the high frequency variability in the overlying atmosphere.

I employ a single-column model of the thermodynamic processes occurring in the

---

[1] There is a loose analogy to the theory of stochastic modeling by Hasselmann (1976) for midlatitude SST anomalies (Frankignoul and Hasselmann, 1977) that would result from random variations in the atmospheric forcing. In the midlatitude case, the heat capacity of the upper ocean exceeds that of the atmosphere by about a factor of 20. In my case, the heat capacity of the sea ice is comparable to that of the atmosphere. Here the slow adjustment of ablation and accretion strongly influence the low frequency response.

coupled arctic atmosphere and sea ice system (see section 2.2.1). The model is forced by the annual cycle of insolation and the meridional atmospheric transport of energy into the Arctic as well as specified cloudiness and snowfall, as described in section 2.2.2. In section 2.3 I will examine the sensitivity of the sea ice thickness to changes in the energy transport including the annual mean and the temporal variance spectrum. The effect of correlating the clouds and snowfall with atmospheric energy transport will be presented. I will also investigate the minimal model physics that is required to simulate arctic climate variability with a thermodynamic atmosphere/sea ice/upper-ocean model. The implications of this study for the simulation and detection of natural and anthropogenic climate changes in the Arctic will be discussed in section 2.5.

## *2.2 Description of the model and forcing data*

### *2.2.1 Model*

The single-column model is designed to study regional arctic processes. The model simulates the vertical exchange of energy among atmosphere, sea ice, and the ocean mixed layer in response to prescribed forcing from insolation, meridional transport of atmospheric energy into the column, cloudiness, and snowfall. A schematic is shown in Fig. 2.1.

The conduction of heat through the sea ice is modeled after Semtner (1976) such that the number of sea ice layers remains fixed while the total sea ice thickness varies and consequently the layer thickness varies. The number of sea ice layers may be varied to examine the response of the system to changes in resolution of the sea ice temperature profile. For simplicity, the sea ice is modeled as a horizontally uniform slab with no leads. In the standard case experiment snow falls on the sea ice surface at a prescribed rate which varies with season and is independent of atmospheric energy transport following Maykut and Untersteiner (1971). (In section 2.3.3 I examine

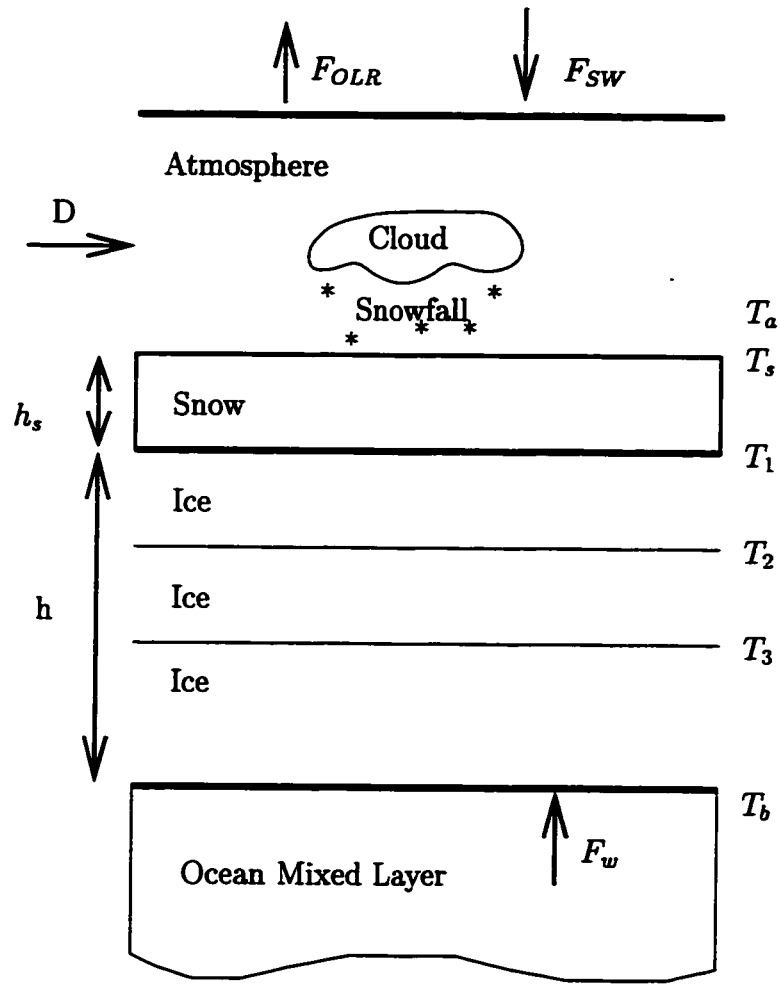


Figure 2.1: Schematic of the coupled atmosphere/sea ice/upper ocean climate model. $F_{SW}$ = incoming solar radiation, $F_{OLR}$ = outgoing longwave radiation, $D$ = atmospheric energy flux convergence, $F_W$ = ocean heat flux, $T_a$ = surface air temperature, $T_s$ = surface sea ice/snow temperature, $T_1$ = temperature of the top of sea ice layer 1, $T_b$ = temperature of ocean mixed layer and the bottom temperature of the sea ice, $h$ = thickness of sea ice, and $h_s$ = thickness of snow.

the model sensitivity to correlating the snow fall rate with the atmospheric energy transport.) When the sea ice surface is snow free, solar radiation penetrates the sea ice, thereby heating the sea ice and the ocean mixed layer. The heat conductivity and the heat capacity of the sea ice are functions of temperature and salinity as in Maykut and Untersteiner (1971). The Saliev method (see Maykut (1969)) is used to solve the heat equation describing the evolution of the ice internal temperature.

The surface albedo, $\alpha$, depends on snow thickness, $h_s$, and sea ice thickness, $h$, as

$$\begin{aligned} \alpha &= \alpha_{ocean} + H(h)\left\{(\alpha_{ice} - \alpha_{ocean})\frac{1}{2}(1 + \tanh(h/2 - 2.5))\right. \\ &\quad \left. + H(h_s)\left[(\alpha_{snow} - \alpha_{ice})\frac{1}{2}(1 + \tanh(h_s/2 - 2.5))\right]\right\}, \end{aligned} \tag{2.1}$$

where $h$ and $h_s$ are given in centimeters, $\alpha_{ocean} = 0.1$, $\alpha_{ice} = 0.55$, $\alpha_{snow} = 0.8$, and $H(h)$ is the unit step function which is defined to be 1 when $h > 0$ and 0 when $h = 0$. With this parameterization, albedo feedback can occur as a result of variability in the date that the snow melts away in spring, and in the date that the upper sea ice surface temperature dips below the freezing point in autumn.

The atmospheric model resolves eighteen vertical layers and is an extension of the radiative-convective model of MacKay and Khalil (1991). Heating rates from absorption and emission of eight atmospheric gases including $H_2O$, $CO_2$, and $O_3$ and atmospheric scattering of solar radiation are computed. Clouds are modeled as a single layer, characterized by a cloud fraction (cloudiness), a grey-body emissivity, and a shortwave optical depth. Vertical convective transport of latent and sensible heat is based on Manabe and Strickler (1964). The most notable changes to the MacKay and Khalil (1991) atmosphere model are the addition of atmospheric energy transport into the column, the randomization of the cloud cover and cloud height, the parameterization of the radiative effects of ice crystal precipitation, and the coupling to the sea ice surface. The prescribed incoming solar flux at the top of the atmosphere is computed for 80° north which is representative of the insolation averaged over the polar cap.

The upper ocean is modeled as a 50 meter slab mixed layer. The salinity of the ocean does not change with time. When the ocean is covered with sea ice, the temperature is fixed at the freezing point of sea water. The heat flux from the ocean to the bottom of the sea ice is equal to the amount of solar radiation that has penetrated through the sea ice.

The single-column model simulates the response of the thermodynamics of the coupled atmosphere/sea ice/upper ocean system averaged over the polar cap. Because the model is one-dimensional, it cannot include the response of atmospheric dynamics and sea ice advection and deformation to the variables simulated by the model. Therefore, I will identify the simulated one-dimensional fluctuations with the variance of corresponding quantities that are integrated over the Arctic Ocean. For example, the modeled variability of sea ice thickness is analogous to the variability of the volume of the sea ice in the Arctic Basin.

### *2.2.2 External Forcing*

Natural climate variability is simulated by the model as a response to the prescribed, aperiodic component of forcing by time dependent cloudiness and meridional atmospheric energy transport. Due to the low frequency variability of the arctic climate system, the model must be integrated for approximately 1000 years to obtain stable estimates of the variance, the spectrum, and other statistics. Because the observations of the forcing span only a few decades, I simulate the required forcing time series using a random number generator. The algorithms that synthesize these random perturbations produce sample statistics consistent with observed variability. The forcing time series for clouds and atmospheric energy flux convergence can be generated independently (see below) or they can be coupled (see section 2.3.3).

In the standard case cloudiness and cloud height are specified at two-day intervals by comparing a random number to daily values from a climatology based on observations at the Soviet NP ice stations (see Fig. 2.11b). For each two-day period, the

sky is clear if the random number is greater than the climatological mean cloudiness for that day, otherwise it is overcast. The two-day timescale is based on the observed decorrelation time of cloud cover and height.

The atmospheric transport of energy, $D$, is the convergences of energy flux into the Arctic Basin. It is the sum of the meridional fluxes of sensible heat, latent heat, and potential energy integrated vertically and horizontally around a latitude circle and divided by the area enclosed by the latitude circle. Hence, for discrete intervals of time, $t = n\tau$ (n is an integer),

$$D(n\tau) = \left( \int c_p[\overline{vT}]\frac{dp}{g} + \int L[\overline{vq}]\frac{dp}{g} + \int [\overline{v\Phi}]\frac{dp}{g} \right) l \Big/ A, \qquad (2.2)$$

where

$$[(\ )] = \frac{1}{2\pi}\int_0^{2\pi} (\ )d\lambda$$

denotes a zonal mean and

$$\overline{(\ )} = \int_0^{\tau} (\ )\frac{dt}{\tau}$$

denotes a time mean (see table 2.1 for a definition of variables). The heating rates forced by $D$ are distributed through the atmosphere of the single-column model with a normalized vertical profile that is independent of time. In the model $D$ is specified as the sum of an annually periodic component and a random component which are based on rawinsonde data at 70° north. I have used monthly mean values of observations from 1965 to 1989 analyzed by Overland and Turet (1994). Figure 2.2 shows the observed mean annual cycle and the monthly standard deviation of $D$. The atmospheric energy flux convergence anomaly (departure from the monthly mean), $D'$, is uncorrelated for time lags of one month and longer and the spectrum is nearly uniform for frequencies less than $(2\ \text{mo})^{-1}$ (see Fig. 2.3).

Each of the three terms in Eq. (2.2) may be broken into four components: the transient eddy flux, the stationary eddy flux, the mean meridional circulation flux, and the net mass flux (see, for example, pg. 324 Peixoto and Oort, 1992). Observations indicate that much of the variance in $D'$ can be attributed to the variability in

Table 2.1: Definition of variables in Eq. 2.2.

| variable | definition |
|---|---|
| $A$ | area enclosed by latitude circle |
| $L$ | latent heat of evaporation |
| $T$ | air temperature |
| $c_p$ | specific heat at constant pressure |
| $g$ | acceleration due to gravity |
| $l$ | distance around latitude circle |
| $p$ | pressure |
| $q$ | specific humidity |
| $t$ | time |
| $v$ | meridional component of velocity |
| $\Phi$ | geopotential |
| $\lambda$ | longitude |
| $\tau$ | time averaging interval |

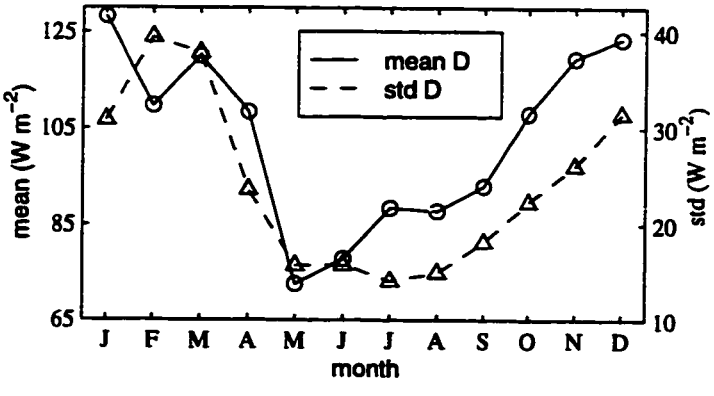


Figure 2.2: The monthly mean (solid line) and monthly standard deviation (dashed line) of the observed atmospheric energy flux convergence, $D$, used to force the single-column model.

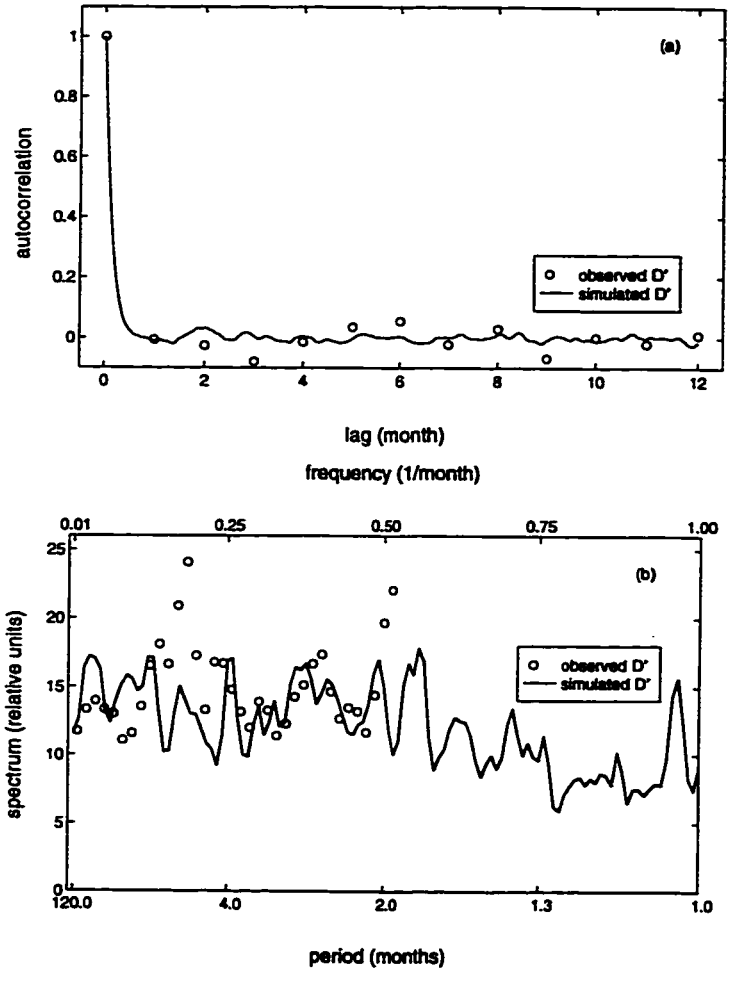


Figure 2.3: (a) Normalized autocorrelation function and (b) power spectrum of the atmospheric energy flux convergence anomaly, $D'$, observed data (circles) and 100 years of the synthesized daily time series (lines) used to force the model. Observations are monthly mean values so spectral information is unavailable for periods below 2 months and the autocorrelation is limited to lag times in monthly intervals.

the sensible heat flux by transient eddies (all year) and standing eddies (in winter) (see Fig 4a Overland and Turet, 1994). Hence, it is plausible that the autocorrelation of $D'$ is similar to mid-latitude baroclinic systems. If so, $D'$ would be correlated for time lags less than about 5 days and the correlation would fall off exponentially with time lag. A time series with these short-term statistical properties would have a spectrum and an autocorrelation consistent with observations (see Fig. 2.3). To simulate a daily time series, I synthesize random perturbations from the discrete Langevin equation,

$$D'(t) = (1 - \beta\Delta t)D'(t - \Delta t) + \Delta t\epsilon(t)z(t), \tag{2.3}$$

where $\Delta t$ is the time step, $\beta^{-1}$ is the characteristic timescale of the fluctuations in $D'$, $\epsilon(t)$ is an annually periodic coefficient that is proportional to the variance of $D'$, and $z(t)$ is a random number with zero mean and unit variance. Note that equation (2.3) describes a discrete first-order Markov process when $\epsilon(t)$ is constant in time and the variance of $D$ is ${\sigma_{D'}}^2 = \Delta t\epsilon^2/(2\beta)$. Figure 2.2 indicates that the observed standard deviation of $D'$ changes slowly with season. To simulate a reasonable seasonal variability for the model, I approximate the time dependence of $\epsilon(t)$ using the seasonal cycle of the observed variance of $D'$. The model is integrated with a time step of $\Delta t = 1$ day, therefore daily values of $\epsilon(t)$ are needed and the observed monthly variance of $D'$ is interpolated to daily intervals by first smoothing the monthly values with a 1-2-1 filter and then using splines. The difference between the observed *monthly* variance and *daily* variance of the true $D'$ depends on the time scale $\beta^{-1}$. For example, if $\beta^{-1} \sim 1$ month the daily variance is nearly equal to the monthly variance, but if $\beta^{-1} \sim 5$ days the daily variance is significantly larger than the monthly variance. An iterative process was used to determine an appropriate amplitude for the annual cycle of $\epsilon(t)$ for a particular $\beta$ in equation (2.3). For the standard case I prescribe $\beta^{-1} = 5$ days which yields a monthly standard deviation of $D'$ equal to $\sim 33$ W m$^{-2}$ in winter (1 November through 31 March) and $\sim 18$ W m$^{-2}$ in sum-

mer (1 June through 31 August). The autocorrelation and spectral variance for the simulated time series are plotted along with those from the observed data in Fig. 2.3.

## 2.3 Experiments

### 2.3.1 Standard Case

In the standard case the single-column model is integrated for 1000 years and is forced by the randomly varying atmospheric energy flux convergence and clouds as described above. Heat conduction through the sea ice is resolved in six layers.

The modeled sea ice thickness, $h(t)$, shown in Fig. 2.4a varies predominantly with the annual cycle and at decadal and longer timescales. The mean sea ice thickness is 3.1 m and the variance of the monthly sea ice thickness anomaly is 0.75 $m^2$. Figure 2.4b shows that the sea ice thickness anomaly, $h'$, exhibits a red-noise power spectrum because the maximum variance is at the lowest frequency and the variance falls rapidly with increasing frequency. The discrete first-order Markov process,

$$h'(t) = ah'(t - \Delta t) + Z(t), \tag{2.4}$$

is a simple linear stochastic model which has red-noise spectrum,

$$H(f) = \frac{c}{1 + a^2 - 2a\cos(2\pi f \Delta t)}. \tag{2.5}$$

Here $c$ is a linear fitting constant related to the total variance, $-\Delta t / \ln a$ is the characteristic timescale of the variance, $f$ is frequency, and $Z(t)$ is white-noise forcing (see Jenkins and Watts, 1968). The modeled sea ice thickness power spectrum is plotted with the best-fit to equation 2.5. See section 2.4 for a physical model of sea ice thickness variability that is consistent with this fit.

From a least-squares fit to the standard case spectrum for $f \leq (4\ \mathrm{yr})^{-1}$, the best fit value for the characteristic timescale for $h'$ is 15 years. A measure of the linearity of the sea ice thickness response to $D'$ is the squared coherency (shown in Fig. 2.4c).

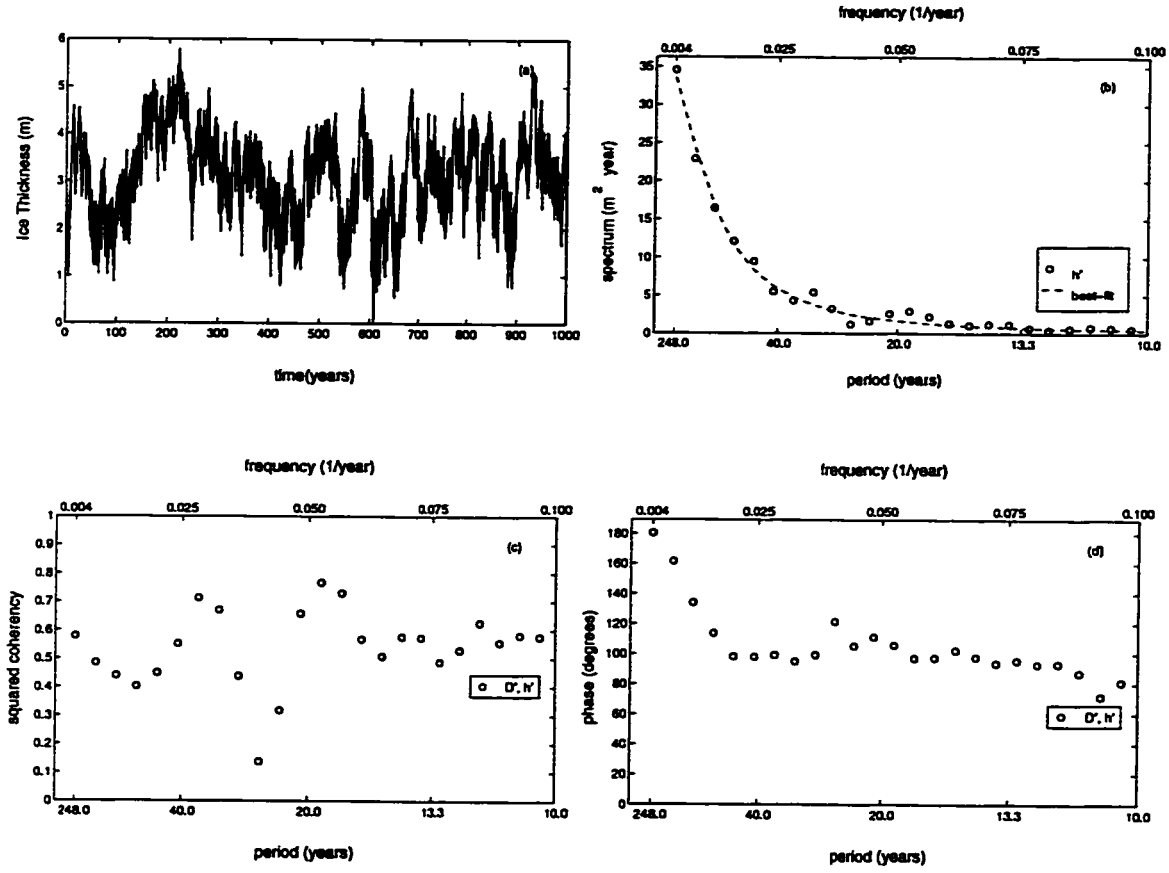


Figure 2.4: The standard case, 1000 year integration (a) monthly sea ice thickness, $h$; (b) power spectrum of yearly sea ice thickness anomaly, $h'$, (circles) and discrete first-order Markov process best-fit (dashed line); and (c) squared coherency and (d) phase spectrum of $h'$ and yearly atmospheric energy flux convergence anomaly, $D'$. The spectra for $h'$ in this figure and in Figs. 2.8, 2.10, and 2.12 are calculated for the last 900 years, $N$, of model output using a lead/lag correlation method smoothed with a 124 year, $L$, Tukey window; therefore, the spectral estimates have $8N/3L = 19$ degrees of freedom (Jenkins and Watts, 1968).

The median squared coherency is 0.5 for $f \leq (10\ \mathrm{yr})^{-1}$. The phase spectrum, shown in Fig. 2.4d, indicates that for $f \gtrsim (50\ \mathrm{yr})^{-1}$, $h'$ and $D'$ vary in quadrature. Hence, for $f \gtrsim (50\ \mathrm{yr})^{-1}$ about 50% of the sea ice thickness variance is consistent with a linear model forced by $D'$. The phase spectrum shows that the sea ice thickness approaches a 180° out-of-phase relation with $D'$ for century timescales.

Figures 2.5a-c show the spectrum of surface air temperature anomaly, $T_a'$, and the squared coherency and phase spectra of ($D'$ and $T_a'$) and ($h'$ and $T_a'$). The surface air temperature is defined as the temperature where the normalized pressure is 0.998, which is approximately 15 meters above the surface. Although the peak variance for $T_a'$ occurs at low frequency, much of the variability is at interannual and intraannual timescales. A discrete, first-order Markov process is fit to the spectral estimates of $T_a'$ in the range of $(10\ \mathrm{yr})^{-1} < f < (6\ \mathrm{mo})^{-1}$ (see Fig. 2.5a). The best fit value for the surface air temperature characteristic timescale is 40 days.

The high squared coherency between $T_a'$ and $D'$ for $f \geq (10\ \mathrm{yr})^{-1}$ in Fig. 2.5b indicates that the surface air temperature responds linearly to $D'$ for the range of frequencies where the ice thickness variability is small. As the frequency approaches zero the power spectrum of $T_a'$ rises sharply which suggests that the surface air temperature is modulated by the large, low frequency, variability in the sea ice thickness. In addition, at the lowest frequencies the squared coherency between $T_a'$ and $h'$ increases while the squared coherency between $T_a'$ and $D'$ falls due to the component of $h'$ that varies non-linearly with $D'$. In Fig. 2.5c, $D'$ leads $T_a'$ by about 10° at $f = (20\ \mathrm{yr})^{-1}$ and it gradually increases its lead to about 45° at timescales shorter than the annual cycle. For the range of frequencies from $(10\ \mathrm{yr})^{-1}$ to $(1\ \mathrm{yr})^{-1}$, $h'$ leads $T_a'$ by 90° (i.e., positive anomalies in the surface air temperature force the sea ice to melt). $h'$ approaches a 180° out-of-phase relationship with $T_a'$ for decadal timescales.

The spectrum of the sea ice/snow surface temperature, $T_s'$, (not shown) is similar to the surface air temperature spectrum. The variance of $T_s'$ is about 95% of the variance of $T_a'$. Table 2.2 lists the monthly standard deviations for the surface air

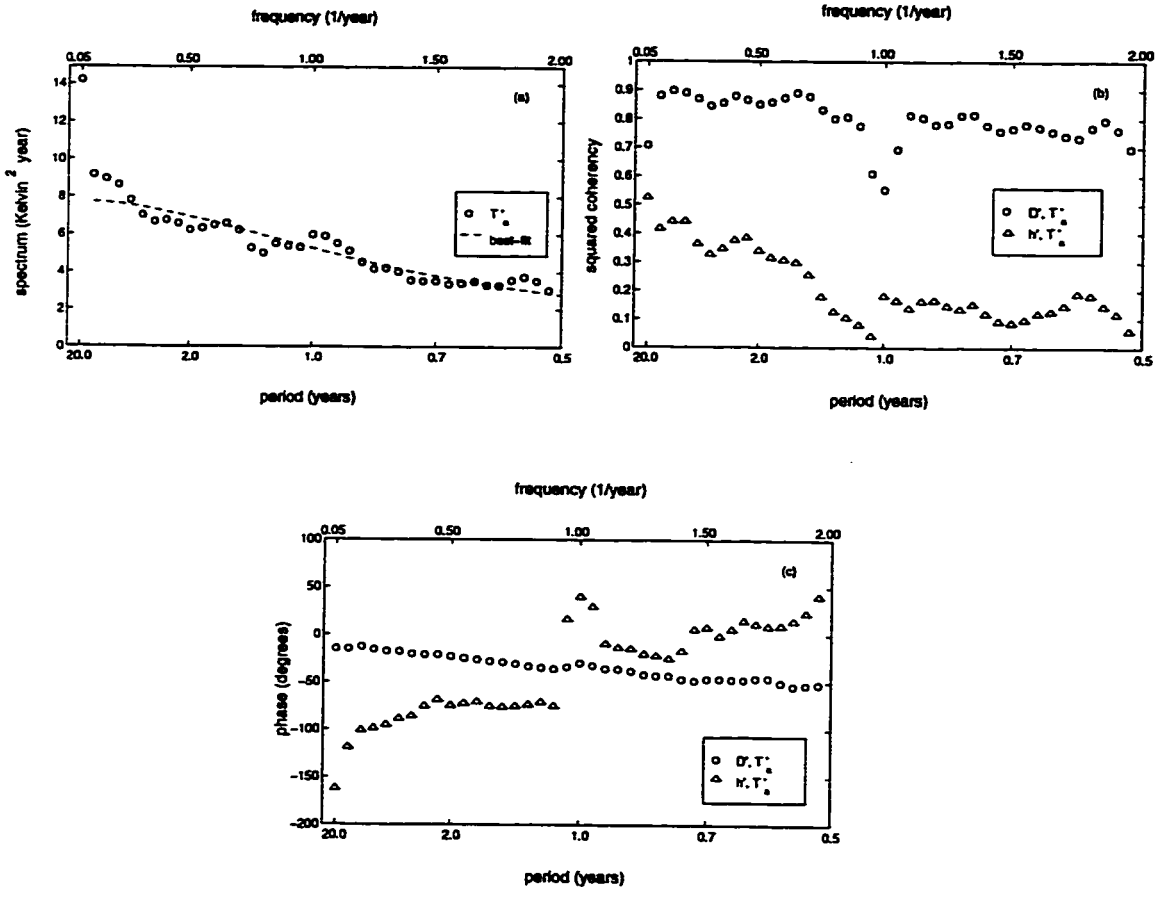


Figure 2.5: (a) Power spectrum of monthly surface air temperature anomaly, $T_a'$, (circles) and discrete first-order Markov process best-fit (dashed-line); (b) squared coherency of $T_a'$ and monthly atmospheric energy flux convergence anomaly, $D'$, (circles) and squared coherency of $T_a'$ and sea ice thickness anomaly, $h'$, (triangles); (c) as in (b), but for phase spectrum. The power spectra for $T_a'$ (this figure) and the outgoing longwave radiation anomaly (Fig. 2.6) are calculated as in Fig. 2.4 except the Tukey window which is 10 years wide; therefore, the spectral estimates have 240 degrees of freedom.

Table 2.2: Standard deviation of the monthly anomalies of surface air temperature, sea ice/snow surface temperature, and flux of outgoing longwave radiation for the standard case.

| | J | F | M | A | M | J | J | A | S | O | N | D |
|---|---|---|---|---|---|---|---|---|---|---|---|---|
| $T_a'$ $(Kelvin)$ | 5.0 | 5.3 | 5.3 | 5.2 | 4.6 | 1.6 | 0.4 | 0.8 | 3.2 | 4.2 | 4.2 | 4.5 |
| $T_s'$ $(Kelvin)$ | 4.8 | 5.1 | 5.1 | 5.0 | 4.4 | 1.4 | 0.3 | 0.7 | 3.1 | 4.0 | 4.0 | 4.3 |
| $F'_{OLR}$ $(W\ m^{-2})$ | 13 | 14 | 14 | 15 | 15 | 8.8 | 7.3 | 7.2 | 8.4 | 9.8 | 11 | 12 |

temperature anomaly sea ice/snow surface temperature anomaly and flux of outgoing longwave radiation anomaly.

The outgoing longwave radiation and planetary albedo are of interest because satellite measurements of these quantities might be used together with observations of $D$ to indirectly monitor the low frequency variability of sea ice thickness. The power spectrum of the outgoing longwave radiation anomaly, $F'_{OLR}$, is shown in Fig. 2.6a with a fit to a discrete, first-order Markov process in the range of $(10\ \text{yr})^{-1} < f < (6\ \text{mo})^{-1}$ which gives a characteristic timescale of 50 days. Figure 2.6b shows that $F'_{OLR}$ responds almost linearly to $D'$ and the squared coherency between $F'_{OLR}$ and $D'$ falls off only slightly for $f < (10\ \text{yr})^{-1}$. The annual mean planetary albedo, $\eta$, defined as the ratio of annual mean outgoing solar radiation to incoming solar radiation at the top of the atmosphere, has a nearly uniform power spectrum (see Fig. 2.7a). Figure 2.7b shows that the squared coherency between the planetary albedo anomaly, $\eta'$, and $D'$ is about 0.4. A comparison of Fig. 2.6b and 2.7b shows that there is a greater coherency between $\eta'$ and $h'$ than between $F'_{OLR}$ and $h'$.

In summary, sea ice thickness varies predominantly at interdecadal timescales with a characteristic timescale of 15 years. About half of the variability of sea ice thickness for $f \gtrsim (50\ \text{yr})^{-1}$ can be explained as a linear response to the atmospheric

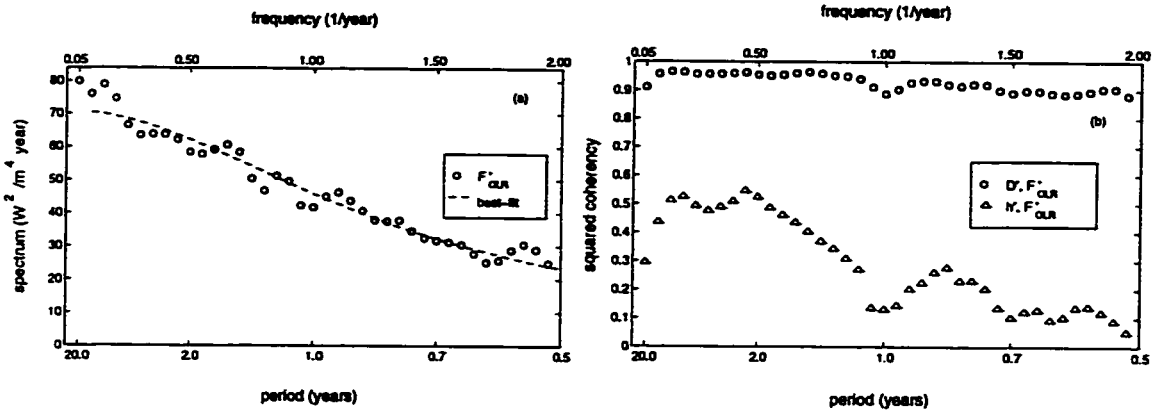


Figure 2.6: (a) Power spectrum of monthly outgoing longwave radiation anomaly, $F'_{OLR}$, (circles) and discrete first-order Markov process best-fit (dashed line) and (b) squared coherency of $F'_{OLR}$ and monthly atmospheric energy flux convergence anomaly, $D'$, (circles) and squared coherency of $F'_{OLR}$ and monthly sea ice thickness anomaly, $h'$, (triangles).

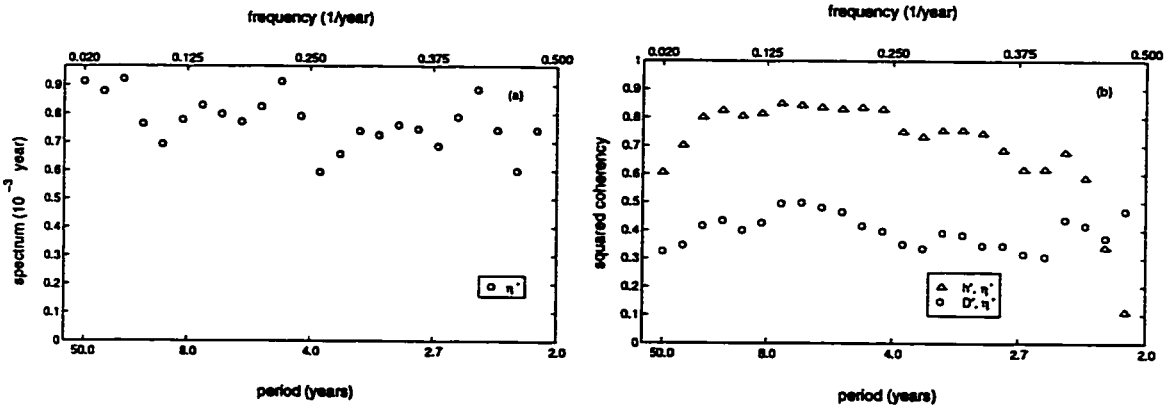


Figure 2.7: (a) Power spectrum of yearly planetary albedo anomaly, $\eta'$, and (b) squared coherency of $\eta'$ and yearly atmospheric energy flux convergence anomaly, $D'$, (circles) and squared coherency of $\eta'$ and yearly sea ice thickness anomaly, $h'$, (triangles). This spectrum is calculated as in Fig. 2.4 except the Tukey window is 25 years wide; therefore, the spectral estimates have 94 degrees of freedom.

energy flux convergence. The variability of the surface air temperature and outgoing longwave radiation have characteristic timescales in the 40-50 day range. About 90% of the variability of the surface air temperature and the outgoing longwave radiation for $f \geq (10\ \mathrm{yr})^{-1}$ can be explained as a linear response to the atmospheric energy flux convergence.

### *2.3.2 Processes responsible for the low frequency variability in sea ice thickness*

In the following section I will present the results of sensitivity experiments that illuminate the key processes responsible for the development of the low frequency variability in the sea ice thickness. I will show that a substantial proportion of the variance of sea ice thickness at decadal and longer timescales is not linearly related to $D'$, but it results from *high* frequency variance in $D'$. I will also show that the system is most sensitive to variability in $D'$ in the late spring and early summer.

To evaluate the response of ice thickness to high frequency forcing, $D'$ was high pass filtered using a cut-off frequency of $f = (5\ \mathrm{yr})^{-1}$ which reduced the monthly mean variance of $D'$ by 25% from the standard case. The power spectrum of the sea ice thickness for this integration is shown in Fig. 2.8. *The sea ice thickness variability is concentrated at low frequencies even though the interdecadal variability has been removed from the forcing.* The variance of ice thickness is reduced to 60% of the variance of the standard case. This value is consistent with my estimate from Fig. 2.4c which indicates that about 50% of the ice thickness spectrum cannot be attributed to forcing by $D'$ at the same frequency.

To isolate the response of sea ice thickness as a function of season, I calculated the mean and the standard deviation of the day of the year when the sea ice surface first begins to melt (i.e., the melt onset date), $d_m$, and the last day that the sea ice surface melts (i.e., the freeze-up date), $d_f$. For the standard case the mean melt onset date is 19 June and the standard deviation is 15 days. The mean freeze-up date is 22 August and the standard deviation is 5 days (see Fig. 2.9a). Observations from

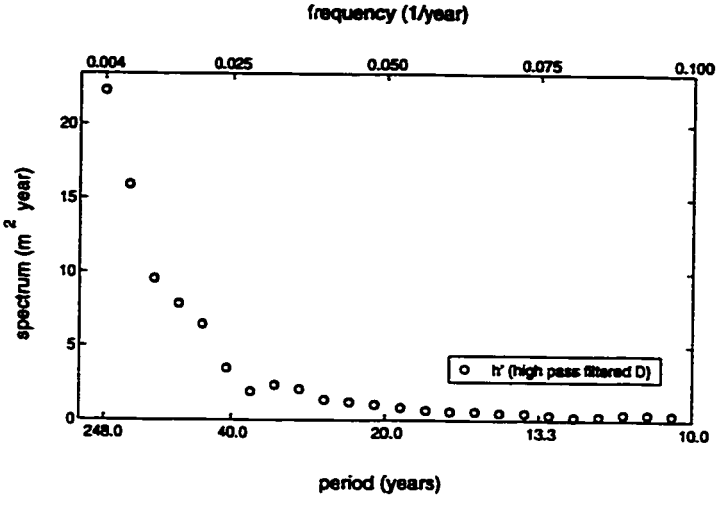


Figure 2.8: Power spectrum of yearly sea ice thickness anomaly, $h'$, when the model is forced with high-pass filtered atmospheric energy flux convergence anomaly, $D'$, with cut-off frequency equal to $(5\ \mathrm{yr})^{-1}$.

the Soviet ice station data show that 10 of the 16 observed melt onset dates occurred between 15-19 June. There is a wider range in the 21 observations of freeze-up dates, with most measured between 12-22 August. The dates of melt onset and freeze-up from the standard case model integration agree with the observed times. However, the model simulates a much wider range of melt onset date than is observed. This difference in the range of simulated and observed melt onset dates may be due to the limited observation record. However, the length of the record does not explain why the simulated range of melt onset is larger than the simulated range of freeze-up dates.

The covariance of $d_m$, $d_f$, and the length of the melt season, $d_f - d_m$, with the annual mean sea ice thickness is shown in Fig. 2.9b. As was suggested by Häkkinen and Mellor (1990), the sea ice thickness depends strongly on the length of the melt season which in the model is determined largely by the variations in the melt onset date. The melt season length leads the annual mean sea ice thickness in Fig. 2.9b which is consistent with the melt season length forcing the sea ice thickness. Conversely, the

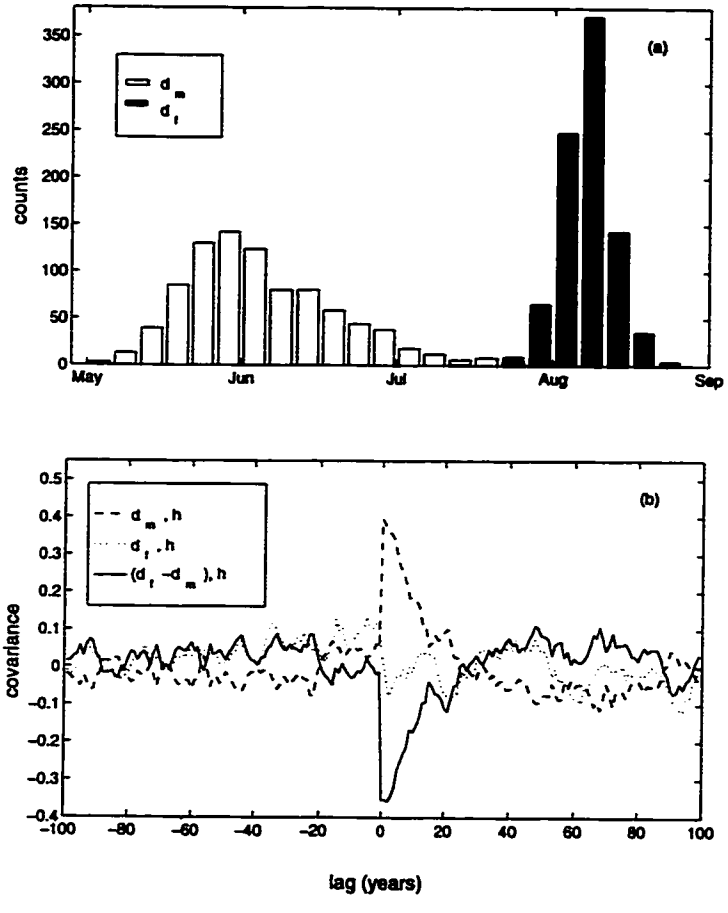


Figure 2.9: For the standard case (a) histogram of melt onset, $d_m$, (white) and freeze-up, $d_f$, (black) denoting the first and last day of the melt season respectively. The months are labeled at the middle of the month and the counts are grouped into five day intervals. These dates are extracted from the last 900 years of the standard case integration. In the 900 year interval there are a few years when the sea ice/snow surface never melts. These exceptionally cool years have not been included in the statistics for melt onset and freeze-up. (b) Mean annual sea ice thickness, $h$, covariance with $d_m$ (dashed), $d_f$ (dot-dashed) and the length of the melt season, $d_f - d_m$ (line). The covariance is normalized so that the covariance at zero lag is equal to the correlation coefficient. The mean sea ice thickness is calculated from 1 June through 31 May.

Table 2.3: Sea ice thickness anomaly monthly variance, ${\sigma_{h'}}^2$, as a function of the season of variability in atmospheric energy flux convergence anomaly, $D'$. The column labeled "impact" denotes the variance in $h'$ relative to the variance in $D'$ normalized with respect to the standard case (see equation 2.6). In the following table winter is defined as 1 November through 31 March, late spring and summer are defined as 1 May through 31 August, melt onset is defined as 6-30 June, and freeze-up is defined as 11 August through 5 September.

| season of variable $D'$ | $\frac{{\sigma_{h'}}^2}{{\sigma_{h'}}^2\|_{standard\ case}}$ | $\frac{{\sigma_{D'}}^2}{{\sigma_{D'}}^2\|_{standard\ case}}$ | Impact |
|---|---|---|---|
| all year (standard case) | 1.00 | 1.00 | 1.00 |
| winter | 0.23 | 0.61 | 0.38 |
| late spring and summer | 0.58 | 0.18 | 3.3 |
| melt onset | 0.12 | 0.028 | 4.3 |
| freeze-up | 0.04 | 0.020 | 2.0 |

melt season length is *not* sensitive to the ice thickness in previous years.

I integrated the model with stochastic forcing in $D'$ limited to only a portion of the year. The sensitivity of the sea ice thickness response to the seasonality of the perturbations in $D'$ indicates that perturbations during late spring and summer are more important than in winter (see Table 2.3). If $D$ is perturbed only during a 24 day window at the beginning of the melt onset (freeze-up), the variance of sea ice thickness is 12% (4%) of the variance of the standard case. The relative impact of the seasonal perturbations in $D'$ are presented in Table 2.3 based on the equation

$$impact \equiv \left(\frac{{\sigma_{h'}}^2}{{\sigma_{D'}}^2}\right) \Big/ \left(\frac{{\sigma_{h'}}^2}{{\sigma_{D'}}^2}\Big|_{standard\ case}\right). \tag{2.6}$$

When $D'$ varies only during melt onset or freeze-up, the power spectra in Fig. 2.10 indicate that the interdecadal variability in sea ice thickness remains prominent. Therefore, the low frequency variability in the system is very sensitive to anomalies in $D'$

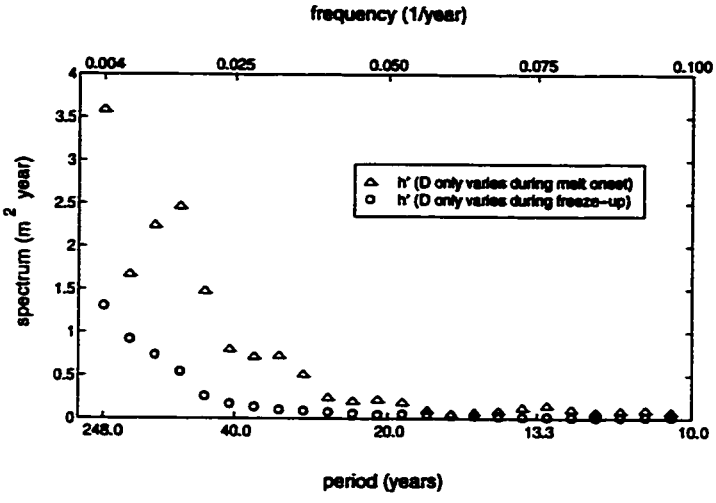


Figure 2.10: The power spectrum of yearly sea ice thickness anomalies, $h'$, when the atmospheric energy flux convergence anomaly, $D'$, varies only during a 24 day window at melt onset (triangles) and freeze-up (circles).

during melt onset.

Table 2.4 shows the changes to the mean sea ice thickness when the annual mean atmospheric energy flux convergence, $\langle D \rangle$, is increased by a fixed percentage throughout the year. The mean sea ice thickness is reduced by 0.5 m and 2.1 m when $\langle D \rangle$ is increased by 1% and 10% respectively. I find a decrease in the variance and the characteristic timescale of sea ice thickness as $\langle D \rangle$ is increased because sea ice thickness variability is strongly dependent on the *mean sea ice thickness*. If the mean sea ice thickness is reduced by varying the solar constant or the oceanic heat flux, I find the variability in sea ice thickness is also reduced.

### *2.3.3 Sensitivity Studies*

*Sensitivity to cloud forcing*

In the standard case experiment cloudiness and cloud height are modeled as random forcing functions that have prescribed statistical properties (as described in section 2.2.2) so that on average there is about 50% cloud cover in winter and 90% cloud

Table 2.4: Sea ice thickness annual mean, $\langle h \rangle$; variance of the monthly mean anomaly, ${\sigma_{h'}}^2$; and characteristic timescale from the spectral variance as a function of the mean annual value of atmospheric energy flux convergence, $\langle D \rangle$. The mean is calculated over the last 900 years of a 1000 year integration.

| $\langle D \rangle$ (W m$^{-2}$) | $\langle h \rangle$ (m) | ${\sigma_{h'}}^2$ (m$^2$) | Characteristic Time Scale (yr) |
|---|---|---|---|
| 97 (standard case) | 3.1 | 0.75 | 15 |
| 98 | 2.6 | 0.56 | 11 |
| 107 | 1.0 | 0.08 | 1.6 |

cover in summer. Cloud cover is so prevalent in the Arctic that day-to-day variations may not affect the low frequency variability of the climate system. In this section I will show that the variability of sea ice thickness is relatively insensitive to the treatment of cloud forcing variability.

In reality, the atmospheric energy flux convergence is likely to be correlated with clouds in the Arctic. To investigate the effects of correlating clouds and $D$, I first compute a linear regression between the annual cycles (denoted by overbar) of the observed climatological mean cloud cover and the latent heat component of the atmospheric energy flux convergence, $\overline{D_L}$, (see Fig. 2.11). Hence

$$\overline{C} = a + b\overline{D_L},$$

where a=0.2 and b=0.04. Finally, the cloud cover for each day is computed according to

$$C = a + bD_L, \text{ subject to } C = [0, 1],$$

where $D_L = wD$ and $w$ is the faction of $\overline{D}$ from latent heating for each day, i.e., $w = \overline{D_L}/\overline{D}$.

When cloud cover and atmospheric energy flux convergence are correlated, there is a significant impact on the mean annual cycle of surface temperature and sea ice thickness, but there is little change in the low frequency variability of the system. The mean winter time surface temperature is lower and the mean sea ice thickness is greater. To maintain a sea ice thickness consistent with the standard case, $D$ is increased by 3.5 W $m^{-2}$ all year. When $D$ is increased to compensate for the cooling, correlating $D$ and $C$ reduces the variance of sea ice thickness by only 10% from the standard case.

I have just shown that correlating cloudiness with the atmospheric energy flux convergence slightly reduces the variability in the climate system from the standard case where the clouds are allowed to vary randomly. If instead I remove all stochastic variability in the cloudiness, so that the cloud cover is the prescribed annual cycle shown in Fig. 2.11b and the cloud height is fixed, the total variance of sea ice thickness is reduced by 25% from the standard case, although the spectral distribution of the variability is nearly unchanged from the standard case. Therefore, variability of sea ice thickness depends on the stochastic variability in the cloud forcing, but it is not necessary for the variability of the cloudiness to be correlated with the atmospheric heat flux convergence.

*Sensitivity to snowfall rate*

In the standard case experiment snowfall is prescribed with a periodic annual cycle. However, I expect that snowfall is correlated with the atmospheric energy flux convergence because the contribution of latent heat to the total energy flux is proportional to the flux of moisture into the Arctic. In section 2.3.2 I showed that variability in the date of sea ice melt onset is linked to the variability in sea ice thickness. If the snowfall rate is correlated to anomalies in $D$, then positive anomalies in snow depth could insulate the surface and reduce the impact of positive anomalies in $D$. Also the positive correlation between snow depth and $D$ prior to melt onset may tend to

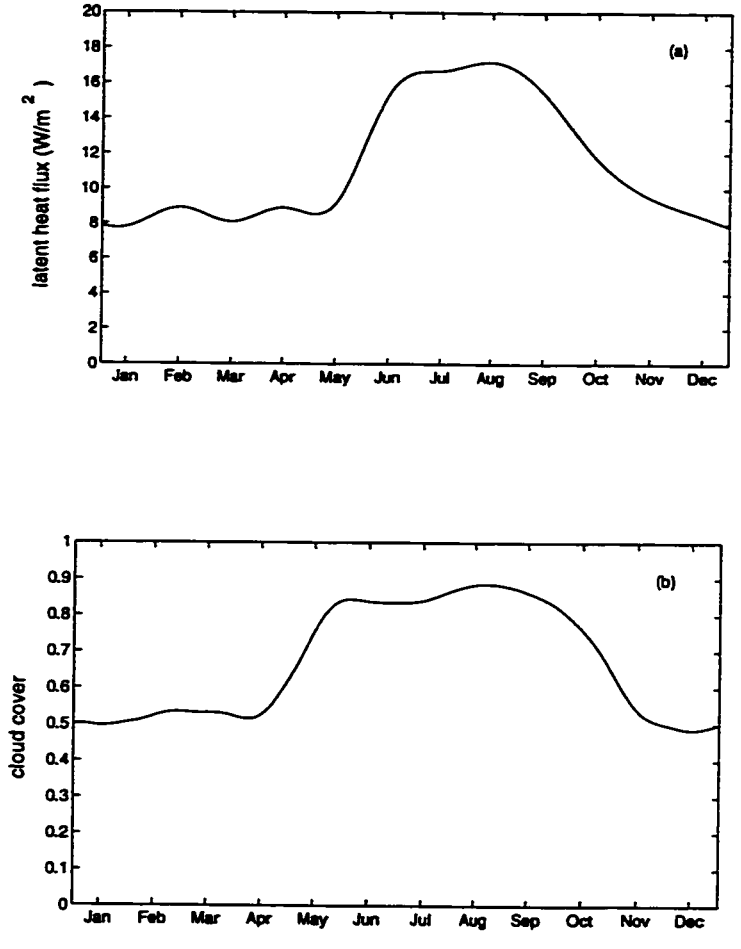


Figure 2.11: (a) Component of the mean annual cycle of atmospheric energy transport that comes from latent heat (daily values splined from observed monthly mean Overland and Turet (1994) and (b) mean annual cycle of cloud cover (daily values splined from observed 3 day mean of Soviet ice station data).

narrow the range of melt onset date, which has been shown to affect the variability of sea ice thickness.

To obtain an estimate of the importance of variability in the snowfall rate, I assume the snowfall rate is proportional to the moisture flux, i.e., I do not account for storage of moisture in the atmosphere and subsequent snowfall at a later time. The moisture flux across the 70° latitude circle is $D_L/L$, where L is the latent heat of evaporation. Observations indicate that, on average, the total amount of moisture that crosses the latitude circle at 70° north during the time of the year when the upper sea ice/snow surface is below the melting temperature is 90 kg $m^{-2}$ (Overland and Turet (1994)). To accumulate an average annual snowfall depth equal to $\sim$ 0.3 m (as in the standard case), the snowfall rate is equal to the moisture flux multiplied by (275 kg $m^{-3}$)$^{-1}$.

When the snowfall rate and atmospheric energy flux convergence are correlated, I find that there is a modest effect on the mean and the variability of the climate. The mean wintertime surface temperature is lower than the standard case and the mean sea ice thickness is greater. To maintain a sea ice thickness consistent with the standard case, $D$ is increased by 2.5 W $m^{-2}$ all year. When $D$ is increased to compensate for the cooling, the variance of the sea ice thickness is 35% less than the standard case. The standard deviation of the melt onset date is reduced from 15 days for the standard case to less than 14 days when the snowfall rate and $D$ are correlated. This suggests that increasing snow depth during anomalously warm events in $D$ can reduce the influence of $D$ on the variability of sea ice thickness.

*Sensitivity to model resolution*

I have varied the number of layers in the sea ice model to see how the variability of sea ice thickness depends on the resolution of the temperature profile. Table 2.5 demonstrates that both the total variance of sea ice thickness and the characteristic time scale increase with increased temperature resolution. This shows that the low

Table 2.5: Sea ice thickness anomaly variance, $\sigma_{h'}{}^2$, as a function of number of sea ice layers. To keep the mean ice thickness approximately equal to the standard case value, the mean value of the atmospheric energy flux convergence was adjusted for the integrations with less than six sea ice layers.

| number of layers | $\sigma_{h'}{}^2$ ($m^2$) | Characteristic Time Scale (yr) |
|---|---|---|
| 6 (standard case) | 0.75 | 15 |
| 4 | 0.72 | 15 |
| 2 | 0.61 | 13 |
| 1 | 0.33 | 6 |

frequency variability is greatest in simulations where the temperature profile in the sea ice is well resolved. The variance of surface air temperature, sea ice/snow surface temperature, and outgoing longwave radiation are not sensitive to changes in the number of layers in the sea ice model because a substantially higher portion of the total variance in these variables is associated with the higher frequency variance in the atmospheric energy flux convergence and hence they are decoupled from the low frequency response in the sea ice.

In addition to changing the vertical resolution of the sea ice model, I have replaced the more elaborate MacKay and Khalil (1991) radiative-convective atmosphere model with a simple two stream, radiative equilibrium atmosphere as in Thorndike (1992b). This change eliminates the time lag associated with radiative transfer. The sea ice thickness power spectrum, shown in Fig. 2.12a, indicates that the variability is still concentrated at low frequencies. However, the spectrum of sea ice thickness falls off faster with frequency than the standard case. The squared coherency and phase spectrum of sea ice thickness and atmospheric energy flux convergence (Fig. 2.12b and

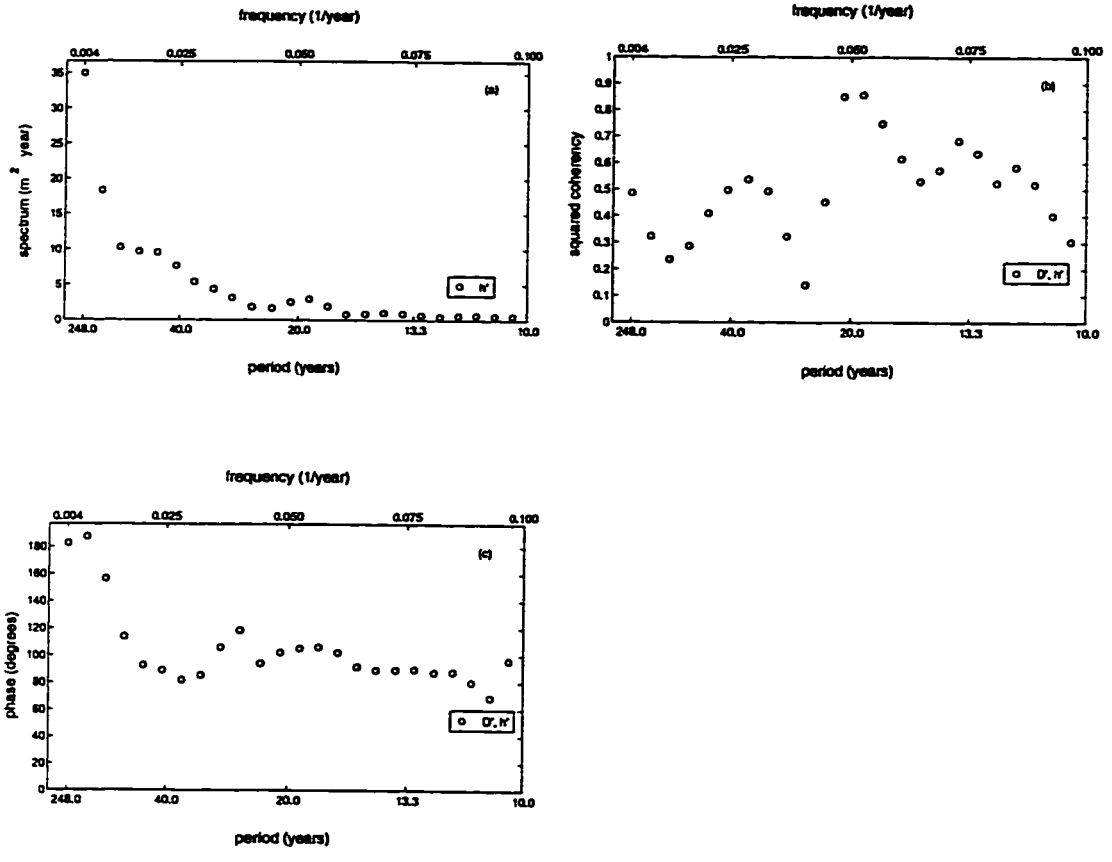


Figure 2.12: (a) Power spectrum of yearly sea ice thickness anomaly, $h'$; (b) squared coherency and (c) phase spectrum of $h'$ and yearly atmospheric energy flux convergence anomaly, $D'$ for an integration where the radiative/convective atmosphere model is replaced with a two stream atmosphere model.

c) are similar to those of the standard case. The power spectrum of the sea ice/snow surface temperature (not shown) is also similar to the standard case spectrum.

*Ice export and the arctic climate*

The general circulation of arctic sea ice includes the anticyclonic Beaufort Gyre and the transpolar drift stream. Ultimately, most of the ice in the these circulating regimes exits through Fram Strait. This export amounts to approximately 10% of the total mass of sea ice in the Arctic Ocean each year (e.g., Rothrock, 1975). Hence, sea ice has a limited lifetime due to transport out of the Arctic which may affect the low frequency variability of the sea ice volume. Colony and Thorndike (1985) estimate that the mean lifetime ranges from essentially zero at Fram Strait to approximately six years north of Ellsmere Island.

To mimic qualitatively the effects of mean sea ice export through Fram Strait, an additional term is added to the equation for bottom ablation/accretion from the standard case, $-\kappa h$, where $1/\kappa = 10$ yr is the time constant for ice export. To maintain a sea ice thickness consistent with the standard case, the annual mean of $D$ is lowered by 7.5 W m$^{-2}$ all year. The results, displayed in Fig. 2.13, indicate the variance of monthly sea ice thickness is diminished by about 50% and the characteristic timescale for the variability of sea ice thickness is reduced to 6 years. Thus, while this simple representation of ice export does not change the qualitative result that significant low frequency variability is forced by thermodynamic processes, I anticipate that ice export has an important quantitative effect on the sea ice thickness variability.

## 2.4 Physical model

A simple model describing the growth of perennial sea ice due to thermodynamic processes with both annually and interannually varying forcing can be written

$$h_{n+1} = h_n + \overline{G(h_n)} - \overline{M} + G'_n - M'_n, \tag{2.7}$$

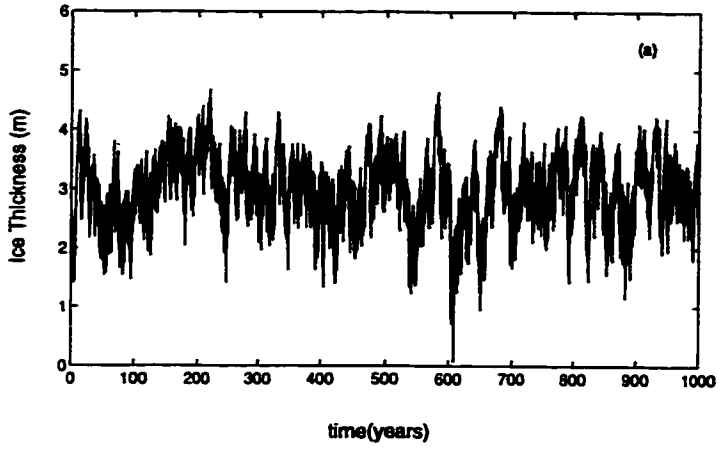


Figure 2.13: Sea ice thickness from integration to qualitatively examine the effects of mean sea ice export through Fram Strait.

where $h_n$ denotes the ice thickness at the start of the growth season during the $n$th year, $G$ and $M$ are the annual thickness changes from growth and melt respectively. The terms with overbars (primes) represent thickness changes from annually periodic forcing (interannually varying forcing). With the addition of the influence from interannually varying forcing, this model is an extension to that given in section 5 of Thorndike (1992b). Note that in Eq. 2.7, $\overline{G}$ is written as an explicit function of $h_n$ because the growth rate is quite sensitive to the thickness while the thickness dependence of $\overline{M}$ is neglected.

If we ignore the effects of aperiodic forcing in the ocean, then Eq. 2.7 can be simplified by neglecting $G'_n$. This approximation is justified because the integrated effect of aperiodic atmospheric forcing on growth is small over the relatively long growth season (see table 2.3). Defining the equilibrium thickness $h_{eq}$ such that the change from growth equals that from melt, $\overline{G(h_{eq})} = \overline{M}$, and letting $h' = h - h_{eq}$, allows Eq. 2.7 to take on a particularly simple form

$$h'_{n+1} - h'_n = h'_n \left.\frac{\partial \overline{G}}{\partial h}\right|_{h_{eq}} - M'_n. \tag{2.8}$$

The first term on the right hand side represents negative feedback in the system

where $(-\partial\overline{G}/\partial h)^{-1}$ evaluated at $h_{eq}$ is a decay time constant (in years). The second term on the righthand side represents variations in the melt which are related (but not equal) to anomalies of the atmospheric heat flux convergence. $M'$ depends on processes in the ice, hence some fraction of $M'$ may be non-linearly related to the atmospheric heat flux convergence. If $M'$ has the characteristics of white-noise, then Eq. 2.8 has the form of a discrete first-order Markov process (see Eq. 2.4) which was used for the fit shown in Fig. 2.4(b) for the ice thickness power spectrum. According to Eq. 2.8, the non-linear fitting parameter $a$ is

$$a = 1 + \left.\frac{\partial\overline{G}}{\partial h}\right|_{h_{eq}}. \tag{2.9}$$

For the simple stochastic model in Eq. 2.4, the variance of the yearly[2] ice thickness ($\sigma^2_{h'}$) is related to the variance of the melt ($\sigma^2_{M'}$) by

$$\sigma^2_{h'} = \sigma^2_{M'}\frac{\tau}{2}. \tag{2.10}$$

The characteristic timescale, $\tau$, which equals $1/ln(a)$, depends on processes and approximations that affect the growth rate such as the snow depth, the vertical resolution of heat conduction in the ice, and the equilibrium ice thickness (see section 2.3.3). For example, table 2.5 shows that the timescale depends on the number of layers in the sea ice. Computing $\sigma^2_{M'}$ as a residual from $\tau$ and $\sigma^2_{h'}$ (see table 2.6, shows that the variance of the melt is relatively insensitive to the number of layers. This might be expected because the ice is nearly isothermal during the melt season. In contrast, the experiments with stochastic forcing in the atmosphere limited to only a portion of the year (see end of section 2.3.2) all had the same characteristic timescale (not shown), and so ${\sigma_{M'}}^2$ is 0.059 $m^2yr^{-1}$ (0.022 $m^2yr^{-1}$ ) for the experiments with stochastic forcing in summer (winter).

---

[2] Although in this chapter $\sigma'_h$ is cited for *monthly* anomalies and Eq. 2.10 refers to *yearly* anomalies, due to the long time scale for the volume variability, there is little difference.

Table 2.6: Variance of annual ice melt, $\sigma^2_{M'}$, as a function of number of sea ice layers $\sigma_{h'}{}^2$, as a function of number of sea ice layers.

| number of layers | $\sigma_{M'}{}^2$ $m^2yr^{-1}$ |
|---|---|
| 6 (standard case) | 0.10 |
| 4 | 0.096 |
| 2 | 0.094 |
| 1 | 0.11 |

With Eq. 2.8 I have developed a physical model to describe the time evolution of the sea ice thickness anomalies that is consistent with that simulated in the standard case integration of the single-column model. Relationships from the physical model are consistent with the dependence of the characteristic timescale on the model processes and approximations tested with sensitivity studies using the single-column model.

## *2.5 Discussion and conclusions*

The single-column model model predicts that the variability of sea ice thickness averaged over the central Arctic Ocean when it is forced by realistic atmospheric perturbations occurs predominantly at low frequencies. A characteristic timescale, estimated by least-squares fitting of the ice thickness spectrum to the spectrum of a discrete, first-order Markov model, is 15 years for the standard case. Although the single-column model is a very simple model, the standard deviation and characteristic timescale of the modeled sea ice thickness agree to within about a factor of two with two more physically complete models which are forced by monthly air temperature

anomalies (Häkkinen and Mellor, 1990; Flato, 1995).

The phase spectrum between sea ice thickness and atmospheric energy flux convergence is nearly constant at 90° for the range $f \gtrsim (50\ \mathrm{yr})^{-1}$, and the squared coherency in this range is approximately 0.5 (Fig. 2.4). Therefore, half of the variability of ice thickness in this range is consistent with the features of a linear model, directly forced by perturbations of atmospheric energy flux convergence. However, it is clear that about half of the variability is *not* explained by such a model, and experiments with high pass filtered forcing (Fig. 2.8) suggest that high frequency variability in the atmospheric energy flux convergence induces the unexplained low frequency variability through nonlinear processes.

It appears likely that the nonlinearities in the sea ice response arise because the sea ice adjusts to thermal forcing by changing its temperature and thickness in a complicated way. In particular, the physical mechanisms governing these processes undergo step changes at the onset of melt and at freeze-up. Figure 2.9 shows that a typical anomaly in the melt onset date influences the sea ice thickness for several decades. It appears that anomalous melting associated with the onset of the melt season can induce a very broad, low frequency response in the sea ice thickness.

The relevance of the onset of melting to the low frequency variability is also suggested by the fact that the sea ice thickness variance is most sensitive to atmospheric energy flux convergence perturbations in late spring. For example, when the atmospheric energy flux convergence is anomalously high in late spring, the snow begins to melt earlier. As the snow melts, the surface albedo decreases and "locks" in the effect of the anomalously high atmospheric energy flux convergence by lengthening the melt season which ultimately thins the sea ice. There is not an equivalent interaction between the atmospheric energy flux convergence and the effect of the surface albedo at freeze-up partly due to the low elevation angle of the sun in late August.

The total variance and characteristic timescale of the sea ice thickness increase with the mean thickness and with the number of sea ice layers in the model. When the

modeled ice temperature profile is constrained to be linear so that the heat capacity and the effects of brine pockets are neglected, the model over estimates the annual cycle. The timescale of the variability, according to the simple physical model in section 2.4, depends on the annual cycle of ice growth.

If the large, low frequency variability in the sea ice thickness is realistic, then one would have to measure sea ice thickness in the Arctic over several decades to obtain an accurate estimate of the climatological mean. My model results imply that the best variables for indirectly detecting low frequency fluctuations in the sea ice thickness are the surface temperature and the planetary albedo because there is significant squared coherency between the sea ice thickness and surface temperature (0.5) and the sea ice thickness and planetary albedo (0.7) for frequencies less than $(10\ \mathrm{yr})^{-1}$. In contrast, the squared coherency of the sea ice thickness with outgoing longwave radiation is only 0.4 for low frequencies.

The results presented do not depend on the details of the atmospheric radiation model. I have found the same qualitative variability in the sea ice thickness and surface sea ice/snow temperature when the entire atmosphere model is reduced to a simple two stream radiative equilibrium model. I have modeled cloud cover as highly correlated with the atmospheric energy flux convergence and found little change in the variability of the climate system. On the other hand, the sea ice thickness variability is affected by the resolution of the ice temperature profile, the variability in annual accumulated snowfall, and by the abrupt change in the surface albedo and the sea ice surface temperature at melt onset. This suggests that it is important to use adequate temperature resolution in the ice (at least four ice layers) and to include the effects of accumulated snowfall in surface heat conduction and the surface albedo in models of the arctic climate system. A simple, qualitative experiment suggests that the sea ice export will have a significant impact on the low frequency variability in the sea ice volume.

From these results, I can estimate how long one must wait to detect a change

in the mean sea ice thickness by using statistical decision theory. To determine if a step change has occurred in the climatological mean sea ice thickness, I pose a simple null hypothesis: *there is no difference between the mean ice thickness before and after the supposed climate change.* Rejection of the null hypothesis implies that *the mean ice thickness has changed,* with some probability given by a significance level. The significance of the difference between the two sample means depends on the number of independent measurements used to estimate each mean and the variance of the ice thickness. I assume that the number of independent measurements of sea ice thickness equals the length of time that the thickness has been monitored divided by the characteristic timescale of the sea ice thickness variability. I use results for the variance ($\sigma_{h'}^2 = 0.75$ m$^2$) and characteristic timescale (15 yr) of sea ice thickness from the standard case. For example, to obtain 4 independent measurements of sea ice thickness before a supposed climate change, one would have to monitor the sea ice thickness for 60 years. The solid lines in Fig. 2.14 show contours of the significance level to reject the null hypothesis for the standard case, as a function of the number of independent measurements and the estimated difference in mean thickness. For example, sea ice thickness must be monitored for 60 years for a 1.4 m change in the mean sea ice thickness to be significant at the 95% confidence level (see letter A in Fig. 2.14). Suppose one only wants to wait 30 years, then the difference of the means must be at least 0.7 m to detect a climate change at the 75% confidence level (letter B in Fig. 2.14). In contrast, if the sea ice thickness variance is 0.35 m$^2$ and the characteristic timescale is 6 years (e.g., in the case that includes a simple parameterization for sea ice export, section 2.3.3), the criteria for significance are more readily met (dashed line in Fig. 2.14). Therefore, a 1.3 m change would require measurements taken over 12 years in order to detect a climate change at the 95% confidence level (see letter C in Fig. 2.14).

Finally, I note that much has been written about the importance of convection in the subpolar seas to the global thermohaline circulation as mentioned in the in-

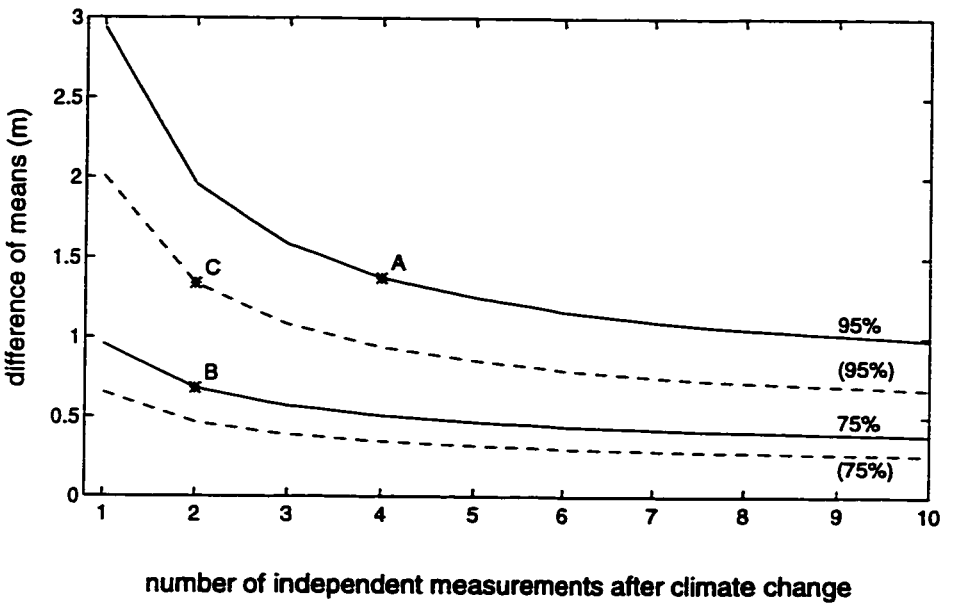


Figure 2.14: Contours show the significance level as a function of the estimated difference in the climatological mean sea ice thickness before and after a climate change and the degrees of freedom of the measurement after the climate change. The solid contours are computed using the results from the standard case and the dashed contours are computed using the results from the case which includes a simple parameterization for sea ice export. I assume that there are four independent thickness measurements before the climate has changed. The t-statistic, derived from Student's T distribution, is used to determine the 75 and 95% significance levels.

troduction. A weak salinity stratification characterizes the density structure in the North Atlantic. Aagaard and Carmack (1989) estimate that the principal source of fresh water in the Greenland, Iceland and Norwegian Seas region is the influx of sea ice and low salinity polar surface water through Fram Strait. The freshwater transport into the North Atlantic from sea ice flux through Fram Strait given in Aagaard and Carmack (1989) is 2800 $km^3$ $yr^{-1}$. Dickson et al. (1988) estimate that the total freshwater excess during the Great Salinity Anomaly (GSA) in the 1970's was approximately 2200 $km^3$. If it is true that ice export is the dominant source for freshwater transport into the North Atlantic, from the model results I estimate that even without anomalies in the ice velocity at Fram Strait, the standard deviation of the freshwater transported by ice would be $\sim$ 780 $km^3$ $yr^{-1}$ which is found by multiplying 2800 $km^3$ $yr^{-1}$ by the ratio of the standard deviation to mean sea ice thickness, $\sigma_h/\bar{h} = 0.28$. Hence, it may be possible that thermodynamic processes alone can account for freshening of the North Atlantic comparable to the freshening during the GSA. For example, a sea ice volume anomaly that is one standard deviation above the mean for 3 years translates to a 2300 $km^3$ freshwater volume.

My objective in this study was to assess the potential for natural interannual, decadal, and longer timescale variability in the arctic sea ice that results because of the special thermodynamics associated with the coupled arctic atmosphere, sea ice, and upper ocean system. I have shown that significant, natural, low frequency variability in the arctic sea ice is expected solely due to thermodynamic processes associated with the arctic climate system and the nature of the atmospheric energy transport into the Arctic. Additional processes not considered in this chapter may contribute to the low frequency variability in the sea ice. These include the effects of open water, new ice growth, sea ice export, and dynamics and thermodynamics in a distributions of sea ice thicknesses. How these processes affect sea ice variability is further explained in chapter 5. It is also likely that low frequency variability in the sea ice volume is affected by variability in the ocean circulation below the mixed layer.

An examination of how the ocean thermohaline circulation affects sea ice variability is beyond the scope of this dissertation.

# Chapter 3

# COMPARISON OF NATURAL VARIABILITY IN THE ARCTIC CLIMATE SIMULATED BY THE COLUMN MODEL AND BY THE GFDL GCM

## *3.1 Overview of chapter 3*

In this chapter I examine the natural variability of the arctic climate system simulated by two very different models: the Geophysical Fluid Dynamics Laboratory (GFDL) global climate model, and the single column model (SCM) from chapter 2 which is an area-averaged model of the arctic atmosphere/sea ice/upper ocean system. A 1000 yr integration of the SCM is performed in which the model is driven by a prescribed, stochastic atmospheric energy flux convergence ($D$) which has spectral characteristics that are identical to the spectra of the observed $D$. The standard deviation of the yearly mean sea ice thickness from this model is 0.85 m; the mean sea ice thickness is 3.1 m. In contrast, the standard deviation of the yearly averaged sea ice thickness in the GFDL climate model is found to be about 6% of the climatological mean thickness and only 24% of that simulated by the SCM.

I present a series of experiments to determine the cause of these disparate results. First, after changing the treatment of sea ice and snow albedo in the (standard) SCM model to be identical thermodynamically to that in the GFDL model, I drive the SCM with $D$ from the GFDL control integration to demonstrate that the SCM model produces an arctic climate similar to that of GFDL model. I then examine integrations of the SCM in which the different prescriptions of the sea ice treatment (GFDL vs. standard SCM) and $D$ (GFDL vs. observed) are permutated. My results

indicate that unarguable improvements in the treatment of sea ice in the GFDL climate model should amplify significantly the natural variability in this model. I present calculations that indicate the variability in the sea ice thickness is extremely sensitive to the spectrum of the atmospheric energy flux convergence. Specifically, the differences between the GFDL and observed $D$ at time scales *shorter* than three years are shown to have a significant, impact on the sea ice variability *on all time scales.* A conservative best-estimate for the amplitude of the natural variability in the arctic sea ice volume is presented; this estimate is a significant fraction (about 25%) of the mean sea ice thickness.

My results suggest that most of the global climate models that have been used to evaluate climate change may also have artificially quiescent natural variability in the Arctic.

## *3.2 Introduction*

The Arctic is portrayed in current climate models as a region of high sensitivity and widespread influence. State-of-the-art numerical models of the earth's climate system (each of which contains sophisticated modules for the ocean, atmosphere, cryosphere and land surface[1]) indicate that the surface warming associated with increasing levels of greenhouse gases in the Earth's atmosphere is greatest in the Arctic. However, little has been reported about the ability of these models to simulate the natural low frequency variability in the arctic climate system which, in reality, may obscure greenhouse gas warming.

Sea ice thickness varies on much longer time scales than the atmospheric forcing on the sea ice. Hence, variability in the arctic sea ice thickness may be used to measure the low-frequency variability in the arctic climate system. In the previous chapter I used an arctic atmosphere/sea ice/upper ocean climate system (in this chapter the

[1] Hereafter, I refer to these models as General Circulation Models, or GCM's.

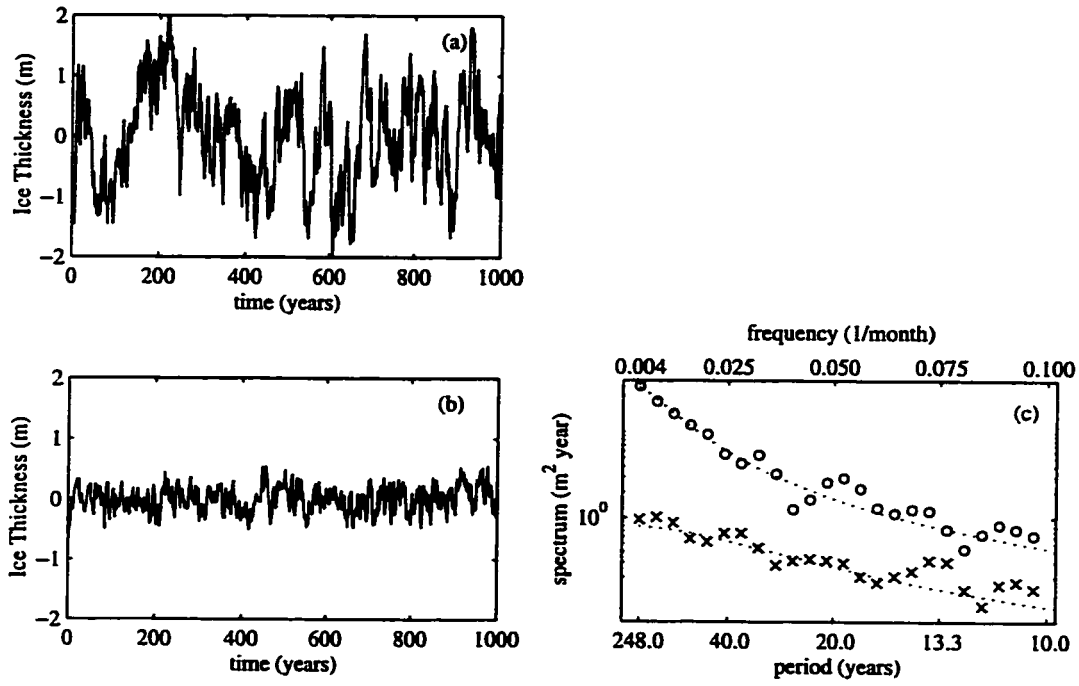


Figure 3.1: One thousand year time series of the annual mean sea ice thickness anomaly averaged over perennial ice area in the Arctic from (a) the SCM and (b) the GFDL climate model. Spectra (c) of the ice thickness from SCM (o) and GFDL (x), each with a best fit (dotted line) to a discrete first order Markov process. The spectra are calculated for the last 900 years ($N$) of model output using a lead/lag correlation method smoothed with a 124 year ($L$) Tukey window, yielding $8N/3L = 19$ degrees of freedom (Jenkins and Watts, 1968).

model is referred to as the single column model, or 'SCM') to examine the natural variability of the climate system, averaged over the arctic polar cap. Variability in the arctic climate stems from variability in the transport of energy into the Arctic by atmospheric circulation (see, e.g., Nakamura and Oort, 1988). The sea ice thickness anomaly from chapter 2, (repeated here in Fig. 3.1a) indicate that variance in the arctic climate system occurs on time scales longer than a decade and at remarkably large amplitude (overall standard deviation in yearly ice thickness of 0.85 $m$). This result is consistent with the calculations presented in Häkkinen and Mellor (1990) and Flato (1995) using sea ice models forced with observed surface atmospheric conditions, and the interannual changes in the springtime ice thickness of order 1 m at the North Pole from a dozen submarine voyages, reported in McLaren et al. (1994). Analysis of the ice draft from moored sonars in the Beaufort Sea indicate changes in the multi-year ice thickness of 1.5 m during the period 1990 to 1995 (Moritz, personal communication). Nonetheless, there are too few observational data to determine whether the climate variability that is demonstrated by the model in chapter 2 is consistent with that in nature. I can, however, compare the results in Fig. 3.1a from the SCM to that realized in a global climate model that includes a comprehensive treatment of each component of the hydrologic cycle. Fig. 3.1b shows a time series of the anomalies of the mean annual arctic sea ice thickness for the area identified in Fig. 3.2 from a 1000 year, "present climate" integration of the Geophysical Fluid Dynamics Laboratory (GFDL) GCM (Manabe and Stouffer, 1996).

The amplitude of the simulated climate variability, evidenced here by the sea ice thickness in the GCM, is fundamentally different from that in the SCM. The standard deviation for the annual sea ice thickness is 0.20 meters for the GFDL GCM and 0.85 meters for the SCM, though the power spectrum of sea ice thickness (Fig. 3.1c) from the GFDL GCM and the SCM indicate both models exhibit greatest variance in the sea ice thickness at low frequencies (see section 2.4). The difference in the natural variability depicted in Fig. 3.1a and that in Fig. 3.1b strongly affects the number of

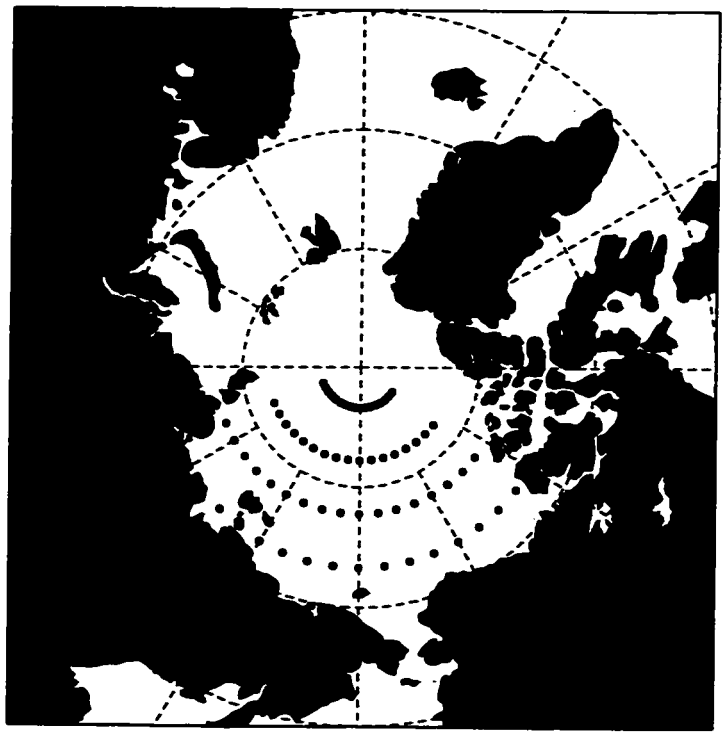

Figure 3.2: Grid points from the GFDL model area that are used for comparison with the SCM model output. This region is chosen because the sea ice is predominantly perennial.

years one would have to monitor ice thickness to detect a climate change of $1-2$ m, as simulated by most GCMs in response to a doubling of $CO_2$ (see, e.g., fig. 2.14).

Does the GFDL GCM underestimate the variability in the sea ice, or is the area averaged ice thickness from the SCM model in error? There are insufficient observations to answer this question definitively. In this study I will determine why there are large differences in the arctic climate simulated by the two models. In the process, I will reveal some insight concerning which of the two estimates in Fig. 1 is a more reliable estimate of the variability in the arctic climate system.

In this study I perform multiple, 1000 year integrations of the SCM to evaluate the sensitivity of the coupled climate system to the formulations of ice physics and to atmospheric forcing. I present results in which the (standard) sea ice module is modified in the SCM to be identical thermodynamically to the sea ice module that is in the GFDL climate model. I then perform integrations which independently exchange several of the oversimplified physical formulations in the GCM ice module for the more realistic treatment that is used in the standard version of the SCM; ultimately, I arrive back at the formulation of sea ice that is used in the standard version of the SCM. I will demonstrate that adding realism to the parameterization of ice physics and increasing the resolution of temperature structure in the sea ice will lead to a substantial increase in the low frequency variability in the arctic climate simulated by the GFDL GCM and other climate models[2].

A brief overview of the physical formulation of the sea ice in the GFDL general circulation model is found in section 3.3. Section 3.4.1 contains a discussion of the observed flux of moist static energy into the Arctic which is important for variability in the arctic climate and provides an important component in the forcing of the SCM. Differences in this energy flux realized from the GCM and that from the observational record are identified, and in section 3.5 I examine the effect of these differences on the

[2] I use the output from the GFDL model in this study because it is available and widely recognized. Other GCMs employ similar simplifications to sea ice, though details differ.

simulated variability in the arctic climate system using the standard SCM. In section 3.6 I incrementally alter the SCM to include several physical formulations in the sea ice module that are presently in the GFDL GCM, and illustrate the sensitivity of the natural variability that is simulated in the model to these formulations. An estimate of the variability in the sea ice in nature is provided in section 3.7, and a summary and discussion are presented in section 3.8.

## *3.3 Geophysical Fluid Dynamics Laboratory general circulation model*

The GFDL GCM is a global coupled atmosphere, sea ice, and ocean model. The model physics are described in Manabe et al. (1992), so here I review only the treatment of arctic sea ice. The ice is a slab of uniform thickness in each grid box without leads. Snow accumulation is converted immediately to equivalent sea ice thickness, therefore the thermal insulating capacity of snow is neglected and the surface albedo does not depend explicitly on snow depth. Heat conduction through the sea ice is calculated by assuming a linear temperature profile between the top and bottom surfaces of the ice; hence, sea ice is treated as a single layer with zero heat capacity (i.e., changes in the sea ice temperature require no energy). The sea ice is advected with the surface current, unless ice thickness exceeds four meters.

To mimic the effects of snow cover, melt ponds and open water, the GFDL GCM surface albedo is specified as a function of the surface temperature,

$$\alpha^* = \begin{cases} \alpha_{ice}, & \text{when } T_s \geq T_m \\ \alpha_{ice} + 0.025(T_m - T_s), & \text{when } T_m - 10°K \\ & \quad < T_s < T_m \\ \alpha_{snow}, & \text{when } T_s \leq T_m - 10°K, \end{cases}$$

and sea ice thickness,

$$\alpha_{GFDL} = \begin{cases} \alpha^*, & \text{when } h \geq 1\ m \\ \sqrt{h}(\alpha^* - \alpha_{ocean}) + \alpha_{ocean}, & \text{when } h < 1\ m. \end{cases} \tag{3.1}$$

In Eq. 3.1, $h$ is the sea ice thickness in meters, $T_s$ is the upper surface temperature, $T_m$ is the upper surface melting temperature, $\alpha_{ice} = 0.55$, $\alpha_{snow} = 0.8$, and $\alpha_{ocean} = 0.1$.

## *3.4 Discrepancies due to atmospheric forcing in the arctic region*

The natural variability in the Arctic is rooted fundamentally in the variability of energy transported by the atmosphere into the Arctic. Natural variability in the climate of the polar cap modeled by the SCM is a response to the prescribed, time dependent atmospheric energy flux convergence, $D$, and cloudiness as described in section 2.2.2. Could the discrepancy in the sea ice variability in the two models (see Fig. 3.1a and b) be due to the differences in the energy transport to the Arctic that is realized in the GFDL GCM and the energy transport that is prescribed (based on observations) in the SCM? To answer this question, I will compare SCM simulations forced by (i) $D$ based on observations and (ii) $D$ from the GFDL GCM.

### *3.4.1 Atmospheric energy transport into the Arctic in nature and in the GFDL GCM*

The observed monthly values of $D$ for a polar cap bounded by 70° N are computed by Overland and Turet (1994) based on rawinsonde data from 1965 to 1989 (see section 2.2.2) . The values of $D$ from the GFDL GCM output are computed as a residual from the energy budget of the polar cap (see Nakamura and Oort, 1988),

$$\Delta E/\Delta t = F_o + D + F_s \tag{3.2}$$

where $\Delta E/\Delta t$ is the rate of storage of energy in the atmosphere, $F_o$ is the net incoming flux of short wave and long wave radiation at the top of the atmosphere, and $F_s$ is the upward energy flux at the Earth's surface[3]. The GFDL model output is given as monthly mean values. $\Delta E/\Delta t$, $F_o$, and $F_s$ are computed at each grid point and then averaged over all of the grid points shown in Fig. 3.2. Therefore, $D$ represents

[3] $D$ is not directly calculable from the information that is saved from the GCM integration.

the monthly poleward transport of energy across the boundary of the area covered by the grid points[4].

Figure 3.3(a) and (b) show the mean annual cycle and the standard deviation of $D$ from observations and GFDL model output. The mean monthly $D$ from the GCM is $5-10\%$ larger than the observed $D$ in all months except November through January. The standard deviation of monthly $D$ from the GFDL GCM is about 60% of observed during the winter and about 80% of observed during the melt season. The power spectrum and autocorrelation for the observed and GFDL derived monthly anomaly of $D$ are shown in Figure 3.3(c) and (d). The power spectrum of the observation-based $D$ is nearly constant for monthly and longer time scales, while the variance in $D$ from the GFDL model output is skewed towards short time scales (at least as short as two months). The power spectrum of $D$ from the GFDL model output is similar to observations for monthly time scales, but it is considerably lower for time scales greater than about 5 months (see also section 3.7).

To examine the sensitivity of the climate variability in the Arctic requires long integrations (e.g., 1000 years each) because of the long time scale associated with the thermodynamic adjustment of sea ice. The observed time series of $D$, however, spans less than 30 years. In addition, only the mean monthly $D$ is available from both observations and the GFDL GCM, though $D$ probably varies considerably on shorter time scales. Hence, to force the SCM with a one-day time step, synthetic time series of $D$ must be obtained for both the observations and the GCM.

Based on observations I obtain a *synthetic* $D$ from a discrete form of the Langevin equation (p560f Reif, 1965) so that the standard deviation and power spectrum of

---

[4] The areas used to calculate $D$ from the model and the observations differ because the region that is most appropriate for input to the area-averaged model (i.e., over the perennial arctic sea ice) is void of observations with which to calculate the observed $D$. Note, however, in the GFDL model $D$ along $70°N$ is *less* than $D$ over the region of perennial sea ice, which suggests the observations at $70°N$ are likely to provide an *underestimate* of the true $D$ over the perennial sea ice.

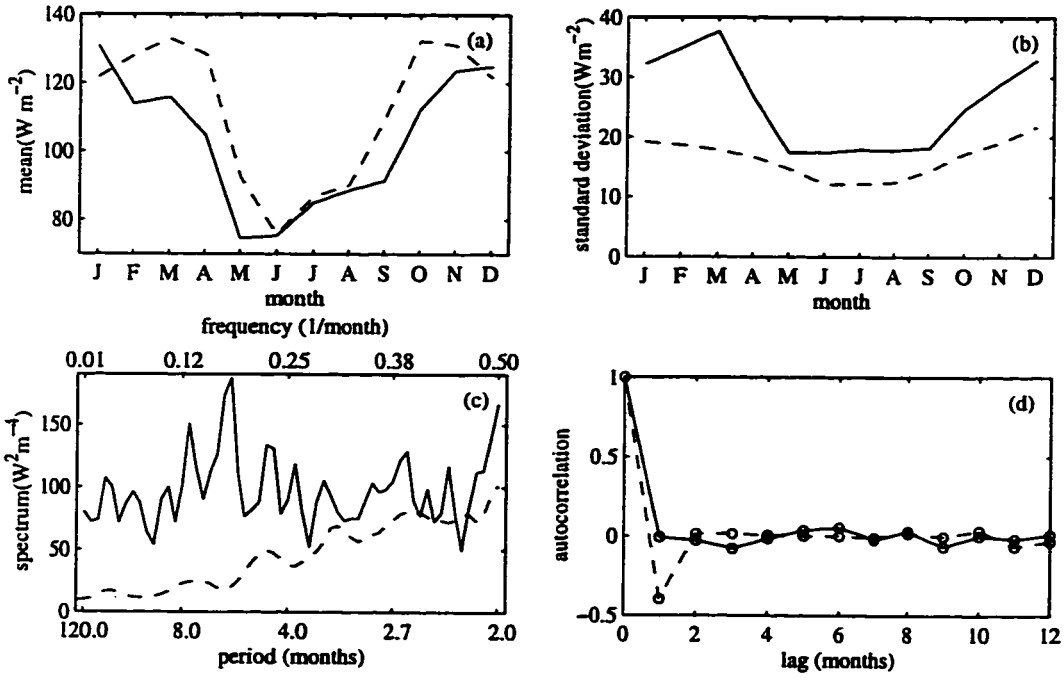


Figure 3.3: The mean monthly atmospheric energy flux convergence: (a) The annual cycle; (b) standard deviation; (c) power spectrum; and (d) autocorrelation. Data are presented for both observations (solid line) and the GFDL model (dashed line). The power spectra are calculated as in Fig. 3.1c, but here the annual cycle is removed and the window width is four years. Hence, there are 600 (16) degrees of freedom in the GFDL output (observations).

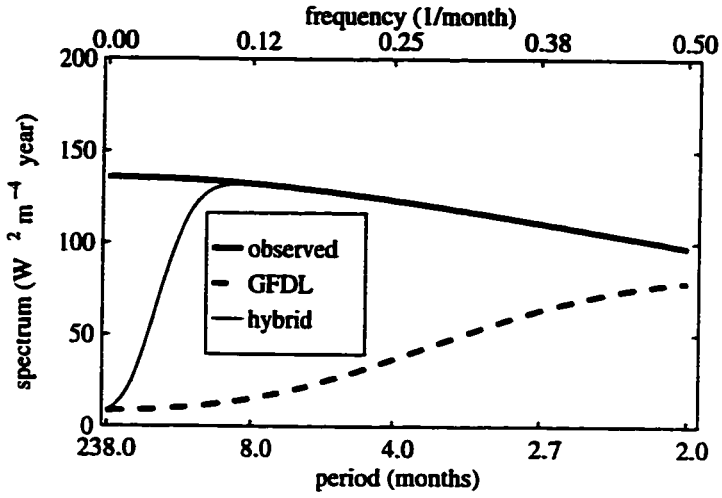


Figure 3.4: Spectra of *synthetic D* based on observations (heavy solid) and the GFDL GCM (heavy dashed). Also plotted is the spectrum of the hybrid $D$ (light solid), discussed in section 3.7. All curves are computed analytically from the difference equations and spectral filters used to synthesize $D$.

monthly mean values are consistent with those in Fig. 3.3(b) and (c), and the power spectrum of the daily time series of $D$ is red with a characteristic time scale of 5 days (see section 2.2.2). Based on GFDL output, again, I simulate $D$ from a discrete form of the Langevin equation; however, now the daily time series is partially high pass filtered to render the synthetic spectrum commensurate with that from the GFDL model. Power spectra of the synthetic time series are shown in Fig. 3.4; the spectral properties of the synthetic $D$ are statistically indistinguishable from their observed counterparts in Fig. 3.3c and d.

## *3.5 Sensitivity of ice thickness variability due to differences in the atmospheric forcing*

I first demonstrate that the area-averaged SCM model reproduces the sea ice variability simulated by the GFDL GCM. The sea ice module in the SCM is replaced

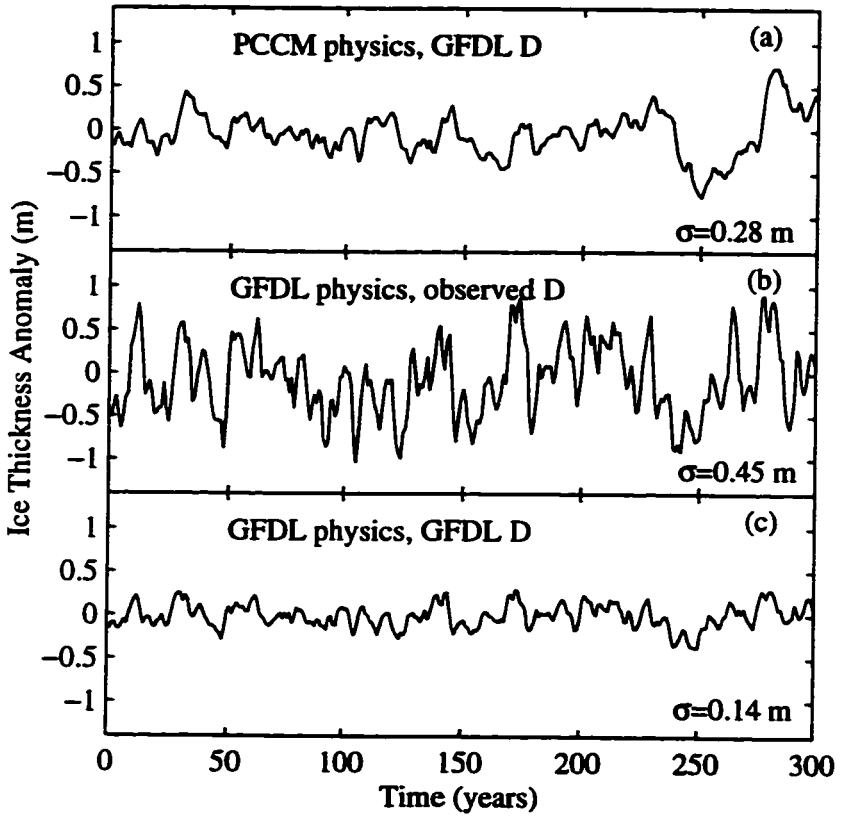


Figure 3.5: Anomalies of yearly sea ice thickness from the SCM output for integrations with (a) $D$ based on GFDL, standard SCM surface physics for snow and albedo, 6 sea ice layers; (b) $D$ based on observations, GFDL surface physics for snow and albedo, 1 sea ice layer; (c) $D$ based on GFDL, GFDL surface physics for snow and albedo, 1 sea ice layer.

with the thermodynamic treatment of sea ice that is identical to that in the GCM. The modified SCM was able to reproduce a significant portion of the low-frequency variability in the GFDL 1000 yr time series of sea ice that is shown in Fig. 3.1b when forced by the accompanying $D$ taken directly from the GFDL climate model. Specifically, about 45% of the sea ice variance in the GFDL control integration is accounted for in the hindcast (not shown) even though I have neglected the ocean heat transport variability and used only monthly averaged values of $D$ from the GCM, using a cubic spline to produce a daily time series. As a second test, a 1000 yr integration is performed while forcing the modified SCM with the GFDL synthetic $D$[5] (Fig. 3.4). A 300 yr segment of the time series of the sea ice thickness from this model is displayed in Fig. 3.5c. The standard deviation ($\sigma$) of the yearly sea ice thickness from the SCM with the GFDL GCM sea ice physics (e.g., albedo as per Eq. 3.1, one layer of ice, and no snow cover) is $\sigma = 0.14m$, similar to that from the GCM ($\sigma = 0.20m$) and very different from that realized by the standard physics SCM forced by the observed $D$ ($\sigma = 0.85m$).

To examine how much of this remarkable difference in the sea ice variability can be attributed to the differences in the forcing, I re-ran the SCM model with the sea ice physics of the GFDL GCM, but this time the forcing $D$ was prescribed based on the observations. This integration also yielded sea ice variability (variability is used synonymously with standard deviation) that is predominantly at low frequencies (Figs. 3.5b and 3.6 (heavy dashed line) ) but with amplitude ($\sigma = 0.45m$) that is intermediate between the amplitude achieved in the standard physics SCM forced by the observed $D$ ($\sigma = 0.85m$) and the amplitude realized by the SCM with the GFDL GCM $D$ and the GCM ice physics ($\sigma = 0.14m$).

Finally, I integrated the standard physics SCM, forcing it with the $D$ based on the GFDL GCM. The standard deviation is reduced to one-third (0.28/0.85) of that from

[5] Henceforth, when I refer to forcing of the SCM with the GFDL GCM $D$ or the observed $D$, I am referring to the synthesized $D$ that are described at the end of section 3.4.1

Table 3.1: The standard deviation of yearly sea ice thickness anomalies for four integrations of the SCM, described in section 3b. Each integration uses a unique permutation of the forcing ($D$) and treatment of sea ice.

| Experiments with different sea ice physics packages | | |
|---|---|---|
| | GCM (GFDL) ice-physics | SCM ice-physics |
| $D$ as per GFDL GCM | 0.14 m | 0.28 m |
| $D$ as per observations | 0.45 m | 0.85 m |

the integration using the observed $D$; the variance remains in the lower frequencies (Figs.3.5a and 3.6 (heavy solid line)).

In summary, the results of these four SCM integrations (see Table 3.1) demonstrate the following:

- When the SCM is modified to contain the GFDL GCM thermodynamic sea ice package and is forced by the energy transport that is realized by the GCM, the variability in the sea ice is statistically very similar to the sea ice variability from the full GCM;

- The variability in arctic sea ice in the area-averaged (SCM) regional climate model is substantially affected by the different formulations of the sea ice physics (see section 3.3), and by the differences between the energy transport into the Arctic realized by the GFDL GCM and that which is observed in nature.

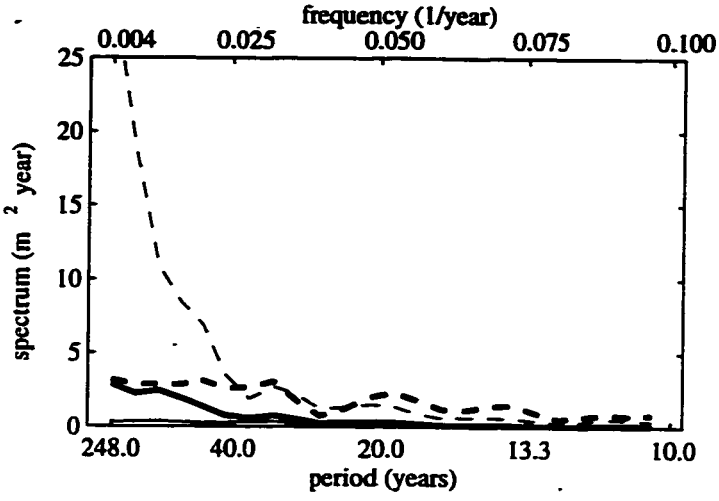


Figure 3.6: Power spectra of yearly sea ice thickness anomalies from the SCM output for integrations: $D$ based on GFDL, standard surface physics for snow and albedo, 6 sea ice layers (heavy solid); D based on observations, GFDL surface physics for snow and albedo, 1 sea ice layer (heavy dashed); D based on GFDL, GFDL surface physics for snow and albedo, 1 sea ice layer (light solid); the hybrid $D$ and the SCM standard physics (light dashed) . The power spectra are calculated as in Fig. 3.1c.

## *3.6 Sensitivity studies reveal the fundamental physics that accounts for the quiescent arctic climate in the general circulation model*

The experiments of the last section showed that the sea ice variability in the SCM almost doubles[6] when the simple module for sea ice from the GCM (section 3.1) is replaced by the more realistic formulation in the standard SCM, described in Eq. 2.1. In this section I will isolate aspects of the sea ice treatment that significantly affect the variability in the sea ice and in the arctic climate system that is simulated by the SCM.

The two fundamental differences between the ice models used in the SCM and

[6] The increase in the standard deviation of annual mean ice thickness due to the inclusion of a more realistic sea ice module is 0.28/0.14 = 2 when the SCM is forced by the GCM $D$ and 0.85/0.45 = 1.9 when the SCM is forced by the observed $D$.

Table 3.2: The standard deviation of yearly sea ice thickness anomalies from eight integrations which differ by the number of sea ice layers, $n$, and the surface physics which either explicitly include the effect of snow or (as in the GFDL model) there is no snow cover and the albedo is described by Equation 3.1. The integrations in the left (right) quartet were forced with the variability in $D$ that is based on GFDL model output (the observed data). The schematic indicates the percent change in standard deviation as one moves through the quartet of experiments, using either prescription of D.

| | GFDL D | | observed D | |
|---|---|---|---|---|
| | $n = 1$ | $n = 6$ | $n = 1$ | $n = 6$ |
| $\alpha_{\text{surface}}$=GFDL | 0.14 m | 0.18 m | 0.45 m | 0.57 m |
| $\alpha_{\text{surface}}$=explicit | 0.19 m | 0.28 m | 0.57 m | 0.85 m |

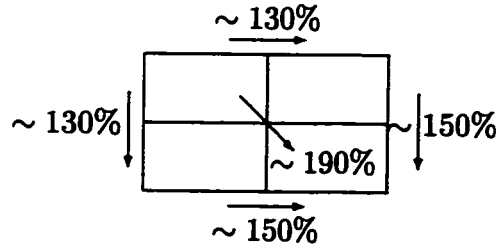

GCM are:

(i) **GFDL GCM**: The surface physics do not resolve snow cover. The albedo parameterization depends on the upper surface temperature and sea ice thickness, but does not depend on snow depth explicitly. Insolation effects and energy storage in snow cover are excluded.

**SCM**: The snow depth is treated as a prognostic variable in the sea ice model. The surface albedo parameterization reflects the sea ice thickness and the snow depth. The surface is insulated by accumulated snow cover, and energy is required to melt it.

(ii)**GFDL GCM**: The vertical temperature profile is constrained to be uniformly linear. Hence, the sea ice model has one layer.

**SCM**: The temperature profile is well resolved by six sea ice layers.

Table 3.2 summarizes the results from the (1000 yr) integrations of the SCM using all possible permutations of the forcing (GFDL GCM or observed), sea ice resolution (one layer (GFDL GCM) or six layers (standard)), and snow/albedo formulation (see section 2.2). The quartet of experiments on the left (right) summarizes results for varying sea ice resolution and the treatment of snow/albedo while keeping the forcing $D$ prescribed as in the GCM (from observations).

For forcing by the observed $D$ and with the treatment of snow/albedo as in the GFDL GCM, increasing the number of layers in the sea ice from a purely linear ($n = 1$) profile to $n = 6$ layers (hence better resolving conduction) causes an increase of 27% (0.45 to 0.57 m) in the standard deviation of sea ice thickness; using the standard SCM albedo/snow formulation yields an increase in the variability of 49% (0.57 to 0.85 m). The percent increase of the sea ice variability associated with the adequate resolution of conduction depends on the treatment of snow/albedo, yet it is relatively insensitive to the prescription of $D$ (compare rows in Tables 3.2).

For forcing by the observed $D$, changing the snow/ albedo formulation from the GFDL GCM formulation (Eq. 3.1) to the explicit treatment in the standard version

of the SCM leads to an increase in the standard deviation of sea ice thickness of 27% (0.45 to 0.57 m) with $n = 1$ and 49% (0.57 to 0.85 m) with $n = 6$. Again, the percent increase of the sea ice variability resulting from improving the formulation of snow/albedo is relatively insensitive to the prescription of $D$ (compare columns in Tables 3.2).

In summary, either increasing the resolution of the temperature profile in the sea ice or implementing the improved snow/albedo formulation from that in the GFDL GCM, independently, leads to a substantial increase in sea ice variability in the regionally averaged arctic climate (SCM) model. Implementing these improvements *simultaneously* causes the variance to increase by about four-fold, independent of the different prescriptions of forcing $D$ (see footnote 7).

### *3.7 An estimate of the variability of sea ice thickness in nature*

The natural variability in the arctic climate system is driven by changes in the energy transport into the Arctic by the atmosphere ($D$) and by the ocean. I have shown that the differences between the atmospheric energy transport in the GFDL GCM and that in nature (Figs. 3.3c and 3.4) have a large impact on the variability of the arctic climate in the SCM (e.g., a factor 0.85/0.28 = 3 difference in the standard deviation of sea ice thickness; Table 3.1). Hence, to obtain a reliable estimate for the amplitude of the natural variability in the arctic climate system requires that $D$ be known accurately on a wide range of time scales.

For periods of less than a few years, the differences in $D$ from the observations and from the GFDL model are statistically significant (based on sample size) and are too large to be attributed to observational error. In contrast, for periods greater than about five years, the observational record is too short to determine the true spectrum of $D$: significant uncertainties are introduced from both measurement and sampling error. However, I anticipate that in the decadal range, nature has at least as much

variability in $D$ as does the GFDL model[7].

To obtain a conservative "best estimate" of the sea ice variability in the arctic climate system, I assemble a hybrid $D$ which has spectral properties that are consistent with the observations on time scales shorter than two years, and is intermediate between the $D$ from the GFDL model and from observations for time scales longer than two years. This hybrid spectrum is plotted in Fig. 3.4, along with the spectra based on the GFDL and observed $D$.

When the standard physics SCM model is forced by this hybrid $D$, the variability in the sea ice thickness still accumulates at the lowest frequencies (Fig. 3.6, light dashed line) and the overall variability is 0.72 $m$ - only slightly reduced from that obtained using the SCM and the full-spectrum observed $D$ ($0.85m$). Thus, the "best estimate" of the standard deviation due to natural variability in sea ice is more than a factor of three (0.72/0.20) greater than that simulated by the GCM. The remaining experiments with the SCM using the hybrid $D$ and various mixes of sea ice physics are summarized in Table 3.3. Using the hybrid $D$, the sensitivity of the simulated sea ice variability to specific changes in the treatment of sea ice is consistent with that obtained using the observed and GFDL $D$ (contrast rows and columns between the two tables, Tables 3.2 and 3.3).

I have not yet examined the impact of sea ice dynamics or leads on the *variability* in the arctic climate system. Section 2.3.3 present a calculation that suggests the uniform advection of sea ice acts to dampen the variability displayed in the standard physics SCM (Fig. 3.1). A discussion of the variability that is due to the mechanical forcing (wind and current stresses) of the sea ice is found in chapter 5. I anticipate that variability in the ocean heat transport, which is neglected in this study, will increase the variability in the sea ice from the 'best estimate' presented here that is

[7] The interannual to multi-decadal variability in the global *tropics* of the GFDL GCM is anemic compared to nature (Lau et al., 1992); one may expect that this problem is communicated via atmospheric dynamics to the polar regions.

Table 3.3: As in Table 3.2, but the forcing $D$ has spectral characteristics that represent a hybrid of the spectra from the GCM and from observations.

| | Hybrid D | |
|---|---|---|
| | $n = 1$ | $n = 6$ |
| $\alpha_{surface}$=GFDL | 0.28 m | 0.38 m |
| $\alpha_{surface}$=explicit | 0.42 m | 0.72 m |

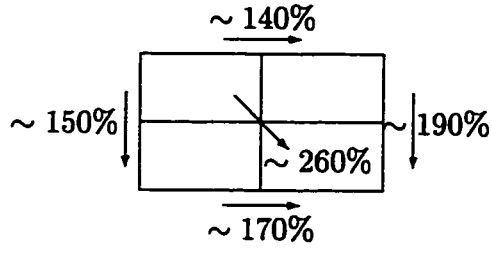


due solely to the stochastic nature of the atmospheric energy transport.

### *3.8 Discussion and conclusions*

In this chapter I have used a model of the area-averaged, coupled arctic atmosphere/sea ice/ocean system to examine the variability in the arctic climate that may be expected because of the natural variability in the transport of energy into the Arctic *via* the atmospheric circulation. I use sea ice thickness as a useful indicator of the state of the arctic climate system.

The motivation for this work stems from the results of chapter 2, which suggest that the variability in the arctic climate may be surprisingly large and predominantly at multi-decadal and longer time scales. Though the scant observations are not inconsistent with the model results, the observational record is too short to determine the veracity of this result. Hence, I contrasted the SCM results to those found in a global general circulation (climate) model, and found that the variability in the sea

ice of the GCM was one quarter of that in the SCM (see section 3.2). In this study, I have used the SCM diagnostically to help determine the reasons for the qualitative differences between the SCM and the arctic climate simulated by the GFDL GCM, and summarize the reasons below. Some of the results from the present study are relevant to most - if not all - of the GCMs in use today to study natural climate variability and the climate change associated with increasing greenhouse gases; they suggest that the variability in the arctic climate is probably much more energetic than is being simulated in these general circulation (climate) models (see sections 3.8.1 and 3.8.2 below).

### *3.8.1 Arctic sea ice variability in the GFDL GCM*

I inserted the GFDL sea ice physics into the SCM and then forced the model with the synthetic energy transport that is statistically identical to that in the GFDL GCM (section 3.5). The sea ice thickness variance is similar to that from the "present climate" integration of the GFDL climate model. Thus, results that I have presented concerning the impact of improving the sea ice treatment on the variability in the arctic climate are likely to be quantitatively relevant to the GFDL climate model[8].

My results suggest that the GFDL GCM will exhibit substantially more natural variability in the arctic climate system (e.g., a factor of four in sea ice thickness variance) if unarguable improvements are made in the treatment of sea ice in the model (see section 3.6). Furthermore, there is a *fundamental* difference in the variability in the sea ice thickness displayed in the SCM driven by the atmospheric energy transport ($D$) from the GFDL model and derived from observations. The standard deviation

[8] It is unlikely that differences in the details of the GFDL and SCM atmosphere models *within the arctic* would render the SCM model not applicable to the GCM. Results from chapter 2 showed that the modeled sea ice thickness variability is relatively insensitive to the details of the stochastic cloud forcing; correlating perturbations in the cloud forcing with the atmospheric heat flux convergence has a modest effect on the model variability.

of the sea ice thickness in the SCM forced by the GCM $D$ is about one-third of that from the model forced with the observed $D$ (see section 3.5). Combining the improvements in the treatment of the sea ice physics with (unidentified) changes to the GCM so that the atmospheric energy transport into the Arctic is consistent with that observed, my calculations indicate that the variance in the arctic sea ice simulated by this GCM will increase by a factor of ten!

The variance of the atmospheric energy transport in the GFDL GCM is less than that from observations on all time scales (Fig. 3.3). Most important for the variability in the arctic climate system, the GFDL GCM severely under represents the variability on the seasonal to interannual time scales - the time scales at which the observed energy transport is accurately determined. The literature indicates this is a problem ubiquitous to low-resolution models (see, e.g., Held and Phillipps (1993) and Boyle (1993) for a discussion of the resolution dependence of energy transport in the synoptic band), and herein lies a fundamental problem with using a GCM to examine the variability in the arctic climate system: the significant variability in the arctic sea ice thickness is on multidecadal time scales and it is sensitive to the amplitude of the variability in the meridional energy transport by the atmosphere into the Arctic at all frequencies but particularly to the amplitude of the *high* frequency variability (section 2.3.2). Thus, to study the natural variability in the arctic climate with a GCM will require multiple very long (multi-century) integrations at high resolution (at least T42).

### *3.8.2 Arctic sea ice variability simulated by other models*

In this section, I compare the sea ice variability demonstrated by the SCM with results from other models. Two other classes of models have been used to assess the natural variability in the arctic sea ice: (a) sea ice/upper ocean models of the Arctic, and (b) full climate models that couple an atmospheric GCM to a sea ice model and a model of the oceans. The class (a) models require prescribed time-dependent

forcing as a boundary condition at the surface of the sea ice. The necessary data to do this have only recently become of sufficient duration to determine this forcing over the Arctic (but there are insufficient data to determine the observed arctic ice volume at any time in the historical record). The results from the model studies of Walsh et al. (1985), Häkkinen (1993), Flato (1995) and Häkkinen and Mellor (1990) using type (a) models are pertinent to this study. I note, however, that because the variability is likely to be dominated by multidecadal and longer time scales, for all of the studies discussed below (excepting perhaps Häkkinen and Mellor (1990)) the model integrations are too short to determine, even qualitatively, the amplitude of the variability in the arctic climate system.

*Coupled Sea Ice/Ocean Models of the Arctic*

Häkkinen (1993) used a dynamic-thermodynamic sea ice model of the Arctic to study the freshwater export from Fram Strait for the period 1955-1975. The prescribed forcing of the model was heat flux derived from the climatological *mean* annual cycles of air temperatures and the observed wind stress for that period. The variability in the simulated sea ice volume for this period was about 10% of the mean sea ice volume. Walsh et al. (1985) and Flato (1995) used different dynamic-thermodynamic sea ice models to perform hindcasts of the sea ice variability in the Arctic from 1951-1980 (Flato's hindcast extends to 1990). The standard deviation of the averaged sea ice thickness in these simulations is also much smaller than that obtained with the SCM, but comparable to that in Häkkinen (all three studies found variability greater than that from the GFDL climate model).

In the studies of Häkkinen (1993) and Flato (1995), the heat fluxes used to force the model are calculated using the bulk formula and the climatological *mean* surface air temperatures[9], which ensures an artificial, strong damping of the sea ice vari-

[9] The forcing of the sea ice model in Flato's study is largely confined to the observed wind stress

ability[10]. In contrast, the sea ice in the SCM experiences *only* thermodynamic (not dynamic) processes and atmospheric anomalies that are affected by interactions between the atmosphere/sea ice/ocean system. Note that Häkkinen and Mellor (1990) performed a study of the arctic sea ice from 1880 to 1985 using a one-dimensional sea ice/upper ocean model. In this study, the forcing included the observed surface heat fluxes calculated (in part) from the observed surface atmospheric temperature *anomalies*. The spectral variance of the sea ice mass displayed in this hindcast was consistent with that simulated by the SCM (Häkkinen, personal communication 1995).

In summary, the results from these three studies suggest that thermodynamic processes are a major conduit for affecting variability in the sea ice volume in the Arctic. In addition, the results from the dynamic/thermodynamic sea ice models indicate that ice dynamics does not damp out the ice variability.

*Global Climate Models*

There are about two dozen global climate models that are presently being used to study the variability in the global atmosphere/ocean/land/sea ice climate system. Apparently, the natural variability in the sea ice has been examined in only three of these models (this includes the documentation of the GFDL model in this study). In the Hadley Center climate model (HADCM2; Mitchell et al. (1994)), the standard deviation in the sea ice volume is about 10 to 20% of the mean sea ice volume (T. Johns, personal communication, 1995). The standard deviation in the sea ice volume from a twenty year control integration of the CSIRO climate model is about 20% of the mean sea ice volume ( Hunt et al. (1995)). Note that a significant portion of the variability in the sea ice volume in these two GCMs arises from variability

anomalies: the model experienced interannually varying air temperatures only near the coasts.

[10] For analogous reasons there is an artificial reduction of the variance in the atmosphere when atmospheric GCMs are integrated using climatologically prescribed SSTs (see, e.g., Barsugli (1995) and Manabe and Stouffer (1996)).

in the sea ice extent. Hence, it is likely that the variability of the perennial sea ice volume in these global climate models is much less than that displayed in the SCM, and this is expected from the sensitivity studies using the SCM in sections 3.6 and 3.5. Specifically, the atmosphere component of the CSIRO climate model discussed in Hunt et al. (1995) has low horizontal resolution (R15) which enables long integrations to be made but ensures a deleterious affect on the sea ice variability *via* distortions in the atmospheric energy transport (see section 3.5). The HADCM2 model uses a moderate horizontal resolution in its atmosphere model, but has a one-level sea ice formulation which, according to the results in section 3.6, will artificially reduce (by about half) the variance in the sea ice from that which would be realized in the same climate model but with the conduction of heat in the sea ice is adequately resolved. Hence, the sea ice variability in the GFDL, HADCM2 and CSIRO climate models is likely to be less than that in nature.

### *3.8.3 Implications*

I have confirmed that in the regionally averaged model of the coupled atmosphere/sea ice/ocean arctic climate system, the natural climate variability is extremely sensitive to the formulation of the sea ice. Specifically, the variance in the sea ice thickness simulated by the coupled model nearly doubles when snow is explicitly included in the model and a more realistic parameterization for the albedo of snow/ice is used in place of the standard formulation of albedo used in several GCMs. When there is adequate resolution of the temperature profile in the sea ice, again the sea ice variance nearly doubles. Implementing these improvements simultaneously causes the variance to increase by about four-fold. The result from increasing the temperature resolution may have been anticipated by combining the results from Semtner (1976) (concerning the sensitivity of the annual cycle of sea ice to the number of layers in the sea ice) with those from section 2.3.3, which demonstrated that low-frequency variability in arctic climate is largely a result of nonlinear physics that are associated with sea ice

that is undergoing both annual cycle forcing and stochastic (high frequency) forcing.

There are two implications from these results for detecting an anthropogenically forced climate change in the Arctic. To detect a climate change the amplitude and character of the natural variability (the noise) must be known. There are insufficient observations to document the natural variability in the arctic climate system (due to the presence of sea ice, the arctic climate system adjusts slowly (Thorndike, 1992b)). My results suggest that the treatment of sea ice in the global climate models used to address the detection problem results in a serious underestimation of the natural arctic climate variability. Furthermore, because the variability in the arctic climate is extraordinarily sensitive to the full spectrum of the variability in the meridional energy transport ($D$) into the Arctic, it is important that these climate models simulate accurately all of the many processes that constitute $D$.

Second, climate models that are presently used to evaluate climate change due to increasing carbon dioxide suggest that the greatest changes will be in the mean arctic climate and inherently tied to changes in the sea ice thickness, particularly to large changes in the mean sea ice thickness. To my knowledge (also, personal communications (1995) to D Battisti from G. Flato, J. Maslanik, J. Walsh, and J. Weatherly), excepting the two studies mentioned in section 3.8.2 and the analysis of the GFDL climate model presented here, the *natural* variability of arctic sea ice thickness simulated by these models has not been examined. However, because these global climate models have in common low horizontal resolution atmospheres (see, e.g., Houghton et al. (1990)), the climate change simulated by these GCMs is likely to be large compared to the natural variability within the arctic in the control integrations of these climate models (e.g., the standard deviation of the area-averaged sea ice thickness is 0.20 m for the control integration of the GFDL climate model, while the change in the mean sea ice thickness associated with a doubling $CO_2$ is typically more than 2 m (Manabe et al., 1991)). In contrast, my results indicate that the natural variability within the arctic is much larger than that simulated by these models, and it may

be a substantial fraction of the predicted change in mean ice thickness. Hence, the present estimate of the ratio "signal (climate change)" to "noise (natural variability plus observational error)" is likely to be greatly overestimated in the Arctic. Finally, my results raise serious questions concerning the viability of the predicted equilibrium climate change using these models because of the strong nonlinearities and long time scales inherent to the variability in the Arctic (due to sea ice).

It is commonly stated that the arctic climate is sensitive to external (e.g., anthropogenic) forcing because of the feedback involving changes in the ice extent and the surface albedo. In light of my results, it is not surprising that the widest variations among different GCM simulations of the *present* mean climate, and of the climate response to greenhouse gas increase, occur in the Arctic (e.g., Houghton et al., 1990). Indeed, the *differences* in the annual cycle of the arctic surface temperature response simulated by different GCMs would represent enormous climate changes, with important implications both inside and outside the Arctic. Based on the results presented in this and the previous chapter and the results of others, it is likely that the wide variability of the arctic climate simulated by the GCMs result from the model formulations of arctic physical processes that determine the surface albedo, sea ice thickness, snow depth, and cloudiness.

# Chapter 4

# A NEW DYNAMIC/THERMODYNAMIC SEA ICE MODEL DESCRIPTION

## *4.1 Introduction*

In chapter 2 using a single column model of the arctic climate system I have shown that energy transport into the Arctic by the atmospheric forces low-frequency variability in the modeled sea ice thickness through thermodynamics processes alone. In the second half of this dissertation, I will investigate how dynamical processes (i.e., advection, ridging, and opening) affect low frequency variability in the system. I will reexamine the estimate of the variance of sea ice that was made with the single column model (SCM) in section 2.3.3 in which a crude parameterization that showed export weakened the variability in the ice thickness. Additionally, I will explore the role of ice deformation. Deformation is potentially an important mechanism for properly determining low-frequency variability of ice because (1) the amount of ridging depends inversely on the volume which is a negative feedback on thickness variations and (2) open water production also depends inversely on the volume which is a positive feedback on thickness variations. I will use a model to quantitatively assess how the proposed dynamical mechanisms interact to effect the low frequency variability of sea ice.

## *4.2 Overview of the model formulation*

In this section I will summarize the elements that are essential to simulate low frequency variability in sea ice, based in part on the results from the SCM.

- Low-frequency variability in the SCM is very sensitive to atmospheric anomalies during melt onset, when the snow-albedo feedback mechanism can effectively "lock" in the effect of warm anomalies. Model physics that affect the state of the sea ice surface in the spring and fall play a role in determining how the ice will respond. Hence the model must accurately allow snow to accumulate on the ice surface and the albedo to depend explicitly on the snow depth.

- The simple physical model that explains low-frequency variability of ice thickness due to thermodynamics processes given in section 2.4 links the timescale of the variations to the ice growth rate which depends on thickness and the distribution of energy within the ice. Consistent with the physical model, SCM results show that the total variance and timescale of the sea ice thickness increase with the mean thickness and with the number of sea ice layers in the model. When the modeled ice temperature profile is constrained to be linear so that the heat capacity and the effects of brine pockets are neglected, the model over estimates the amplitude of the annual cycle, while the variance and timescale of the thickness anomalies are greatly reduced compared to the standard case. The insulating effect of snow also influences the ice temperature profile and growth rate. Therefore, the vertical temperature profile in the model must be well resolved and must include the effects of brine pockets.

- I have argued that ice export and ridging in the Arctic influences variations in the ice. A realistic treatment of thin ice and open water is essential in the Arctic due to the tremendous influence thin ice and open water have on the surface energy balance (Maykut, 1982). Hence the representation of the ice dynamics and the ice thickness distribution in the ice model must properly reproduce open water production through ice deformation and export and must resolve thin ice explicitly.

Because I want to resolve the vertical temperature profile in the sea ice and accumulating snow on top of the ice, the number of state variables in the model will increase rapidly with the number of ice thicknesses (or ice categories) in each gridbox. My objective is to keep the number of categories as small as possible yet sufficient to properly simulate thin ice and the evolution of the rest of the ice. Recently, Stern et al. (1995) formulated a three-category sea ice model consisting of open water, thin ice, and thick ice which takes into account shear deformation in the production of open water and allows for redistribution between categories as a result of ridging. I will evaluate how the evolution of the ice mass depends on the number of ice categories (between two and four). I will use the formulation for two and three categories from Stern et al. (1995) with minor modifications. and I derive the equations for four categories in this chapter.

Previous sea ice models used in climate studies have generally either incorporated (1) a thorough treatment of ice thermodynamics (e.g., the single-column model used in chapters 2 and 3), or (2) a thorough treatment of dynamics, but an overly crude representation of the thermodynamics (e.g., the Hibler viscous-plastic model used by Chapman et al., 1994). Almost without exception, the dynamic (thermodynamic) models severely compromise the ice thermodynamics (dynamics). To accomplish the goals outlined above, I will develop a new model that includes the viscous-plastic ice dynamics model from Zhang and Hibler (1997) to which I have added the essential thermodynamic physics that I described above. The fundamental difference between this model and other dynamic sea ice models used in climate studies lies in the detail given to the thermodynamic treatment of sea ice and the implementation of a three- and four-category ice thickness distribution.

This chapter begins with the definitions of the state variables and basic equations governing their evolution. The following sections describe the physical processes and parameterizations that are components of these basic equations and the numerical methods I use to solve the system of equation. The last sections compares this model

to other commonly used models.

### *4.3 Fundamental equations*

Equations governing the evolution of ice and snow velocity, concentration, volume, and energy are developed in this section. I have chosen state variables, listed in table 4.1, that are related to the governing equation.

Ice velocity ($\mathbf{u}$) is determined from the momentum balance equation,

$$m\frac{D\mathbf{u}}{Dt} = -mf\mathbf{k}\times\mathbf{u} + \tau_a + \tau_w - mg\nabla Y + \mathbf{F}, \tag{4.1}$$

where $m$ is the mass per unit area of the ice, $f$ is the Coriolis parameter, $\tau_a$ and $\tau_w$ are forces due to air and water stresses, $g$ is the gravitational constant, $Y$ is the ocean surface dynamic height, and $\mathbf{F}$ is the force due to internal ice stress.

The evolution of ice concentration ($A_i$) and ice volume[1] per unit area ($H_iA_i$) for each category $i > 0$ (category 0 is open water) is governed by a pair of continuity equations,

$$\frac{\partial A_i}{\partial t} = -\nabla\cdot(\mathbf{u}A_i) + \Psi_i + \mathcal{A}_i \tag{4.2}$$

and

$$\frac{\partial H_iA_i}{\partial t} = -\nabla\cdot(\mathbf{u}H_iA_i) + \Theta_i + \mathcal{V}_i, \tag{4.3}$$

respectively, where $\mathbf{u}$ is the horizontal velocity[2] of the ice, $H_i$ is ice thickness, $\Psi_i$ and $\Theta_i$ are contributions by mechanical redistribution, and $\mathcal{A}_i$ and $\mathcal{V}_i$ are contributions by thermodynamic processes. Equation 4.3 describes the evolution of snow volume when $H_i$, $\Theta_i$, and $\mathcal{V}_i$ are replaced with $H_i^s$, $\Theta_i^s$, and $\mathcal{V}_i^s$, respectively.

---

[1] The three-category model presented in Stern et al. (1995) gives equations for the evolution of ice thickness rather than volume. Volume is used here because (unlike thickness) it evolves by the same equation as the concentration.

[2] All ice categories share the same velocity, so $\mathbf{u}$ has no subscript.

Employing a vertical coordinate normalized by the sea ice thickness, $z_i^* = z/H_i$, the specific enthalpy ($Q_i(x, y, z_i^*)$) evolves according to

$$\frac{\partial(Q_i H_i A_i)}{\partial t} = -\nabla \cdot (\mathbf{u} Q_i H_i A_i) + \Pi_i + \mathcal{E}_i, \tag{4.4}$$

where $\Pi_i(x, y, z_i^*)$ is the contribution by mechanical redistribution and $\mathcal{E}_i(x, y, z_i^*)$ is the contribution by thermodynamic processes. Equation 4.4 describes the evolution of the heat content in the snow layer when $Q_i$, $H_i$, $\Pi_i$ and $\mathcal{E}_i$ are replaced with $Q_i^s$, $H^s$, $\Pi_i^s$ and $\mathcal{E}_i^s$, respectively. The vertical coordinate in the snow is normalized by the snow thickness, $z_i^{s*} = z/H_i^s$.

Table 4.1: State Variables

| symbol | description |
|---|---|
| $\mathbf{u}$ | velocity of the sea ice |
| $A_i$ | concentration of sea ice in category $i$ |
| $H_i$ | thickness of sea ice in category $i$ |
| $H_i^s$ | thickness of snow in category $i$ |
| $Q_i$ | specific enthalpy (relative to melting, see Eq. 4.6) of sea ice in category $i$ |
| $Q_i^s$ | specific enthalpy (relative to melting) of snow in category $i$ |
| $T_w$ | temperature of ocean mixed layer |

*Vertical heat transfer*

Vertical heat transport in the sea ice is governed by the heat equation, modified to include absorption of solar radiation:

$$C_p \frac{\partial T}{\partial t} = \frac{\partial}{\partial z} k \frac{\partial T}{\partial z} + \kappa I_0 e^{-\kappa z} + \mathcal{T}, \tag{4.5}$$

where T is the temperature, $C_p$ is the specific heat, $k$ is the conductivity, $I_0$ is the solar radiation that penetrates the upper surface, $\kappa$ is the extinction length from Beer's Law, and $\mathcal{T}$ represents the contribution from horizontal advection of thermal energy and other thermodynamic processes. The category index, $i$, is implied. Boundary conditions for equation 4.5 follow from top surface energy balance and from the mixed layer/open water energy balance which will be described below.

The temperature is computed from the specific enthalpy relative to the melting temperature $T_m$,

$$Q(T) = \int_{T_m}^{T} C_p \, dT - L, \tag{4.6}$$

where $L$ is the latent heat of sea ice. Mathematically it is possible to combine 4.5 and 4.6, eliminating $T$ from the set of fundamental equations. However, the equation is unnecessarily complicated. Instead, I include both equations and include $T$ in the set of unknown variables which also includes the state variables.

*Top surface energy balance*

The top surface energy balance for each ice category is

$$F_{net}(T) = F_r(1-\alpha) - I_0 + F_L - \sigma T^4 + F_{si} + F_{ei} + k\frac{\partial T}{\partial z}, \tag{4.7}$$

where $F_r(1-\alpha)$ is the net solar radiation above the top surface, $F_L$ is the incoming longwave radiation, $\sigma T^4$ is the outgoing longwave radiation, $F_{si}$ and $F_{ei}$ are the sensible and latent heat fluxes over an ice surface, respectively. If $F_{net}(T_m) \geq 0$, then the upper surface is fixed at the melting temperature (i.e., $T_s = T_m$). If $F_{net}(T_m) < 0$ then the upper surface is not melting and Eq. 4.7 is solved for $T_s$.

*Mixed layer/open water energy balance*

The mixed layer in the model represents the upper most ocean layer, including the water beneath the sea ice and areas of open water between sea ice floes. The net heat flux into the mixed layer ($F_{mix}$) is balanced by a temperature change in the water and can be written

$$F_{mix} = C_{po} D_0 \frac{dT_w}{dt}, \tag{4.8}$$

where $C_{po}$ is the specific heat of the ocean and $D_0$ is depth of water in the mixed layer which is assumed to be independent of the ice cover.

The bottom of the ice is in contact with sea water with temperature $T_w$. Therefore, the bottom temperature $T_b = T_w$, unless $T_w > T_m$ when $T_b$ is fixed at $T_m$. This limits the minimum $T_b$ to the freezing temperature of sea water ($T_f$), where $T_f = 271.2K$ for typical values of salinity in the Arctic, following Maykut and Untersteiner (1971).

## 4.4 *Physical processes and parameterizations*

In this sections, I will give details of the model dynamics, mechanical redistribution, and thermodynamics to complete the descriptions of the fundamental equations. Section 4.4.1 describes the terms in the momentum equation and mechanical redistribution. This will lead to simple expressions for the $\Psi_i$, $\Theta_i$, and $\Pi_i$ for the conservation equations above. Next I will define the thermodynamic parameters in section 4.4.2. Finally, in section 4.4.3, I will derive expressions for the thermodynamic processes that contribute to $\mathcal{A}_i$, $\mathcal{V}_i$, $\mathcal{E}_i$, and $F_{mix}$.

### *4.4.1 Ice dynamics*

*Air and water stress*

Following Hibler (1979) the stress terms in the momentum equation (Eq. 4.1) are from nonlinear integral boundary-layer theories (McPhee, 1975; Brown, 1980),

$$\begin{aligned}\tau_a &= \rho_a C_a |\mathbf{u_g}|(\mathbf{u_g}\cos\phi + \mathbf{k}\times\mathbf{u_g}\sin\phi),\\ \tau_w &= \rho_w C_w |\mathbf{u_w}-\mathbf{u}|\left[(\mathbf{u_w}-\mathbf{u})\cos\theta + \mathbf{k}\times(\mathbf{u_w}-\mathbf{u})\sin\theta\right],\end{aligned} \tag{4.9}$$

where $C_a$ and $C_w$ are drag coefficients, $\rho_a$ and $\rho_w$ are densities, $\mathbf{u_g}$ is the geostrophic wind, $\mathbf{u_w}$ is the geostrophic ocean current, and $\phi$ and $\theta$ are turning angles.

*Ice rheology and the constitutive law*

The momentum equation depends on the ice internal force which in turn depends on the ice stress tensor, thus

$$\mathbf{F} = \frac{\partial}{\partial \mathbf{x_j}}\sigma_{\mathbf{ij}}, \tag{4.10}$$

in Cartesian coordinates. A constitutive law characterizes the stress $\sigma$ resulting from a given strain rate $\dot{\epsilon}$ and ice thickness and concentration, defining the nature of the ice interaction. The rheology used in this model is from Hibler (1979) where the ice behavior is plastic at normal strain rates and viscous at very small strain rates. The viscous-plastic constitutive law from Hibler (1979) is summarized below.

The constitutive law can be cast in terms of the principal components of stress ($\sigma_I$ and $\sigma_{II}$) and strain rate ($\dot{\epsilon}_I$ and $\dot{\epsilon}_{II}$) with the pair of equations

$$\begin{aligned}\sigma_I &= \zeta\dot{\epsilon}_I - P/2\\ \sigma_{II} &= \eta\dot{\epsilon}_{II}\end{aligned} \tag{4.11}$$

where $P$ is the ice strength ($\dot{\epsilon}_I$ and $\dot{\epsilon}_{II}$ are the divergence and shear of $\mathbf{u}$, respectively). The nonlinear bulk $\zeta$ and shear $\eta$ viscosities are also functions of $\dot{\epsilon}_I$, $\dot{\epsilon}_{II}$. The functional forms are chosen so that the stress state lies on an elliptical yield curve,

$$\frac{(\sigma_I + P/2)^2}{(P/2)^2} + \frac{\sigma_2^2}{(P/2e)^2} = 1, \tag{4.12}$$

where $e$ is the ratio of the principal axes of the ellipse[3]. Thus requiring

$$\begin{aligned} \zeta &= \frac{P}{2\Delta} \\ \eta &= \frac{\zeta}{e^2} \\ \Delta &= \left(\dot{\epsilon}_I^2 + \dot{\epsilon}_{II}^2 e^{-2}\right)^{1/2} \end{aligned} \tag{4.13}$$

for plastic behavior. To avoid infinite viscosities as $\Delta \to 0$, $\zeta$ and $\eta$ are constrained to large limiting values corresponding to very small strain rates. In this case the stress state lies inside the elliptical yield curve and the ice behaves like a viscous fluid, exhibiting creep.

*Ice strength*

The ice strength is a quadratic function of the average ice thickness including the open water fraction ($h$) and the total concentration of ice (A), as suggested by Overland and Pease (1988), so that

$$P = P^* h^2 A \exp(-C(1 - A)), \tag{4.14}$$

where $P^*$ and C are fixed empirical constants. Overland and Pease (1988) based the functional form for $P$ on an energetics argument from Rothrock (1975) where the compressive strength is equated with the potential energy increase per unit strain in pure convergence plus the rate of frictional energy loss in ridging. Using the rule for mechanical redistribution that transforms ice into a thickness that is proportional to its original thickness, the compressive strength has a quadratic dependence on the regional ice thickness.

---

[3] Hibler (1979) chose $e = 2$ which is also used in this model.

*Mechanical redistribution*

The development of mechanical redistribution ($\Psi_i$, in Eq. 4.2) comes from the theory of the ice thickness distribution from Thorndike et al. (1975),

$$\Psi = |\dot{\epsilon}|[\alpha_0(\theta)\delta(h) + \alpha_r(\theta)w_r(h,g)], \tag{4.15}$$

where $|\dot{\epsilon}| = (\dot{\epsilon}_I^2 + \dot{\epsilon}_{II}^2)^{1/2}$, $\theta = \tan^{-1}\dot{\epsilon}_{II}/\dot{\epsilon}_I$, $\delta(h)$ is the Dirac delta function, $w_r(h,g)$ is the ridging mode, and $g(h)$ is the thickness distribution. The coefficients $\alpha_0(\theta)$ and $\alpha_r(\theta)$ depend on the yield curve (and vice versa) and are related by $\alpha_0(\theta) - \alpha_r(\theta) = \cos\theta$. For a plastic yield curve, Rothrock (1975) derived the relationship

$$\alpha_r(\theta) = -\frac{1}{2}\cos\theta + \frac{1}{2}\sqrt{\cos^2\theta + e^{-2}\sin^2\theta}. \tag{4.16}$$

The ridging mode is the sum of two distributions describing the ice participating in ridging ($-a(h)$) and the ice transformed from ridging ($n(h)$), normalized to properly conserve area and volume. The ice participating in ridging comes from weighting $g(h)$ by a function $b(h)$ that is designed to make thinner ice more likely to ridge than thicker ice. Thorndike et al. (1975) argues that a plausible $b(h)$ might depend linearly on the cumulative thickness distribution $G(h) = \int_0^h g(h)dh$ according to

$$b(h) = \begin{cases} \frac{2}{G^*}\left[1 - \frac{G(h)}{G^*}\right] & G \le G^* \\ 0 & G > G^*, \end{cases} \tag{4.17}$$

where $G^*$ is the limiting fraction below which all ridging occurs. With little data to base their assumption, Thorndike et al. (1975) used a rule for deriving $n(h)$ from $a(h)$ that forces all ice participating in ridging to be transformed into ice that is five times its original thickness. Hence,

$$\begin{aligned} a(h) &= b(h)g(h) \\ w_r(h) &= \frac{-a(h) + (1/25)a(h/5)}{4/5}. \end{aligned} \tag{4.18}$$

*Two categories*

The Evaluation of the ridging mode for the popular two-category sea ice model can be derived from the ice thickness distribution equations above. Following Stern et al. (1995), the thickness distribution is a sum of two delta functions,

$$g(h) = (1 - A)\delta(h) + A\delta(h - H). \tag{4.19}$$

For simplicity, the index $i = 1$ is dropped. The two categories of sea ice have thicknesses as follows: category 0 is zero-thickness, category 1 is thickness $H$ which is always greater than $H_0^*$.

Using the viscous-plastic rheology ($|\dot{\epsilon}|\alpha_r = (\Delta - \dot{\epsilon}_I)/2$), the redistribution term is

$$\Psi_2 = \int_{H_0^*}^{\infty} \Psi dh = \frac{1}{2}(\Delta - \dot{\epsilon}_I)W. \tag{4.20}$$

Substituting Eq. 4.19 into Eq. 4.17 and integrating Eq. 4.18, Stern et al. (1995) showed

$$W = \begin{cases} \left[1 - \frac{1-A}{G^*}\right]^2 & 1 - A \leq G^* \\ 0 & 1 - A > G^*. \end{cases} \tag{4.21}$$

With just one non-zero thickness category, mechanical redistribution does not change the volume or enthalpy of category 1, so $\Theta_1 = \Pi_1 = 0$.

*Three categories*

The special case of redistribution for three-categories of ice is derived in Stern et al. (1995) using Eqs. 4.17 and 4.18. For three categories the thickness distribution takes the simple form

$$g(h) = A_0\delta(h) + A_1\delta(h - H_1) + A_2\delta(h - H_2), \tag{4.22}$$

where $A_0 = 1 - A_1 - A_2$ is the concentration of open water. The three categories of sea ice have thicknesses as follows: category 0 is zero-thickness, category 1 is bounded

from below by $H_0^*$ and above by $H_1^*$, and category 2 is greater than $H_1^*$. Hence category 0 represents open water and category 1 and 2 are often called the thin and thick ice categories, respectively.

The redistribution terms can be written

$$\begin{aligned}\Psi_1 &= \int_{H_0^*}^{H_1^*} \Psi dh = \frac{1}{2}(\Delta - \dot{\epsilon}_I)W_1 \\ \Psi_2 &= \int_{H_1^*}^{\infty} \Psi dh = \frac{1}{2}(\Delta - \dot{\epsilon}_I)W_2.\end{aligned} \tag{4.23}$$

Again substituting Eq. 4.22 into Eq. 4.17 and integrating Eq. 4.18, Stern et al. (1995) found

$$\begin{aligned}W_1 &= -5(V_1 - V_2)/4 \\ W_2 &= (V_1 - 5V_2)/4,\end{aligned} \tag{4.24}$$

where the auxiliary functions are defined as

$$\begin{aligned}V_1 &= \begin{cases} \left[1 - \frac{A_0}{G^*}\right]^2 & A_0 \le G^* \\ 0 & A_0 > G^* \end{cases} \\ V_2 &= \begin{cases} \left[1 - \frac{A_0 + A_1}{G^*}\right]^2 & A_0 + A_1 \le G^* \\ 0 & A_0 + A_1 > G^*. \end{cases}\end{aligned} \tag{4.25}$$

According to this formulation, ice from the thin category that ridges is transfered to the thick category. However when thick ice ridges, it has no place to go, so its concentration decreases and thickness increases, but the volume does not change. Hence

$$\begin{aligned}\Theta_1 &= -\Theta_2 = \Psi_1 H_1, \\ \Theta_1^s &= -\Theta_2^s = \Psi_1 H_1^s.\end{aligned} \tag{4.26}$$

For simplicity, I assume that mechanical redistribution does not mix heat vertically. Hence,

$$\begin{aligned}\Pi_1(x, y, z_1^*) &= -\Pi_2(x, y, z_2^*) = \Psi_1 Q_1(x, y, z_1^*) H_1, \\ \Pi_1^s(x, y, z_1^{s*}) &= -\Pi_2^s(x, y, z_1^{s*}) = \Psi_1 Q_1^s(x, y, z_1^{s*}) H_1^s.\end{aligned} \tag{4.27}$$

Data from which to develop a less restrictive model are lacking.

*Four categories*

A fourth category can be added, making

$$g(h) = A_0\delta(h) + A_1\delta(h - H_1) + A_2\delta(h - H_2) + A_3\delta(h - H_3). \tag{4.28}$$

The four categories of sea ice have thicknesses as in the three category case except category 2 is bounded from above by $H_2^*$ and category 3 is greater than $H_2^*$. A third redistribution term is required,

$$\Psi_3 = \int_{H_2^*}^{\infty} \Psi dh = \frac{1}{2}(\Delta - \dot{\epsilon}_I)W_3. \tag{4.29}$$

The factors of $\Psi$ for the four categories are

$$\begin{aligned} W_1 =& -5(V_1 - V_2)/4 \\ W_2 =& (V_1 - V_2)/4 - 5(V_2 - V_3)/4, \\ W_3 =& (V_2 - 5V_3)/4, \end{aligned} \tag{4.30}$$

where $V_1$ and $V_2$ are defined as in 4.25 and the third auxiliary function is

$$V_3 = \begin{cases} \left[1 - \frac{A_0+A_1+A_2}{G^*}\right]^2 & A_0 + A_1 + A_2 \le G^* \\ 0 & A_0 + A_1 + A_2 > G^* \ . \end{cases} \tag{4.31}$$

Hence

$$\begin{aligned} \Theta_1 =& \Psi_1 H_1 \\ \Theta_2 =& -\Psi_1 H_1 + (\Psi_2 + \Psi_1/5)H_2 \\ \Theta_3 =& -\Psi_2 H_2, \end{aligned} \tag{4.32}$$

and

$$\begin{aligned} \Pi_1 =& \Psi_1 Q_1 H_1 \\ \Pi_2 =& -\Psi_1 Q_1 H_1 + (\Psi_2 + \Psi_1/5)Q_2 H_2 \\ \Pi_3 =& -\Psi_2 Q_2 H_2. \end{aligned} \tag{4.33}$$

where $\Pi_i$ and $Q_i$ are functions of the normalized vertical coordinate. Equations 4.32 and 4.33 are easily modified to give expressions for $\Theta_i^s$ and $\Pi_i^s$ (not shown).

### *4.4.2 Thermodynamic definitions and parameterizations*

Before developing the equation that describe the terms in Eqs. 4.2-4.4, I will present a few basic thermodynamic definitions.

*Heat capacity, latent heat, and enthalpy*

The specific heat of sea ice $C_p(T,S)$ is parameterized[4] according to Untersteiner (1961) such that

$$C_p(T,S) = C_{pf} + \frac{\gamma S}{(273.2 - T)^2}, \tag{4.34}$$

where $C_{pf} = 1.88$ MJ m$^{-3}$ K$^{-1}$ is the specific heat of fresh ice, $S$ and $T$ are the ice salinity and temperature, respectively. This parameterization accounts for internal melting at the brine pocket/ice interface as the temperature approaches the melting temperature ($T_m$) to the extent that when it reaches $T_m$, it is completely melted. Hence the latent heat of sea ice is zero ($L = 0$) and Eq. 4.6 is simply

$$\begin{aligned} Q(T) &= \int_{T_m}^{T} C_p(T',S)dT' \\ &= C_{pf}(T - T_m) - \frac{\gamma S}{273.2 - T_m} + \frac{\gamma S}{273.2 - T}, \end{aligned} \tag{4.35}$$

The parameter $\gamma$ is determined by equating the energy needed to heat sea ice from 0 K to melting with the energy needed to do the same to fresh ice. Hence,

$$\frac{\gamma}{\alpha} = L_f \tag{4.36}$$

defines $\gamma$ based on the latent heat of fresh ice $L_f = 306$ MJ m$^3$ and the empirical constant $\alpha = 0.054$ K ppt$^{-1}$ where $T_m = 273.2 - \alpha S$.

---

[4] The index $i$ for each category is implied throughout this section.

*Conductivity*

Brine pockets also influence the conduction of heat through the ice which is parameterized

$$k(T,S) = k_f - \frac{\beta S}{273.2 - T}, \tag{4.37}$$

where $k_f = 2.034$ W m$^2$ K$^{-1}$ is the conductivity of fresh ice and $\beta$ is determined experimentally to be 0.1172 W m$^2$ ppt$^{-1}$.

*Salinity profile*

Melting at the brine pocket/ice interface makes sea ice very porous when it warms. In reality the ice drains as it becomes porous and its salinity decreases markedly before it melts at the upper surface [e.g., see *Weeks and Ackley, 1986*]. Also runoff of melt water from the upper surface draining through the ice flushes away brine and salt. Hence the salinity of ice tends to decrease towards the upper surface of the ice.

For simplicity the salinity profile is approximated as homogeneous, independent of space and time, within each ice category. New ice growing over open water is assumed to have 10 ppt and in all other categories the salinity is fixed at 3.2 ppt. This may seem to be a gross approximation, but at this time the few measurements of salinity indicate that it is nearly constant in the ice below freeboard. As a result of this approximation, the simulated temperature gradient near the upper surface is larger than it would be if the salinity was lower at the upper surface.

Relaxing the constant salinity approximation would complicate the method for conserving thermal energy in the ice as it grows and melts. At this time, I am unaware of any models that have a salinity profile in the ice and conserve thermal energy. This possible weakness in this and other thermodynamic treatments is being addressed elsewhere (B. Lipscomb, personal communication, 1997).

*Snow parameters*

I assume the snow is fresh, therefore the specific and latent heat of snow are $C_p^s = C_{pf}\rho^s/\rho$ and $L^s = L_f\rho^s/\rho$, where $\rho^s/\rho = 0.36$ is the ratio of snow and ice densities. The enthalpy of snow is

$$Q^s(T) = C_p^s(T - 273.2) - L^s. \tag{4.38}$$

The conductivity is $k^s = 0.31$ W m$^2$ K$^{-1}$.

*Sensible and latent heat fluxes*

The sensible and latent heat fluxes are parameterized according to bulk aerodynamic formulae,

$$F_{si} = c_{pa}C_H u_g(T_{air} - T_s) \tag{4.39}$$

and

$$F_{ei} = c_{pa}C_E u_g(q_{10m} - q_s), \tag{4.40}$$

where $c_{pa}$ is the specific heat of dry air, $u_g$ is the geostrophic wind speed, $C_H$ and $C_E$ are transfer coefficients approximated by 1.75x10$^{-3}$ as in Parkinson and Washington (1979), $T_{air}$ is the surface air temperature, and $q_{10m}$ and $q_s$ are the specific humidity at 10-m and at the surface. $q_{10m}$ is fixed at 90% relative humidity based on $T_{air}$ and $q_s$ is assumed to be saturated with respect to an ice surface (or an ocean surface, where applicable).

*Penetrating solar radiation*

The solar radiation penetrating the sea ice in Eq. 4.5 is absorbed according to Beer's Law, $I_0e^{\kappa z}$, with extinction length $\kappa = 0.015$ cm$^{-1}$. The fraction of the net solar radiation incident on the top surface that penetrates the surface ($I_0$) depends on the cloudiness (C) according to $I_0 = 0.18(1 - C) + 0.35C$.

*Albedo*

The ice/snow albedo $\alpha$ accounts for patchy snow coverage

$$\alpha = \alpha_{ice} + (\alpha_{snow} - \alpha_{ice})\frac{H_s}{H_s + 10}, \tag{4.41}$$

with $H_s$ in cm, as in Bettge et al. (1996). I impose the additional constraint that $\alpha$ must be at least 0.05 more than the ocean albedo, $\alpha_0$. The ice albedo depends on the ice thickness (in cm) and surface temperature[5] such that (see Fig. 4.1)

$$\alpha_{ice} = \alpha_0 + \alpha^i \left(\frac{1}{2} + \frac{1}{2}\tanh\frac{H-20}{80}\right) - 0.1\left(\frac{1}{2} + \frac{1}{2}\tanh\frac{Ts-272}{0.3}\right). \tag{4.42}$$

The snow albedo depends on the surface temperature such that

$$\alpha_{snow} = \alpha^s - 0.1\left(\frac{1}{2} + \frac{1}{2}\tanh\frac{Ts-272}{0.3}\right), \tag{4.43}$$

where $\alpha_0 = 0.1$, $\alpha^i = 0.6$, and $\alpha^s = 0.8$. The albedo of new ice that forms over the lead is fixed at $\alpha_{new} = 0.3$. The asymptotic limits of Eqs. 4.42 and 4.43 are designed to approximate measured dry and melting snow and sea ice values from Grenfell and Maykut (1977). The functional dependence on ice thickness and temperature is meant to allow smooth transitions between the asymptotic limits to avoid erroneous numerical oscillations from abrupt changes.

### *4.4.3 Thermodynamic processes*

In this section I derive expressions for the thermodynamic terms $\mathcal{A}_i$, $\mathcal{V}_i$, $\mathcal{V}_i^s$, $\mathcal{E}_i$, $\mathcal{E}_i^s$, and $F_{mix}$ representing contribution by thermodynamic processes in Eq. 4.2-4.4, and 4.8. The first six terms represent changes from top, bottom, and lateral melt; bottom growth; new ice growth over the open water fraction; redistribution when an ice category outgrows its thickness boundary; and vertical heat transfer (diffusion). The last term is the net heat flux into the open water fraction.

[5] The albedo parameterization given here differs from that used in the single column model (Eq. 2.1) because this model is designed to simulate thin ice and open water areas explicitly.

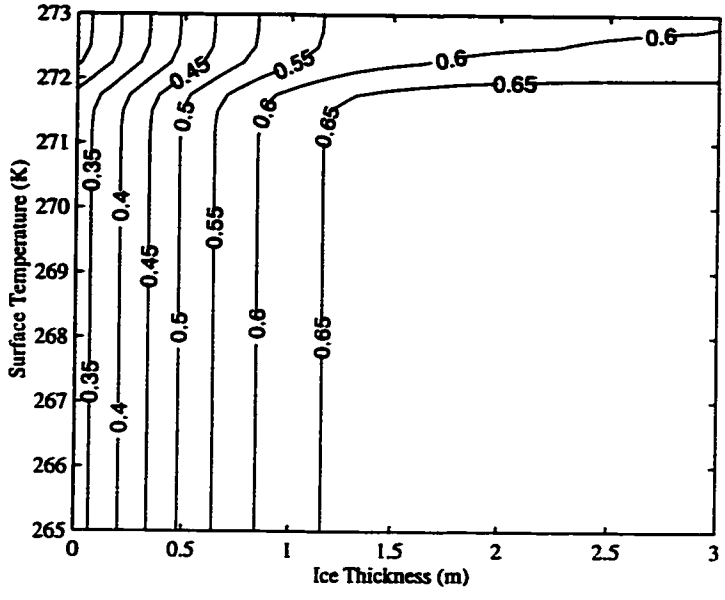


Figure 4.1: Surface albedo parameterization for Eq. 4.42.

To derive explicit equations for the thermodynamic processes in this model, it is necessary to define the vertical grid. Each category has $N_i$ vertical layers of sea ice and one layer of snow. The specific enthalpy is constant throughout the vertical layer in each grid box. Layers are numbered 0 for the snow, 1 for the top layer of the ice, and so on. The index $k$ is used to identify the layer.

Now the thermodynamic terms become

$$\begin{aligned}
\mathcal{A}_i &= \mathcal{A}_{ai} + \mathcal{A}_n\delta_{i1} + \mathcal{A}_{ri}, \\
\mathcal{V}_i &= \mathcal{V}_{ai} + \mathcal{V}_{ti} + \mathcal{V}_{bi} + \mathcal{V}_n\delta_{i1} + \mathcal{V}_{ri}, \\
\mathcal{V}_i^s &= \mathcal{V}_{ai}^s + \mathcal{V}_{ti}^s + \mathcal{V}_{ri}^s, \\
\mathcal{E}_{ik} &= \mathcal{E}_{aik} + \mathcal{E}_{(t\&b)ik} + \mathcal{E}_{nk}\delta_{i1} + \mathcal{E}_{rik} + \mathcal{E}_{dik}, \\
\mathcal{E}_i^s &= \mathcal{E}_{ai}^s + \mathcal{E}_{ti}^s + \mathcal{E}_{ri}^s + \mathcal{E}_{di}^s,
\end{aligned} \tag{4.44}$$

where $\delta_{i1}$ is the Kronecker delta symbol, defined such that $\delta_{i1} = 1$ when $i = 1$, otherwise $\delta_{i1} = 0$. The subscripts $a$, $t$, $b$, $n$, $r$ and $d$ refer to lateral, top, bottom, new, redistribution, and diffusion, respectively.

The solution to the heat equation, Eq. 4.5, accounts for thermal diffusion. There is no simple closed form expression for the thermal diffusion terms, $\mathcal{E}_{dik}$ and $\mathcal{E}^s_{di}$, therefore these terms are only meant to represent thermal diffusion and will not be defined explicitly. I will explain the method for including the effects of thermal diffusion on the state of the system in section 4.5.

*Freezing and melting at the top and bottom surfaces*

The enthalpy of each layer of ice depends on the mean temperature of the layer ($T_k$) according to Eq. 4.35,

$$Q_k = C_{pf}(T_k - T_m) - L_f + \frac{\gamma S}{273.2 - T_k}. \tag{4.45}$$

Energy balance at the top and bottom surfaces determines sea ice melt and growth rates. From the top surface energy balance in Eq. 4.7, if $F_{net}(T_m) \geq 0$, then the upper surface is fixed at the melting temperature and $F_{net}$ is used for melting according to

$$F_{net}(T_m) = -Q^s \eta^s \tag{4.46}$$

until the snow layer is gone and then

$$F_{net}(T_m) = -Q_1 \eta, \tag{4.47}$$

where $Q^s$ and $Q_1$ are specific enthalpies of the snow and the top layer of the ice and $\eta^s$ and $\eta$ are the changes to the snow and ice thickness due to melting at the top surface.

The bottom surface energy balance is

$$X_b - k\frac{\partial T}{\partial z} = -Q_b \nu, \tag{4.48}$$

where $X_b$ is the heat flux from the mixed layer and $\nu$ is the change to the ice thickness due to growth/melt. The bottom surface grows (melts) when the lefthand side of Eq. 4.48 is negative (positive). $Q_b = Q_N$ when ice is melting, otherwise

$$Q_b = C_{pf}(T_w - T_m) - L_f + \frac{\gamma S}{273.2 - T_w} \tag{4.49}$$

as ice is growing at the ice/mixed layer interface which is at $T_w$.

The specific enthalpy of the ice and snow layers needs to be adjusted when the layer spacing changes after growth and melt at the surfaces (see Fig. 4.2). The adjusted specific enthalpy is

$$Q'_k = \sum_l w_{l,k} Q_l + w_{b,k} Q_b. \tag{4.50}$$

The $w_{l,k}$ are weights computed from the relative overlap of the layer k with with each layer l from the old layer spacing (including both snow and ice layers). $w_{b,k}$ is non-zero when ice grows at the bottom surface.

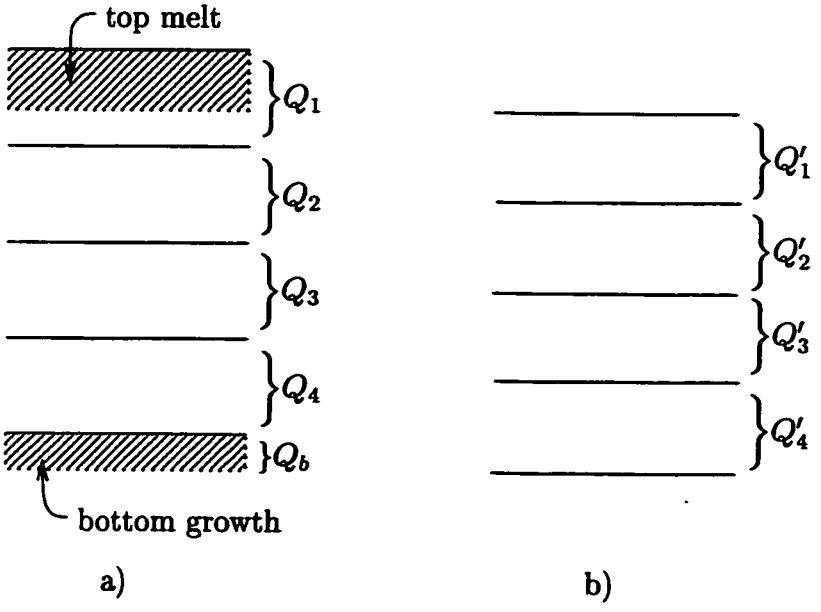


Figure 4.2: Diagram showing heat content before (a) and after (b) changing the layer spacing for an ice model with four vertical layers that has experience melt at the top surface and growth at the bottom surface.

Referring back to Eq. 4.44, now I can evaluate the terms with subscripts $t$ and $b$.

Hence

$$\begin{aligned} \mathcal{V}_t &= \eta A, \\ \mathcal{V}_b &= \nu A, \\ \mathcal{V}_t^s &= (\eta^s + \mu^s) A, \\ \mathcal{E}_{(t\&b)k}\delta t &= Q_k' - Q_k, \\ \mathcal{E}_t^s &= Q^s(\eta^s + \mu^s) A, \end{aligned} \tag{4.51}$$

where $\mu^s$ is the (prescribed) snowfall rate and the index $i$ is implied. $\delta t$ represents the time spent freezing/melting before the energy is adjusted. In practice, the model equations are discretized so $\delta t$ is equal to the timestep $\Delta t$.

*Mixed layer/open water energy balance*

Heat transfer between the mixed layer and ice is partitioned between lateral melt and bottom melt according to parameterizations that depend on the temperature of the water in the mixed layer. The lefthand side of Eq. 4.8 can be expanded so

$$F_{mix} = A_0 F_0 + F_w + \sum_i A_i (I_i - X_{ai} - X_{bi} + R_i) = C_{po} D_0 \frac{dT_w}{dt}, \tag{4.52}$$

where $F_0$ is the net heat flux into the top surface, $F_w$ is the heat flux from the deep ocean, $I_i$ is the solar radiation passing through the bottom of thickness category $i$, $X_{ai}$ and $X_{bi}$ are the lateral and bottom heat fluxes into the ice, $R_i$ is the flux of heat from melt water runoff by the ice top surface (see fig. 4.3). When the heat balance is such that $T_w$ is below $T_f$, $T_w$ is fixed at $T_f$ and the excess (negative) heat is used to grow new ice on the open water fraction. (The following section is devoted to describing the process of new ice growth.)

The net heat flux into the open water is

$$F_0 = F_\tau (1 - \alpha_0) + F_L - \sigma T_w^4 + F_{so} + F_{eo}, \tag{4.53}$$

where $\alpha_0$ is the albedo of the ocean and $F_{so}$ and $F_{eo}$ are the sensible and latent heat fluxes over open water, respectively. The solar radiation passing through the bottom

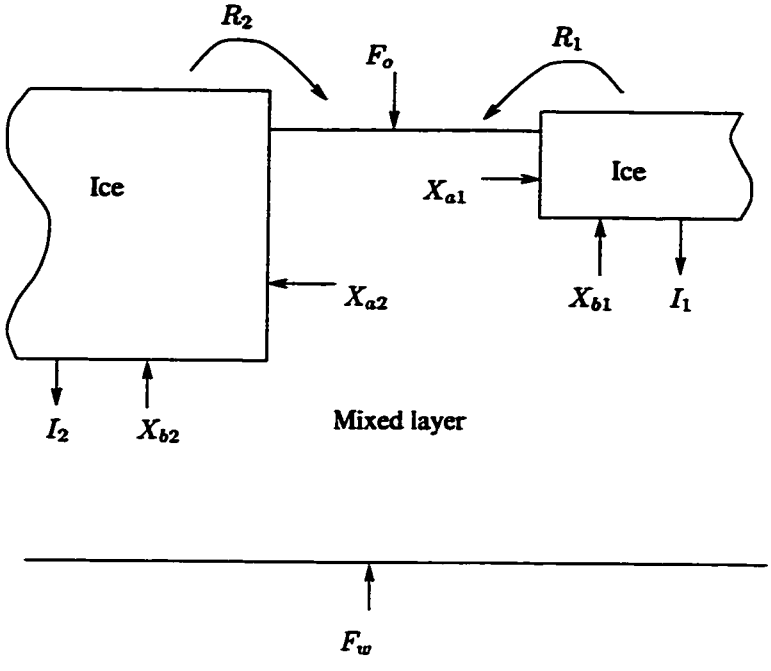


Figure 4.3: Schematic of mixed layer/open water energy balance.

of thickness category $i$ in Eq. 4.7 is

$$I_i = I_0 e^{-H_i \kappa}. \tag{4.54}$$

In Eq. 4.52 assumes all solar radiation that enters the top surface of the mixed layer is absorbed by the mixed layer.

Parameterizations for lateral and bottom heat fluxes into the ice ($X_a$ and $X_b$ in Eq. 4.52, with the index $i$ implied) depend on the rates the lateral and bottom interfaces are receding ($M_a$ and $M_b$) which, in turn, are functions of the mixed layer temperature. I assume lateral melting occurs uniformly over the interface,

$$X_a = [-\tilde{Q} + C_{po}(T_w - T_m)]HpM_a, \tag{4.55}$$

where $\tilde{Q}$ is the vertically averaged specific enthalpy of the sea ice, $C_{po}(T_w - T_m)$ is the energy needed to warm the melt water to the mixed layer temperature; $p$ is the

perimeter of the interface. The rate of heat exchange with the bottom is

$$X_b = -Q_b A M_b. \tag{4.56}$$

The lateral melt rate is parameterized according to Maykut and Perovich (1987) as

$$M_a = m_1(T_w - 271.2)^{m_2}. \tag{4.57}$$

From their analysis of ablation data taken during the Marginal Ice Zone Experiment, Maykut and Perovich (1987) determined best fit estimates for $m_1 = 3\text{x}10^{-6}$ and $m_2 = 1.36$. The bottom melt rate due to heat exchange with the mixed layer is parameterized according to McPhee (1992) as

$$M_b = c_h u_\tau (T_w - 271.2)\frac{C_{po}}{-Q_b}, \tag{4.58}$$

with empirical constant $c_h = 0.0058$ and skin friction velocity taken to be $u_\tau = 0.01$ m s$^{-1}$.

The perimeter depends on the floe distribution and geometry. Rothrock and Thorndike (1984) developed the concept of a "mean caliper diameter" ($d$) as the average over all angles of the distance between to parallel lines set against the floe's side walls (see fig. 4.4). Thus the floe perimeter is simply $p = \pi d$. Using aerial photographs of summer pack ice in the Beaufort Sea, Rothrock and Thorndike (1984) found a relationship for the floe area, $s = \xi d^2$, where $\xi = 0.66$. Following Steele (1992), it is assumed that the sea ice floe size in each thickness category can be described by an "average diameter" representing a regional ensemble average. Then the perimeter of the of the interface of open water is

$$p = n\pi d, \tag{4.59}$$

where the number of floes is $A/\xi d^2$. For simplicity, $d$ is taken to be 1 km and is independent of ice thickness category.

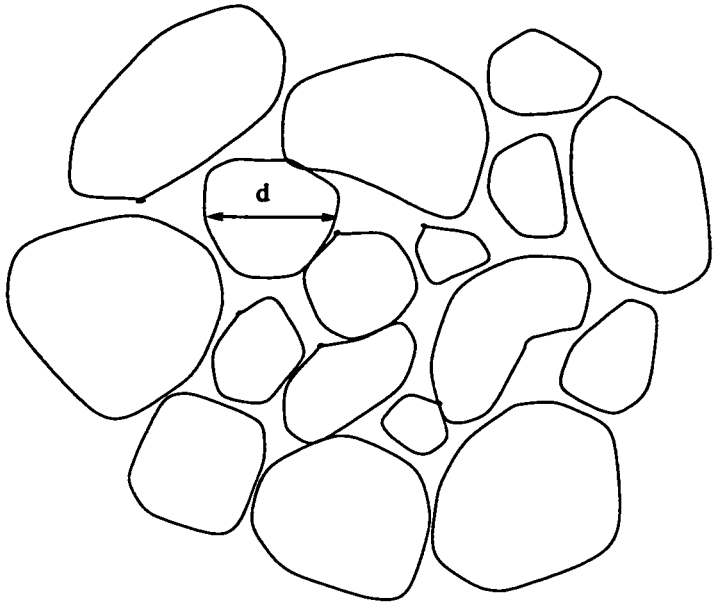


Figure 4.4: Hypothetical ice floe distribution.

Referring back to Eq. 4.44, now I can evaluate the terms with subscripts $a$,

$$\begin{aligned} \mathcal{A}_a &= -M_a p, \\ \mathcal{V}_a &= -M_a p H, \\ \mathcal{V}_a^s &= -M_a p H^s, \\ \mathcal{E}_{ak} &= -\tilde{Q} M_a p H / N, \\ \mathcal{E}_a^s &= -Q^s M_a p H^s. \end{aligned} \tag{4.60}$$

*New ice growth over open water*

New ice grows on the open water when the energy balance (Eq. 4.8) is such that $T_w$ is below the freezing temperature of sea water. Once new ice begins to grow the net heat flux into the mixed layer including the new ice (see section 4.5) is

$$F_{mix}^* = A_0 F_{new} + F_w + \sum_i I_i, \tag{4.61}$$

where the downward net heat flux from above the top surface of the new ice $F_{new}$ is

$$F_{new} = F_r(1 - \alpha_{new}) + F_L - \sigma T_{new}^4 + F_{si} + F_{ei}, \tag{4.62}$$

where $\alpha_{new}$ is the albedo of the new ice.

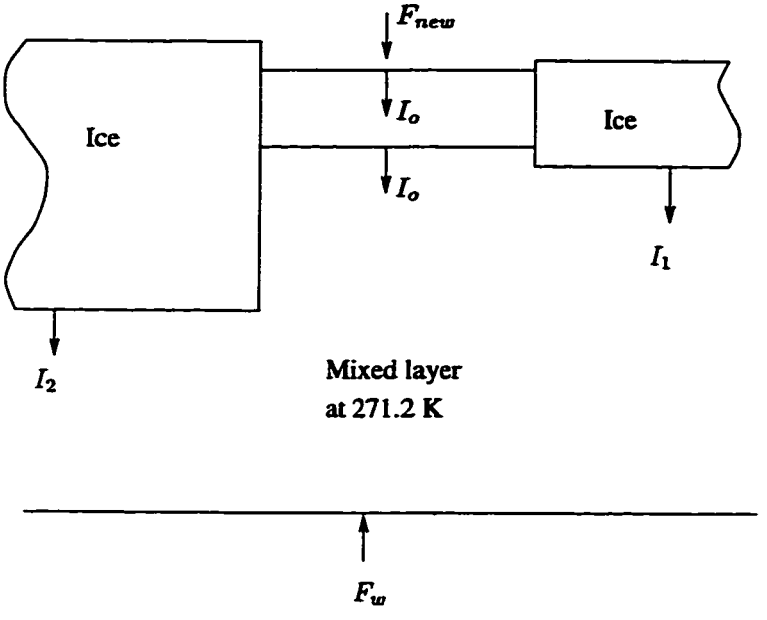


Figure 4.5: Schematic of mixed layer heat balance with new ice growing at the top surface.

Assuming a linear temperature profile in the new ice, the thickness ($H_{new}$) and top surface temperature ($T_{new}$) are determined from a pair of coupled equations,

$$\int 0.5(F_{mix} + F_{mix}^*)dt - A_0 H_{new} Q_{new} = 0 \tag{4.63}$$

and

$$F_{new} - I_0 + \frac{k}{H_{new}}(271.2 - T_{new}) = 0. \tag{4.64}$$

In Eq. 4.63, $0.5(F_{net} + F_{net}^*)$ is the average of the net flux into the mixed layer before and after the new ice grows and $Q_{new}$ is the specific enthalpy of the new ice. The solar radiation penetrating the top surface of the new ice ($I_0$) is assumed to pass

through the ice. Hence solar heating occurs only at the top sea ice surface for new ice growing over open water.

New ice that grows over open water is added to the thinnest ice thickness category (category 1). Category 1 ice is constrained to be at least $H_0^*$ so if $H_{new} < H_0^*$ then the new ice is reshaped so its thickness is equal to $H_0^*$, by conserving volume. Referring back to Eq. 4.44, now I can evaluate the terms with subscripts $n$. Hence

$$\begin{aligned} \mathcal{A}_n =& A_0 \left[ \mathcal{H}(H_{new} - H_0^*) + \frac{H_{new}}{H_0^*} \mathcal{H}(H_0^* - H_{new}) \right], \\ \mathcal{V}_n =& A_0 H_{new}, \\ \mathcal{E}_{nk} =& Q_{new} A_0 H_{new} / N, \end{aligned} \tag{4.65}$$

where $\mathcal{H}(z)$ is the unit step function which is defined to be 1 when $z > 0$ and 0 when $z \leq 0$.

### *4.4.4 Redistribution of ice between categories when the thickness outgrows its limits*

There is no dynamical or thermodynamical process that keeps the ice from outgrowing its thickness range for a given category, so a periodic adjustment must be made. For example, if the thin ice should should grow thicker than its upper thickness limit $H_1^*$, it is combined with the next thicker category. It is also possible for the thin ice to melt below $H_0^*$, then it must be reshaped so its thickness is $H_0^*$ and its concentration is adjusted to conserve volume.

Referring back to Eq. 4.44, now I can evaluate the terms with subscripts $r$. Hence for the special case when all $N_i = N$ the terms for the thinnest ice category are

$$\begin{aligned} \mathcal{A}_{r1}\delta t =& A_2 \mathcal{H}(H_2^* - H_2) - A_1 \left[ \frac{H_0^* - H_1}{H_0^*} \mathcal{H}(H_0^* - H_1) + \mathcal{H}(H_1 - H_1^*) \right], \\ \mathcal{V}_{r1}\delta t =& A_2 H_2 \mathcal{H}(H_2^* - H_2) - A_1 H_1 \mathcal{H}(H_1 - H_1^*), \\ \mathcal{V}_{r1}^s \delta t =& A_2 H_2^s \mathcal{H}(H_2^* - H_2) - A_1 H_1^s \mathcal{H}(H_1 - H_1^*), \\ \mathcal{E}_{r1k}\delta t =& \frac{A_2 H_2 Q_{2,k}}{N} \mathcal{H}(H_2^* - H_2) - \frac{A_1 H_1 Q_{1k}}{N} \mathcal{H}(H_1 - H_1^*), \\ \mathcal{E}_{r1}^s \delta t =& A_2 H_2^s Q_2^s \mathcal{H}(H_2^* - H_2) - A_1 H_1^s Q_1^s \mathcal{H}(H_1 - H_1^*), \end{aligned} \tag{4.66}$$

and for $i > 1$,

$$
\begin{aligned}
\mathcal{A}_{ri}\delta t =& A_{i-1}\mathcal{H}(H_{i-1} - H^*_{i-1}) + A_{i+1}\mathcal{H}(H^*_{i+1} - H_{i+1}) \\
& - A_i[\mathcal{H}(H^*_{i-1} - H_i) + \mathcal{H}(H_i - H^*_i)], \\
\mathcal{V}_{ri}\delta t =& A_{i-1}H_{i-1}\mathcal{H}(H_{i-1} - H^*_{i-1}) + A_{i+1}H_{i+1}\mathcal{H}(H^*_{i+1} - H_{i+1}) \\
& - A_iH_i[\mathcal{H}(H^*_{i-1} - H_i) + \mathcal{H}(H_i - H^*_i)], \\
\mathcal{V}^s_{ri}\delta t =& A_{i-1}H^s_{i-1}\mathcal{H}(H_{i-1} - H^*_{i-1}) + A_{i+1}H^s_{i+1}\mathcal{H}(H^*_{i+1} - H_{i+1}) \\
& - A_iH^s_i[\mathcal{H}(H^*_{i-1} - H_i) + \mathcal{H}(H_i - H^*_i)], \\
\mathcal{E}_{rik}\delta t =& \frac{A_{i-1}H_{i-1}Q_{i-1,k}}{N}\mathcal{H}(H_{i-1} - H^*_{i-1}) + \frac{A_{i+1}H_{i+1}Q_{i+1,k}}{N}\mathcal{H}(H^*_{i+1} - H_{i+1}) \\
& - \frac{A_iH_iQ_{ik}}{N}[\mathcal{H}(H^*_{i-1} - H_i) + \mathcal{H}(H_i - H^*_i)], \\
\mathcal{E}^s_{ri}\delta t =& A_{i-1}H^s_{i-1}Q^s_{i-1}\mathcal{H}(H_{i-1} - H^*_{i-1}) + A_{i+1}H^s_{i+1}Q^s_{i+1}\mathcal{H}(H^*_{i+1} - H_{i+1}) \\
& - A_iH^s_iQ^s_i[\mathcal{H}(H^*_{i-1} - H_i) + \mathcal{H}(H_i - H^*_i)],
\end{aligned}
\tag{4.67}
$$

where the thickest ice category has a limitless upper thickness bound $H^*_i \to \infty$ and $A^{\rightarrow}_{i+1}0$. $\delta t$ represents the time it takes for a process to cause the ice thickness to outgrow its boundary (also see Eq. 4.51).

## 4.5 *Methodology*

The above equations constitute a closed set of partial differential equations and algebraic equations[6] for the unknown variables. I propose to solve this system as a set of coupled, initial/boundary value problems.

### *4.5.1 Time splitting*

Figure 4.6 shows a block diagram of the key physical processes. Variables shown below a box are changed by the processes represented by the box above them. Temporal

[6] Except for the vertical diffusion terms $\mathcal{E}_{dik}$ and $\mathcal{E}^s_{di}$ which are found in a separate step from the solution of heat equation and cannot be expressed simply.

evolution is indexed by $j$. For example, the momentum equation affects only ice velocity, but advection changes all the state variables except ice velocity.

I use time splitting to separate the problem into multiple steps, updating the state after each. For example, time changes of the ice concentration are caused by advection, mechanical redistribution, (lateral) melting, and thermodynamic redistribution. Symbolically these steps are written

$$\begin{aligned} A^{j+1/4} &= A^j - \Delta t \nabla \cdot \mathbf{u}^{\mathbf{j+1}} A^j, \\ A^{j+1/2} &= A^{j+1/4} + \Delta t + \Psi(\mathbf{u}^{\mathbf{j+1}}, \mathbf{A}^{\mathbf{j+1/4}}), \\ A^{j+3/4} &= A^{j+1/2} + \mathcal{A}_a(T_w^j, Q^{j+1/2}, H^{j+1/2}), \\ A^{j+1} &= A^{j+3/4} + \Delta t \mathcal{A}_r(A^{j+3/4}, H^{j+3/4}) + \Delta t \mathcal{A}_n(T_w^{j+1}, A^{j+3/4}, H^{j+3/4}), \end{aligned} \tag{4.68}$$

where $\Delta t$ is the timestep and the category index $i$ is implied.

### *4.5.2 Solution for ice velocity*

The velocity is found from an iterative solution to Eqs. 4.1 and 4.9-4.14. A description of the numerical method is given in (appendix A Hibler, 1979). The solution used in this updated version of the model includes a more efficient numerical scheme that is documented in Zhang and Hibler (1997).

### *4.5.3 Numerical scheme for Advection*

Hibler (1979) used a centered difference advection scheme with harmonic and biharmonic diffusion to stabilize long integrations. The scheme is second order accurate, however the non-physical diffusion reduces the accuracy to some extent. One undesirable side effect of this numerical scheme is it allows negative quantities to exist in a grid box. Currently several modeling groups have modified the original Hibler advection scheme to avoid the negative quantities by using upstream differencing which is numerically diffusive and first order accurate. I adopt this method as well.

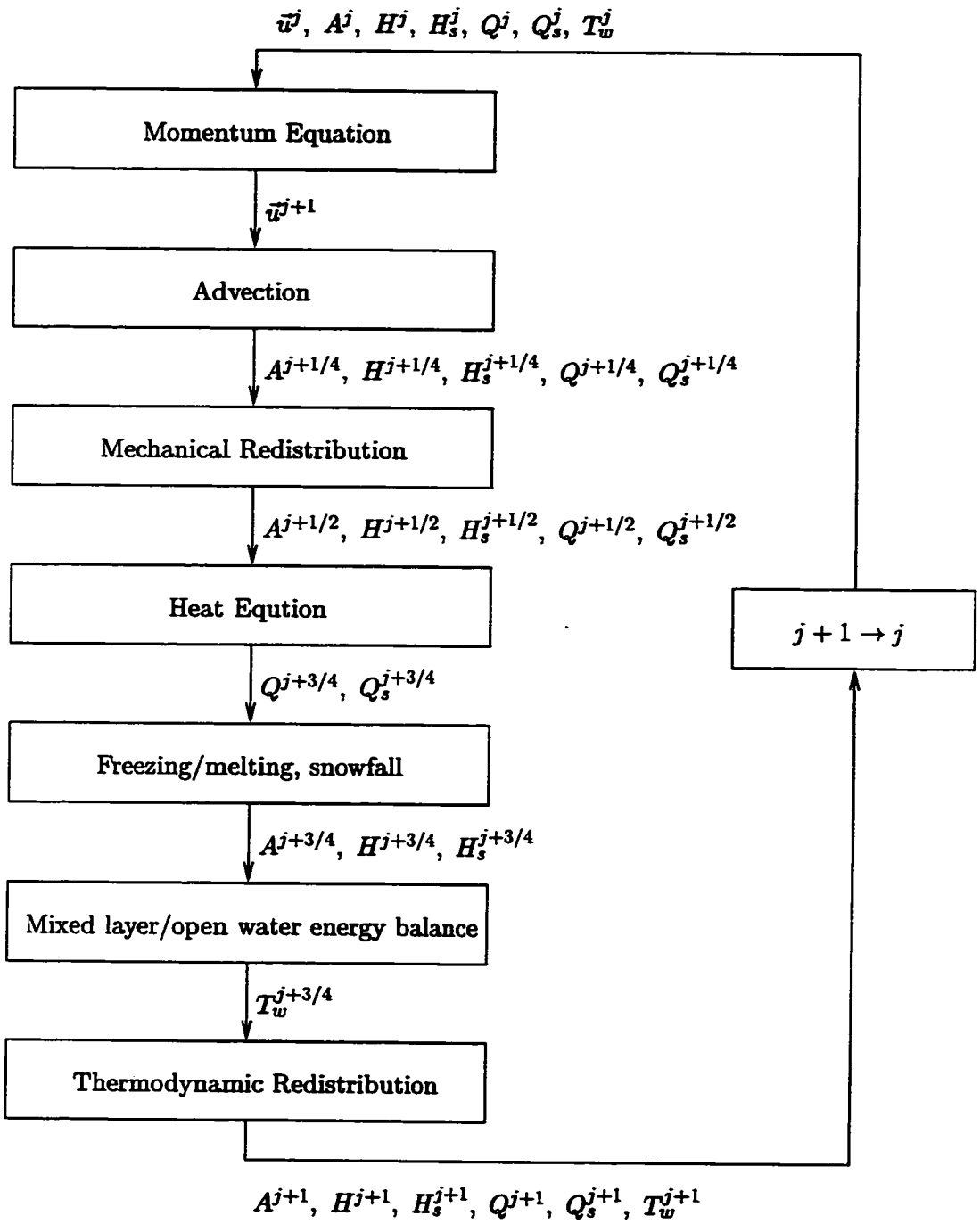


Figure 4.6: Block Diagram of model flow. Indices for thickness category and position are implied.

Advection of a quantity $g$ is written

$$\frac{\partial g}{\partial t} = -\nabla \cdot (g\vec{u}). \tag{4.69}$$

Using upstream differencing for an Arakawa-B grid (Fig. 4.7a), Eq. 4.69 becomes

$$\frac{\partial g}{\partial t} = (u_l g_l - u_r g_r + v_b g_b - v_t g_t)/\Delta x, \tag{4.70}$$

where $g_{(l,r,b,t)}$ are the upstream values of $g$ on the left, right, bottom, and top sides of the grid box and $u, v_{(l,r,b,t)}$ are the average velocity components along each side. For example, in Fig. 4.7b for grid box $i, j$,

$$u_l = u_{i-1,j-1} + u_{i-1,j}$$

and

$$g_l = \begin{cases} g_{i,j} & \text{when } u_l < 0 \\ g_{i+1,j}, & \text{when } u_l > 0. \end{cases}$$

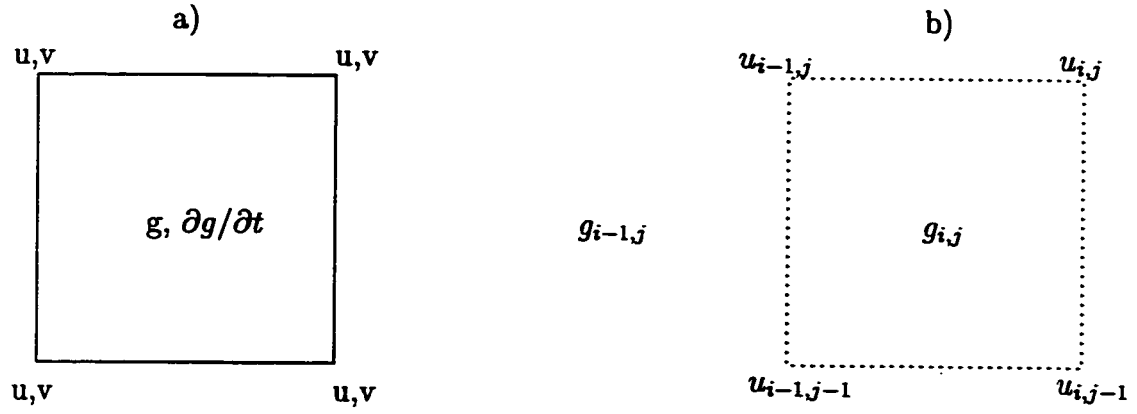


Figure 4.7: The staggered spatial Arakawa-B grid (a), with horizontal indices (b), used for computation.

### *4.5.4 Solution of the heat equation*

The solution of the heat equation is the most complicated part of the thermodynamic treatment because of the brine pockets present in sea ice. Vertical heat transfer is solved for $N$ vertical layers in the sea ice and one layer in the snow. Figure 4.8 shows a schematic of the vertical grid of the sea ice and illustrates the notations used in this section. A staggered vertical grid is used, with temperature and specific heat defined at the layer midpoint and conductivity defined at the layer interfaces. Hence $C_{pl} = C_p(T_l)$ for $l = 1, N$ (from Eq. 4.34), $k_l = k((T_l + T_{l+1})/2)$ for $l = 2, N$ (from Eq. 4.37), $k_{N+1} = k(T_{N+1})$, $C_{p0}$ and $k_0$ are fixed, and $k_1$ is described below.

When snow is present, it is useful to define an effective conductivity $k_1$ at the snow/ice interface so the conductive flux at the interface is $-2k_1(T_1 - T_0)/(\Delta H + H_s)$ (fluxes are positive downward as is the coordinate $z$). $k_1$ is derived by assuming the conductive fluxes above and below the interface are equivalent which is written numerically,

$$k_0 \frac{T_I - T_0}{hs/2} = k(T_1) \frac{T_1 - T_I}{\Delta H/2}, \tag{4.71}$$

where $T_I$ is the interface temperature and the snow conductivity $k_0$ is independent of temperature. Hence the effective conductivity is

$$k_1 = \frac{k_0 k(T_1)(\Delta H + H_s)}{\Delta H k_0 + H_s k(T_1)}. \tag{4.72}$$

The heat equation (Eq. 4.5) is discretized using an implicit scheme with two-levels in time and centered in space,

$$\begin{aligned} C_{pl}^j \frac{T_l^{j+1} - T_l^j}{\Delta t} = & \frac{1}{\Delta z_l} \left\{ \theta \left[ k_l^j \frac{T_{l+1}^{j+1} - T_l^{j+1}}{\Delta z_l} - k_{l-1}^j \frac{T_l^{j+1} - T_{l-1}^{j+1}}{\Delta z_{l-1}} \right] \right. \\ & \left. + (1-\theta) \left[ k_l^j \frac{T_{l+1}^j - T_l^j}{\Delta z_l} - k_{l-1}^j \frac{T_l^j - T_{l-1}^j}{\Delta z_{l-1}} \right] \right\} + I_l^j, \end{aligned} \tag{4.73}$$

where $\Delta z_l = H_s$ when $l = 0$; otherwise $\Delta z_l = \Delta H$. Equation 4.73 is solved with a tri-diagonal matrix solver. Experimentally I find Eq. 4.73 gives stable solutions for $\theta$=0.5 or 1.0 over the range of timesteps and layer spacing used in this study.

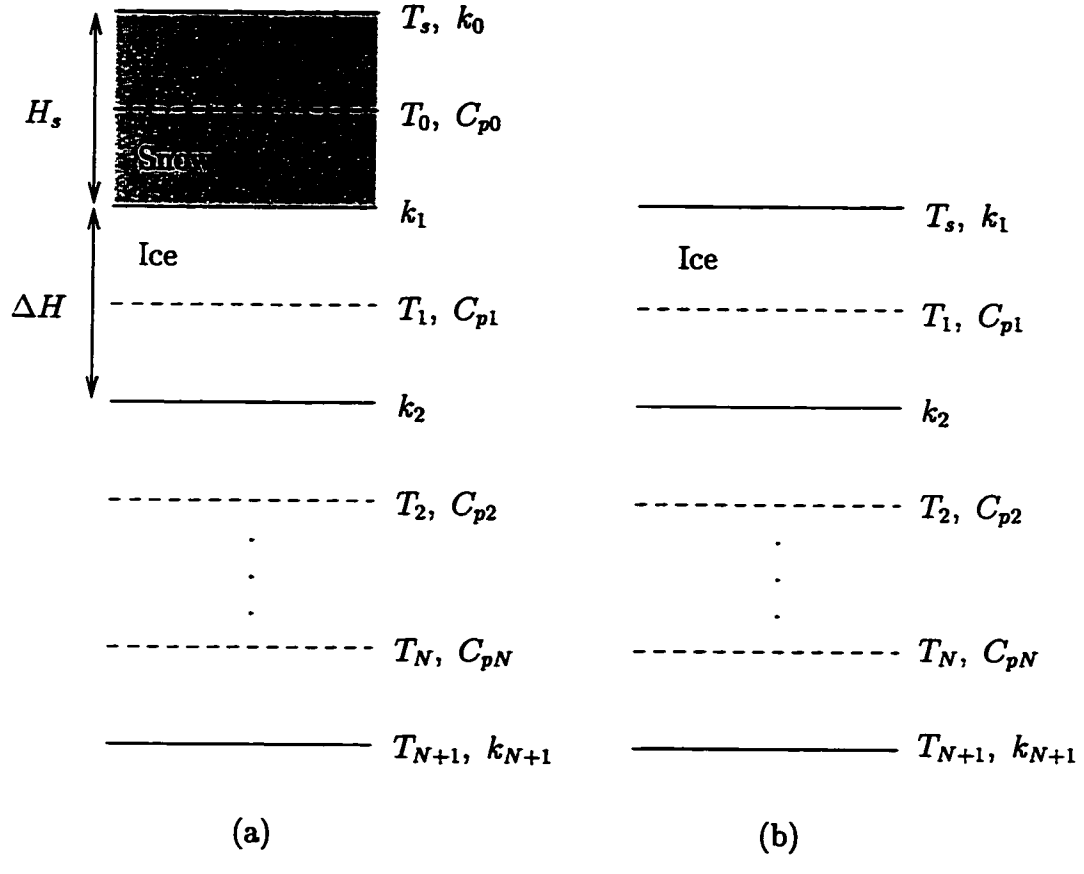


Figure 4.8: Vertical grid of the sea ice (a) when snow is present and (b) when the ice is snow-free. $\Delta H$ is the thickness of an ice layer and $H_s$ is the thickness of the snow layer. The surface temperature in either case is $T_s$.

The accuracy of Eq. 4.73 is a matter of some interest. Schemes with two-levels (e.g., Eq. 4.73 with $\theta$=0.5) in time are attractive because the truncation error can be second order in time $\mathcal{O}(\Delta t^2)$. However, the coefficients $C_{pl}^j$ and $k_l^j$ are fixed at a single level for the timestep, so Eq. 4.73 may not be second order accurate. To make Eq. 4.73 truly second order accurate would require replacing $C_{pl}^j$ with $\theta C_{pl}^{j+1} + (1-\theta)C_{pl}^j$ and the first two occurrences of $k^j$ with $k^{j+1}$. The resulting solution would be nonlinear and would need to be solved iteratively, an undesirable method for models used in long (climate) integration. An alternative to an iterative method is a predictor-corrector method whose error is intermediate between first and second order accurate.

The predictor-corrector method entails solving two tri-diagonal systems. First the predictor step is the solution of Eq. 4.73 with $\theta = 1$ to give an estimate of $T_l$ at the $(j+1)$ time, written $\widehat{T}_l^{j+1}$. Then $\widehat{T}_l^{j+1}$ is used to estimate $C_{pl}$ and $k_l$ at the $(j+1)$ time, giving $\widehat{C_{pl}}^{j+1}$ and $\widehat{k}_l^{j+1}$. Now the corrector step is

$$\left[\theta\widehat{C_{pl}}^{j+1} + (1-\theta)C_{pl}^j\right]\frac{T_l^{j+1}-T_l^j}{\Delta t} = \frac{1}{\Delta z_l}\left\{\theta\left[\widehat{k}_l^{j+1}\frac{T_{l+1}^{j+1}-T_l^{j+1}}{\Delta z_l} - \widehat{k}_{l-1}^{j+1}\frac{T_l^{j+1}-T_{l-1}^{j+1}}{\Delta z_{l-1}}\right]\right.$$
$$\left. + (1-\theta)\left[k_l^j\frac{T_{l+1}^j-T_l^j}{\Delta z_l} - k_{l-1}^j\frac{T_l^j-T_{l-1}^j}{\Delta z_{l-1}}\right]\right\} + I_l^j. \tag{4.74}$$

Both Eqs. 4.73 and 4.74 are modified for the surface layers in order to maintain second order accuracy with the change in layer spacing and to include boundary conditions. The top boundary condition for the heat equation depends on the net heat flux $F_{net}$ at the top surface such that if

$$F_{net} = F(T_m) + k\left.\frac{\partial T}{\partial z}\right|_{T_s=T_m} \geq 0, \tag{4.75}$$

then the top boundary condition is $T_s^{j+1} = T_m$; otherwise the top surface has the following flux boundary condition,

$$F(T_s) + k\frac{\partial T}{\partial z} = 0, \tag{4.76}$$

where F is defined by Eq. 4.75. The second-order accurate, finite-difference form of Eq. 4.76 is

$$F(T_s^{j+1}) + k_l^j \left[a(T_l^{j+1} - T_s^{j+1}) + b(T_{l+1}^{j+1} - T_s^{j+1})\right] = 0. \tag{4.77}$$

Coefficients $a$ and $b$ depend on the layer spacing such that when the ice is snow-free ($l = 1$, in Eq. 4.77) $a = 3/\Delta H$ and $b = -1/3\Delta H$ and when snow is present ($l = 0$),

$$\begin{aligned} a &= \frac{H_s + \Delta H/2}{H_s/2} \frac{2}{H_s + \Delta H} \\ b &= \frac{-H_s/2}{H_s + \Delta H/2} \frac{2}{H_s + \Delta H}. \end{aligned} \tag{4.78}$$

When the predictor-corrector method is used, $k_l^j$ is replaced by $\widehat{k}_l^{j+1}$ for the boundary condition in the corrector step. $F$ is a non-linear function of $T_s$, so a Newton-Rhapson iterative solution is used when the flux boundary condition applies.

The bottom boundary is in contact with sea water at $T_w$ which changes very slowly so $T_{j+1}^{j+1} = T_{j+1}^j = T_w^j$ unless $T_w^j$ is above the melting temperature of sea ice in which case $T_{j+1}^{j+1} = T_{j+1}^j = T_m$.

Table 4.2 shows a comparison of the relative error in the temperature for the solution with and without the predictor-corrector step and $\theta = 1$ and 0.5. The integrations were performed with the model run in column mode with a fixed concentration and thickness, $A_2 = 0.95$, $H_2 = 320$-cm, $H_2^s = 0$, and $A_1 = 0$. The model is forced with surface air temperature and geostrophic winds from 1979 at 86°N 10°W. Solar radiation and incoming longwave radiation are calculated as in Parkinson and Washington (1979) with climatological cloud cover. Further details about the external forcing are reserved for the following chapter when the full dynamic/thermodynamic model is run in hindcast mode.

The error of the interior temperature ($L(T_k)$) is measured by computing the rms of the difference between temperature from the integrations listed in table 4.2 and an temperature ($T_k^0$) from integration with very fine resolution and a small time step.

Hence

$$L(T_k) = \sqrt{\sum_k (T_k - T_k^0)^2}. \tag{4.79}$$

Table 4.2: Numerical error of temperature in ice interior $L(T_k)$ and at the surface $L(T_s)$ for the following schemes: backwards (B); backwards, predictor-corrector (BPC); Crank-Nicholson (CN); and Crank-Nicholson, predictor-corrector (CNPC). The model was run in column mode. There is a seasonal cycle to the error (not shown), with the error being largest in September and decaying roughly linearly in time throughout the winter, until it is negligible in summer. The errors listed are averaged from September to June. Error is reported in milli-Kelvin (mK).

| scheme | $\Delta H$ | $\Delta t$ | $L(T_k)$ | $L(T_s)$ | $\Delta H$ | $\Delta t$ | $L(T_k)$ | $L(T_s)$ |
|---|---|---|---|---|---|---|---|---|
| | cm | day | mK | mK | cm | day | mK | mK |
| B | 80 | 1 | 677 | 305 | 20 | 1/4 | 135 | 56 |
| BPC | 80 | 1 | 439 | 274 | 20 | 1/4 | 70 | 42 |
| CN | 80 | 1 | 659 | 276 | 20 | 1/4 | 128 | 41 |
| CNPC | 80 | 1 | 420 | 244 | 20 | 1/4 | 62 | 24 |

The backwards scheme ($\theta = 1$) has the largest error as it should because it is only first order accurate in time. The Crank-Nicholson ($\theta = 0.5$), predictor-corrector method has the lowest error. Because there is little difference in computing costs between the backwards and Crank-Nicholson methods, the second-order method is used generally without the corrector step for all but the thinnest ice category. The thin ice category heat equation is solved with the backwards method because the Crank-Nicholson method occasional gave poor results for certain initial conditions with very thin layers. Whether the extra computing time to perform the predictor-corrector justifies the improvement over the error without the corrector step is not clear.

Table 4.3: Numerical error of temperature in ice interior and at the surface for the Crank-Nicholson, predictor-corrector scheme.

| $\Delta H$ | $\Delta t$ | $L(T_k)$ | $L(T_s)$ |
|---|---|---|---|
| *cm* | *day* | mK | mK |
| 80 | 1 | 420 | 244 |
| 40 | 1/2 | 161 | 86 |
| 20 | 1/4 | 62 | 24 |
| 10 | 1/8 | 32 | 10 |
| 5 | 1/16 | 17 | 4 |

Integration with various layer spacings and time steps were performed to determine the accuracy of the scheme. Table 4.3 shows the experiments designed to test the Crank-Nicholson, predictor-corrector method. For a second-order accurate method, the error should fall by one-quarter when $\Delta H$ and $\Delta t$ are halved. These experiments verify that the method is more likely first-order accurate. Roughly the same accuracy is achieved for all four methods (only CNPC is shown). The model is influenced by many processes beyond the solution of the heat equation whose error can reduce the accuracy of the temperature.

Varying the layer spacing from 4-16 layers and the timesteps from 1/4-1 day independently (not shown) indicates the error is dominated by spatial resolution. It is difficult to argue for a particular layer spacing that adequately resolves the vertical processes without defining adequate. Because this study is focusing on ice mass variability, an appropriate test might be to examine the variability as a function of layer spacing. However, the ice response should be examined in a model coupled to an atmosphere which is beyond the scope of this dissertation. A discussion of the

results from uncoupled experiments will be postponed until the following chapter. For completeness here an estimate of how the growth and melt depends on resolution is examined below.

### *4.5.5 how growth/melt depend on vertical resolution*

The amount of melt/growth at the top and bottom surface are computed from Eqs. 4.47 and 4.48 as a diagnostic from the temperature profile $(T_s^{j+1}, T_k^{j+1})$ and prescribed forcing. The mixed layer heat flux changes slowly so $X_b$ is prescribed based on the temperature $T_w^j$.

The total annual growth and melt at top and bottom surfaces as a function of vertical resolution are shown in table 4.4. The top melt and bottom growth increase (as does the range) with smaller layer layer spacing, so the net change in thickness is perhaps fortuitously insensitive to layer spacing.

Table 4.4: Total annual growth (G) and melt (M) at top and bottom surfaces for CNPC and BPC schemes. The model was run in column mode with ice thickness fixed at 320-cm and concentration fixed at 1.0.

| CNPC | | | | | | BPC | | | | | |
|---|---|---|---|---|---|---|---|---|---|---|---|
| | | top | bottom | | net | | | top | bottom | | net |
| $\Delta H$ | $\Delta t$ | M | G | M | | $\Delta H$ | $\Delta t$ | M | G | M | |
| *cm* | *days* | *cm* | *cm* | *cm* | *cm* | *cm* | *days* | *cm* | *cm* | *cm* | *cm* |
| 80 | 1 | 36.1 | 41.4 | 1.6 | 3.6 | 80 | 1 | 37.7 | 39.0 | 2.0 | -0.6 |
| 40 | 1/2 | 37.0 | 43.5 | 1.4 | 5.1 | 40 | 1/2 | 38.1 | 42.3 | 1.6 | 2.5 |
| 20 | 1/4 | 38.3 | 44.2 | 1.3 | 4.6 | 20 | 1/4 | 39.1 | 43.6 | 1.4 | 3.1 |
| 10 | 1/8 | 39.4 | 44.1 | 1.2 | 3.4 | 10 | 1/8 | 39.9 | 43.7 | 1.3 | 2.5 |
| 5 | 1/16 | 40.3 | 44.1 | 1.2 | 2.7 | 5 | 1/16 | 40.6 | 43.9 | 1.2 | 2.1 |

### *4.5.6 Heat exchange between mixed layer/open water due to lateral melt and bottom melt*

Table 4.5 shows the total annual energy transferred through the mixed layer/open water into to lateral melt and bottom melt. The integrations were performed with the model run in column mode with concentration and thickness fixed as shown in the table during each integrations. The forcing is as described above.

For ice concentrations typical of the central Arctic, the energy that goes into bottom melt is more than 50 times that which goes into lateral melt. The factor can be even more for higher ice concentration and/or thinner ice. The flux into the bottom of the ice is about 0-5 W $m^{-2}$ for average central Arctic conditions.

Table 4.5: Total annual energy transferred through the mixed layer into lateral melt and bottom melt based on the model run in column mode with ice thickness and area fixed during each integration. The equivalent, time-averaged heat flux is also given. Units are per horizontal area.

| Initial Conditions | | | | Heat Exchange | | Average Flux | |
|---|---|---|---|---|---|---|---|
| $A_1$ | $H_1$ ($cm$) | $A_2$ | $H_2$ ($cm$) | Lateral ($MJm^{-2}$) | Bottom ($MJm^{-2}$) | Lateral ($Wm^{-2}$) | Bottom ($Wm^{-2}$) |
| 0 | 0 | 0.99 | 320 | 0.09 | 11.7 | 0.003 | 0.37 |
| 0 | 0 | 0.9 | 320 | 1.3 | 78.8 | 0.04 | 2.5 |
| 0 | 0 | 0.8 | 320 | 2.8 | 151.6 | 0.09 | 4.8 |
| 0 | 0 | 0.6 | 320 | 5.4 | 286.5 | 0.17 | 9.1 |
| 0 | 0 | 0.4 | 320 | 6.0 | 385.5 | 0.19 | 12.2 |
| 0.4 | 50 | 0.4 | 320 | 0.99 | 178.9 | 0.03 | 5.7 |
| 0.8 | 50 | 0.0 | 0 | 0.56 | 204.8 | 0.02 | 6.5 |

## 4.6 Comparison to other models

### 4.6.1 Dynamics

The viscous plastic rheology (e.g., Hibler, 1979) is likely to become popular for climate simulation. In the past few years a few general circulation models (e.g., the Climate System Model from the National Center for Atmospheric Research (NCAR)) adopted the cavitating fluid rheology of Flato and Hibler (1992) because it is simpler and integrates more quickly than models with a viscous plastic rheology. However there are three compelling reasons to the choose viscous plastic rheology: (1) it is less restrictive because it computes deformation from shear stress, (2) it is stable on an Arakawa B-grid which is the typical grid used for large-scale ocean models, and (3) Zhang and Hibler (1997) made the viscous plastic model run with comparable speed.

Multi-category (thickness distribution) models in dynamic/thermodynamic sea ice models have been used by Hibler (1980), Flato and Hibler (1995), and Flato (1995). The latter is the only study with direct climate implications (see section 3.8.2). The thickness distribution described here is distinct from these model in one essential way: the thickness within each category is allowed to vary within the boundaries that define the category. The multi-category models fix the ice thickness within each category and conserve mass by adjusting the concentration. Hence compared to the fixed thickness, multi-category model, the three and four category models described in this chapter have more degrees of freedom per category associated with the conservation of mass.

### 4.6.2 Thermodynamics

The fundamental equations representing heat conduction, freezing, and melting in the ice described in this chapter resemble that of Maykut and Untersteiner (1971), however I assume salinity is fixed and account for internal melting when determining the melt rate. The ice internal temperature profile is determined essentially in the

same fashion as in the one dimensional sea ice model of Ebert and Curry (1993).

Currently the most thermodynamically realistic dynamic/thermodynamic climate models use the Semtner (1976) three layer (two ice and one snow) model (Ross and Walsh, 1987; Häkkinen, 1993; Chapman et al., 1994). The Semtner model uses a fictitious heat reservoir to mimic the effect of brine pockets in the fall. The reservoir method is highly restrictive for variability issues. The ice model employed in the NCAR Community Climate Model number (CCM3) has multiple layers (hence a non-zero heat capacity) but does not parameterize brine pockets nor does it have a fictitious reservoir (Kiehl et al., 1996).

Conservation of internal energy of the ice when the ice is in motion requires a horizontal advective term. Advection of the ice internal energy has been implemented previously in the NCAR Genesis and Climate System Models (Pollard and Thompson, 1994; Bettge et al., 1996). However, these NCAR models have just two-categories of sea ice, use the highly simplified thermodynamics of Semtner (1976), and the cavitating-fluid rheology of Flato and Hibler (1992). Hence the method developed here is considerably more realistic, albeit more complicated.

In typical dynamic/thermodynamic sea ice models the energy absorbed by the open water/mixed layer is transferred to the sea ice laterally and at the bottom by splitting the energy in some matter (e.g., 50% to each). In this model the mixed layer stores energy and transfers it to the ice laterally and to the ice bottom according to the temperature of the mixed layer.

# Chapter 5

# A STUDY OF NATURAL VARIABILITY OF ARCTIC SEA ICE SIMULATED BY A DYNAMIC/THERMODYNAMIC SEA ICE MODEL

## *5.1 Introduction*

The goal of this chapter is to examine how thermodynamic and dynamic processes interact to affect sea ice variability. Ice deformation creates ridges and open water, while ice transport moves ice to locations where it is not in thermodynamic equilibrium. Perturbations in ice thickness affect the ice dynamics because ice strength depends on the thickness distribution. Ridging serves to dampen thickness perturbations because anomalously thin ice will also be anomalously weak (ridging more easily) and vice versa. Ice dynamics also allows ice to leave the Arctic Basin mainly through Fram Strait. The time scale for variations in sea ice mass is likely limited by advection which constrains the lifetime of sea ice in the Arctic Basin to 5-10 years. As noted by Thorndike et al. (1975), in a Lagrangian framework the thermodynamic processes tend to make a uniform thickness that is intermediate to the extremes caused by opening and ridging.

Much has been written about the importance of open water (leads) for the mean response to a climate change (e.g., Ledley, 1988). However, little is known about how open water may influence the natural variability in the system. If ice experiences an atmospheric anomaly that causes additional melt, then the ice will open more readily, increasing the open water fraction. During the melt season, increasing the open water fraction creates a positive feedback due to greater solar absorption. Thus atmospheric

anomalies occurring during the melt season may have a disproportionately large affect on the sea ice when there is open water present. On the other hand, increasing the open water fraction will also increase the total volume of ice grown during the cold season, acting as a negative feedback, because ice grows at a faster rate over open water and for thin ice.

Variations in sea ice and freshwater advected out of the arctic basin have been proposed to govern the near-surface density in the gyre circulations in the Greenland and Iceland Seas (Aagaard and Carmack, 1989; Häkkinen, 1993). These authors argue that there is a link between arctic outflow and the Atlantic thermohaline circulation. Various studies have explored how surface wind anomalies affect ice advection into the North Atlantic. However, the influence of thermodynamic mechanisms on the volume of ice advected into the North Atlantic has received little attention.

This chapter begins with a description of the model domain and the external forcing fields. Next I will present the results from the standard case integration: a hindcast of the sea ice for the period 1979-1994. Sensitivity studies will be performed to reveal how the dynamic and thermodynamic processes interact to determine the sea ice response to atmospheric forcing. Finally, I will examine how sensitive the results are to the number of sea ice thickness categories ranging from two-four.

## *5.2 The model domain*

The sea ice model domain is limited to ocean covered regions in the Arctic as shown in Fig. 5.1. Figure 5.1 defines the three subregions used in this chapter (see figure caption).

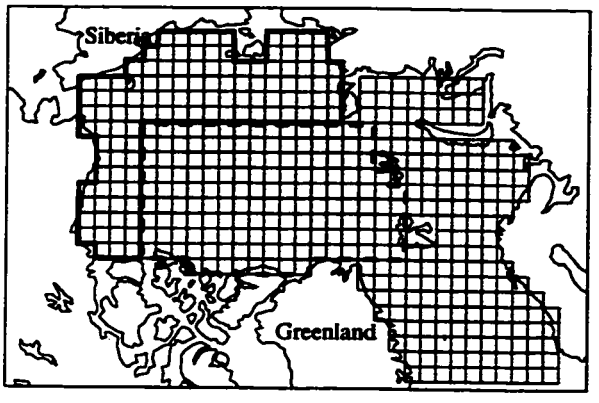


Figure 5.1: The horizontal grid with 160-km square grid boxes based on a stereographic projection. Subregions used throughout this chapter are "shelf" (enclosed by heavy solid line), "central" (enclosed by heavy dashed line), and "basin" (the sum of shelf plus central regions). The areas of the shelf and central regions are 2.97 and 3.94 $x$ $10^6$ km$^2$, respectively. This grid was used previously by Flato and Hibler (1992) and Flato (1995).

## *5.3 External forcing*

### *5.3.1 Two meter air temperatures*

The basin-wide reliable surface air temperature record is limited in duration. Valuable measurements were taken at Soviet manned drifting ice stations, which were in regular operation from 1950 to 1991. The total dataset represents over 27,000 stations days, though there are data from only about two stations per day on average. Hence these data do not constitute a spatial field of daily varying surface temperature over the entire Arctic Ocean. Beginning in 1979 a network of drifting buoys resting on the sea ice was deployed which is presently maintained by the International Arctic Buoy Program (IABP). Because the accuracy of the buoy data suffers from mal-functioning equipment and solar heating, the Soviet data provide a valuable means of calibration.

The Polar Exchange at the Sea Surface (POLES) project (see Martin and Munoz (1997)) have compiled a two meter air temperature set with a six hour frequency

between 1979-1994. The observations that comprise the POLES data set are from land stations, ship observations from the Comprehensive Ocean-Atmosphere Data Set (COADS), drifting Soviet NP ice stations, and buoys. For this study I compute daily means from the 6 hourly record. Then I convert the data from the POLES grid to the model grid by linear interpolation.

### *5.3.2 Geostrophic winds*

Daily geostrophic winds are computed from pressure fields taken at 12 GMT which are provided by the IABP for the period of 1979-1994. The IABP data is a blend of the pressure measured from the buoys with the gridded pressure data from NCAR analysis product. These data are archived at the World Data Center A: Glaciology.

I use an inverse linear interpolation method to convert the IABP pressure grid to the model grid shown in Fig 5.1. The IABP grid only covers the region north 70°N, but the model domain extends below 70°N, so I extrapolate the buoy data in a few places. The main region is in the Norwegian Basin/North Sea where ice concentrations and thicknesses are low and the ice has little influence on the rest of the Arctic.

### *5.3.3 Cloudiness and snowfall*

Cloudiness and snowfall rates are specified to be annually periodic and independent of position in the model domain. Cloudiness is taken to be the climatological mean measured from the Soviet NP ice stations (see Fig. 2.11b). Snowfall rates are those from Maykut and Untersteiner (1971).

### *5.3.4 Parameterizations for the air/ice and air/ocean surface fluxes*

Fluxes of downward longwave and shortwave radiation for clear skies are parameterized as in Parkinson and Washington (1979). Minor modifications are made to their

parameters for cloud depletion of the solar flux, $(1-\alpha c^{\beta})$, and cloud enhancement of the longwave flux, $(1+\gamma c)$. Parkinson and Washington (1979) used $\alpha = 0.6, \beta = 3$, and $\gamma = 0.275$ respectively, while here I use 0.65, 2.3, and 0.225 to reproduce reasonable ice thicknesses in the Arctic. The relative humidity is fixed at 90%.

### *5.3.5 Oceanic forcing*

Currents and oceanic heat flux are steady (no annual cycle). Both are derived from the diagnostic ice-ocean calculation of Hibler and Zhang (1993).

## *5.4 Demonstration of the model: The standard case*

The standard case, as well as other simulations reported, is a 37 year integration, which includes a spin-up period using forcing from 1979 repeated 5 times and then two repetitions of the 1979-1994 forcing. The results presented are for the final cycle for 1979-1994 of this integration.

The standard case integration has the full model physics for three ice categories as described in the previous chapter. There are four vertical layers in the thick ice category and two in the thin ice category, with $H_0^* = 10$ cm and $H_1^* = 50$ cm defining the boundaries of the thin and thick categories.

### *5.4.1 Annual cycle for the standard case*

Histograms shown in Fig. 5.2 characterize the evolution of the thickness distribution over the course of an annual cycle averaged over the Arctic Basin for 1979-1994. The thick ice category which includes first year and multi-year ridged and unridged ice has basin wide mean thickness ranging from 290 cm (fall) to 350 cm (spring). The thin ice includes only unridged, first year ice and ice from the thick ice category that melts below $H_1^*$. The thickness of thin ice, averaged over the basin, only ranges from 22-36 cm during the course of the year, although the model is designed to allow thin ice to

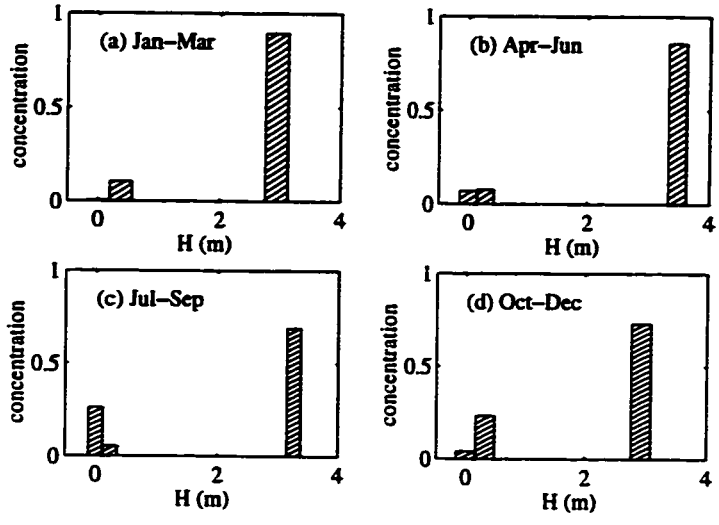


Figure 5.2: Representation of the modeled thickness distribution averaged over the Arctic Basin for 1979-1994. The annual cycle is averaged over (a) January-March, (b) April-June, (c) July-September, and (d) October-December. The bars are positioned along the abscissa at the mean thickness while the height of the bars represent the mean concentration. There are three thickness categories (hence three bars) including open water. In January-March, the open water concentration is $\sim 0$ (see footnote 1). The width of the bars is arbitrary.

range from 10-50 cm. The concentration of thin ice represents a balance primarily of the input of new ice that grows over the leads and the transfer of ice from thin to thick category by ridging.

The upper panel from Fig. 5.3 shows the simulated annual cycle of the ice concentration averaged over the Arctic Basin. The simulated concentration in winter is nearly 100% because the model output is written *after* the thermodynamics portion of the timestep so that the open water produced by ridging is usually already covered by new ice. However, for January-April the simulated opening rate (not shown) is 1.2% and 1.8% per day for the central region and shelf regions, respectively. The thin ice concentration is a maximum in the fall when the large concentration of open water that exists during the melt season is covered with new ice. The thin ice concentration reaches a maximum of 40% in October-November. During the winter season (January

through April) the thin ice concentration is 4-10% in the central region and 13-16% in the shelf region.

Using the passive-microwave record for 1979-1991 from the Scanning Multichannel Microwave Radiometer (SMMR) and the Special Sensor Microwave/Imager (SSM/I) from (Schweitzer, 1995), I can compare the modeled ice concentration to monthly mean observed concentrations. From a summary of studies of measurement error, Gloerson et al. (1992) estimate the accuracy of passive-microwave concentrations is $\pm 2 - 3\%$ (absolute error) in the winter and up to $\pm 10\%$ (absolute error) in the summer. Studies show that the error in high concentration regions during winter months is mainly due to the instrument's inability to distinguish between open water and ice in the thickness range from 0-20cm. Melt water and open water near the ice edge and in coastal regions can cause a substantial negative bias in the passive microwave measurements compared to direct measurements, leading to higher error estimates during the summer.

Open water concentrations measured by passive microwave in the winter are 0.03 to 0.04 in the central regions and 0.04 in the shelf region. Because ice takes several days to grow thicker than 20cm (the minimum thickness that is reliably distinguished from open water by passive microwave), it is no surprise that the simulated opening for one day is roughly half of the passive-microwave "open water" concentration.

The simulated ice concentration reaches a minimum in late August in the central region (80%) and in early September in the shelf region (43%). The observed minima occurs in September in both region (the passive microwave data are only available for *monthly* intervals due to the frequency that swathes are taken). The minimum monthly ice concentration for 1979-1991 from the model is on average 2% higher than observed in both regions.

The lower panel from Fig. 5.3 shows the simulated annual cycle of the ice growth rate averaged over the Arctic Basin. During the fall, the growth is primarily controlled by the thin ice category (10-50 cm range) when the concentration of thin ice is

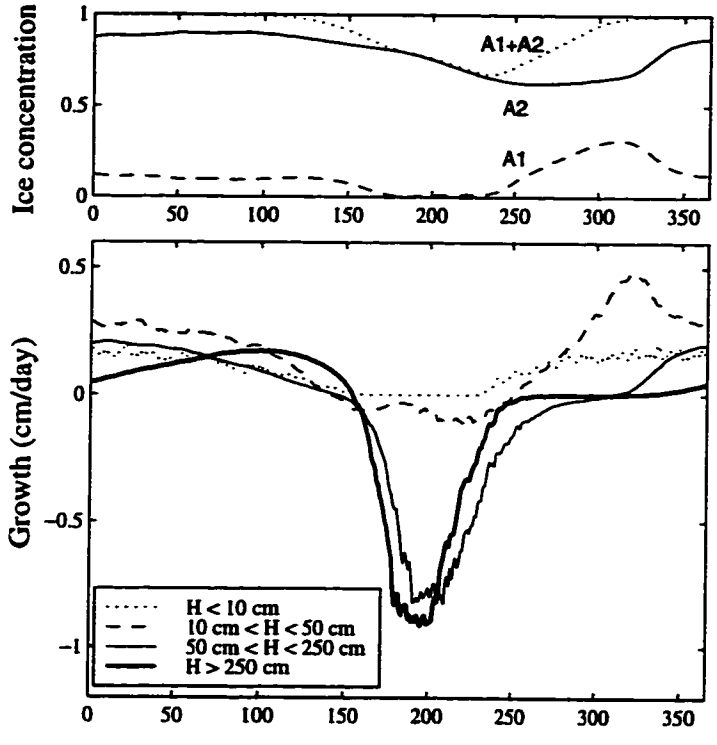


Figure 5.3: The simulated mean annual cycle of ice concentration and ice growth averaged over the Arctic Basin for 1979-1994. Concentration is shown for thin ($A_1$) and thick ($A_2$) categories and the total ice concentration ($A_1 + A_2$). Growth is broken into four curves representing new ice growing over open water (dotted), thin ice (dashed), and thick ice which is separated into two curves for gridboxes with thickness greater than (heavy solid) or less than (light solid) 250 cm. The growth is weighted by the concentration (e.g., new ice growth in winter contributes about 0.15 cm/day to the basin wide average thickness).

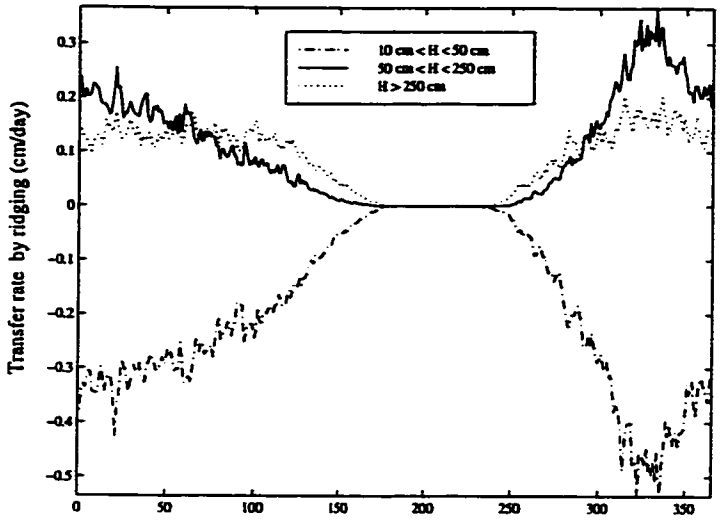


Figure 5.4: The simulated mean annual cycle of ice transfer rate by ridging averaged over the Arctic Basin for 1979-1994 for thickness ranges as described in Fig 5.3.

greatest. Although thinner ice grows faster than thicker ice, the rates are weighted by the concentration, so we see that the thin ice and thick ice in the 50-250 cm range[1] contribute about the same amount during the winter. The ice thicker than 250 cm creates a thermodynamic sink for the ice volume, because it melts much more than it grows.

Fig. 5.4 shows the annual cycle of the ice transfer rate by ridging averaged over the Arctic Basin. The curve for the thin ice (10-50cm range) shows the basin average $\Psi_1 H_1$ (see Eq. 4.26). The sum of the three curves is always zero because there is no net volume change from ridging. The transfer rate is very small in summer when most of the thin ice has melted and the strain rate is small due to weak summer winds. Transfer rates are highest in the fall as is the concentration of thin ice.

The annual averaged volume of ice transferred from thin to thick categories in the standard case hindcast (minus the integral of the lowest curve in Fig. 5.4) is equal to

[1] The growth rate for the thick ice category is separated into two curves for gridboxes with thickness greater/less than 250 cm for comparing with an integration using four ice categories below.

a 70 cm thick layer of ice covering the Arctic Basin. During most of the cold season more thin ice is transferred into gridboxes in the 50-250 cm thick range compared to the thicker range.

The total annual volume of ice transferred between categories can be compared to an estimate from a 28 thickness category model by Flato (1995) who found the volume[2] transferred is equal to a 55 cm thick layer averaged over the Arctic Basin (approximated from his Fig. 9) or about 25% lower than the annual volume of ice transferred between categories in my standard case integration. The true value is not known. The volume transferred from the thin to thick category due to ridging is sensitive to the parameterize of ice strength. However, the correct way to parameterize ice strength for models with so few categories is not known. See section 5.6.2 on the ice strength for further discussion of this issue.

The mean sea ice coverage for April and September from the model and passive-microwave satellite measurements is shown in Fig. 5.5. I chose to compare the simulated concentration to observations in April when the extent is maximum and the new ice growth is relatively low and in September when the extent is minimum and meltponds have partly drained and/or refrozen.

In April the modeled sea ice extent tends to be too high in the Greenland and Barents Seas, where the ice edge is strongly influenced by the ocean heat flux during the winter. In this model the heat flux is fixed in time so the ice extent in April cannot differ much from year to year. The modeled ice coverage in September is greater than observed. The modeled ice extends too far toward Franz Josef Land and Svalbard and into the Kara Sea.

Figure 5.6 shows the mean ice thickness for April and September for 1979-1991. The thickness is 0-2 m near Siberia and gradually increases from west to east in the Arctic Basin to obtain a thickness of 4-6 meters near Greenland and the Canadian

[2] Flato (1995) calls the same quantity the ridged ice production.

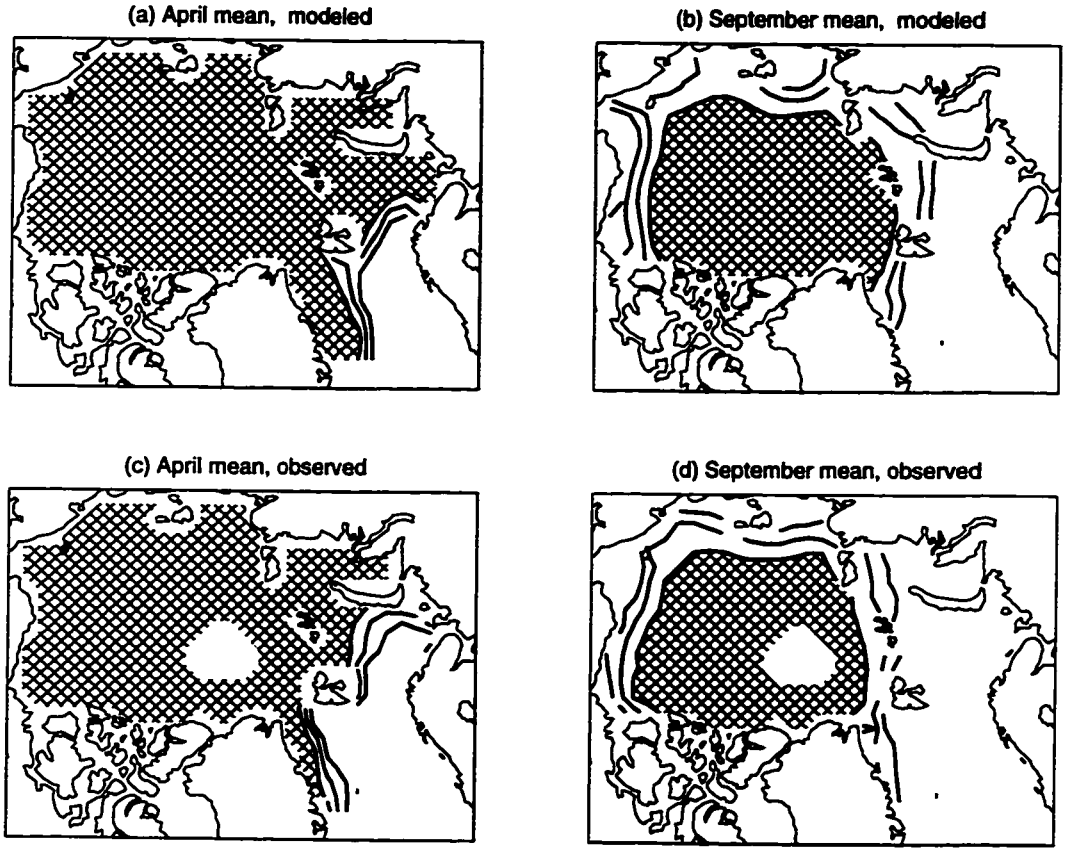


Figure 5.5: Mean sea ice concentration for April and September 1979-1991 for the standard case model integration and observations from SMMR and SSM/I passive microwave viewers. Contours mark 25% intervals, the crosshatched region denotes ice concentrations exceeding 75%. The region near the pole is blank in the observations because microwave viewers cannot view there.

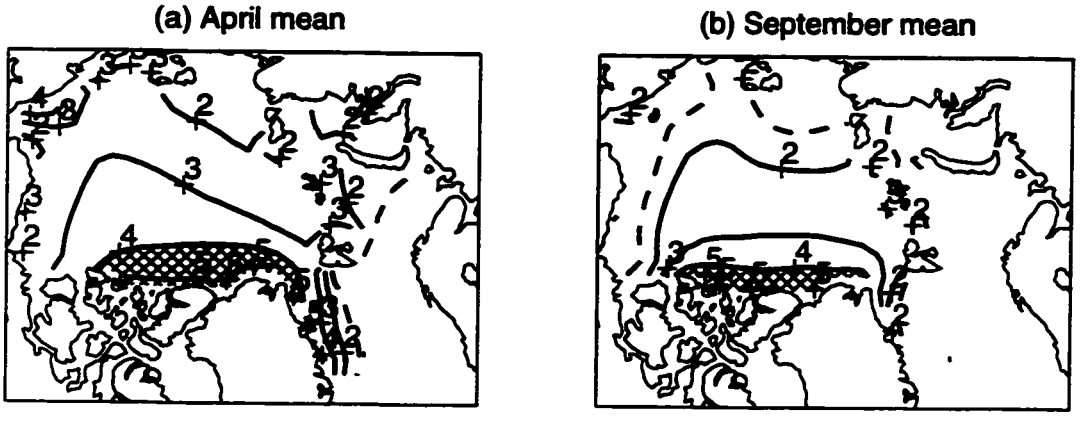


Figure 5.6: Modeled mean sea ice thickness fields for (a) April and (b) September, 1979-1991. Contours mark 1-m intervals beginning with the 1 m contour which is dashed. The crosshatched region denotes ice thickness exceeding 4 m. Ice thickness includes the average of the ice covered and open water fractions of the gridbox.

Archipelago. This is consistent with thickness measurements by upward looking sonar on submarines (see Bourke and Garret, 1987).

### *5.4.2 Sea ice variability for the standard case*

Figure 5.7 shows the sea ice volume and concentration averaged over the subregions defined in Fig. 5.1. In the early 1980's and in the early 1990's, pronounced minima are simulated in the summer and fall ice concentration and volume of the shelf region (see dashed lines in Fig. 5.7(a) and (b), respectively). The two minima share similar features, except that the 1990's minimum is more severe.

Ice concentrations in the central region have relatively little interannual variability compared to the shelf region. The ratio of the standard deviation to mean is 0.04 and 0.32 for the annual minimum in ice concentration in the central and shelf regions, respectively. The ice concentrations averaged over the central region are uncorrelated with those over the shelf region in summer and fall.

The interannual anomalies in the volume in the central region are *out of phase* with the anomalies in the shelf region. When the volume of ice in the shelf and central

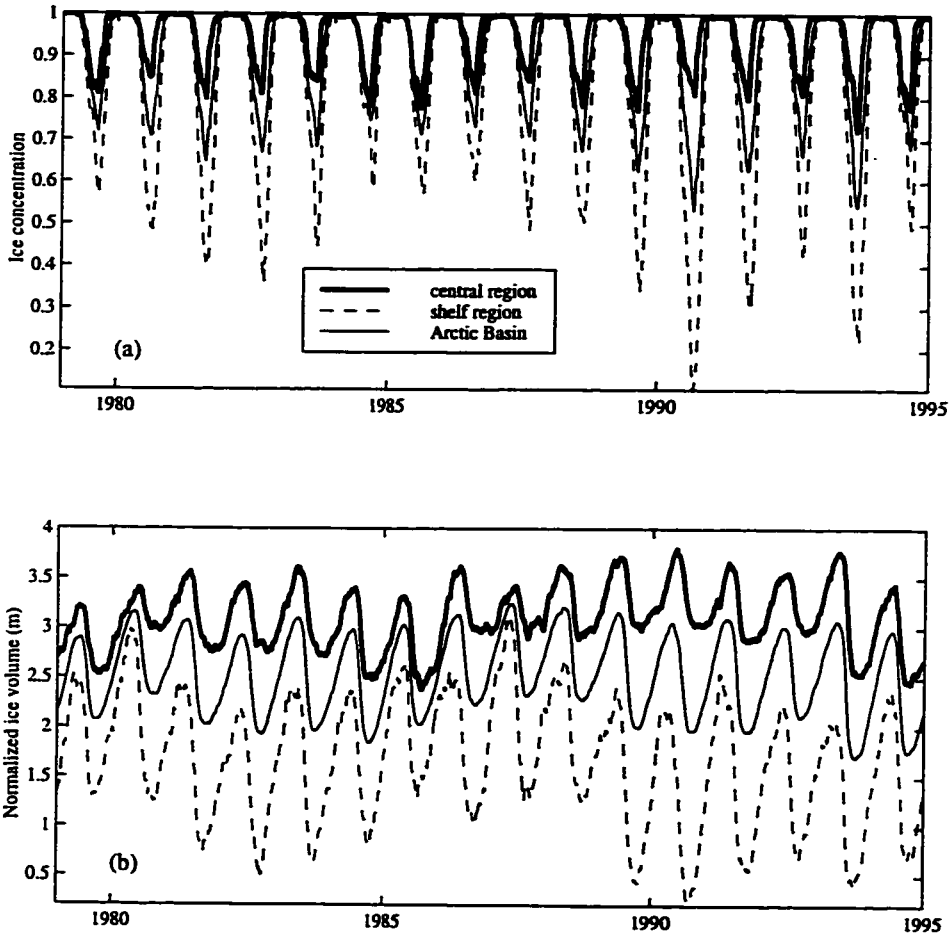


Figure 5.7: Daily sea ice (a) concentration and (b) volume of the subregions identified in Fig. 5.1. Volume is normalized by the area of each region so it is equivalent to the average ice thickness for the region.

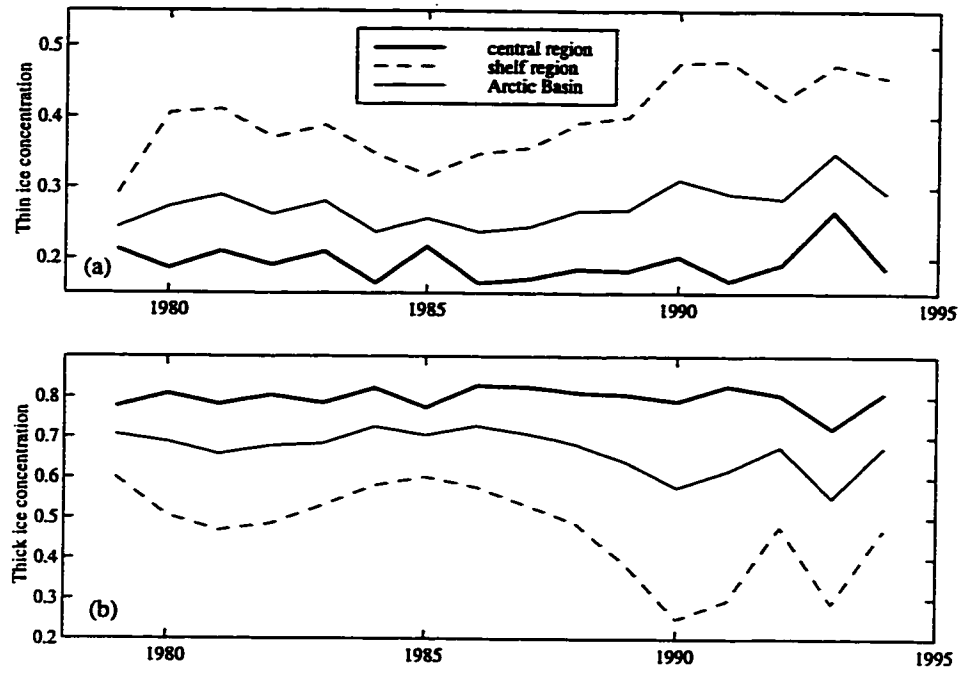


Figure 5.8: Fall (October-November) mean sea ice concentration for (a) thin and (b) thick ice categories averaged over the subregions identified in Fig. 5.1.

regions are combined to give the mean ice volume for the Arctic Basin, the variations are less apparent. Indeed the standard deviation of the monthly mean normalized volume anomalies in the shelf and central regions are 27 cm and 17 cm, respectively, while the standard deviation of the basin wide average is only 13 cm.

Mean ice concentrations for the thick and thin ice categories during October-November are shown separately in Fig. 5.8. During fall, the concentration of thick ice and thin ice are anticorrelated. The simulated mean ice thickness (not shown) indicates that the ice in the central region was anomalously thick during the late 1980's and early 1990's which could be due to increased convergence of ice there. Curiously the concentration of ice in the central region is remarkable steady compared to the relatively large variability seen in the volume (Fig. 5.7(b)).

There are two possible explanations for the out-of-phase relationship between sea ice volume in the central Arctic and shelf regions: (1) anomalous winds transport

unusually large quantities of thick ice out of the shelf regions and into the central arctic (and vice versa) and (2) the air temperature anomalies in the central and shelf regions are anticorrelated. Positive correlations for monthly mean air temperatures (not shown) averaged over the central and shelf regions rule out (2).

### *5.4.3 Sea ice minimum of 1990*

Serreze et al. (1995) argued that the minimum in sea ice in 1990 was due to warm windy off-shore flow in May associated with an unusual low pressure center at about 80°N, 100°E, followed by warmer than average conditions in June. Serreze et al. (1995) speculate that in July and August, the anomalous flow along the east Siberian coast caused enhanced breakup and poleward advection of the ice.

Figure 5.9 shows the mean sea ice coverage for April and September 1990 from the model and from observations (SSM/I). The model simulation of the large open water region in September resembles the observations, but subtle regional differences exist.

Figure 5.10(a) shows the modeled mean ice thickness in April, 1990 is anomalously thin (compare Figs. 5.10(a) and 5.6(a)) in the Siberian sector prior to the summer of 1990. It appears that the modeled ice is preconditioned in the Siberian Arctic for the appearance of the extensive open water in the summer. Others have noticed that wintertime conditions play a roll in determining summer anomalies. For example, the simulated December ice concentration in a model study by Walsh and Zwally (1990) proved to be well correlated with the following summer ice severity (both observed and simulated).

The September 1990 thickness field (Fig. 5.10(a)) also reveals interesting features. The Siberian shelf region with anomalous area of open water seen in the ice concentration also features anomalously thin ice (as expected). What is not apparent from the ice concentration alone is the anomalously thick ice in the Canadian Basin in April and September. The simulated ice near Svalbard and the Canadian Archipelago is

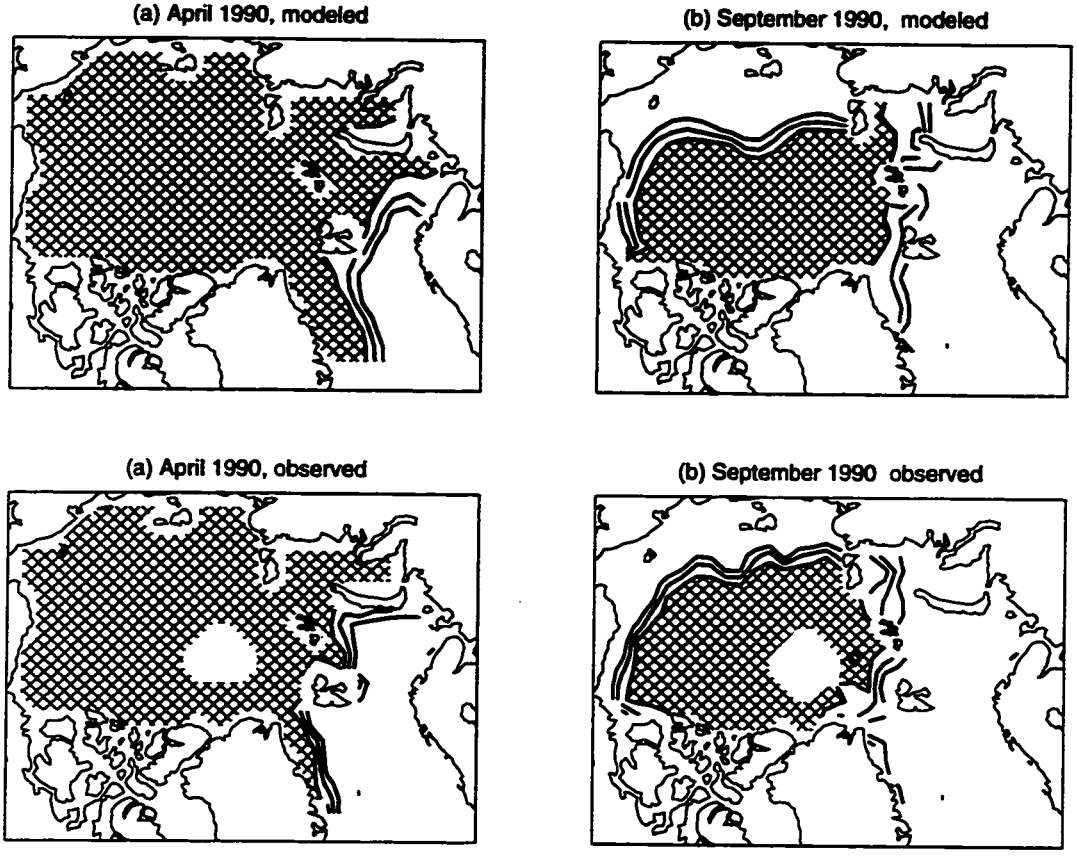


Figure 5.9: As in Fig. 5.5, except for the year 1990.

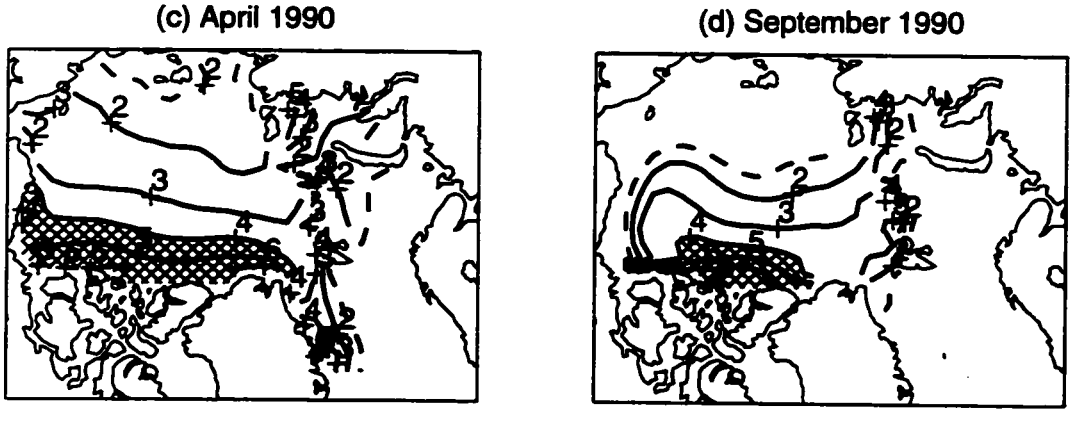


Figure 5.10: As in Fig. 5.6, except for the year 1990.

thicker than average in September 1990.

Serreze et al. (1995) note that the anomalous atmosphere conditions that are thought to have changed the negative sea ice anomalies in the Siberian sector were also present in the Alaskan sector, and yet no negative ice anomalies were observed there. Figure 5.10(a) reveals a possible explanation. The modeled ice thickness prior to the summer of 1990 was anomalously thick in the Alaskan sector, obscuring the affect of the atmospheric anomalies on the ice concentration. In fact, near the Alaskan coast in the model, conditions went from an average 4-meter thick ice cover in April to ice-free in September. Therefore the simulated ice volume near Alaska eroded considerably in the summer of 1990, but it was so thick at the beginning of summer that the ice extent remained near normal.

The results from the standard case support the conclusion by Serreze et al. (1995) that this minimum can be explained by atmospheric forcing (the oceanic forcing for this model is steady). Furthermore the model shows an increase in the thickness of ice in the central region despite positive air temperature anomalies that exist in May and June (see Fig. 2, Serreze et al., 1995), because in the next section I will explore whether the anomalously thick ice near Svalbard during this event has implications for the ice export from Fram Strait.

### *5.4.4 Variability in the ice export through Fram Strait*

In June of 1991, moorings were established at three location in Fram Strait to measure ice transported out the Arctic Basin. While three sites were monitored in 1991, only one was monitored throughout the period of record shown in Fig. 5.11(a). The observed ice draft and simulated thickness at the same location are plotted in Fig. 5.11(a) and (b), respectively. The phase of the annual minimum is several months earlier in the model than in the observations. This is possibly due to the lack of proper data for prescribing an annual cycle of the ocean heat flux ($F_w$) and currents. The modeled mean thickness is about 25 cm to thin. However the overall decreasing

trends in the model and observations are similar. The model trend is -100 cm for 1991-1994 for the curve in 5.11(a): the observed trend is about -120 cm for June 1991 through July 1994. (The change in the yearly mean modeled thickness from 1991 to 1994 is -44 cm.)

The simulated annual ice export through Fram Strait (the sum of all the ice that crosses a straight line intersecting Spitzbergen and the northeastern corner of Greenland each year) shows a negative trend for the same period (see 5.12). For the period 1979-1994, the simulated mean export rate is 2600 $km^3yr^{-1}$ which is about 16% less than the estimate from observations by Aagaard and Carmack (1989) (3100 $km^3yr^{-1}$, for sea ice with salinity 3.2 psu). There is considerable variability in the simulated annual mean transport: the standard deviation is greater than 25% of the mean. About 70% of the variance in the annual annual ice export over the 16 years can be explained by deviations in the annual mean ice thickness at the location of the mooring in Fram Strait.

Ice transport can be correlated with mean thickness and mean component of the ice velocity at Fram Strain (averaged along a straight line intersecting Spitzbergen and the northeastern corner of Greenland). The annual mean ice export rate is more highly correlated with the annual mean ice thickness than it is with the annual mean normal component of the ice velocity (see table 5.1). In contrast, the monthly mean ice export depends more on the monthly mean normal component of the ice velocity than it does on the monthly mean ice thickness.

The correlation between the annual mean ice export rate and the *annual mean* ice volume for the central region (Arctic Basin) is $r = 0.71$ ($r = 0.59$). These correlations are lower for *monthly mean* ice volumes because the ice export rate is influenced more strongly by the ice speed on monthly timescales.

The standard deviation of the annual mean ice export rate from the Arctic Basin is 650 $km^3yr^{-1}$, or about 25% of the mean. Dickson et al. (1988) estimated that the total freshwater excess during the Great Salinity Anomaly (GSA) in the 1970's

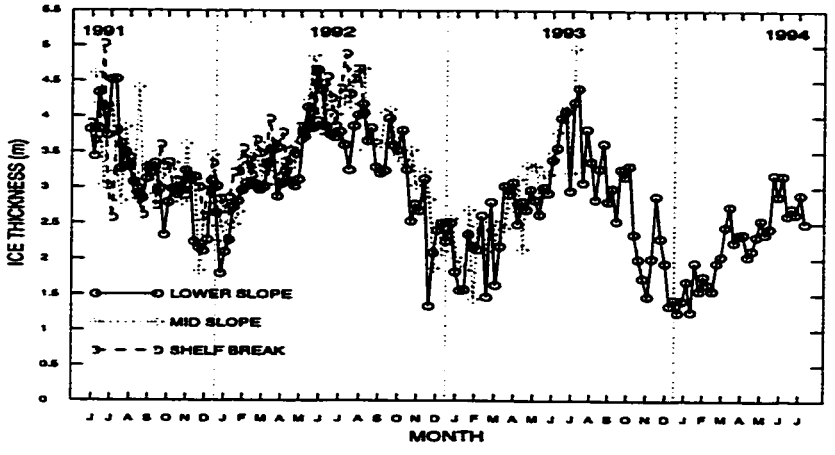


(a)

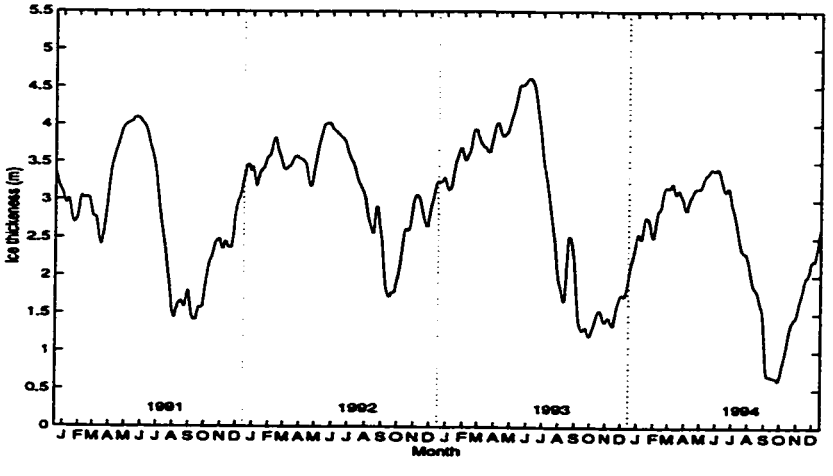


(b)

Figure 5.11: (a) Ice thickness measured by moorings in Fram Strait using upward looking sonar. (b) Simulated daily ice thickness at the position of the mooring from the period that the mooring data is available. Each point in (a) represents a seven day mean, excluding instantaneous measurements of ice less than 0.20 m thick. The curve in (b) is computed by linearly interpolating ice thickness from the model grid to the location of the buoy and it is smoothed with a seven day running mean. (The observed data in (a) are courtesy of *Aagaard, Roach, and Moritz*, manuscript in preparation.)

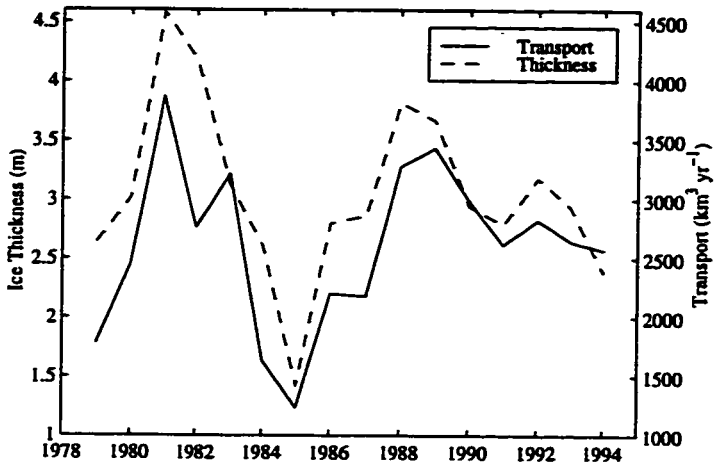


Figure 5.12: Simulated annual mean ice export rate through Fram Strait and the annual average ice thickness at the equivalent mooring position in the model.

Table 5.1: Correlation matrix for average thickness (h), normal component of the ice velocity (s), and export rate (e) for a straight line intersecting Spitzbergen and the northeastern corner of Greenland at Fram Strait.

annual means

| | h | s | e |
|---|---|---|---|
| h | 1.00 | -0.12 | 0.75 |
| s | | 1.00 | 0.51 |
| e | | | 1.00 |

monthly mean anomalies

| | h | s | e |
|---|---|---|---|
| h | 1.00 | 0.10 | 0.46 |
| s | | 1.00 | 0.86 |
| e | | | 1.00 |

was approximately 2200 km$^3$. Hence the standard deviation of the simulated annual mean export model is about 1/3 of the GSA freshwater anomaly.

The 1991-1994 measurements are the first direct observations of ice export from the arctic into the North Atlantic. The trend in these data have generated much interest in the community. Nonetheless, from the 16 yr simulation shown in Fig. 5.12, it appears that the period of record for measurements at the Fram Strait mooring correspond to an unusually steady time. The large variance and the long time scales associated with ice export (Fig. 5.12) suggest that large freshwater anomalies should be a ubiquitous decadal scale feature of the climate system (see also Deser and Blackmon, 1993).

## 5.5 *Sensitivity studies to reveal the interaction between dynamic and thermodynamic processes and how they contribute to the natural variability*

### *5.5.1 Sensitivity of ice volume to air temperature and wind anomalies*

To investigate the model's sensitivity to the variability of the external forcing, I compare integrations where I force the model with all possible combinations of daily varying air temperature ($T_{air}$) and winds (**G**), and climatological[3] air temperature ($< T_{air} >$) and winds ($< \mathbf{G} >$). These experiments are designed to investigate how variability in the external forcing influences the mean and variability of the ice volume. Part of the motivation for this work is to see whether previous studies that were performed with climatological air temperatures (or weakly varying air temperatures) have correctly estimated the variability in the ice volume.

Figures 5.13(a) and (b) show how the monthly ice volume depends on the variability in the forcing by the atmosphere. (Because the volume is normalized by the area

[3] "Climatological" winds (air temperatures) are computed from the 16 yr mean annual cycle of pressure (air temperature).

of the region, the volume is equivalent to the mean thickness of the region and has units of cubic meters per meter squared.) The mean volume is on average lower for the standard case than the cases forced with either climatological air temperatures or winds. The mean volume is moderately sensitive to variability in air temperature: the mean volume is about 15-cm greater for the model forced with climatological mean air temperatures than for the standard case[4]. The effect of replacing variable winds with climatological winds on the mean volume is even greater: the ice is about 1-m thicker in both the central and shelf regions. The ice has not reached equilibrium in the integration forced with both climatological air temperatures and winds ($< T_{air} = 0 >$ and $< \mathbf{G} >$), but clearly the mean thickness will exceed all the other integrations shown.

The climatological winds lack the wind speeds that are necessary to create realistic ridging and export rates. Because ridging and export are sources of open water, the minimum ice concentration (not shown) in the central (shelf) region is about 4% (40%) higher for the integrations with climatological winds compared to variable winds. Bottom and lateral melt rates are strong functions of how much solar radiation is absorbed in the open water fraction of the gridbox. The annual total volume of ice transferred between thick and thin categories by ridging ice is equal to only a 6 cm layer of ice covering the Arctic Basin for the integration with climatological wind forcing the model - less than 10% of that in the standard case. Although ridging is a source of ice production during the cold season, here the lack of open water in the summer dominates the effects of reduced ridging and export. Hence without variable winds, less ice melts each year and the ice becomes thicker.

The variability of the ice volume is more easily seen when the annual cycle is removed (see Fig 5.13(c) and (d)). Forcing with climatological versus variable air temperatures has a considerable effect on the ice volume anomaly in the central

[4] A similar increase in the mean thickness is found when the single column model is forced with climatological mean forcing.

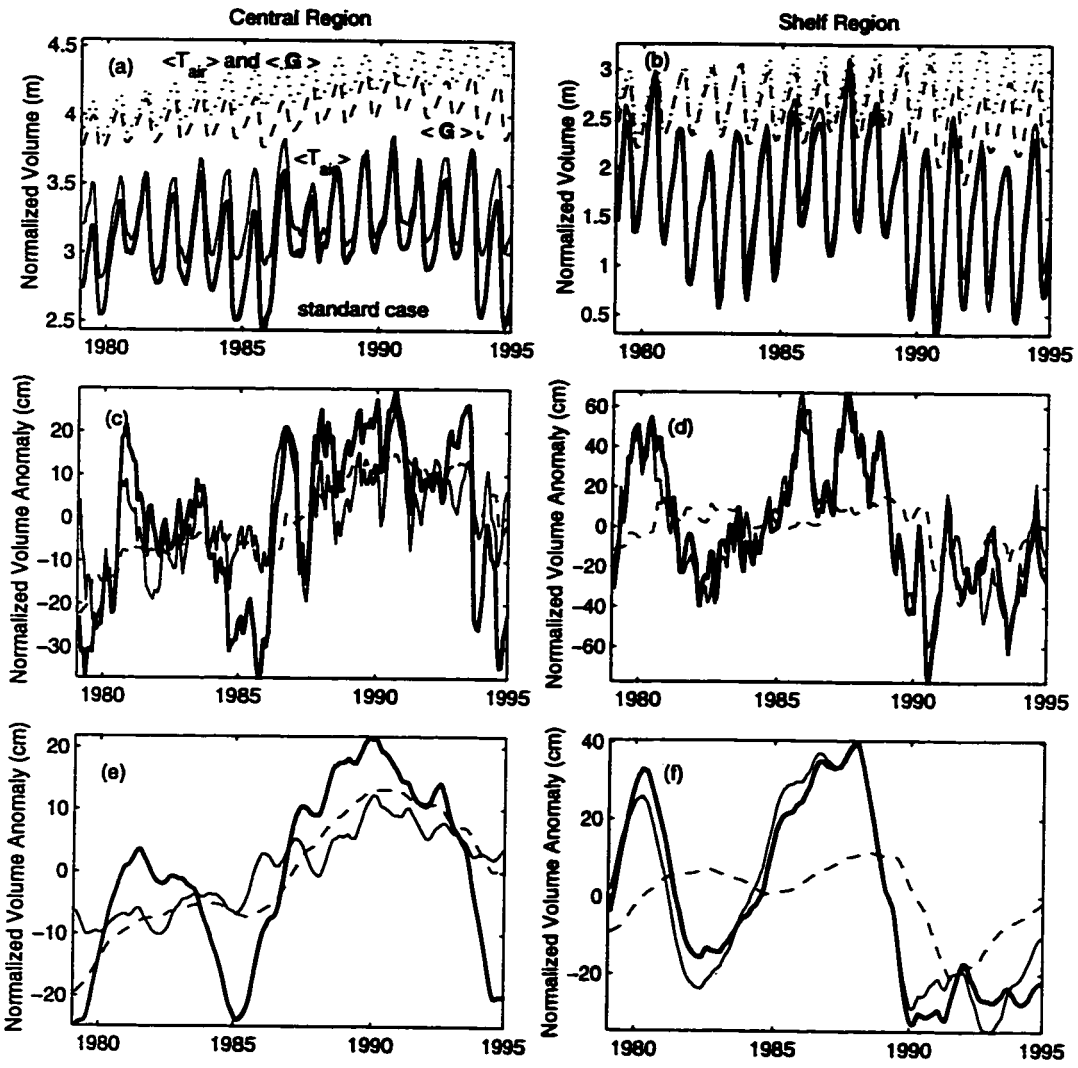


Figure 5.13: Monthly mean ice volume, volume anomaly, and volume anomaly filtered by 2-yr running mean for the central region (a,c,e) and shelf region (b,d,f). The curves are as follows: (heavy solid line) the standard case which has variable air temperatures and winds, $T_{air}$ and $\mathbf{G}$; (light solid line) case with climatological air temperatures and variable winds, $< T_{air} >$ and $\mathbf{G}$; (dashed) case with variable air temperature and climatological winds, $T_{air}$ and $< \mathbf{G} >$; and (dots) case with climatological air temperatures and climatological winds, $< T_{air} >$ and $< \mathbf{G} >$. Only the first three curves are shown in the (c,d,e,f) because the anomalies for the case with climatological air temperature and winds are nearly zero. Volume is normalized by the area of each region.

region and little effect on the shelf regions. In the shelf region, $\sigma_h$ decreases by only about 20% from the standard case when the model is forced by climatological air temperatures. This suggests that volume anomalies in the shelf region are only modestly influenced by air temperature anomalies. In the central region, however, the standard deviation of the monthly mean ice volume anomaly ($\sigma_h$) for the integration with climatological air temperature is about half of that for the standard case (see table 5.2(a)). Hence about 50% of the variability of the ice volume on monthly timescales in the central region is due to air temperature anomalies.

Replacing variable winds by climatological mean winds has a substantial affect on the monthly volume anomaly (compare columns 4 and 6 in table 5.2(a)). In both the central and shelf regions when the model is forced by climatological winds, $\sigma_h$ is about 1/3 of the standard case values. The interpretation of this result is not straightforward, however, because in the absence of variable winds the mean state of the model is very different from the standard case. Results with the SCM given in chapter 2 showed that the ice thickness response due to atmospheric anomalies depends strongly on the mean ice thickness. It is likely that the response also depends on the amount of open water that is present.

When the ice volume anomaly is filtered with a 2-yr running mean (see Fig 5.13(e) and (f)), the influence of variable versus climatological forcing on the low frequency ice volume anomalies becomes apparent. Without variable air temperature, much of the low-frequency variability is absent in the central region. Specifically, $\sigma_h$ is 3.5 cm with climatological air temperatures, compared to 12 cm for the standard case: $\sigma_h$ is reduced by more than a factor of three. By comparing the last columns in table 5.2(a) and (b), note that most of the variability of the ice volume forced by variable air temperatures and climatological winds occurs at 2-yr and longer timescales. However, $\sigma_h$ for 2-yr and longer timescales for the shelf region is virtually independent of variability in the air temperature. Hence variable air temperatures are essential for creating low-frequency variability in the central Arctic and are insignificant in the

Table 5.2: (a) Simulated mean $h$ and standard deviation $\sigma_h$ of ice volume for the subregions defined in Fig. 5.1 for integrations as follows: the standard case which has variable air temperatures and winds, $T_{air}$ and **G**; climatological air temperatures and variable winds, $< T_{air} >$ and **G**; and variable air temperatures and climatological winds, $T_{air}$ and $< \mathbf{G} >$. (b) Ice volume is filtered with a 2-yr running mean before computing the standard deviation. Volume is normalized by the area of each region. Statistics are for the hindcast years 1979-1994.

(a)

| Region | mean $h$ (cm) | | | $\sigma_h$ (cm) | | |
|---|---|---|---|---|---|---|
| | $T_{air}$ **G** | $< T_{air} >$ **G** | $T_{air}$ $< \mathbf{G} >$ | $T_{air}$ **G** | $< T_{air} >$ **G** | $T_{air}$ $< \mathbf{G} >$ |
| Central | 310 | 329 | 402 | 17 | 8.9 | 5.7 |
| Shelf | 167 | 177 | 260 | 28 | 23 | 10 |
| Basin | 253 | 269 | 346 | 14 | 11 | 5.9 |

(b)

| Region | $\sigma_h$ (cm), 2-yr running mean | | |
|---|---|---|---|
| | $T_{air}$ **G** | $< T_{air} >$ **G** | $T_{air}$ $< \mathbf{G} >$ |
| Central | 12 | 3.5 | 5.0 |
| Shelf | 20 | 21 | 8.0 |
| Basin | 11 | 8.8 | 4.8 |

shelf regions.

These results strongly suggest that previous studies that hindcast the sea ice in the arctic which do not include realistic air temperature variations have seriously underestimated the variability on 2-yr and longer timescales in the sea ice volume for the central region.

### *5.5.2 Sensitivity of ice volume to annually periodic winds and no winds*

It has been argued that the net effect of ice dynamics is to reduce the variability in the ice volume that is borne of anomalous air temperatures. If true, then the ice volume in an integration with no ice motion ($\mathbf{u} = \mathbf{0}$), called the "thermodynamics only" integration, should have higher variance than integrations performed with climatological winds or with winds from one year repeated annually (to maintain high frequency synoptic variability while eliminating interannual variability in the winds).

With $\mathbf{u} = \mathbf{0}$, there is no ridging and opening. The ice in each gridbox reaches a homogeneous thickness, and there is never open water in the perennial ice regions in the thermodynamics only integration. I added 1.5 W $m^{-2}$ to the ocean heat flux ($F_w$) everywhere to compensate for the lack of heat entering the mixed layer that normally occurs through the absorption of solar radiation in open water. Without increasing $F_w$, the mean ice thickness would exceed 6 m in most of the central region. Some modelers use an arbitrary lead fraction to allow heat to reach the bottom surface of the ice. Increasing $F_w$ serves the same purpose.

To maintain high frequency synoptic variability while eliminating interannual variability, I include an integration with winds from 1988 repeated annually. (Winds from 1988 are meant to represent a typical year.) For this integration, $F_w$ is prescribed as in the standard case.

The results, summarized in table 5.3 and shown in Fig. 5.14, compare the standard case to the three integrations without interannually varying wind forcing as follows: thermodynamics only, climatological winds, and 1988 winds repeated each year. If we

focus on the central region where the ice edge does not play a roll in the variability an interesting picture develops. Compared to the integration forced with climatological winds, in the central region the ice volume from the thermodynamics only integration is more variable, so it appears that dynamics forced by climatological (i.e., weak) winds tend to dampen variability[5]. The opposite is true for the case with dynamics forced by repeating the winds from 1988 throughout the integration (winds with typical synoptic variability but no interannual variability). The relative magnitudes of the standard deviations change very little when the ice volume is first filtered with a two year running mean. These relations suggests that for the central region, winds which cause unusually weak sea ice motion dampen variability, but winds which cause typical sea ice motions enhance variability. One interpretation of this result is that strong winds are needed to create enough open water to enhance the effect of atmospheric anomalies. Weak winds do not create adequate opening, but they do ridge and advect ice in a way that slightly decreases the variability.

For the shelf region, the ice volume from the thermodynamics only integration is less variable than in the standard case. With the addition of either climatological winds or 1988 winds repeated, the volume is slightly more variable than in the thermodynamics only case, although still much less than in the standard case. Thus interannually varying winds are essential for developing realistic variability in the shelf region.

### *5.5.3 Sensitivity of ice export to changes in the external forcing*

While the integration with 1988 winds repeated annually reproduces most of the interannual variability in the volume of the central region, it seriously underestimates

[5] In chapter 2 we found the standard deviation is higher for thicker ice. In the central region this relationship serves to strengthen my arguments because for the thermodynamics only case, the standard deviation is higher than the climatological winds case although the mean thickness is lower.

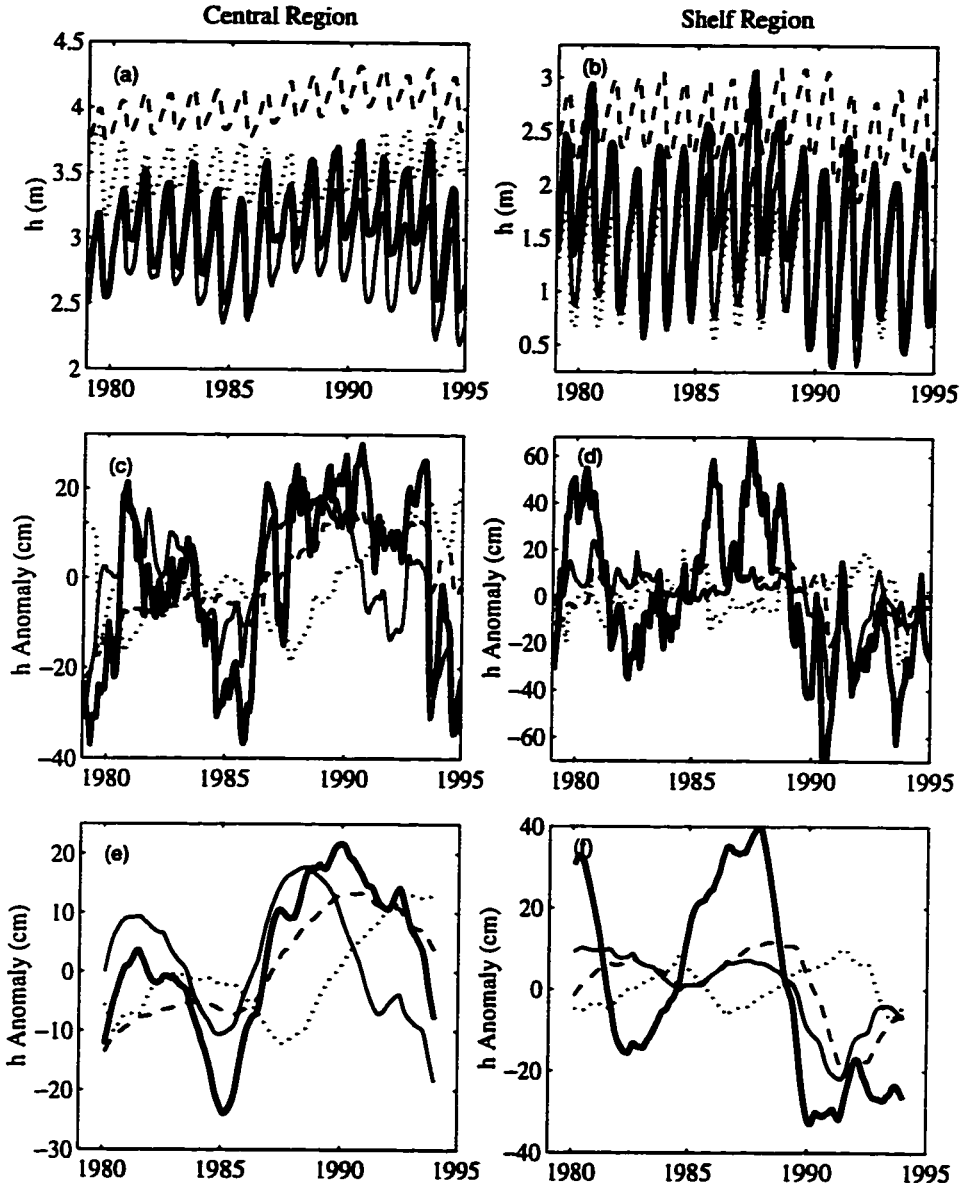


Figure 5.14: Monthly mean ice volume, volume anomaly, and volume anomaly filtered by 2-yr running mean for the central region (a,c,e) and shelf region (b,d,f). All integrations have interannually varying temperature. The curves are as follows: (heavy solid line) the standard case which has interannually varying winds **G**, (dots) case with no winds $\mathbf{G} = 0$, (dashed) case with climatological winds $< \mathbf{G} >$, and (light solid line) case with 1988 winds repeated **G(1988)**. Volume is normalized by the area of each region.

Table 5.3: (a) Simulated mean $h$ and standard deviation $\sigma_h$ of ice volume for standard case which has variable winds (**G**), thermodynamics only (**G = 0**), climatological winds (**< G >**), and winds from 1988 repeated annually (**G(1988)**). (b) Ice volume is filtered with a 2-yr running mean before computing the standard deviation. Volume is normalized by the area of each region.

(a)

| Region | mean $h$ (cm) | | | | $\sigma_h$ (cm) | | | |
|---|---|---|---|---|---|---|---|---|
| | **G** | **G = 0** | **< G >** | **G(1988)** | **G** | **G = 0** | **< G >** | **G(1988)** |
| Central | 310 | 353 | 402 | 287 | 17 | 7.3 | 5.7 | 14 |
| Shelf | 167 | 129 | 260 | 141 | 28 | 8.7 | 10 | 11 |
| Basin | 253 | 264 | 346 | 229 | 14 | 5.9 | 5.9 | 11 |

(b)

| Region | $\sigma_h$ (cm), 2-yr running mean | | | |
|---|---|---|---|---|
| | **G** | **G = 0** | **< G >** | **G(1988)** |
| Central | 12 | 5.9 | 5.0 | 11 |
| Shelf | 20 | 4.7 | 8.0 | 5.8 |
| Basin | 11 | 4.2 | 4.8 | 7.8 |

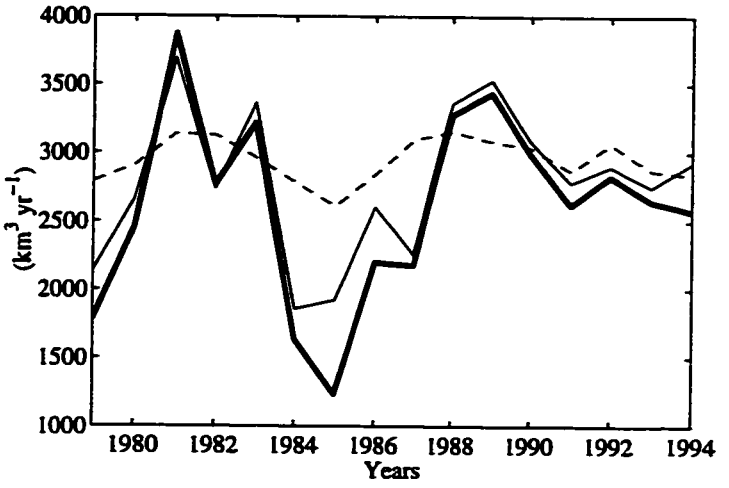


Figure 5.15: Mean annual export through Fram Strait from integrations as follows: (heavy solid line) the standard case which has variable air temperature and winds, $T_{air}$ and **G**; (light solid line) case with climatological air temperature and variable winds, $< T_{air} >$ and **G**; (dashed) case with variable temperature and 1988 winds repeated $T_{air}$ and **G(1988)**.

the variability in the export at Fram Strait (see dashed line in Fig. 5.15). In fact, for this integration the ratio of the standard deviation to mean for Fram Strait export is only 5% (compared to more than 25% for the standard case). Yet, as in the standard case, the correlation between the annual mean ice export rate and volume for the central region exceeds is 70%.

On the other hand, the integration with climatological annual mean air temperature in the Arctic reproduces less than half[6] of the interannual variability in the volume of the central region, yet the export at Fram Strait is similar to that from the standard case (see light solid line in Fig. 5.15). Furthermore, the correlation between the annual mean ice export rate and volume for the central region is just 37%.

[6] This estimate comes from comparing standard deviations of monthly volume anomalies filtered with 2-yr running mean for this integration and the standard case.

## 5.6 Sensitivity to model physics

### 5.6.1 Sensitivity to number of sea ice categories

I integrated the model with two and four thickness categories to see how the results with three thickness categories (standard case integration) differs from two and four. (The thickness distribution for two-four thickness categories is described in section 4.4.1.) Table 5.4 shows how the mean and standard deviation of the ice volume (normalized by the area of the central, shelf, and basin regions) depends on the number of thickness categories. Both statistics increase with the number of thickness categories, more so in the central region than in the shelf region.

Table 5.4: Simulated mean $h$ and standard deviation $\sigma_h$ of monthly mean ice volume for two, three, and four category models. The numbers in the second row refer to the number of ice categories. The statistics are separated for the various subregions defined in 5.1. Volume is normalized by the area of the regions.

| Region | mean $h$ (cm) | | | $\sigma_h$ (cm) | | |
|---|---|---|---|---|---|---|
| | 2 | 3 | 4 | 2 | 3 | 4 |
| Central | 241 | 310 | 348 | 15 | 17 | 19 |
| Shelf | 129 | 167 | 190 | 21 | 28 | 32 |
| Basin | 197 | 253 | 286 | 12 | 14 | 15 |

The histograms shown in Fig. 5.16 are analogous to those shown in Fig. 5.2 for the three category integration. The concentrations of thin ice for three and four category integrations are similar, but the two category case fails to simulate anything like thin or first year ice for the basin average.

The thickness distribution for the four category integration begins to represent some distinct features that appear in measurements of the thickness distribution in

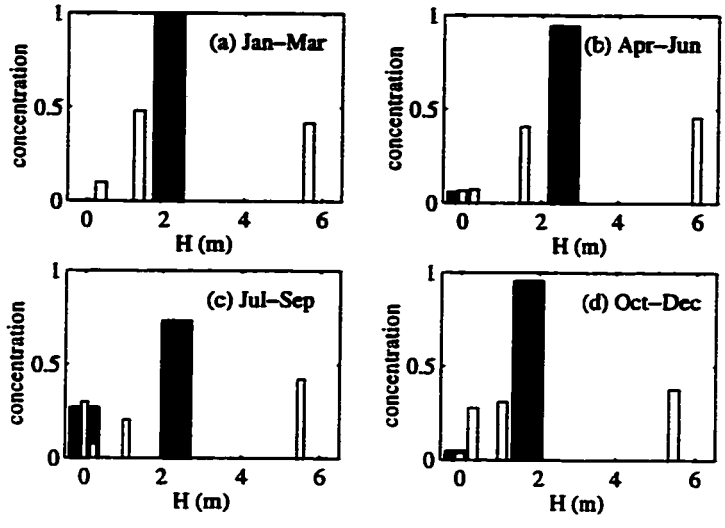


Figure 5.16: As in Fig. 5.2, but for two (black bars) and four (white bars) category integrations.

the Arctic (see, e.g., Thorndike, 1992a; Rothrock, 1986). In the fall we see the thin and intermediate categories have concentrations and thicknesses that resemble first and multi-year modes in observations. By summer the thin ice nearly vanishes and the open water concentration is large while the intermediate ice thickness reaches a minimum. Observations show a similar picture where the multiyear and first year ice are blended into one mode by summer. The winter shows stages that are intermediate between fall and sumer conditions. If we imagine that the thick ice category represents a broad range of thicknesses then it resembles the ice that has ridged to thicknesses beyond thermodynamics equilibrium in the Arctic. The four category thickness distribution has some deficiencies too. For example, the intermediate thickness category is too thin to properly depict unridged multi-year ice. A better interpretation of the unridged multi-year ice is that it partly represents the intermediate and thick categories, neither of which have the right thickness.

The two category does not even begin to resolve the thickness distribution. While the three category case represents the thin ice, it cannot represent first year ice (except

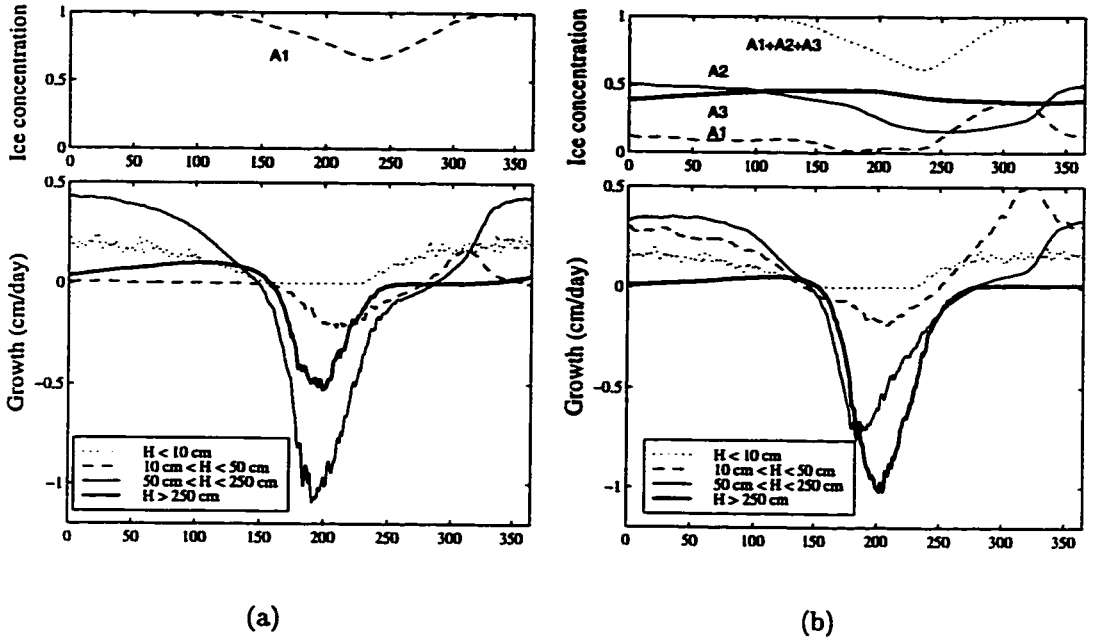


(a) (b)

Figure 5.17: As in 5.3 but for cases with (a) two and (b) four thickness categories. In (a) the three curves for ice thickness greater than 10 cm are from one category which is separated by gridbox into three thickness ranges as labeled. In (b) the curves are each from a separate ice category.

in fall) and ridged and unridged multi-year ice. The four category thickness distribution begins to look more reasonable; however, it is still very crude. An important question for climate modelers is whether these differences influence the evolution of the state of the ice in an essential way. In this section, I will begin to explore this idea.

Figure 5.17 shows the simulated annual cycle of the ice concentration averaged over the Arctic Basin for integrations with two and four thickness categories (compare to Fig. 5.3 for three categories). We see that the growth rate for the 10-50 cm range increases with the number of categories resolved in the integration, as does the relative size of the melt rate for the $> 250$ cm range compared to the 50-250 cm range.

Comparing three and four category integrations we see that despite the larger

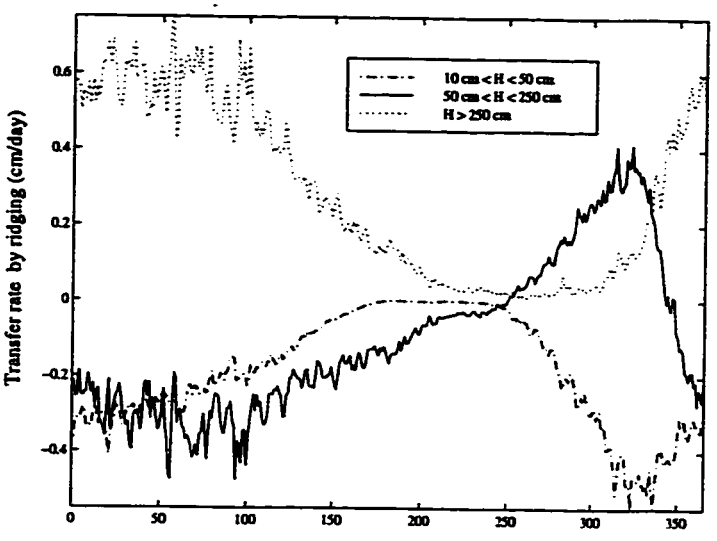


Figure 5.18: As in 5.4 but for four categories case. The three curves are each from a separate ice category.

overall mean thickness, the four category integration has a higher concentration of thin ice ($A_1$). More ice is transferred from the intermediate to the thin category during the melt season in the four category integration than from the thick to the thin category in the three category integration.

Figure 5.18 shows the annual cycle of the ice transfer rate by ridging averaged over the Arctic Basin for the four category integration (there is no ice transfered by ridging in the two category case). The behavior of the 50-250 cm thickness range indicates that it is a sink for ridged ice in the fall and a source the rest of the year in Fig. 5.18. Also the $>$ 250 cm thickness range gains more ice from ridging than in the three category case. The total annual amount of ice transferred from the thin to the intermediate category is 67 cm (slightly less than three category case) and from the intermediate to the thick category is 37 cm (incomparable to three category case).

The time series of the normalized ice volume (Fig. 5.19(a) and (b)) highlights the difference between the mean for the two, three, and four category integration. It seems that the volume has not approached its asymptotic limit even with four

categories in the central region. For the ridging parameterizations I used in this model (see section 4.4.1) the solution has not converged for four categories and if the ice does converge with more than four categories, it will likely be too thick. This suggests that the ridging parameterizations for three and four thickness categories need further refinement. An obvious place to start is with the function that defines which ice will participate in ridging ($a(h)$ in Eq. 4.18) and the rule that determines the thickness of ridged ice. This should be followed by developing a more physical parameterization for the ice strength. Unfortunately such refinements cannot be examined here, but will be the subject of future work.

The anomalies shown in Fig. 5.19(c) and (d) and the standard deviations given in 5.4 indicate the variability of the ice volume is not very sensitive to the number of categories in the thickness distribution. The small increase in $\sigma(h)$ with the number of categories might be due to the increase in mean $h$ with the number of categories. There are subtle differences between the two and three category integrations and even weaker differences between the three and four category integrations. Therefore the results in this section suggest that varying the number of thickness categories resolved by the model has only a modest affect on the variability of the ice volume, but, given the simplicity of the parameterizations used here, it has a substantial affect on the mean ice volume.

### *5.6.2 Sensitivity to ice strength*

The ice strength is parameterized with a quadratic dependence on the ice volume as described in section 4.4.1. Overland and Pease (1988) argued that the empirical constant $P^*$ in Eq. 4.14 should be $1.44 \times 10^3$ N/m$^2$ for modeling ice on the coastal seas. Häkkinen (1993) used $P^* = 3 \times 10^3$ N/m$^2$ for the Arctic region simulated with her thermodynamic dynamic sea ice model. I have tested the three category model with a range of values and chose $P^* = 3 \times 10^3$ N/m$^2$ in order to best represent buoy trajectories, the Fram Strait export rate, and a reasonable amount of ridging.

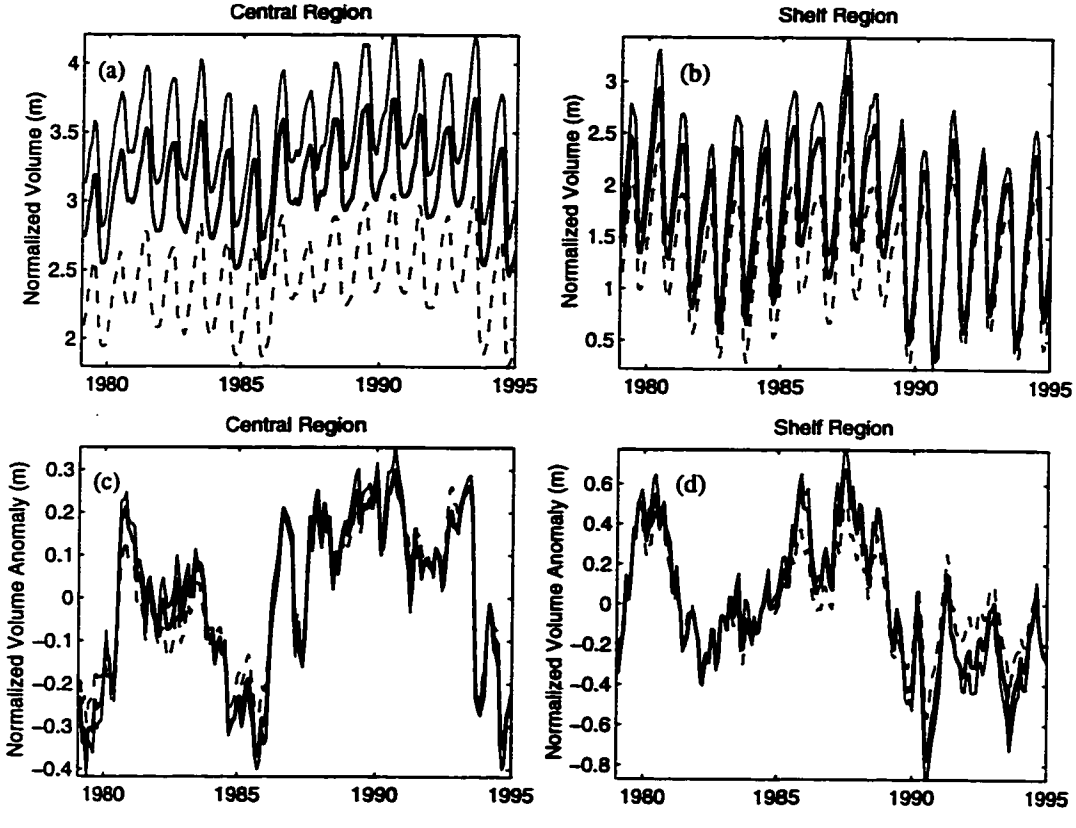


Figure 5.19: Monthly normalized ice volume for integrations with two (dashed line), three (thick solid line), and four (thin solid line) ice categories in the central region (a) and shelf region (b). Monthly normalized ice volume anomalies are shown in (c) and (d).

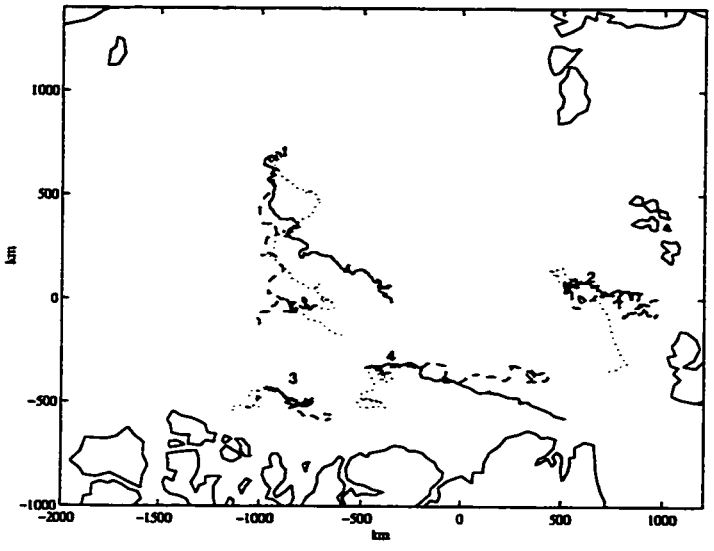


Figure 5.20: Observed and simulated buoy trajectories for four buoys in the Arctic Basin during the period 1991-1994. The solid line is the observed trajectories and the dashed and dotted lines are those simulated by the model standard case and for the case when $P^*$ is doubled, respectively. The drifts shown last for approximately 250 days.

The linear strength parameterization from Hibler (1979) which is commonly used for two category models is equivalent to this parameterization when $A = 1$ for $h = 3.5$ m and it is higher (lower) for $h < 3.5$ m ($h > 3.5$ m).

When an integration is performed with $P^*$ doubled from that of the standard case, the mean ice thickness for the Arctic Basin is 23 cm less, the total annual amount of ice transferred between categories is reduced by 14%, and the export rate at Fram Strait is 16% less. The variability in ice volume and export changes very little.

Modeled buoy trajectories are computed for four buoys based on daily drift vectors along the course of the modeled trajectories. A qualitative assessment from Fig. 5.20 indicates the modeled trajectories from the standard case are more like the observed buoy trajectories. The trajectories for the double $P^*$ case are particularly poor north of the Canadian Archipelago.

## 5.7 *The limitations of using prescribed forcing*

Important feedbacks between the ice-atmosphere and ice-ocean in develop coupled model integrations that do not occur with the prescribed forcing fields used here. In particular, the air temperature should respond to changes in the ice top surface energy balance. In turn the fluxes of downward longwave radiation, sensible heat and latent heat should adjust. Horizontal gradients probably play a roll in the adjustment process as well.

## 5.8 *Conclusions*

During the 16 year period of the standard integration for 1979-1994, the model simulates two periods with pronounced minima in the mean ice volume along the Siberian shelf in the early 1980's and 90's with a maximum in 1987. The volume of ice simulated in the central Arctic experiences local *maxima* coincident with the *minima* in the shelf region: the volume in the central and shelf regions are anticorrelated. Because the air temperature anomalies in these two regions are typically in phase, ice transport is mainly responsible for the out-of-phase relationship between the volume anomalies.

I have analyzed the model simulation of the 1990 minimum in the ice extent that has recently been studied by Serreze et al. (1995). The model results lend support to the conclusion by Serreze et al. (1995) who determined that the minimum ice extent can be explained by atmospheric forcing. The model also shows details of the ice thickness where no observations exists. I find the ice is anomalously thin in the Siberian sector for April prior to the summer of 1990. In September the model has anomalously thick ice in the central region despite positive air temperature anomalies during May and June (Fig. 2 Serreze et al., 1995). This suggests that more ice than usual is swept out of the shelf region, depleting the volume of ice in the shelf region, and moving it into the central region where it piles up, increasing the local volume

of ice there.

The mean ice exported through Fram Strait for the period 1979-1994 in the model is 2600 $km^3yr^{-1}$, comparable to the observed estimate of 3100 $km^3yr^{-1}$ (Aagaard and Carmack, 1989). The variability of the simulated export is striking: the standard deviation exceeds 25% of the mean. The annual mean ice export is highly correlated with thickness in Fram Strait and central region volume anomalies. The largest deviations from the mean occur in 1981 (positive), 1885 (negative), and 1989 (positive).

Since 1991, the ice draft at Fram Strait has been monitored using upward looking sonar moored to buoys. I have computed the ice thickness at the same location in the model and compared the simulated time series to the observations of ice draft. The average simulated ice thickness for June 1991 through July 1994 is 30 cm thinner than the observed draft for the same period and the minimum in the simulated annual cycle of the thickness is shifted a few months earlier. Although the trend in the observations and in the model is considerable, about -100 cm over 3 years, the variability simulated by the model for the full period of the integration indicates that the decrease in the last 3-4 years is not unusual when compared to the full hindcast record (1979-1994).

Sensitivity tests to determine how variability in air temperatures and winds contribute to the volume anomalies reveal that air temperature anomalies primarily influence interannual (greater than 2 yr timescales) variability in the central region. Wind anomalies influence variability in the central region on interseasonal and, to a lesser extent, interannual timescales. Air temperature anomalies affect the variability in ice volume in the shelf region, although wind anomalies are the more important forcing there.

I performed sensitivity tests to determine how ice dynamics affects the model sensitivity to thermodynamic forcing by comparing results from the standard case, an integration with no wind forcing, and integrations with annually periodic wind forcing. Compared to the standard case, the integration with no winds indicates that

the net effect of dynamics is to increase variability in the ice volume. Forcing by annually periodic winds can either increase the variance of the ice volume that is generated by air temperature anomalies or decrease it by hastening the return to the equilibrium ice volume. The strength of the winds determines which is dominate. Strong winds appear to be necessary to create enough open water to enhance the effect of atmospheric anomalies. Weak winds do not create adequate opening, but they do ridge and advect ice in a way that slightly decreases the variability.

I have tested the model sensitivity to the number of thickness categories. When I compared integrations with two-, three-, and four-thickness categories, I found the mean ice thickness increases with the number of thickness categories, as did the variability. Because variance in ice thickness depends on the mean ice thickness, it is not possible to separate the influence of the number of categories from the changes in the mean.

# Chapter 6

# LONG INTEGRATION OF THE DYNAMIC/THERMODYNAMIC SEA ICE MODEL USING SYNTHETIC FORCING

## *6.1 Introduction*

In the previous chapter, the dynamic/thermodynamic sea ice model was used to hindcast the period 1979-1994. Although the integration is less than two decades long, the simulations show evidence for interannual and perhaps even decadal timescales in the Arctic. In this chapter I will describe the results from a 1000 year long integration with the same dynamic/thermodynamic sea ice model forced by synthesized fields of pressure and temperature. My analysis will examine low-frequency variability in the sea ice.

I begin by describing a method for creating long forcing fields of pressure and temperature anomalies based on statistical relationships between the observed fields. I use singular value decomposition to explore the relationship between the pressure and temperature for the period 1979-1994. With the results I show that pressure tends to control the temperature patterns. It is possible to synthesize pressure fields based on a separate statistical analysis of pressure and subsequently synthesize temperature fields that are related in part to the synthesized pressure fields. Finally, I analyze the synthesized fields with singular value decomposition to verify that the relationship is reasonable.

Of course the synthesized fields will not depend a priori on the sea ice. There is some evidence that local surface atmospheric conditions depend on sea ice concen-

trations in preceding months (Rogers, 1978; Overland and Pease, 1982; Deser and Blackmon, 1993), although there is stronger evidence that atmospheric variability forces sea ice concentration anomalies (Rogers, 1978; Lemke et al., 1980; Walsh and Sater, 1981; Wang et al., 1994; Fang and Wallace, 1994).

## *6.2 Creating the synthetic pressure and temperature fields*

### *6.2.1 Singular value decomposition of observed fields*

Singular value decomposition (SVD) is performed on the temporal covariance matrix of the observed daily surface pressure and temperature anomalies from 1979-1994 for the grid shown in Fig. 5.1 to produce two orthogonal sets of patterns known as the singular vectors. The technique selects the modes such that the leading mode explains the largest fraction of the squared covariance between the pressure and temperature fields. The second mode explains the largest fraction of the remainder, and so on.

The covariance matrix is the time average of the product of the pressure anomaly at every grid point $i$ and temperature anomaly at every grid point $j$ for the model domain (see Fig. 3.2). The covariance matrix may be computed with one field lagging the other to determine what lag interval reveals the strongest correlations. In table 6.1 (upper) I show statistics from SVD analysis on covariance matrices at various lag intervals. The correlation coefficient (r) and squared covariance ($Cov^2$) are highest when pressure leads the temperature by 1-2 days for the first six modes.

The six leading singular vectors ($\mathcal{P}$ and $\mathcal{T}$) for the SVD analysis with pressure leading temperature are similar for the 1-4 day lag interval. Hence only those for 1-day lag are shown in Fig. 6.1 with their respective squared covariance fraction ($\lambda^2$). The geostrophic flow associated with the first pressure singular vectors ($\mathcal{P}_1$) advects warm Atlantic air to the region centered around Svalbard and Franz Josef Land which is consistent the center of action in $\mathcal{T}_1$. When $\mathcal{P}_1$ occurs with opposite sign, flow across the Siberian sector brings cold air to the same region. The geostrophic flow for the

Table 6.1: Correlation coefficients (r) between expansion coefficients for the first six SVD modes and squared covariance ($Cov^2$) summed over all pairs of grid points. Rows in the upper table are for various lag intervals where positive lags correspond to pressure leading the temperature. Rows 2-6 in the lower table are for scrambled ordered fields and the first row is for the properly order fields at one day lag. The units of $Cov^2$ are arbitrary.

| | r(%) | | | | | | $Cov^2$ |
|---|---|---|---|---|---|---|---|
| | mode | | | | | | |
| lag | 1 | 2 | 3 | 4 | 5 | 6 | |
| -1 | 32 | 41 | 21 | 25 | 26 | 20 | 46 |
| 0 | 42 | 47 | 31 | 39 | 33 | 31 | 71 |
| 1 | 53 | 49 | 39 | 41 | 38 | 28 | 86 |
| 2 | 54 | 47 | 40 | 38 | 31 | 22 | 81 |
| 3 | 51 | 45 | 36 | 33 | 23 | 18 | 68 |
| 4 | 46 | 42 | 30 | 28 | 18 | 15 | 54 |

| | r(%) | | | | | | $Cov^2$ |
|---|---|---|---|---|---|---|---|
| | mode | | | | | | |
| order | 1 | 2 | 3 | 4 | 5 | 6 | |
| 0 | 53 | 49 | 39 | 41 | 38 | 28 | 86 |
| 1 | 11 | 11 | 10 | 11 | 8 | 8 | 5 |
| 2 | 13 | 12 | 10 | 7 | 10 | 11 | 4 |
| 3 | 12 | 9 | 8 | 10 | 11 | 8 | 5 |
| 4 | 10 | 9 | 8 | 9 | 7 | 8 | 3 |
| 5 | -8 | -6 | 2 | 4 | 4 | 0 | 6 |

second mode creates sharp temperature gradients in the Laptev and Barents Seas, near the maximum pressure anomaly. The center of action for $\mathcal{T}_2$ is shifted towards the coast of Greenland and is smaller scale than for $\mathcal{T}_1$. The pattern for $\mathcal{P}_3$ has strongest pressure gradients rotated 90° with respect to those for the first two modes. This pattern is associated with to have temperature anomalies with opposite sign the western and eastern Arctic. The singular vectors for higher modes tend to have smaller scale structures.

Modes beyond the first six were not analyzed because they explain less than 1.5% of the variance. Table 6.1 (lower) shows the correlation coefficients for SVD on scrambled ordered fields. Clearly the correlation coefficients for all six modes modes for the properly ordered fields (first row) stand out above the rest.

The fraction of the explained variance for the singular vector patterns and their respective expansion coefficients is given with the patterns in Fig. 6.1. The first 6 modes of the pressure SVD explain 83% of the variance of the observed variance while the first 6 modes of the temperature SVD explain 65% of the variance of the observed variance (variance is summed over all grid points). This suggests that the most prominent patterns in pressure often appear with typical patterns in temperature. Common temperature patterns are more often unrelated to pressure than vice versa. The results from this section indicate that the pressure leads and forces a considerable portion of the temperature variability, although another portion of the temperature variability is unrelated to the pressure. Hence I will construct pressure fields independent of the temperature and then build the temperature fields based on the correlation with pressure, and additional variability in temperature unrelated to the pressure.

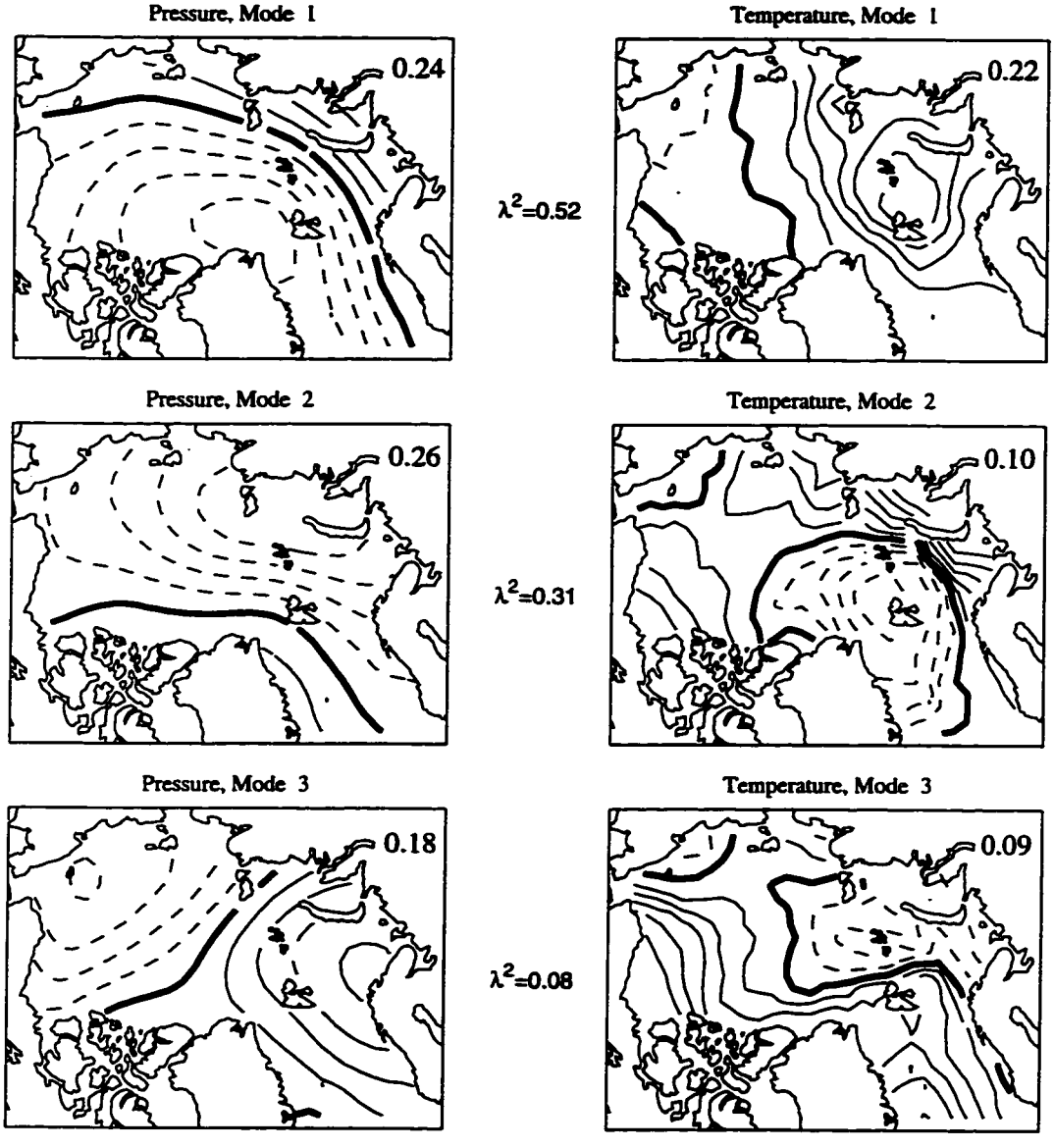


Figure 6.1: First six singular vectors of pressure and temperature for observed fields with the fraction of explained squared covariance ($\lambda^2$). The fraction of explained variance for the respective fields is given in the upper right corner of each pattern. The patterns are nondimensional. Contours are evenly spaced with heavy solid line for zero contour and dashed (solid) for negative (positive) contours.

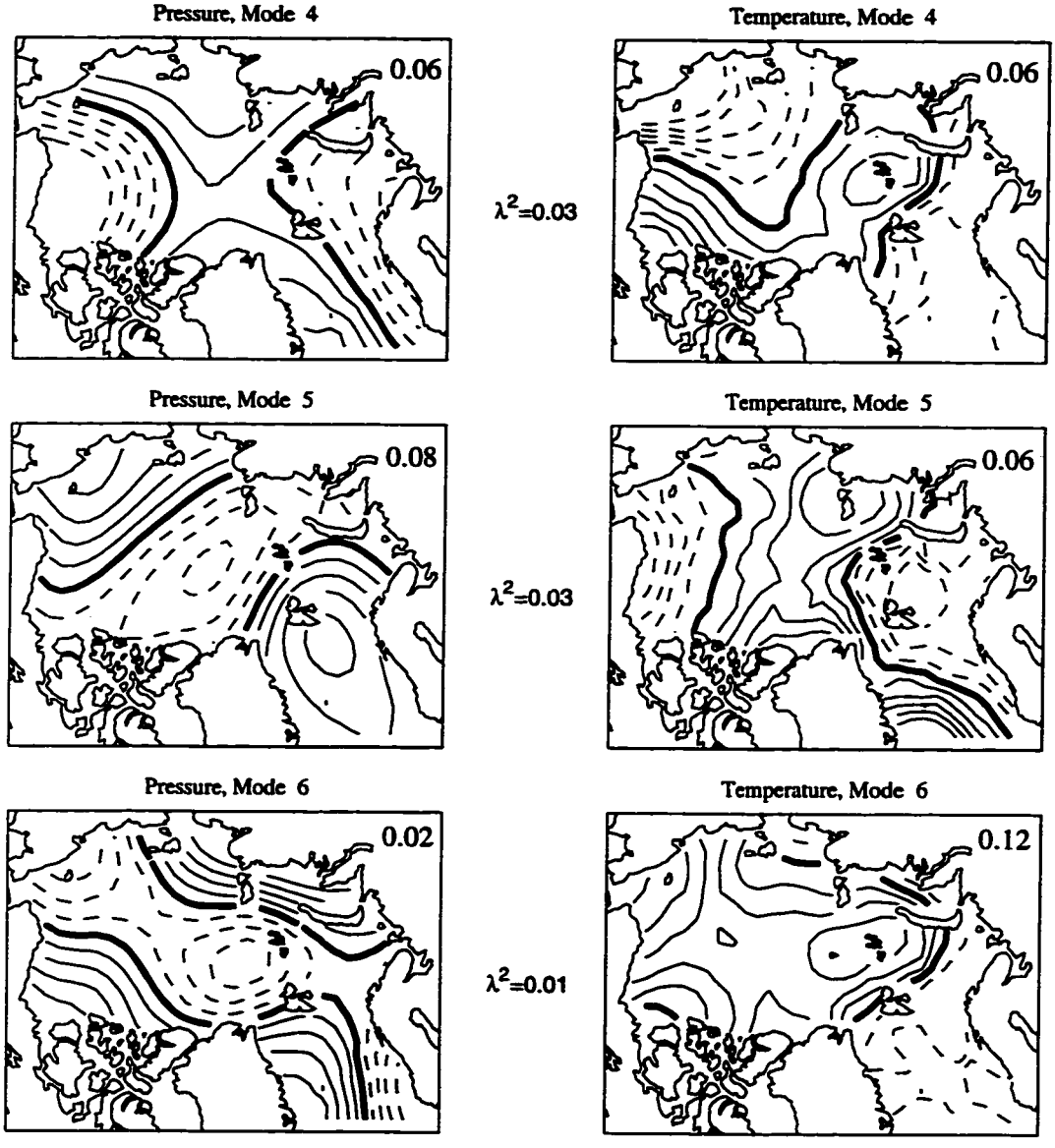


Figure 6.1: continued

### 6.2.2 *Empirical orthogonal functions of observed pressure fields and synthesizing pressure*

I construct synthetic pressure fields with the empirical orthogonal functions (EOFs) of the observed pressure anomalies using a first-order autoregressive model (Markov model) to make principal components (pc's). The EOFs are computed from the variance matrix for the observed pressure anomalies for 1979-1994.

Figure 6.2 shows the six leading EOFs ($\Psi$) with their respective explained variance fraction (pv). The first EOF ($\Psi_1$) explains 40% of the variance and resembles the climatological mean winter pressure pattern known as the Beaufort high. This indicates that variations in the intensity of the Beaufort high dominates the variability in the pressure. $\Psi_2$ resembles the third singular vector in Fig. 6.1 and is likely to be associated with the NPO as mentioned above. $\Psi_3$ bears some resemblance to the first and second singular vectors in Fig. 6.1 and is perhaps associated with the NAO as is the first singular vector.

The cumulative fraction of the variance explained by the first six pressure EOFs is 89%. The structures of the EOFs for modes higher than 6 have relatively small-scale features which suggests that errors in the measurements are obscuring the patterns. In order to represent as much real variance as possible without including modes associated with measurement error, I will use just the first six modes to construct the synthetic fields. Hence only 89% of the pressure variance will be captured because I truncate the number of modes to six, assuming the synthesized principal components are scaled properly.

Power spectra of the pc's for each of the six leading pressure EOFs (Fig. 6.3) show that the temporal dependence of the EOF patterns resembles red-noise. I show the observed spectrum for each pc with the best-fit to a theoretical spectrum of a discrete Markov model (as in section 2.3). The fitting parameter $a$ is associated with a timescale, $-1/\log a$, which is 10 days for the first pc and 2-3 days for pc's two

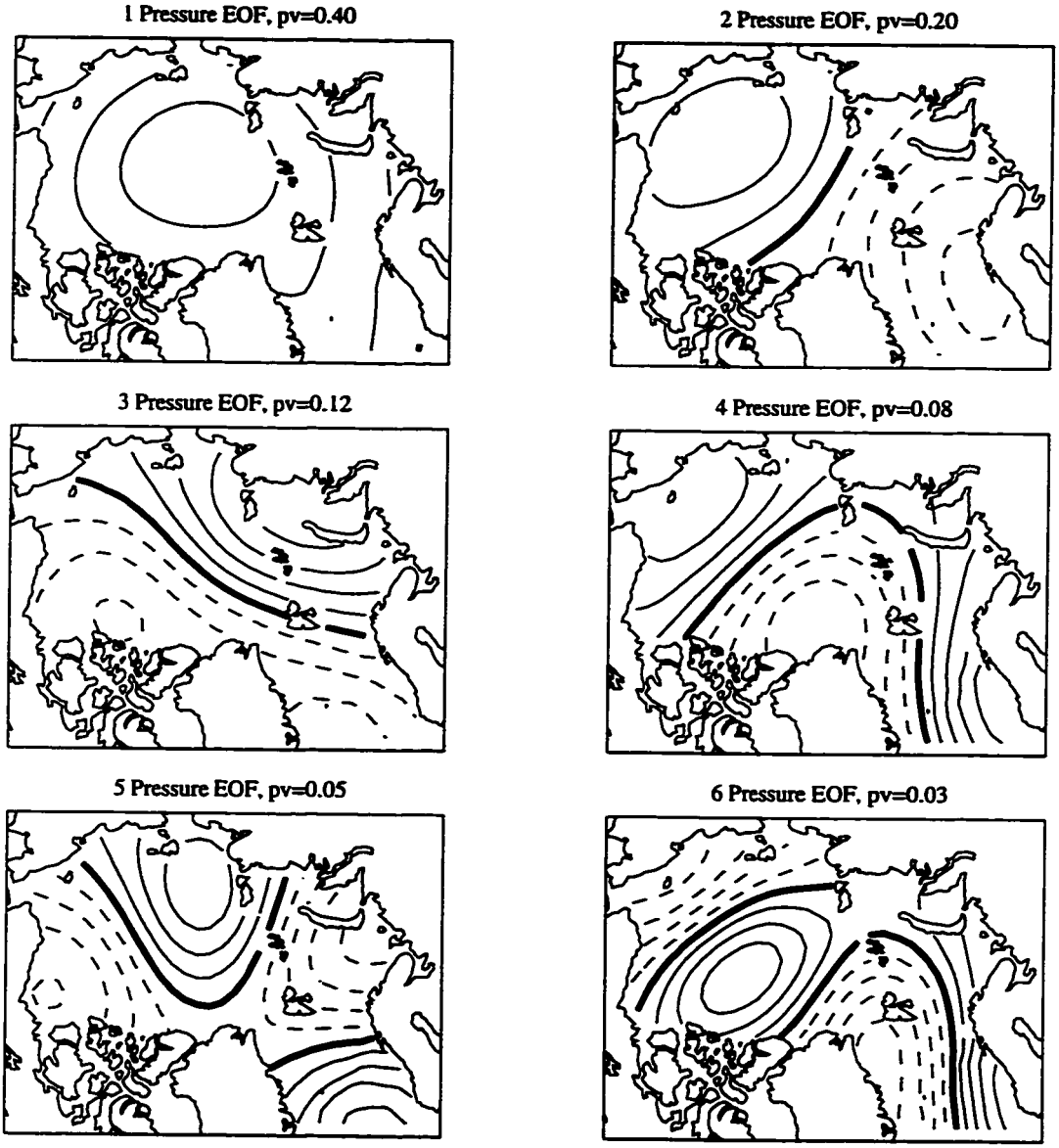


Figure 6.2: First six EOFs for observed pressure with their respective explained variance fraction (pv). Fields are nondimensional. Contouring convention as in Fig. 6.1.

through six. Hence, $\Psi_1$ is associated with the lower frequency variations than the higher modes. Modes two through six have mainly synoptic frequency variability.

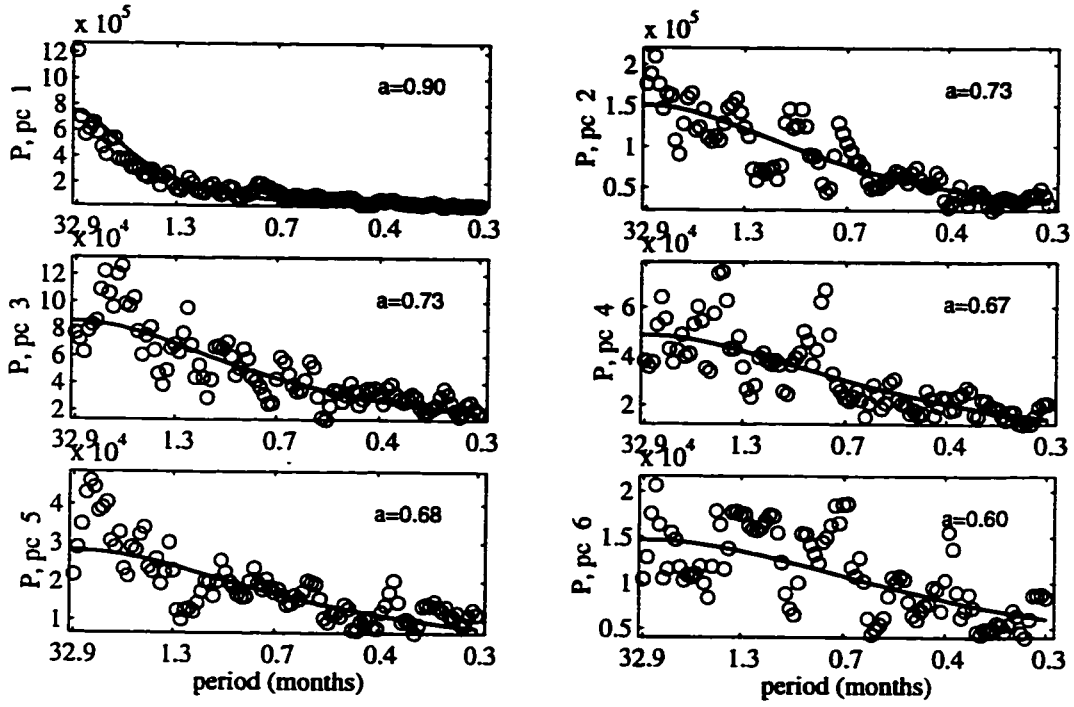


Figure 6.3: Power spectra of first six principal components (pc's) for observed pressure with fit to Markov process and fitting parameter $a$.

It is important to consider the annual cycle of the pc's separately because is not represented by the Markov model. Figure 6.4 shows the annual cycle of first six pc's with fits to

$$C_k(d_o) = 1 + A_k \cos(2\pi(d_o - \phi_k)/365). \tag{6.1}$$

The fitting parameter $A_k$ is a measure of the range of the amplitude of the variation at the maximum and minimum time during the year, $d_o$ is the Julian day, $\phi_k$ is the number of days past the first day of year when the annual cycle reaches a maximum, and $k$ is the mode number. Hence the first EOF has a strong annual cycle with phase such that there is more amplitude in the spring than in the fall. Compared to the other modes, it has an especially important annual cycle for creating opening in the

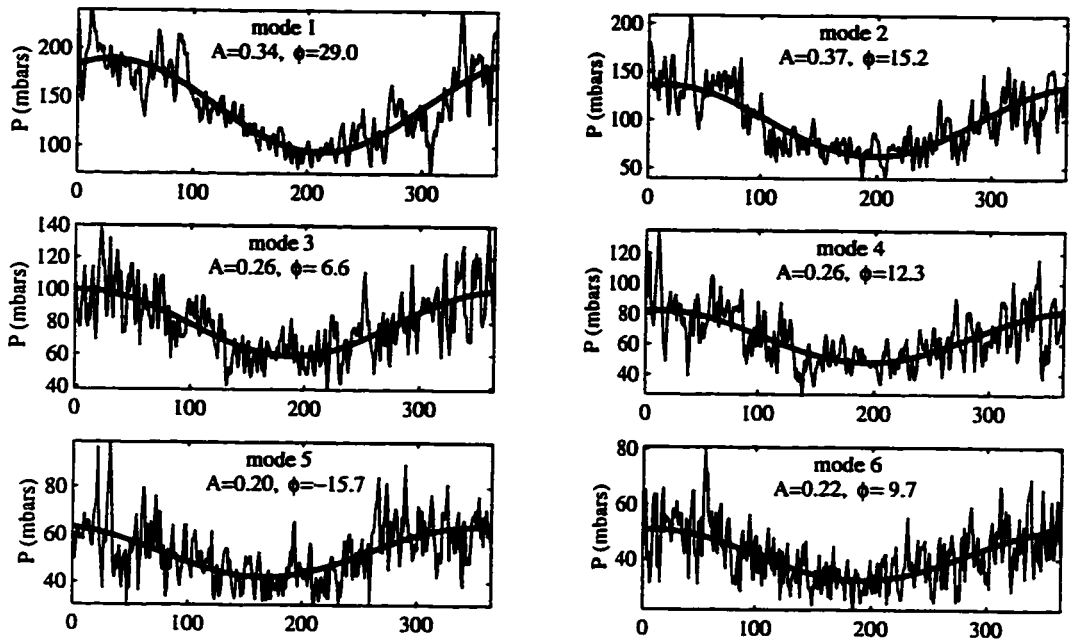


Figure 6.4: Annual cycle of first six principal components (pc's) with fit to cosine function and fitting parameters $A$ and $\phi$ for each mode.

spring.

I synthesize pressure anomalies by numerically constructing daily timeseries for the pc's ($\hat{\varphi}_k$) for the first six EOFs (where $\hat{}$ denotes "synthetic"). Then the synthetic pressure anomalies ($\hat{P}$) are simply

$$\hat{P} = \sum_{k=1}^{6} \hat{\varphi}_k \Psi_k. \tag{6.2}$$

The synthetic pc's ($\hat{\varphi}_k$) depend on the fitting parameters from fitting a Markov spectrum to the observed pc's ($\varphi_k$) and the annual cycle of the observed pc's.

First I use a Markov model to create a stochastically varying time series,

$$\hat{\varphi}'_k(d) = a_k \hat{\varphi}'_k(d-1) + z_k(d), \tag{6.3}$$

where $d$ is time in days, $a_k$ is the fitting parameter from Fig. 6.3, and $z_k(d)$ is a set of normal random deviates. Then the timeseries $\hat{\varphi}'_k$ is modulated by the corresponding

fit to the annual cycle from Eq. 6.1 and the product is normalized so the standard deviation is equal to the standard deviation of the observed pc ($\overline{\varphi_k^2}^{1/2}$). Hence

$$\hat{\varphi}_k = \frac{\overline{\varphi_k^2}^{1/2}}{\overline{(\hat{\varphi}_k' C_k)^2}^{1/2}} \hat{\varphi}_k' C_k, \tag{6.4}$$

for $C_k$ at $d$ modulo 365.

### 6.2.3 *Observed pressure principal components regressed on temperature and synthesizing part I of the temperature*

The synthesis of temperature anomaly fields is a two step process. First in this section, I construct the portion of temperature anomaly that varies linearly with the pressure (defined as $T_I$). Then in section 6.2.4, I construct the residual temperature anomaly (defined as $T_{II}$) portion.

I synthesize $\hat{T}_I$ by computing temperature regression maps ($R_k$) by regressing the observed pressure pc's on the temperature anomaly field and then I multiply these regression maps by the synthesized pressure pc's ($\hat{\varphi}_k$) from Eq. 6.4,

$$\hat{T}_I = \sum_{k=1}^{6} \hat{\varphi}_k R_k. \tag{6.5}$$

For the first mode at each grid point $i$, I regress $\varphi_1$ on the temperature anomaly time series ($t_i$) to compute the regression coefficient,

$$r_{i1} = \frac{\overline{t_i \varphi_1}}{\overline{\varphi_1^2}}; \tag{6.6}$$

then multiply the pc by the regression coefficient to obtain a fitted time series; and finally remove this fitted time series from the original one to obtain the residual temperature anomaly field. The second regression coefficients is computed from $\varphi_2$ and the residual temperature field, and so on. This operation is performed six times for the first six observed pressure pc's with the residual temperature computed each time between operations. The set of $r_{ik}$ at each grid point comprise the regression map $R_k$ for mode $k$.

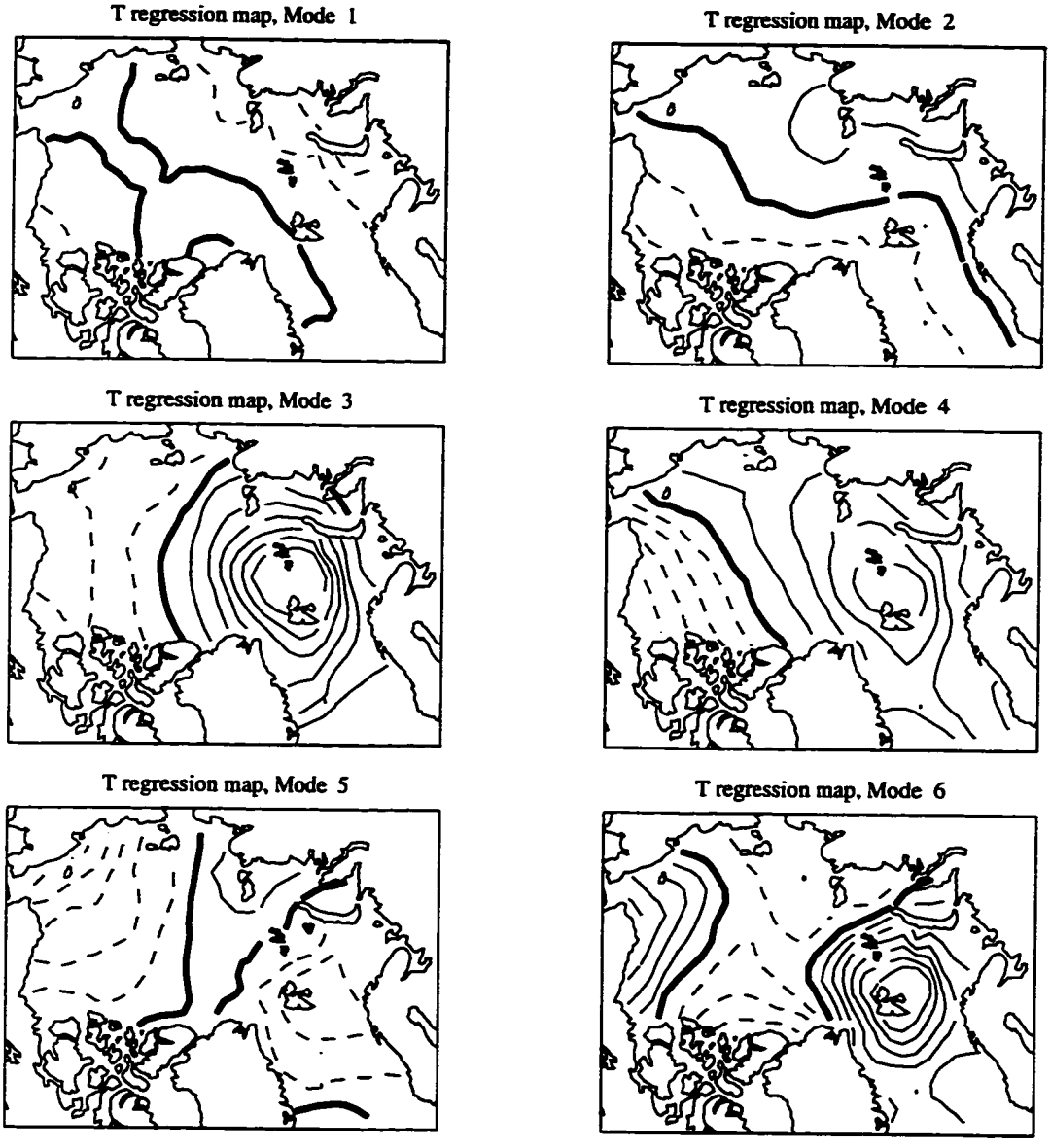


Figure 6.5: Maps of first six observed pressure pc's regressed on observed temperature fields. Contours show 5 mK/mbar increments with heavy solid line for zero contour and dashed (solid) for negative (positive) contours.

I allow for the possibility that the pressure pc and temperature anomaly relationship might be stronger at some lag by computing $r_{ik}$ for every lag between -5 and 5 days at 1 day intervals. I select $r_{ik}$ at the lag that maximized the map's spatial variance. The lags which maximized the variance for the first six modes are 1, 1, 2, 1, 2, and 0 days, respectively, with pressure pc's leading the temperature for modes one through five.

Figure 6.5 shows the temperature regression maps. The first regression pattern ($R_1$) verifies the notion that high (low) pressure and cold (warm) air are observed together during the Arctic winter: the corresponding pressure EOF, $\Psi_1$, has large scale high pressure (using sign convention shown in Fig. 6.2) centered in the Beaufort Sea. Geostrophic flow for $\Psi_2$ is from the west Siberian Arctic toward Greenland and the Canadian Archipelago, bringing warm air into the west Siberian Arctic and cold air toward Greenland and the Canadian Archipelago as is apparent in $R_2$. Compared to the other regression maps, $R_1$ and $R_2$ have relatively weak amplitudes; therefore, the first two pressure EOFs drive relatively weak temperature responses. $R_3$ resembles the first temperature singular vector which is not surprising because the corresponding pressure EOF, $\Psi_3$, looks like the first pressure singular vector, $\mathcal{P}_1$ in Fig. 6.1. The next three regression maps look like combinations of the four leading temperature singular vectors.

### *6.2.4 Empirical orthogonal functions of observed temperature residual fields and synthesizing part II of the temperature*

I compute EOFs of the observed residual temperature anomaly ($T_{II}$) for 1979-1994 to synthesize the part of the temperature anomaly that does not covary linearly with pressure,

$$T_{II} = T - \sum_{k=1}^{6} \varphi_k R_k. \tag{6.7}$$

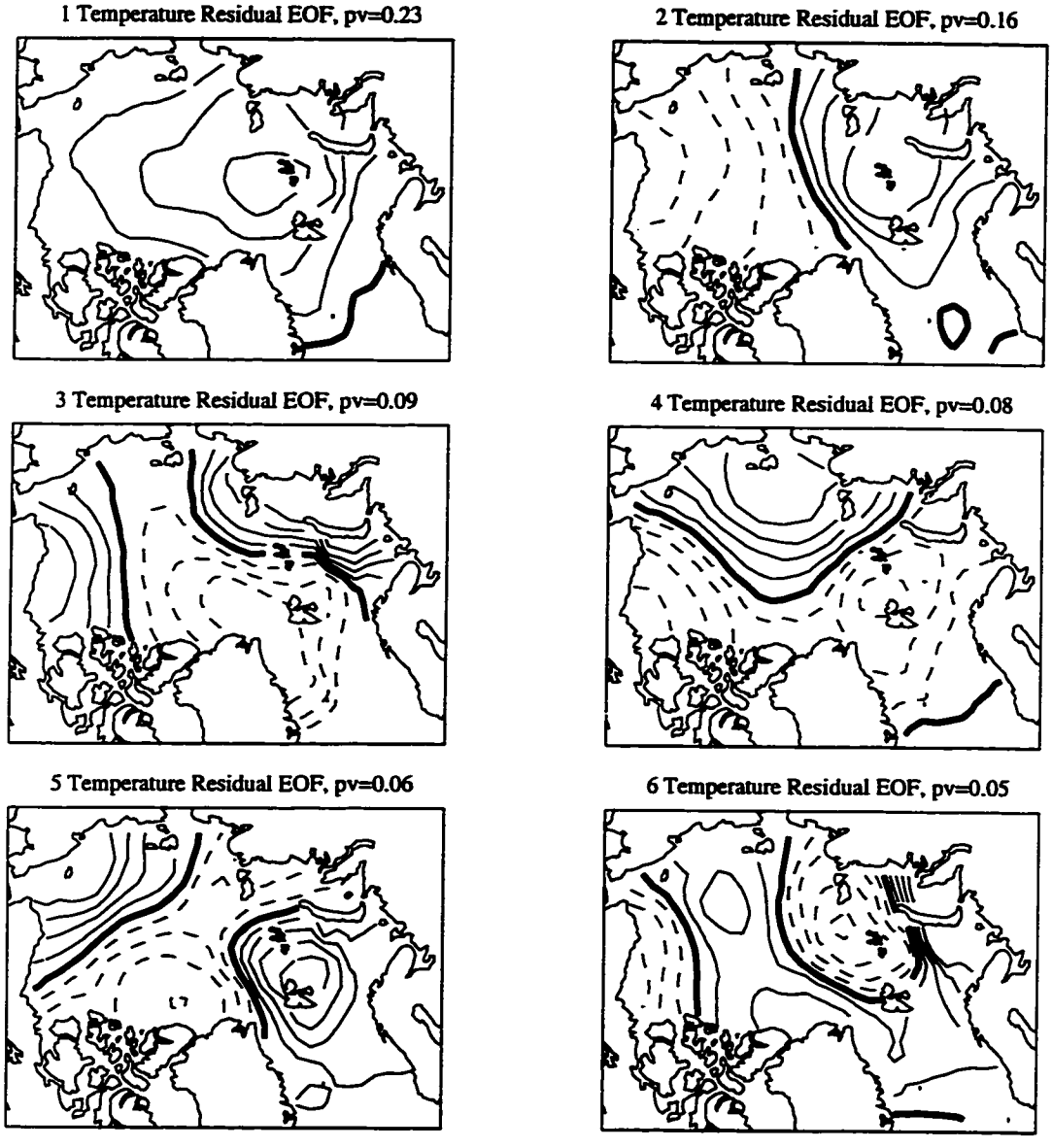


Figure 6.6: First ten EOFs for observed residual temperature with their respective explained variance fraction (pv). Contouring convention as in Fig. 6.1.

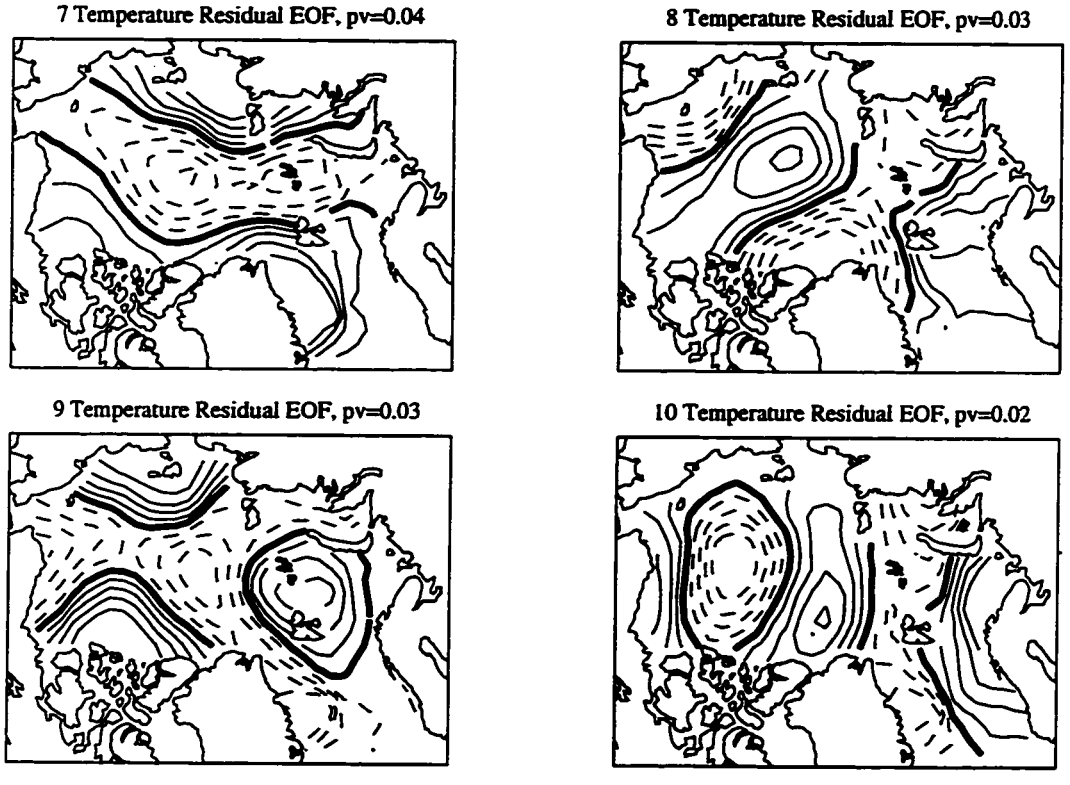


Figure 6.6: continued

The same method is used to construct the synthetic residual temperature pc's ($\hat{\tau}_k$) as was used in section 6.2.3 to construct synthetic pressure pc's.

Figure 6.6 shows the first ten residual temperature anomaly EOFs ($\Theta$) with their respective explained variance fraction (pv). Ten modes are retained because more temperature EOFs are needed to explain the same variance fraction as for pressure EOF's. In fact, the first ten modes only explain 78% of the residual temperature variance, as compared to section 6.2.3 where six modes explain 89% of the pressure variance. By retaining so many modes, there is some risk of reconstructing patterns of that are due to measurement error. However, data is lacking to determine what the real variability is. It is possible that some portion of the variance resembles high frequency, small scale, random noise. Because the pattern of (at least) the first four modes of residual temperature EOFs are quite large scale, they are likely to be physically meaningful modes of variability in the system (instead of noise). The first mode, in particular, is unlike any of the temperature regression maps in Fig. 6.5 or the temperature singular vectors in Fig. 6.1. Most of the contours for this mode are near the ice edge, which suggests that this mode may be correspond to variability in the position of the ice edge.

Figure 6.7 shows the power spectra and fits to a Markov model (as in section 2.3) for the pc's of each of the ten leading residual temperature EOFs. The timescale from the spectral fits is 14 day for the first pc and 2-6 days for pc's 2-10. Generally the residual temperature modes vary more slowly than the pressure modes (see Fig. 6.3. Modes four and seven have unusually fast timescale variability according to the Markov model. The Markov model fits deviate considerably at low frequencies compared to the spectra for the residual temperature pc's. Fits to second order autoregressive models (not shown) did not significantly improve the accuracy.

Figure 6.8 shows the annual cycle of the leading ten pc's with fits to Eq. 6.1. The amplitudes of the annual cycle ($A$) for the residual temperature pc's are higher than the $A$'s for the pressure pc's, reflecting the tendency for the temperature anomalies

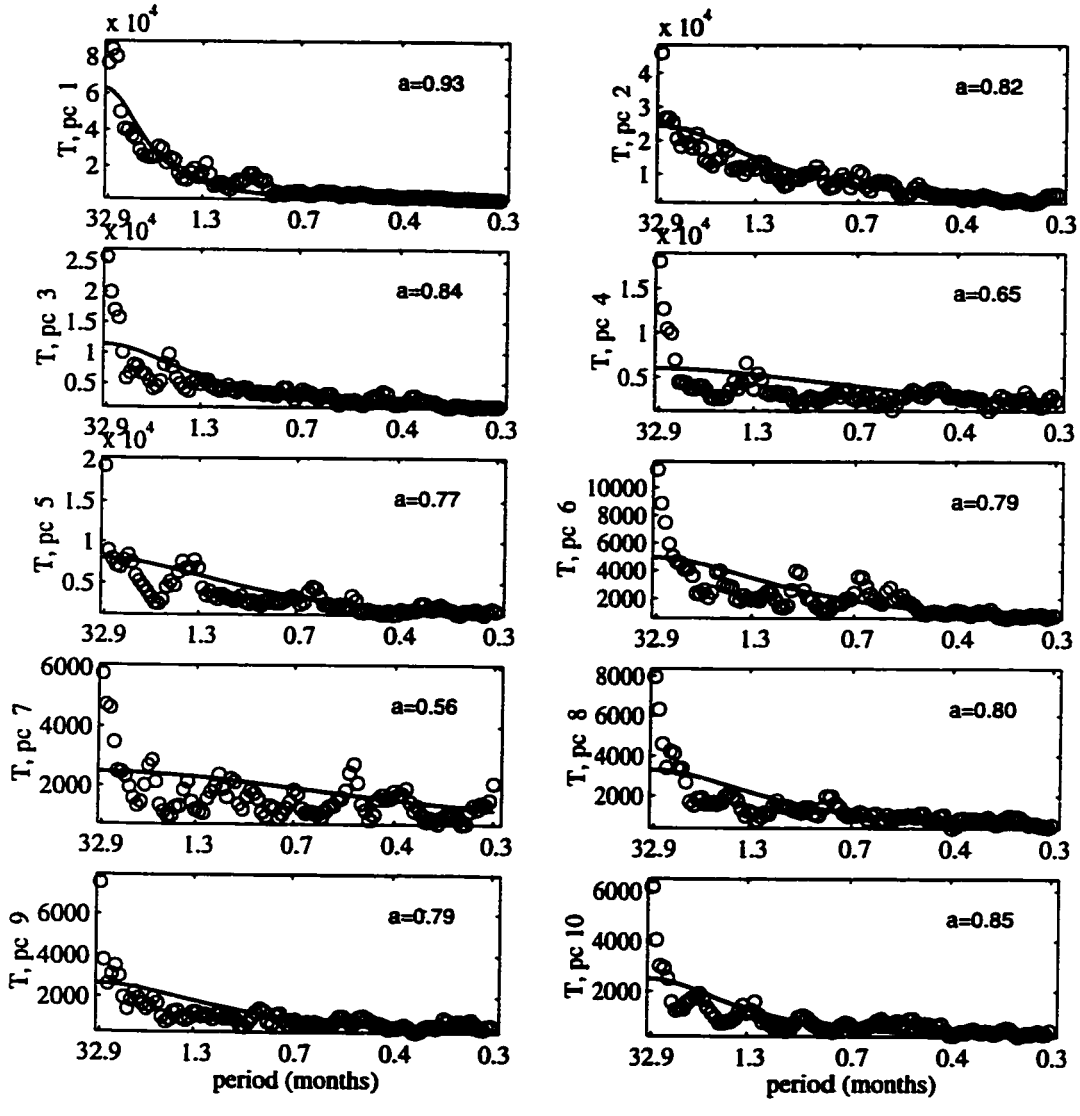


Figure 6.7: Power spectra of the first ten observed residual temperature principal components (pc's) with fit to Markov process and fitting parameter $a$.

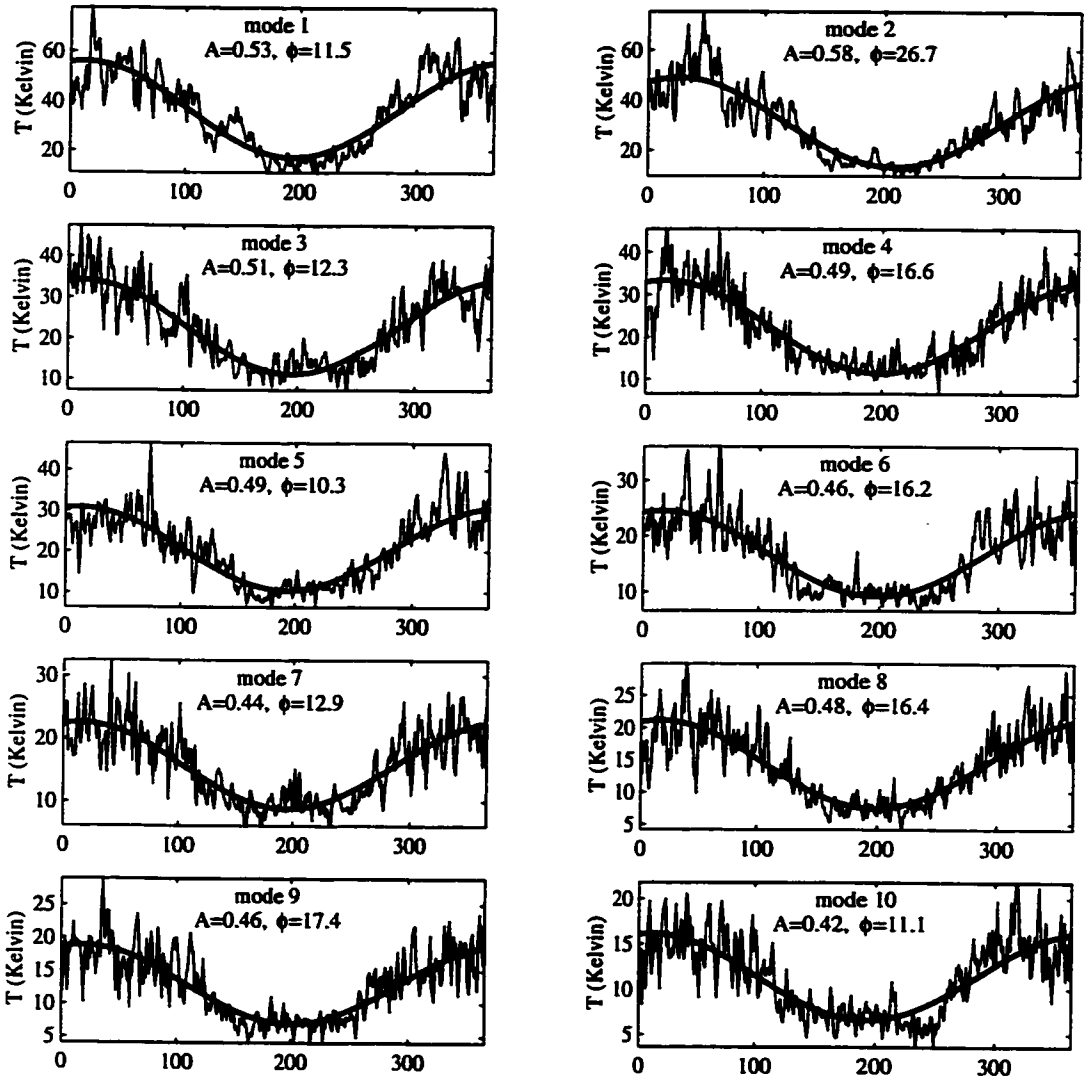


Figure 6.8: Annual cycle of principal components of observed residual temperature thin line) and fit (thick line).

to be small during the summer and large during the winter.

I synthesize the residual temperature anomaly $\hat{T}_{II}$ from

$$\hat{T}_{II} = \sum_{k=1}^{10} \tilde{\tau}_k \Theta_k, \tag{6.8}$$

where

$$\tilde{\tau}_k = \frac{\overline{\tau_k^2}^{1/2}}{\overline{(\hat{\tau}_k' C_k)^2}^{1/2}} \hat{\tau}_k' C_k, \tag{6.9}$$

analogous to Eq. 6.4. Finally, the two parts of combined to give the synthesized temperature anomaly,

$$\hat{T} = \hat{T}_I + \hat{T}_{II}. \tag{6.10}$$

## *6.3 Diagnosing the quality of the synthesized fields*

### *6.3.1 Variance*

Variance maps, shown in Fig. 6.9, for the observed and synthesized pressure and temperature fields reveal how faithfully the synthesized fields represent the spatial distribution of variance. On average, the variance for the synthesized fields is 91% (83%) of the observed variance for pressure (temperature). The regions of the synthesized pressure variance that are weakest are near the climatological mean position of the ice edge. The synthesized temperature variance deficit is more spatially homogeneous.

### *6.3.2 Singular value decomposition*

In this section, a summary of the SVD of the synthetic fields is compared with the SVD of the observed fields from section 6.2.1. I show the first six modes of $\hat{\mathcal{P}}$ and $\hat{\mathcal{T}}$ with squared covariance fraction ($\lambda^2$) for 20 years of synthesized fields in Fig. 6.10. The pressure leads the temperature by one day, as in Fig. 6.1, for all statistics presented in this section.

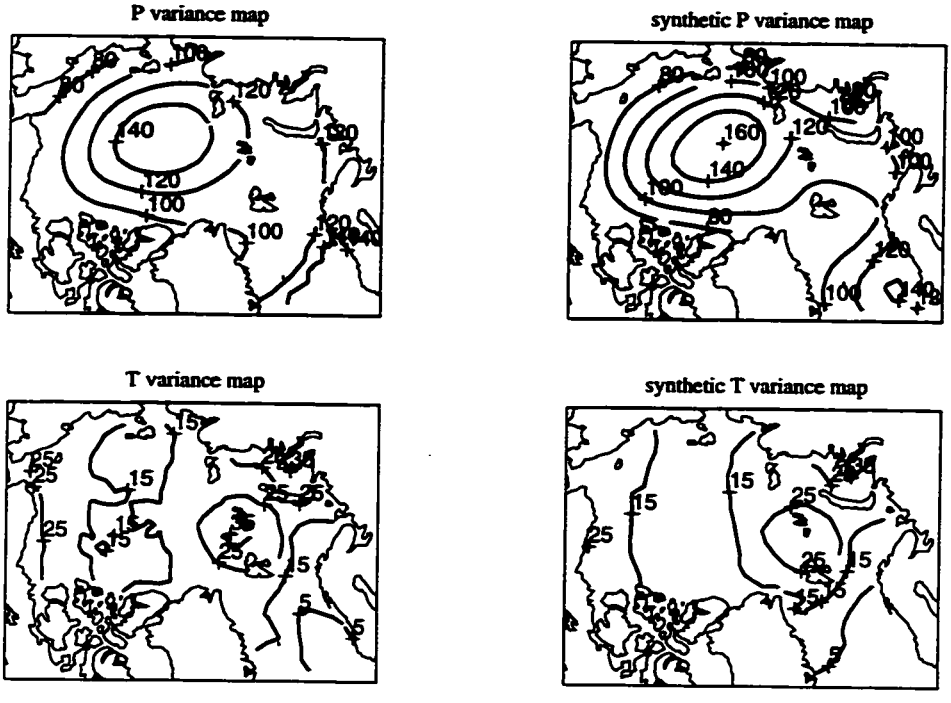


Figure 6.9: Variance map for observed and synthesized pressure and temperature. Units for upper (lower) two panels are mbar$^2$ (Kelvin$^2$).

Comparing the patterns in Figs. 6.10 with 6.1 reveals considerable success in reconstructing the observed spatial patterns of covariance with the techniques described above. $\hat{\mathcal{P}}_1$ and $\hat{\mathcal{P}}_2$ appear to be combinations (or rotations) of $\mathcal{P}_1$ and $\mathcal{P}_2$ and $\hat{\mathcal{T}}_1$ appears to be a combination of $\mathcal{T}_1$ and $\mathcal{T}_2$. However, $\hat{\mathcal{T}}_2$ is remarkably similar to $\mathcal{T}_2$. Singular vectors for modes 3-5 for both fields have much in common with the observed singular vectors for corresponding modes. The agreement for the sixth modes begins to break down.

The sum of the $\lambda^2$'s for the first six modes is 100% (compared to 98.5% for observed). $\lambda^2$ for the first mode is about 10% higher than that for the observed fields. This increase is at the expense of the next 5 modes which are each a few percent less than that of the observed fields. The squared covariance summed over all pairs of grid points is 84, in arbitrary units (compared to 86 for observed); therefore, the

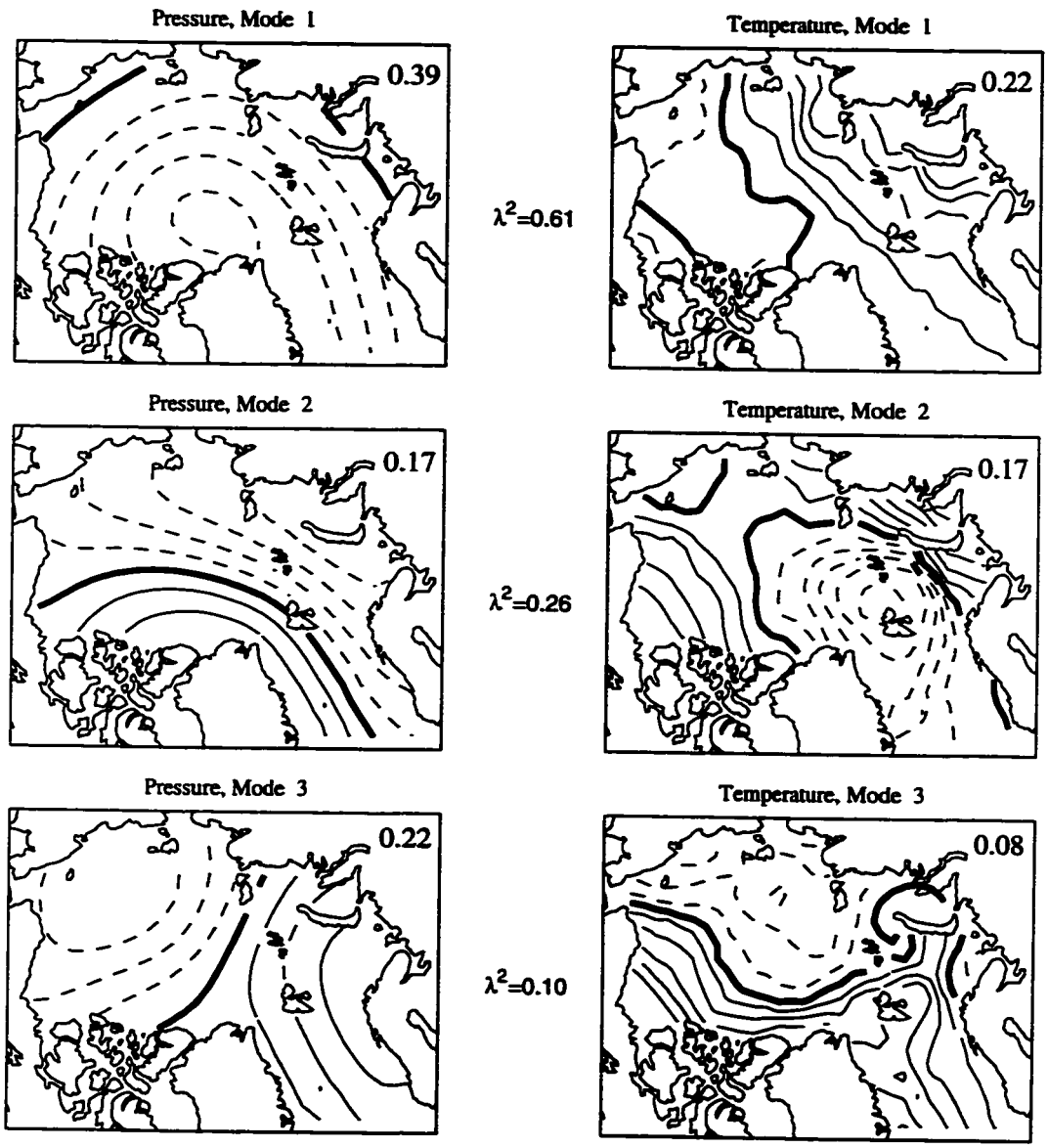


Figure 6.10: As in Fig. 6.1, but for 20 years of the synthesized fields.

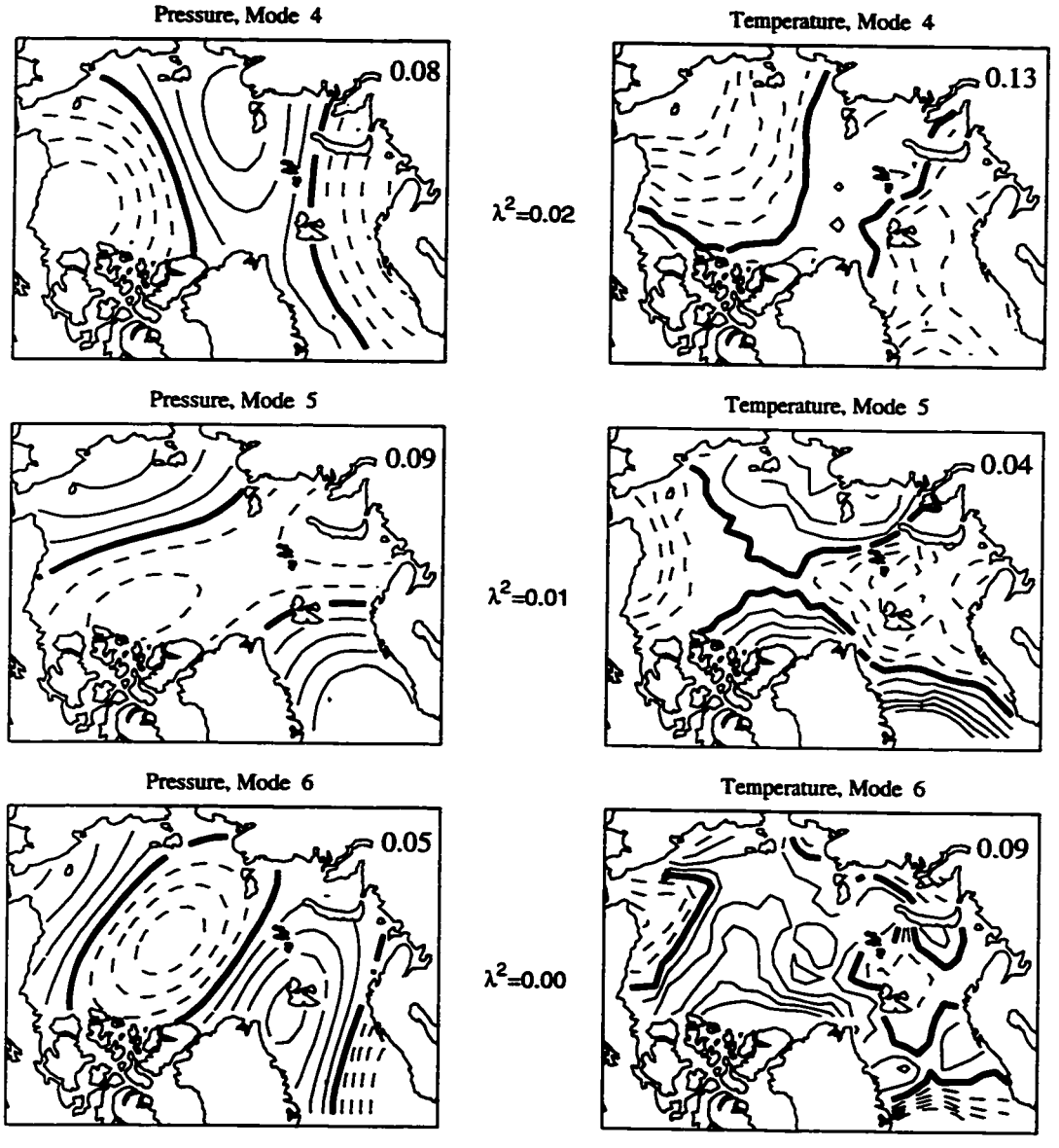


Figure 6.10: continued

synthesized fields retain most of the observed covariance, but it is more condensed into the leading modes.

Correlation coefficients of the expansion coefficients for the first six modes are 43, 48, 39, 25, 28, and 10% (compared to 53, 49, 39, 41, 38, and 28% for observed). The correlations for first three modes compare well with observations, although the first mode is low, perhaps due to the higher $\lambda^2$. The next three modes under represent the correlation in the observed fields more severely. This error is not too serious because these modes explain little of the covariance.

The differences between the SVD for the observed and synthesized fields are primarily due (1) to truncating the expansion of pressure and temperature and (2) to approximating the expansion coefficients with Markov models when building the synthesized fields. Nonetheless, the principal modes of covariance are reasonably well represented in the synthesized fields.

### *6.3.3 Time dependence*

The time dependence of the synthesized pc's generally under represent the inter-annual variance because the spectra (not shown) are essentially equal to the spectra for a Markov model from which they were derived. Because the observed data from which the synthetic data are based only lasts 16 years, nothing directly can be said about the accuracy of the synthesized data on decadal timescales. However, temperature records at Longyearbyen station on Spitsbergen (see section 6.6) which extend back more seven decades suggest that the Markov model under represents decadal variance as well as inter-annual variance.

Results from the single column-model described in section 2.3.2 indicate that there is a strong tendency for the climate system to scatter the relatively high-frequency variability of the atmosphere to low-frequency variability in the sea ice thickness. Therefore the dynamic/thermodynamic sea ice model should develop low-frequency despite the low amplitude of the low-frequency fluctuations in the atmosphere.

## 6.4 *Results from a one-thousand year integration*

Based on the methods developed in section 6.2, pressure and temperature anomaly fields were synthesized for 1,000 years and added to the 16 year climatological means to force the dynamic/thermodynamic sea ice model. In this section, I describe the results of the long, 1,000 year, integrations.

### *6.4.1 Ice concentration and volume*

The annual mean ice volume from the long integration has variability on interannual and longer timescales (see Fig. 6.11). Variability in the central region is concentrated at lower frequencies compared to the shelf region. The standard deviation for the area-averaged sea ice thickness ($\sigma_h$) is 24 cm and 29 cm for the central and shelf regions, respectively. Hence compared to the hindcast, $\sigma_h$ is higher in the central region and the same in the shelf region. Unlike the hindcast, the ice volumes in the central and shelf regions are significantly (albeit weakly) correlated (r=0.30) for the long integration.

When the long integration is broken into 16 yr segments, there are segments where $\sigma_h$ in the central region is equal to that in the hindcast. There are several segments with negatively correlated ice volumes in the central and shelf regions, like in the case of the hindcast. These comparisons suggest that the variability of the ice thickness on interannual and shorter timescales for the hindcast and long integration is indistinguishable.

The mean ice thickness for the Arctic Basin in the long integration is about 35 cm thinner than in the 16 year hindcast. Yet the climatological mean temperature and pressure fields are identical in the runs. There is no 16 year period in the long integration where the mean thickness in the Arctic Basin is as high as that for the hindcast, so the mean thickness difference is too great to be within the natural variability of the sea ice. The difference in the means must be due to subtle differences

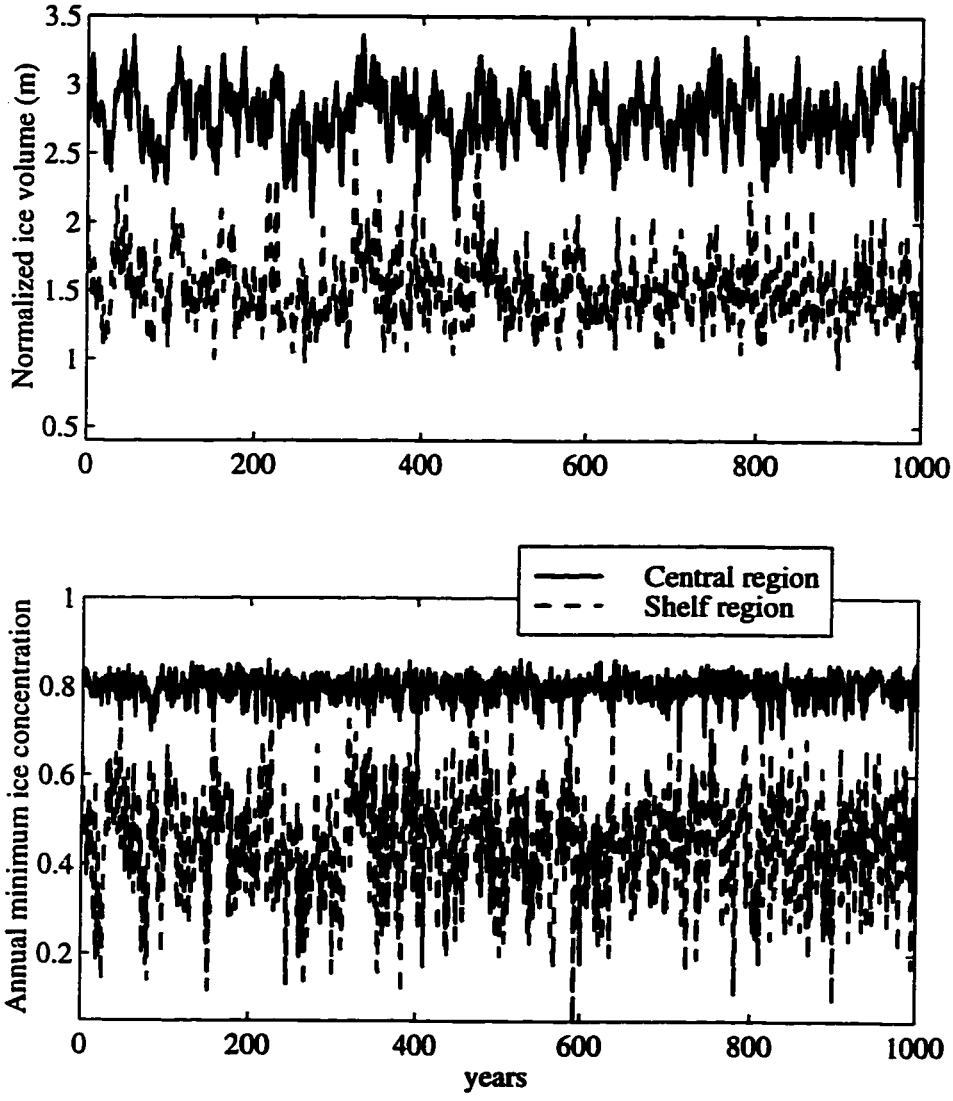


Figure 6.11: Annual mean ice volume and annual minimum concentration for the long integration. The volume is normalized by the area of the region, so it is equivalent to an area-averaged ice thickness for the region.

between the character of the observed and synthesized forcing anomalies.

The ice concentration in the long integration is similar to the that in the hindcast. The ratio of the standard deviation to mean for the annual minimum ice concentration is 0.04 and 0.27 in the central and shelf regions, respectively. Hence compared to the hindcast, the variability of the annual minimum concentration is the same in the central region and lower in the shelf region. In both the hindcast and long integration the concentrations in the central and shelf regions are uncorrelated. For the long integration, the mean of the annual minimum ice concentration is 0.80 (same as hindcast) and 0.43 (0.02 less than in hindcast) in the central and shelf regions, respectively.

Figure 6.12 shows the power spectra of the annual mean ice volume and annual minimum ice concentrations in the central and shelf regions. As predicted by the single-column model (SCM from chapters 2 and 3), the spectrum of the volume is strongest at low frequencies, a characteristic of red noise. If the volume depended only on the ice thickness, according to the SCM, variability of the volume would tend to be confined more towards the low frequencies where the ice is thickest. Comparing the two curves in the upper panel of Fig. 6.12, the variability of ice volume in the dynamic/thermodynamic agrees with this result from the SCM. However, lateral inhomogeneities cause the curves to be closer than expected because variability of the ice concentration in the shelf regions appears to increase the low-frequency variability of the volume in a way that could not be predicted by the SCM.

The spectra shown in Fig. 6.12 are not smooth, instead they have considerable structure. The power spectrum for the ice volume in the central region is repeated in Fig. 6.13 with a fit to the theoretical power spectrum for a Markov model. Error bars show 95% confidence levels based on the chi-squared probability distribution. None of the spectral estimate for periods longer than about 2 years deviates significantly from the fit to a Markov model; therefore, none of the peaks and valleys in the spectrum is significant. The fitting parameter gives a characteristic timescale of 3 years which

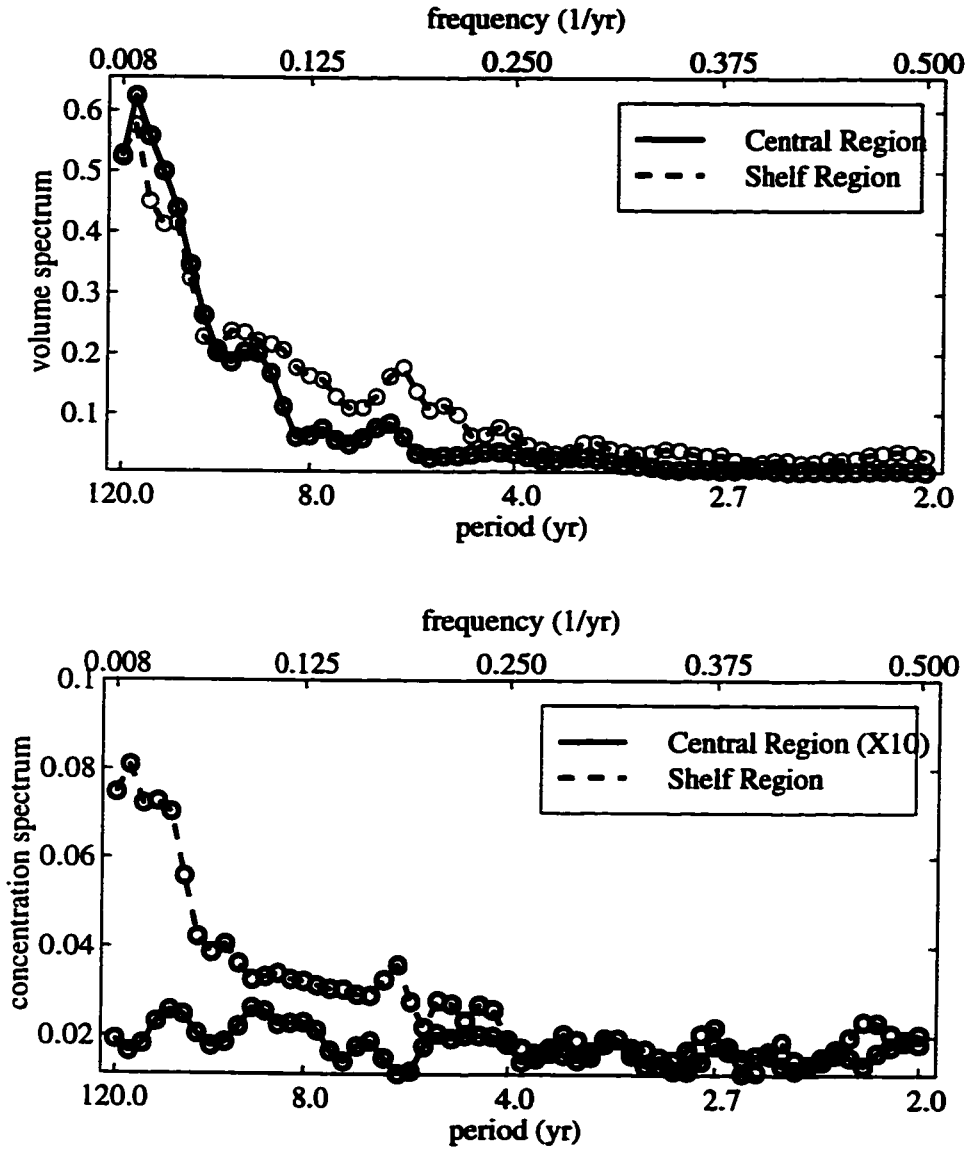


Figure 6.12: Power spectra of annual mean ice volume and annual minimum concentration for the long integration. Units are $m^2yr^{-1}$ and $yr^{-1}$ in the upper and lower panels, respectively. The spectra in this figure and in Figs. 6.13 and 6.15 are calculated for the last 900 years, $N$, of model output using a lead/lag correlation method smoothed with a 60 year, $L$, Tukey window; therefore, the spectral estimates have $8N/3L = 40$ degrees of freedom (Jenkins and Watts, 1968).

is short compared to the ice modeled in the SCM whose timescale is 15 years.

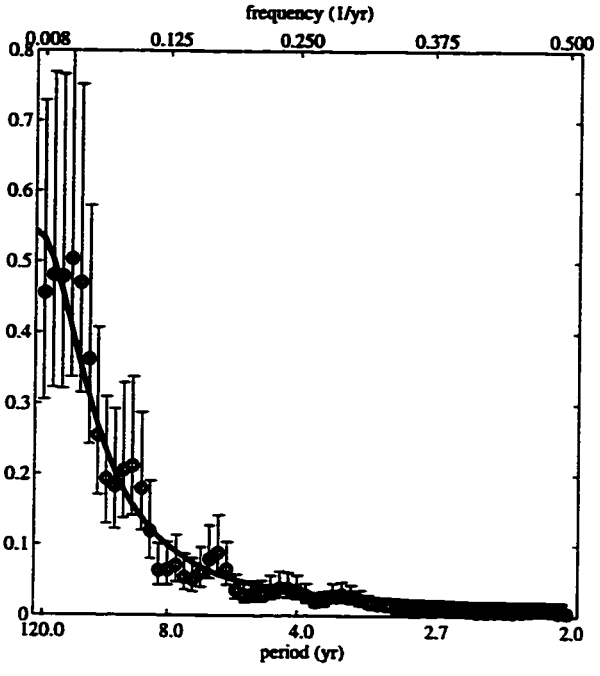


Figure 6.13: As in Fig. 6.12(a) (solid line) except with 95% confidence level and fit to a Markov model.

### *6.4.2 Ice export through Fram Strait*

Figure 6.14 shows the total annual ice export for the long integration. Like the ice thickness, the mean export is lower in the long integration than in the hindcast. It is 2000 $km^3yr^{-1}$, compared to 2600 $km^3yr^{-1}$ from the hindcast. At 500 $km^3yr^{-1}$ the standard deviation is also lower than in the hindcast, although the ratio of standard deviation to mean is about the same.

The power spectrum of the total annual ice export (see Fig. 6.15) has several peaks and valley. The most striking peak at a period of 6 years is not quite significantly above the Markov model power spectrum at the 95% confidence level. The characteristic timescale, determined from the fit in Fig. 6.15 is 1 year.

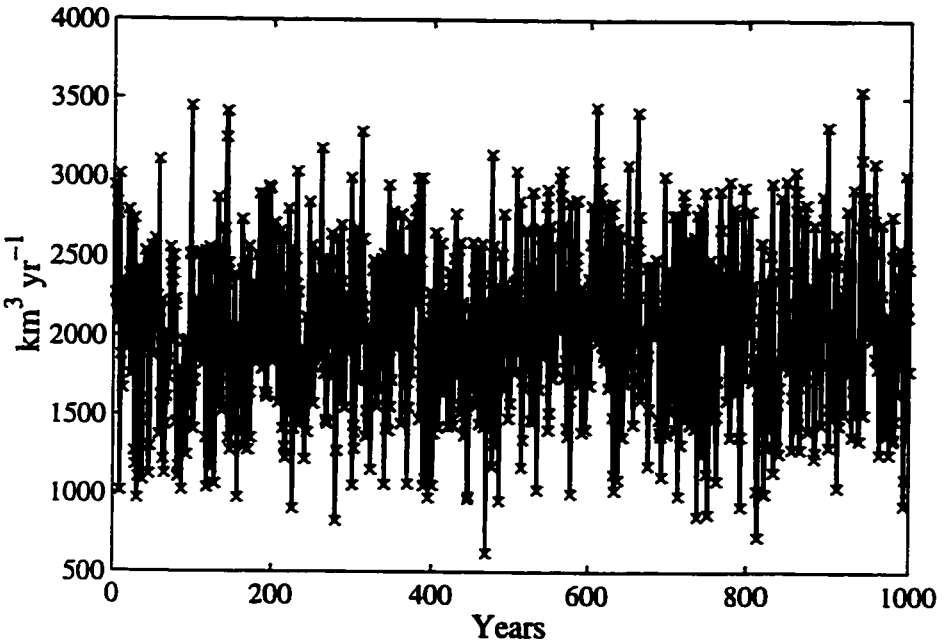


Figure 6.14: Simulate ice export at Fram Strait from the long integration.

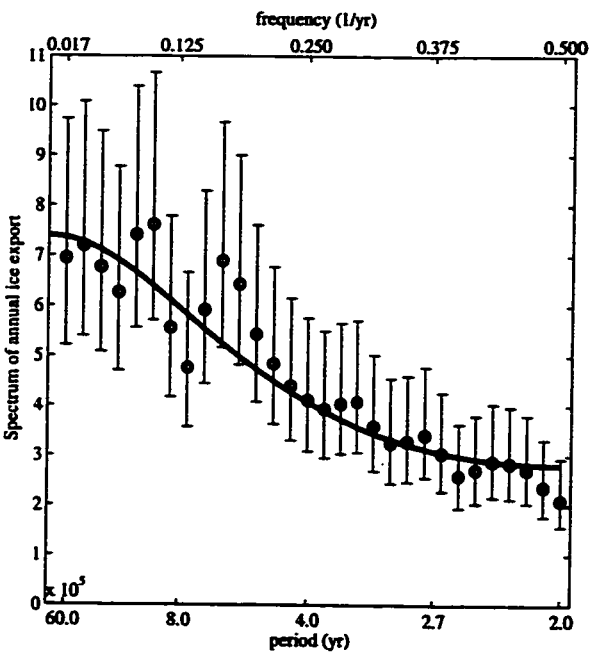


Figure 6.15: Power spectrum of annual mean ice export at Fram Strait for the long integration with 95% confidence level and fit to a Markov model. Units are in km$^6$yr$^{-3}$

## 6.5 *Discussion and summary*

This long integration with synthetic forcing reveals new information about the low-frequency response of the dynamic/thermodynamic sea ice model to high frequency atmospheric forcing. The spectral variance of the ice volume is peaked at low-frequency, like the ice thickness in the single-column model. However the characteristic timescale is about 1/5 as long which indicates that the spectral variance is not as confined to decadal timescales, and fluctuations on interannual timescales contribute a large fraction to the variability.

A curious result from the long integration is the strong low-frequency variability of the ice concentration in the shelf region. The shape of the spectral variance is dissimilar to the theoretical spectrum of the Markov model. Apparently heat storage in the mixed layer influences the simulated ice concentration in a way that cannot be characterized so simply. Because measurements of ice concentration in the Arctic only exist for a few decades, the simulated low-frequency variability cannot be verified directly.

The frequency distribution of the annual minimum ice concentration of the shelf region (see Fig. 6.16) for years 101-1000 exhibits minima at the level of the *observed* 1990 minimum sea ice concentration 22 times, or once every 40 years on average. Recall, however, that the hindcast (section 5.4.2) overestimates the 1990 minimum by 10%. Using the level of the *simulated* 1990 minimum sea ice concentration from the hindcast, there are only 7 years that reach the level of the 1990, or once every 130 years on average.

Dickson et al. (1988) estimated that the total freshwater anomaly during the Great Salinity Anomaly (GSA) was approximately 2200 $km^3$. After developing over a period of several years in the 1960's in the Greenland Sea, the salinity eventually propagated to the Labrador in 1971-72 (Dickson et al., 1988). Based on these measurements, I compare the sea ice export summed over three successive years to

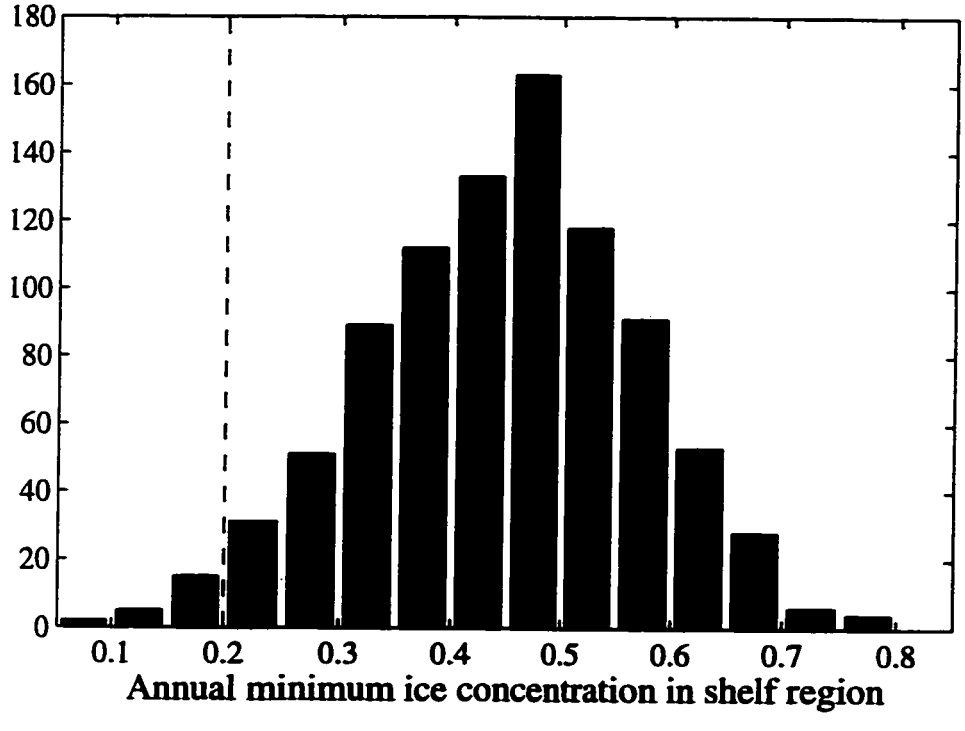


Figure 6.16: Histogram of annual minimum ice concentration of shelf region for last 900 years of the long integration. Dashed line shows the 1990 level of the observed sea ice minimum concentration.

Dickson's estimate of the freshwater anomaly. The frequency distribution of the 3-year sums of ice export for years 101-1000 exhibits 9 maxima at the level of the observed freshening during the GSA, which translates into one GSA every 100 years on average (see Fig. 6.17).

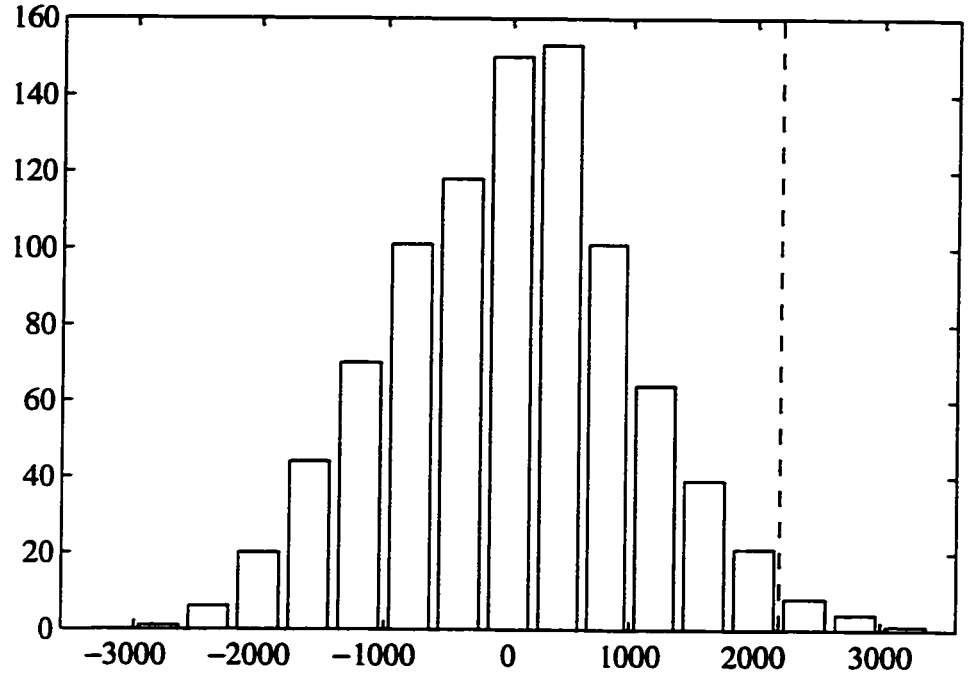


Figure 6.17: Histogram of ice export for 3 year running sum for last 900 years of the long integration. Dashed line shows the level of freshening measure during the Great Salinity Anomaly.

Finally the long integration is likely to underestimate the true variability in the system because the forcing lacks the following:

- The synthesized temperature and pressure anomalies underestimate variability at low-frequencies (compare power spectra of the pressure and temperature principal components with the fits to a Markov model in Figs. 6.3 and 6.7).

- The model neglects interannual variability in the cloudiness, snowfall rate, ocean heat flux, ocean currents.

- The mean ice is too thin. According to the SCM, thicker ice adjust more slowly and has higher (thickness) variance than thinner ice.

- The model is not coupled. On interannual timescales, I expect the surface air temperature anomalies, to some extent, reflect sea ice anomalies, higher concentrations of thick ice making the air temperature colder and vice versa. Sea ice thickness anomalies decay because thick ice grows more slowly than thin ice. Coupling between air and ice should reduce the damping associated with growth depends on thickness.

## 6.6 *Comparison of the simulated natural variability in the sea ice by the SCM, GFDL GCM, and the dynamic/thermodynamic sea ice model*

In this dissertation, I have analyzed the sea ice thickness in three very different models: the dynamic/thermodynamic sea ice model from chapters 4, 5 and 6, the GFDL GCM in chapter 3, and the single column purely thermodynamic model in chapters 2 and 3. The GFDL model computes ice motion in a relatively simplistic way (e.g., ice does not move when its thickness exceeds 4 m), hence ice advection and deformation may play rather different roles in the three-dimensional models. Furthermore, the GFDL model has relatively simple ice thermodynamics, which tends to decrease the model's sensitivity to atmospheric thermodynamic forcing.

From the long integration with the dynamic/thermodynamic model, the standard deviation of the annual mean ice thickness averaged over the central Arctic is $\sigma_h =$ 22 cm. This is much lower than $\sigma_h = 85$ cm from the 1,000 year, standard case integration with the SCM. From section 5.5.2, it is clear that the dynamics in the dynamic/thermodynamic model increases $\sigma_h$ in the central arctic. So this cannot explain the difference between the these two models. Curiously, $\sigma_h$ is the same for the dynamic/thermodynamic model and the 1000 year, "present climate" simulation

of the GFDL climate model. Good agreement between for $\sigma_h$ between these two models does not imply that they behave similarly. To complete this study, I will try to explain the difference and summarize the results.

In table 6.2, I summarize the standard deviation of the annual mean ice thickness averaged over the central Arctic for the three models, including two integrations with the SCM showing the affects of parameterizing export and removing part of the low-frequency variability from the atmospheric forcing. Clearly, $\sigma_h$ is much larger from the SCM.

Table 6.2: Standard deviation of annual mean ice thickness for dynamic/thermodynamic sea ice model, GFDL GCM, and single column model (SCM).

| 1,000 year model integrations | $\sigma_h$ (cm) |
|---|---|
| dyn./therm. sea ice | 22 |
| GFDL GCM | 22 |
| SCM - standard case | 85 |
| SCM - with export | 55 |
| SCM - hybrid $D$ | 72 |

Further understanding about how these models compare is revealed by examining the surface air temperature. In table 6.3, I show a summary of the variability of winter surface air temperatures ($\sigma_T$) from the POLES dataset, from Longyearbyen station (on the coast of Spitsbergen), from the synthesized dataset used to force the thermodynamic/dynamic sea ice model, and from the two coupled models. The synthesized dataset compares well with observed $\sigma_T$ for *monthly* mean temperatures in the central region (from POLES) and retains about 70% of $\sigma_T$ for *monthly* mean sur-

face air temperatures at Spitzbergen. The GFDL model overestimates[1] the observed $\sigma_T$ for *monthly* mean temperatures in the central region by 80% and at Spitsbergen by 26%. Hence, the thermodynamic/dynamic sea ice model has the same $\sigma_h$ as the GFDL model, although it is forced by surface air temperatures with less than half as much $\sigma_T$ during winter months.

Compared to *10-year* means observed at Spitsbergen, the surface air temperature is severely under represented in both the GFDL model and the synthesized dataset (whether or not the observational period includes the temperature "jump" in the 1920's, see caption for table 6.3). The lack of low-frequency variability in $\sigma_T$ from the GFDL model is consistent with the arguments in chapter 3 which indicate that the variability in the ice volume in the central arctic is artificially low. It is not too surprising that the $\sigma_T$ in the synthetic dataset is low because the method for constructing the fields failed to reproduce the full magnitude of even the interannual variability that is present in the POLES 16-year record (see Fig. 6.8).

The SCM is designed to represent the average response of sea ice in the Arctic Basin. However, $\sigma_T$ for monthly means from integrations with the SCM are more like the observations from the single station at Spitsbergen, than the average over the central region from the POLES data. It is possible that the POLES data under-represents the variability in the central region where the data set relies on sparsely sampled temperatures measured by buoys and the soviet NP stations (S. Martin, personal communication, 1997).

Compared to *10-year* means observed at Spitsbergen, the SCM compares favorably with the observations for the period that excludes the 1930's "jump". The origin of the "jump" is still debated, but due to the low-frequency nature, it is probably connected to oceanic processes. Such processes are not simulated by the single column model, but should be in the GFDL model.

---

[1] One explanation is that the winter air temperature does not experience the proper thermal inertial at the surface because the GFDL sea ice has zero heat capacity.

Table 6.3: Standard deviation ($\sigma_T$) of surface air temperature from the POLES data and from Spitsbergen (station at Longyearbyen) and from the two coupled models, GFDL GCM and SCM. $\sigma_T$ of monthly means for November-March and for 10-yr winter means (also November-March) are given. The POLES data are averaged over the central Arctic (see Fig. 5.1). The GFDL GCM output is averaged over a similar region chosen to represent the area covered by perennial ice (see Fig. 3.2). In the 1920's Spitsbergen experienced a 2 K temperature "jump" (seen at many high latitude stations) in temperature which is reflected in $\sigma_T$ for the 10-yr means. The number in parenthesis is $\sigma_T$ for 1932-1993 (to eliminate the "jump").

| model integrations/ observations | $\sigma_T$ (Kelvin) for monthly means | $\sigma_T$ (Kelvin) for 10-yr means |
|---|---|---|
| POLES data (1979-1994) | 2.1 | |
| Spitsbergen (1912-93) | 4.6 | 2.7 (1.6) |
| synthetic T | 2.2 | 0.39 |
| synthetic T near Spitsbergen | 3.2 | 0.39 |
| GFDL GCM | 3.8 | 0.67 |
| GFDL GCM near Spitsbergen | 5.8 | 1.1 |
| SCM - standard case | 4.9 | 1.4 |
| SCM - with export | 5.1 | 1.5 |
| SCM - hybrid $D$ | 3.9 | 0.85 |

The quiescent nature of the low-frequency variability of the surface air temperature jeopardizes the veracity of the estimate for low-frequency variability in the sea ice volume from the long integration with the dynamic/thermodynamic sea ice model. A more accurate estimate could be made if the model is coupled to an atmospheric general circulation model, which is an objective for future work with this model.

# Chapter 7

# DISCUSSION AND CONCLUSIONS

## *7.1 Summary*

I have modeled the low frequency natural variability of the arctic climate system with a single-column, energy balance model (SCM) of the atmosphere/sea ice/ocean system. Variability in the system is induced by forcing with realistic, random perturbations in the atmospheric energy flux convergence and cloudiness. The model predicts that the volume of perennial sea ice varies predominantly on multi-decadal time scales while other arctic climate variables vary mostly on intraannual and interannual time scales. The standard deviation of the monthly volume anomalies exceeds 25% of the mean. The variance of the simulated sea ice volume is most sensitive to perturbations of the atmospheric forcing in late spring, at the onset of melt. This suggests that much of the simulated variability develops during the late spring, when melting snow abruptly exposes the sea ice surface and changes the surface albedo. The variance of sea ice volume increases as the mean sea ice thickness increases and as the number of layers resolved in the sea ice model increases.

I contrasted the SCM results to that found in the Geophysical Fluid Dynamics Laboratory (GFDL) global general circulation model (GCM), and found that the variability in the sea ice of the GCM was one quarter of that in the SCM. I used the SCM diagnostically to help determine the reasons for the qualitative differences between the SCM and the arctic climate simulated by the GFDL GCM, and summarize the reasons below. When I inserted the GFDL sea ice physics into the SCM and then forced the model with the synthetic energy transport that is statistically

identical to that in the GFDL GCM, the sea ice thickness variance is similar to that from the "present climate" integration of the GFDL climate model. My results suggest that the GFDL GCM will exhibit substantially more natural variability in the arctic climate system if the treatment of sea ice is more physically realistic and if the variance of the atmospheric energy transport in the GFDL GCM is as energetic as the observed variability on seasonal to interannual time scales. The results suggest that the variability in the arctic climate is probably much more energetic than is being simulated in most GCMs.

I have constructed a dynamic/thermodynamic sea ice model for use in climate studies. Previous sea ice models used in climate studies have generally either emphasized ice thermodynamics or dynamics: almost without exception, the dynamic (thermodynamic) models severely compromise the ice thermodynamics (dynamics). In contrast, the model I have developed uses the viscous-plastic ice dynamics model from Zhang and Hibler (1997) and the essential thermodynamic physics that I determined are important for studying low frequency variability in chapters 2 and 3. The essential difference between this model and other sea ice models used in climate studies lies in the careful attention given to the thermodynamic treatment of sea ice and the implementation of a three- and four-category ice thickness distribution.

I integrated the dynamic/thermodynamic sea ice model with the historical record of forcing for 1979-1994 which is limited by the duration of reliable measurement of daily varying temperature over the Arctic Ocean. Because the duration of this record is only roughly equal to the timescale of natural variability for the ice thickness simulated by the single column model from chapter 2, the variance of the ice volume simulated by the dynamic/thermodynamic model is likely to underestimate the true variance. However, much can be learned about ice variability by examining the behavior of the model during the 16 yr period. Furthermore I have shown that the model results compare well with observation to demonstrate that this model is suitable for coupling to a atmosphere/ocean climate model.

Sensitivity tests to determine how variability in air temperature (and thus downward longwave flux anomalies) contributes to the volume anomalies reveal that air temperature anomalies primarily influence interannual (greater than 2 yr timescales) variability in the central region: without realistic air temperature anomalies, the low-frequency variance of the volume will be seriously underestimated.

Wind anomalies influence variability in the central region on interseasonal and, to a lesser extent, interannual timescales. Air temperature anomalies in the shelf region are also important but the wind anomalies tend to dominate the ice response in the marginal ice zones. Ice dynamics (including ridging and advection) forced by winds with the proper synoptic scale variability increase the sensitivity of the ice to air temperature anomalies. Interannual variations with typical magnitudes occur with perfectly periodic winds as long as they have realistic synoptic scale events.

I integrated the dynamic/thermodynamic sea ice model with synthetic temperature and wind anomalies to investigate the low-frequency ice variability. For the central region the standard deviation of the monthly volume anomalies is 9% of the mean and the characteristic timescale of the variability is 3 years. I examined the frequency of ice concentration minima at the level of the 1990 ice minimum and found they occur every 130 years. The frequency of export anomalies for 3-yr running sums that could supply a freshwater anomaly at the level of the Great Salinity Anomaly is one every 100 years.

## *7.2 Future Work*

- Study sensitivity of long integration to synthetic forcing in a manner similar to the experiments performed in Chapter 5 with the observed forcing datasets. Integrate the model with thermodynamics only (synthetic temperature fields with no geostrophic winds).

- Repeat the hindcast with the 1979-1994 forcing data sets truncated to the same

number of modes as are kept in the long integration.

- Explore how the individual modes of the pressure and temperature influence the sea ice by performing integrations with the pressure and temperature anomalies constructed one mode at a time.

- Refine the ridging parameterizations for three and four thickness category models.

- Couple the new advanced dynamic/thermodynamic sea ice model to an atmospheric and ocean general circulation model to study sea ice variability in a coupled model and to determine the Arctic sea ice influence on the climate system.

# BIBLIOGRAPHY


Aagaard, K. and E. C. Carmack, 1989: The role of sea ice and other fresh water in the Arctic circulation. *J. Geophys. Res.*, **94**, 14485–14498.

Barsugli, J., 1995: *Idealized models of intrinsic midlatitude atmosphere-ocean interaction.* Ph.D. thesis, University of Washington, Seattle WA.

Bettge, T. W., J. W. Weatherly, W. M. Washington, D. Pollard, B. P. Briegleb and W. G. Strand Jr., 1996: *The NCAR CSM Sea Ice Model.* NCAR Technical Note, TN-425+STR.

Bourke, R. H. and R. P. Garret, 1987: Sea ice thickness distribution in the arctic ocean. *Cold Regions Sci. and Tech.*, **13**, 259–280.

Boyle, J. E., 1993: Sensitivity of dynamical quantities to horizontal resolution for a climate simulation using the ECMWF (cycle 33) model. *J. Climate*, **6**, 796–815.

Brown, R. A., 1980: Planetary boundary layer modeling for AIDJEX. in R. S. Pritchard, editor, *Sea Ice Processes and Models*, p. 474pp. University of Washington Press.

Chapman, W. L. and J. E. Walsh, 1993: Recent variations of sea ice and air temperature in high latitudes. *Bull. Amer. Meteor. Soc.*, **74**, 33–47.

Chapman, W. L., W. J. Welch, K. P. Bowman, J. Sacks and J. E. Walch, 1994: Arctic sea ice variability: Model sensitivies and a multidecadal simulation. *J. Geophys. Res.*, **99**, 919–935.

Colony, R. and A. S. Thorndike, 1985: Sea ice motion as a drunkard's walk. *J. Geophys. Res.*, **90**, 965–974.

Delworth, T., S. Manabe and R. J. Stouffer, 1993: Interdecadal variations of the thermohaline circulation in a coupled ocean-atmosphere model. *J. Climate*, **6**, 1993–2011.

Delworth, T., S. Manabe and R. J. Stouffer, 1997: Multidecadal climate variability in the greenland sea and surrounding regions: a coupled model simulation. *Geophys. Res. Lett.*, **24**, 257–260.

Deser, C. and M. L. Blackmon, 1993: Surface climate variations over the North Atlantic Ocean during winter: 1900- 1989. *J. Climate*, **6**, 1743–1753.

Dickson, R. R., J. Meincke, S. A. Malmberg and A. J. Lee, 1988: The 'Great Salinity Anomaly' in the northern North Atlantic 1968-1982. *Prog. Oceanogr.*, **20**, 103–151.

Ebert, E. E. and J. A. Curry, 1993: An intermediate one-dimensional thermodynamic sea ice model for investigating ice-atmosphere interactions. *J. Geophys. Res.*, **98**, 10085–10109.

Fang, Z. and J. M. Wallace, 1994: Arctic sea ice variability on a timescale of weeks and its relation to atmospheric forcing. *J. Climate*, **7**, 1897–1913.

Flato, G. M., 1995: Spatial and temporal variability of arctic ice thickness. *Annals of Glaciology*, **21**, 323–29.

Flato, G. M. and W. D. Hibler, 1992: Modeling pack ice as a cavitating fluid. *J. Phys. Oceanogr.*, **22**, 626–651.

Flato, G. M. and W. D. Hibler, 1995: Ridging and strength in modelling the thickness distribution of Arctic sea ice. *J. Geophys. Res.*, **C9**, 18611–18626.

Frankignoul, C. and K. Hasselmann, 1977: Stochastic climate models, part II Application to sea-surface temperature anomalies and thermocline variability. *Tellus*, **29**, 289–305.

Gloerson, P., W. J. Campbell, D. J. Cabalieri, J. C. Comiso, C. L. Parkinson and H. J. Zwally, 1992: *Arctic and Antarctic sea ice 1978-1987: Satellite passive microwave observations and analysis.* NASA.

Grenfell, T. C. and G. A. Maykut, 1977: The optical properties of ice and snow in the arctic basin. *J. Glaciol.*, **18**, 445–463.

Häkkinen, S., 1993: An Arctic source for the great salinity anomaly: A simulation of the Arctic ice-ocean system for 1955-1975. *J. Geophys. Res.*, **98**, 16397–16410.

Häkkinen, S. and G. L. Mellor, 1990: One hundred years of Arctic ice cover variations as simulated by a one-dimensional, ice-ocean model. *J. Geophys. Res.*, **95**, 15959–15969.

Hasselmann, K., 1976: Stochastic climate models, Part I. *Tellus*, **28**, 473–485.

Held, I. M. and P. J. Phillipps, 1993: Sensitivity of the eddy momentum flux to meridional resolution in atmospheric GCMs. *J. Climate*, **6**, 499–507.

Hibler, W. and J. Zhang, 1993: Interannual and climatic characteristics of an ice ocean circulation model. in W. R. Peltier, editor, *Ice and the Climate System*, Vol. Series I, Vol.12, pp. 633–652. NATO ASI Series.

Hibler, W. D., 1979: A dynamic thermodynamic sea ice model. *J. Phys. Oceanogr.*, **9**, 815–846.

Hibler, W. D., 1980: Modeling a variable thickness ice cover. *Mon. Wea. Rev.*, **108**, 1943–1973.

Houghton, J. T., G. J. Jenkins and J. J. Ephraums, Eds., 1990: *Climate Change The IPCC Scientific Assessment.* Cambridge.

Hunt, B. G., B. Gordon and H. L. Davies, 1995: Impact of the Greehouse Effect on sea ice characteristics and snow accumulation in the polar regions. *International J. of Climatology*, **15**, 3–23.

Jayne, S. R. and J. Marotzke, 1997: A destabilizing thermohaline circulation - atmosphere - sea ice feedback. submitted to J. Climate.

Jenkins, G. M. and D. G. Watts, 1968: *Spectral Analysis and Its Applications.* Holden-Day.

Kiehl, J. T., J. J. Hack, B. G. B. Bonan, B. A. Boville, P. Briegleb, D. L. Williamson and P. J. Rasch, 1996: *Description of the NCAR Community Climate Model (CCM3).* NCAR Technical Note, TN-420+STR.

Lau, N. C., S. G. H. Philander and M. J. Nath, 1992: Simulation of El Niño/Southern Oscillation phenomenon with a low-resolution coupled general circulation model of the global ocean and atmosphere. *J. Climate*, **5**, 284–307.

Ledley, T. S., 1988: A coupled energy balance climate-sea ice model: Impact of sea ice and leads on climate. *J. Geophys. Res.*, **93**, 15919–15932.

Lemke, P., E. W. Trinkl and K. Hasselmann, 1980: Stochastic dynamic analysis of polar sea ice variability. *J. Phys. Oceanogr.*, **10**, 2100–2120.

MacKay, R. M. and M. A. K. Khalil, 1991: Theory and development of a one dimensional time dependent radiative convective climate model. *Chemosphere*, **22**, 383–417.

Manabe, S., M. J. Spellman and R. J. Stouffer, 1992: Transcient responses of a coupled ocean-atmosphere model to gradual changes of atmospheric $CO_2$. II. Seasonal response. *J. Climate*, **5**, 105–126.

Manabe, S., R. J. Stouffer, M. J. Spellman and K. Bryan, 1991: Transcient responses of a coupled ocean-atmosphere model to gradual changes of atmospheric $CO_2$. Part I. Annual mean response. *J. Climate*, **4**, 785–818.

Manabe, S. and R. F. Strickler, 1964: Thermal equilibrium of the atmosphere with convective adjustment. *J. Atmos. Sci.*, **21**, 361–385.

Manabe, S. J. and R. J. Stouffer, 1996: Low-frequency variability of surface air temperature in a 1000-year integration of a coupled ocean-atmosphere model. *J. Climate*, **9**, 376–393.

Martin, S. and E. A. Munoz, 1997: Properties of the Arctic 2-meter air temperature field for 1979 to the present derived from a new gridded dataset. *J. Climate*, **10**, 1428–1440.

Maykut, G. A., 1969: *A thermodynamic model of sea ice.* Ph.D. thesis, University of Washington.

Maykut, G. A., 1982: Large-sclae heat exchange and ice production in the central Arctic. *J. Geophys. Res.*, **87**, 7971–7984.

Maykut, G. A. and D. Perovich, 1987: The role of shortwave radiation in the summer decay of a sea ice cover. *J. Geophys. Res.*, **92**, 7032–7044.

Maykut, G. A. and N. Untersteiner, 1971: Some results from a time-dependent thermodynamic model of sea ice. *J. Geophys. Res.*, **76**, 1550–1575.

McLaren, A. S., R. H. Bourke, J. E. Walsh and R. L. Weaver, 1994: Variability in sea-ice thickness over the North Pole from 1958 to 1992. in O. M. Johannessen, R. D. Muench and J. E. Overland, editors, *Polar Oceans and their role in shaping the global environment.* American Geophysical Union.

McPhee, M. G., 1975: Ice-ocean momentum transfer for the AIDJEX ice model. *AIDJEX Bull.*, **29**, 93–111.

McPhee, M. G., 1992: Turbulent heat flux in the upper ocean under sea ice. *J. Geophys. Res.*, **97**, 5365–5379.

Mitchell, J. F. B., T. C. Johns, J. M. Gregory and S. F. B. Tett, 1994: Climate response to increasing levels of greenhouse gases and sulfate aerosols. *Nature*, **376**, 501–504.

Mysak, L. A., D. K. Manak and R. F. Marsden, 1990: Sea-ice anomalies observed in the greenland and labrador seas during 1901-1984 and their relation to an inter-decadal arctic climate cycle. *Climate Dynamics*, **5**, 111–133.

Nakamura, N. and A. H. Oort, 1988: Atmospheric heat budgets of the polar regions. *J. Geophys. Res.*, **93**, 9510–9524.

Overland, J. E. and C. H. Pease, 1982: Cyclone climatology of the vering sea and its relation to sea ice extent. *Mon. Wea. Rev.*, **110**, 5–13.

Overland, J. E. and C. H. Pease, 1988: Modeling ice dynamics of coastal seas. *J. Geophys. Res.*, **93**, 15,619–16,637.

Overland, J. E. and P. Turet, 1994: Variability of the atmospheric energy flux across 70 N computed from the GFDL data set. in O. M. Johannessen, R. D. Muench and

J. E. Overland, editors, *Polar Oceans and their role in shaping the global environment.* American Geophysical Union.

Parkinson, C. L. and W. M. Washington, 1979: A large-scale numerical model of sea ice. *J. Geophys. Res.*, **84**, 311–337.

Peixoto, J. P. and A. H. Oort, 1992: *Physics of Climate.* American Institute of Physics.

Pollard, D. and S. L. Thompson, 1994: Sea-ice dynamics and $CO_2$ sensitivity in a global climate model. *Atm. Ocean*, **32**, 449–467.

Reif, F., 1965: *Fundamentals of Statistical and Thermal Physics.* McGraw-Hill, Inc., pp. 651.

Rogers, J. C., 1978: Meteorological factors affecting the interannual variability of summertime ice extent in the beaufort sea. *Mon. Wea. Rev.*, **106**, 890–897.

Ross, B. and J. E. Walsh, 1987: A comparison of simulated and observed fluctuations in summertime arctic surface albedo. *J. Geophys. Res.*, **92**, 13,115–13,125.

Rothrock, D. A., 1975: The steady drift of an incompressible arctic ice cover. *J. Geophys. Res.*, **80**, 387–397.

Rothrock, D. A., 1986: Ice thickness distribution-measurement and theory. in N. Untersteiner, editor, *The Geophysics of Sea Ice*, pp. 551–575. Plenum.

Rothrock, D. A. and A. S. Thorndike, 1984: Measuring the sea ice floe size distribution. *J. Geophys. Res.*, **89**, 6477–6486.

Schweitzer, P. N., 1995: Monthly average polar sea-ice concentration. see http://geochange.er.usgs.gov/pub/sea_ice/A_README.1ST.

Semtner, A. J., 1976: A model for the thermodynamic growth of sea ice in numerical investigaions of climate. *J. Phys. Oceanogr.*, **6**, 379–389.

Serreze, M. C., J. A. Maslanik, J. R. Key and R. F. Kokaly, 1995: Diagnosis of the record minimum in Arctic sea ice area during 1990 and associated snow cover extremes. *Geophys. Res. Lett.*, **22**, 2183–2186.

Shy, T. L. and J. E. Walsh, 1996: North pole ice thickness and association with ice motion history 1977-1992. *Geophys. Res. Lett.*, **23**, 2975–2978.

Steele, M., 1992: Sea ice melting and floe geometry in a simple ice-ocean model. *J. Geophys. Res.*, **97**, 17,729–17,738.

Stern, H. L., D. A. Rothrock and R. Kwok, 1995: Open water production in arctic sea ice: satellite measurements and model parameterizations. *J. Geophys. Res.*, **100**, 20,601–12.

Thorndike, A. S., 1992a: Estimates of sea ice thickness distribution using observations and theory. *J. Geophys. Res.*, **97**, 12601–12605.

Thorndike, A. S., 1992b: A toy model linking atmospheric thermal radiation and sea ice growth. *J. Geophys. Res.*, **97**, 9401–9410.

Thorndike, A. S., D. S. Rothrock, G. A. Maykut and R. Colony, 1975: The thickness distribution of sea ice. *J. Geophys. Res.*, **80**, 4501–4513.

Untersteiner, N., 1961: On the mass and heat budget of arctic sea ice. *Arch. Meteorol. Geophys. Bioklimatol., A*, **12**, 151–182.

Untersteiner, N., 1990: Some problems of sea ice and climate modelling. in *Veröffentlichungen der Universität of Innsbruck*, pp. 209–228.

Walsh, J. E., W. D. Hibler and B. Ross, 1985: Numerical simultion of northern hemisphere sea ice variability 1951-1980. *J. Geophys. Res.*, **90**, 4847–4865.

Walsh, J. E. and J. E. Sater, 1981: Monthly and seasonal variability in the ocean-uce-atmosphere system of the North Pacific and the North Atlantic. *J. Geophys. Res.*, **86**, 7425–7445.

Walsh, J. E. and H. J. Zwally, 1990: Multiyear sea ice in the Arctic: model- and satellite-derived. *J. Geophys. Res.*, **95**, 11613–11628.

Wang, J., L. A. Mysak and R. G. Ingram, 1994: Interannual variability of sea-ice cover in hudson bay, baffin bay and the labrador sea. *Atmosphere-Ocean*, **32**, 421–447.

Weeks, W. S. and S. F. Ackley, 1986: The growth, structure, and properties of sea ice. in N. Untersteiner, editor, *The Geophysics of Sea Ice*, Vol. Series B, Physics Vol.146, pp. 9–164. NATO ASI Series.

Wohlleben, T. M. H. and A. J. Weaver, 1995: Interdecadal climate variability in the subpolar North Atlantic. *Climatic Dynamics*, **11**, 459–467.

Zhang, J. and W. Hibler, 1997: On an efficient numerical method for modeling sea ice dynamics. *J. Geophys. Res.*, **102**, 8691–8702.

# Vita

I was born in Portland, Oregon, in 1966. I earned a bachelors degree in engineering physics from Oregon State University in June, 1988 and a masters degree in physics from University of Washington in June, 1990. After pursuing a Ph.D. in physics for two years at University of Washington, I realized that my true interests lie in the study of climate. I transferred from the department of physics to atmospheric sciences in 1993.

During the 1995-96 academic year, I helped establish and filled a new position to mentor the teaching assistants in the atmospheric sciences department. I have teaching experience in undergraduate atmospheric physics and physics laboratory classes in modern physics and classical mechanics.